NANOPHOTONICS WITH CHARGED PARTICLES

DOCTORAL THESIS

Dissertation submitted by
VALERIO DI GIULIO
in partial fulfilment of the requirements for the degree of
Doctor of Philosophy

Supervisor: PROF. FRANCISCO JAVIER GARCÍA DE ABAJO

ICFO - INSTITUT DE CIÈNCIES FOTÒNIQUES
BARCELONA, 2023

This Thesis was defended in front of a selected committee, composed by the following members:

- *External member:*
  Prof. Mathieu Kociak,
  Université Paris-Saclay, CNRS, Laboratoire de Physique des Solides, 91405, Orsay, France.
- *External member:*
  Prof. Claus Ropers,
  Max Planck Institute for Multidisciplinary Sciences, and Physical Institute – Solids and Nanostructures, University of Göttingen, 37077 Göttingen, Germany.
- *Internal member:*
  Prof. Alejandro Manjavacas,
  Instituto de Óptica (IO-CSIC), Consejo Superior de Investigaciones Científicas, Madrid 28006, Spain, and Department of Physics and Astronomy, University of New Mexico, Albuquerque, New Mexico 87106, USA.

This doctoral dissertation has been carried out in the Nanophotonics Theory Group at ICFO - The Institute of Photonic Sciences in Castelldefels (Barcelona), thanks to the funding of the European Commission through the Marie Skłodowska-Curie Grant n. 713729.

To
my mother
and
my father.

Acknowledgments

After all, it has been almost 5 entire years. I started that I was 24, and I finish the I am 29. During this long period of time, I have interacted, exchanged ideas, had joyful and sad moments with several people. Most of them are still close (or spatially far) to me, while unfortunately others, are not walking with us anymore. However, I dedicate this Thesis to both of them whom I warmly thank for sharing with me such time. Even tough among my best qualities I cannot enumerate *memory*, I believe I will not forget to thank anyone in these acknowledgments as the time spent in doing this research is profoundly impressed in myself.

My special and deep recognition goes to my PhD advisor and mentor Javier. His knowledge of all physical processes and his ability of exploring the world with the only help of paper, pen and a, no so powerful, computer have always surprised me. He taught me how to practically take an idea a made it real, from the far from reality equation to the actual numbers, which could be measured in a lab.

At my mother Roberta, I want to say *thank you!* to be always close to me, which does not mean always taking my side as most of the times you were on the other, but means to be there in helping me and making me feel that whatever happened there was always a place which I could call *home*. I want to also thank my brother Ivan, to also be there, immutable in his relation with me, keeping to be one of the few people who really understands who I am.

Proudly, to my dare Laura, with whom I shared almost all the feelings and memories in these last two and half years, I owe my gratitude for supporting me throughout maybe the darkest moments of my life and reorienting me towards the path leading to light in every occasion. If I had the strength to reach this moment is because you were at my side, and at this point, I am happy to have the chance to say that: the best still needs to come!

I thank also my friends, still colleagues or not, at ICFO, Hani, Robin, Stefano, Francesco and Arvin for the nice discussions, parties and experiences shared together. A profound gratitude goes to all NPT members, especially to my colleagues Eduardo and Alvaro for sharing with me almost the entire path in which we discussed, suffered, laughed and traveled together. *Thanks!* The day-to-day life at the institute would not have been the same without your company.

Impossible to miss are my acknowledgments to the "Gruppo U+1F4A9", namely to its current members Gabriele, Alessia, Arianna, Daniele, Giulio, Matteo D. C., Raul, Rita, Simone e Matteo G., for the ever active support and because luckily after so many years and so many kilometers dividing each other, our fellowship is still so strong.

I want also to thank Susanna for supporting me during the first part of this path.

Grazie, to my friends in Rome. You were always ready to welcoming me whenever I was coming back craving for a taste of home. This happening unavoidably in an osteria in front of a good, maybe not that good wine and a you-need-to-grow size plate of pasta.

I would like also to share my gratitude with Timm, who made the graphics on the bottom part of the Thesis cover. I am sure, it was not easy to capture whatever nonsense impression I gave him when he asked me "What's your thesis about?", and I did not know exactly where to start from. Despite this, he did an incredible job at capturing the uncapturable, in just an image.

Contents

Thesis outline

This PhD Thesis, entitled **Nanophotonics with charged particles**, is composed of several chapters, each one based on one or more published scientific articles. Generally, they address different topics but at the same time, they meaningfully link to each other by following a continuous line of research. In particular, their content and interconnections has been organized in the following chapters:

(1) **Introduction:** the background notions required to be capable of understanding the content of the Thesis are briefly presented in a self-contained manner. In particular, we cover several topics such as classical electromagnetism, quantum electrodynamics, the classical description of photon-induced near-field electron microscopy technique, quantum optics, and the basic theory of electron liquids.

(2) **Quantum photon-induced near-field electron microscopy:** we present a work generalizing the classical theory of photon-induced near-field electron microscopy by describing the optical field to be prepared and evolve quantum mechanically. Here, an analytical solution of the post-interaction electron-field state is found for any initial quantum state of light.

(3) **Free-electron shaping using quantum light:** the solution found in Chapter (2) is exploited in order to discuss the effect of quantum light on the shaping of the wave function of a free electron beam. In addition, such theory is also expanded in order to accommodate free space propagation.

(4) **Electron diffraction by vacuum fluctuations:** the results of this chapter are also intimately connected to Chapter (2). Indeed, it aims at deepening our understanding about a phase appearing in the quantum electrodynamical solution found in Chapter (2). In a systematic way, the phase is analyzed by means of different theoretical tools such as the continuous quantization of the electromagnetic field degrees of freedom.

(5) **Modulation of cathodoluminescence emission by interference with external light:** this chapter is devoted to the analyses of the cathodoluminescence emission from syncronized laser and electron pulses whose wave function has been previously shaped. In this regard, it connects with Chapter (3). In addition, the results of this work are mainly based on the field quantization presented in Chapter (4).

(6) **An image interaction approach to quantum-phase engineering of two-dimensional materials:** we present a work inspired in the application of the knowledge acquired in Chapter (4) to two-dimensional solid-state systems. In particular, the acquired electron phase is exploited to modify the dynamics of the charge carriers and in turn the optical and transport properties of the material itself.

(7) **Nanophotonics for pair-production:** we investigate the possibility of tailoring the rates associated with high-energy processes by leveraging the optical field confinement concept of common use in nanophotonics. In particular, we focus on electron-positron production as a result of the collision between polaritons and high-energy photons. This research represents the only work in this Thesis that does not consider electrons as protagonists and, therefore, is more detached from the rest of the chapters, apart from Chapter (1), where the necessary theoretical tools are discussed.

(8) **Conclusions and outlook:** a summary of all the results achieved and presented in this Thesis is made. Special attention is devoted to the impact that these works have on the related research communities. Finally, a look at current and future possible directions is given by taking the contents of this Thesis as the starting point of an ongoing discussion.

The Thesis is supplemented by appendices on the unit system employed and technical details to make the work self-contained. We conclude with lists of figures, acronyms, and publications and conference contributions derived from the present work.

Abstract

Among the fundamental constituents of matter, charged particles such electrons and positrons are leading protagonists in physical phenomena associated with small ($\sim$ meV) and high ($\sim$ MeV) energy scales. For example, conductive electrons in condensed-matter systems can collectively respond to the action of an external electromagnetic field and sustain plasmon excitations that dominate their visible optical behavior. The presence of material boundaries produces a dramatic modulation of such modes, allowing us to mold their interaction with light for the exploration of fundamental phenomena and the design of practical applications, which are central themes in the field of nanophotonics.

Electrons traveling in free space, such as those in electron microscopes, constitute ideal probes for imaging materials with nanometric resolution. In an effort to push energy resolution down to the meV regime and simultaneously perform time-resolved measurements with fs precision, laser and electron pulses in transmission electron microscopes can now be synchronized to meet at the specimen in the so-called photon-induced near-field electron microscopy (PINEM). Here, efficient electron coupling to intense laser-driven evanescent fields results in a strong energy reshaping of the electron wave function. Over the last decade, PINEM has been used to tailor the wave function of free electrons, thus emphasizing the role of these microscopy probes as information carriers.

This Thesis lies in this general and broad context as an effort to explore new scenarios in the interaction between free electrons and optical excitations. In particular, Chapter 2 addresses the theoretical investigation of quantum-mechanical aspects associated with PINEM interaction by means of a quantum-optics description of the optical field. Building up on those results, in Chapter 3 we show that improved control over electron pulse shaping, compression, and statistics can be gained by replacing coherent laser excitation by interaction with quantum light, such as phase- and amplitude-squeezed optical fields.

Chapter 4 explores the role played by fluctuations of the electromagnetic vacuum in the coupled dynamics of a free-electron beam and a macroscopic object, producing elastic diffraction and decoherence. In particular, we show that diffraction can dominate over decoherence, therefore suggesting a nondestructive approach to microscopy based on the specific choice of parameters that minimize the inelastic interaction with the specimen.

As a radically different aspect of electron-light interaction, Chapter 5 is devoted to the study of the interference produced in the cathodoluminescence emission by the synchronized interaction of free electrons and dimmed laser pulses scattered by the specimen. Here, we argue that such effect may enable measurements combining the spectral and temporal selectivity of the light with the atomic resolution of electron beams to resolve the phase associated with optical modes in the sample.

In Chapter 6, we consider that elastic diffraction, similar to that studied in Chapter 4, is also experienced by conduction electrons in a two-dimensional material, therefore altering the properties of the latter by simply adding a neighboring neutral structure.

Going to higher energy scales, Chapter 7 explores the potential of confined optical modes to assist electron-positron pair production arising from the scattering of gamma rays by surface polaritons propagating along a material interface.

In summary, throughout this Thesis we exploit the coupling between evanescent light, harnessed in the vicinity of material boundaries, and charged free particles in order to access new effects only found at the point where nanophotonics, quantum optics and high-energy physics meet through strong light-matter interaction.

Resum

Entre els constituents fonamentals de la matèria, partícules carregades com electrons i positrons són protagonistes en fenòmens físics associats amb escales d'energia petites ($\sim$ meV) i altes ($\sim$ MeV). Per exemple, els electrons conductors en sistemes de matèria condensada poden respondre col·lectivament a l'acció d'un camp electromagnètic extern, exhibint excitacions de plasmó que dominen el seu comportament òptic en el visible. La presència de límits materials produeix una modulació dramàtica d'aquests modes que permet modelar la seva interacció amb la llum per a l'exploració de fenòmens fonamentals i el disseny d'aplicacions pràctiques, temes centrals en el camp de la nanofotònica.

Els electrons que viatgen a l'espai lliure, com els dels microscopis electrònics, constitueixen sondes ideals per a observar materials amb resolució nanomètrica. Per tal de millorar la resolució energètica fins al règim dels meV i alhora realitzar mesures resoltes en el temps amb precisió de fs, els polsos làser i els electrons en microscopis electrònics de transmissió es poden sincronitzar per trobar-se a la mostra en l'anomenada microscòpia electrònica de camp proper induïda per fotó (PINEM). L'eficiència de l'acoblament de l'electró a camps evanescents intensos produïts per làser provoca una forta remodelació d'energia de la funció d'ona dels electrons. Durant l'última dècada, la tècnica PINEM s'ha utilitzat per adaptar la funció d'ona dels electrons lliures, emfatitzant així el paper d'aquestes sondes de microscòpia com a portadores d'informació.

Aquesta tesi representa un esforç per explorar nous escenaris en la interacció entre electrons lliures i excitacions òptiques. En particular, el Capítol 2 aborda la investigació teòrica dels aspectes de mecànica quàntica associats amb la interacció PINEM mitjançant una descripció d'òptica quàntica del camp òptic. Basant-nos en aquests resultats, en el Capítol 3 mostrem que es pot millorar el control sobre la formació, compressió i estadística del pols d'electrons mitjançant la substitució de l'excitació làser coherent per la interacció amb llum quàntica, com ara camps òptics de fase i amplitud.

El Capítol 4 explora el paper que juguen les fluctuacions del buit electromagnètic en la dinàmica acoblada d'un feix d'electrons lliures i un objecte macroscòpic, produint difracció elàstica i decoherència. En particular, demostrem que la difracció pot dominar sobre la decoherència, suggerint un enfocament no destructiu de la microscòpia basat en l'elecció específica de paràmetres que minimitzen la interacció inelàstica amb l'espècimen.

Com a aspecte radicalment diferent de la interacció entre llum i electrons, el Capítol 5 està dedicat a l'estudi de la interferència produïda en l'emissió de catodoluminescència per la interacció sincronitzada d'electrons lliures i polsos làser enfosquits dispersats per l'espècimen. Argumentem que aquest efecte pot permetre mesures combinant la selectivitat espectral i temporal de la llum amb la resolució atòmica dels feixos d'electrons per resoldre la fase associada amb els modes òptics en la mostra.

En el Capítol 6, considerem que la difracció elàstica, similar a l'estudiada en el Capítol 4, també és experimentada per electrons de conducció en un material bidimensional, alterant així les seves propietats simplement afegint una estructura neutral veïna.

A escales d'energia més altes, el Capítol 7 explora el potencial dels modes òptics confinats per assistir en la producció de parells electró-positró que sorgeix de la dispersió de raigs gamma per polaritons de superfície que es propaguen en la interfície d'un material.

En resum, a través d'aquesta tesi explotem l'acoblament entre la llum evanescent, aprofitada en la proximitat dels límits dels materials, i les partícules lliures carregades per tal d'accedir a nous efectes només observables en el punt on la nanofotònica, l'òptica quàntica i la física d'altes energies es troben a través d'una forta interacció llum-matèria.

1

Introduction

Not all who wander are lost.
J.R.R. Tolkien, The Fellowship of the Ring.

Starting an in-depth reading can increase the chances of getting lost and leaving the reader in a more confused state than when they started. This often happens due to a lack of a solid foundation when jumping directly into advanced sections of the text. To avoid this, this Chapter is meant to guide the reader through the main concepts of the Thesis, saving time and improving understanding.

The use of charged particles such as ions, electrons, and positrons to address different problems can be traced back to the time of the discovery of electricity. For instance, electrons in materials have been used since the 19th century to transmit information through electrical signals in metals and, even before the discovery of the electron itself, in radio communication thanks to their ability to produce free space electromagnetic waves. A few decades later, the invention of instruments such as the electron microscope (E. Ruska, Ref. 1) presented free electrons as candidate probes that, through electromagnetic interaction with a specimen, could retrieve spectral and structural information.

It is therefore clear that control over the coupling between free electrons and electromagnetic fields is of great interest for several communities. In this context, the realm of Nanophotonics (the study of light-matter interaction at the nanometer scale), enters naturally as an important element by suggesting ways to produce fields concentrated in a region of spatial extension commensurate with the one of the free electron. A perfect example is represented by the confined excitations called plasmons, which are collective oscillations of electrons in conductive materials, able to provide nanoscale focusing of the optical field.

This promise of high coupling to increase more with decreasingly structure sizes has resulted in a booming interest in combining Nanophotonics with other research areas: quantum optics with free electrons, dynamical modification of charge carriers in solid state matter, field enhancement boosting of quantum electrodynamics processes such as electron-positron pair production.

In order to be capable of capturing all the details behind these effects, here we review the fundamental theoretical tools used as building blocks for the development and understanding of this Thesis. In particular, the following topics are covered:

- **Classical electrodynamics and nanophotonics:** we first introduce Maxwell's equations in the presence of complex media, focusing on the specific case in which nonlocal effects are negligible. We then review the concept of gauge invariance of the electromagnetic theory including the gauge choice mostly used in this Thesis. We introduce the electromagnetic Green tensor to solve electromagnetic problems, focusing on simple configurations. Among them, the planar interface is also utilized to introduce the concept of surface plasmons. Finally, with the help of these tools, we review how to estimate classical probabilities related to electron energy-loss and cathodoluminescence spectroscopies.

- **The interaction of classical fields with quantum matter:** we begin by reviewing the Dirac equation trough which relativistic quantum charges of spin 1/2 can be described to be coupled to classical electromagnetic fields. Then, we gradually introduce different key approximations needed to transform the complex non-perturbative electron-light interaction to a treatable problem, highlighting the fact that they remarkably work under experimental conditions typical of electron microscopy. Finally, we present the theory behind the classical PINEM interaction in which an electron strongly couples to evanescent optical fields created by a laser pulse scattered by a material boundary.

- **The interaction of quantized fields in complex environments with quantum matter:** we introduce the theoretical framework of macroscopic quantum electrodynamics through which the electromagnetic degrees of freedom are quantized in the presence of local, absorbing, non-magnetic media. We pay special attention to presenting the physical arguments on which the framework is grounded. Furthermore, by reviewing a quantization procedure that employs a discrete number of modes, we introduce the reader to the fundamental building elements of quantum optics.

- **Theory of screening and linear response:** we review the standard theory used to compute linear response functions from first-principles quantum mechanics. We focus on the evaluation of the induced charge density produced in a medium when perturbed by interaction with an external electric scalar potential. This is done through the use of the random-phase approximation (RPA) based on the self-consistent field theory, which is also briefly discussed. Finally, we apply these tools both to introduce the reader to a key analytical result related to the response of a two-dimensional (2D) free-electron gas and to present specific methods used to deal with periodic systems.

1.1 Introduction to classical electrodynamics

If one wishes to describe the interaction among charged particles and with other complex material structures, which ultimately are also formed by the same kinds of particles, one should first understand how all these elements talk to each other and the underlying equations governing their dynamics. The theory describing such interaction between classical particles is known as *classical electrodynamics*.

1.1.1 Maxwell's equations

Charges represent the sources of a field which in turn act on their dynamics in a self-consistent fashion. In particular, the rules determining how such field, the *electromagnetic field*, evolves in space and time were the result of a combined effort involving many scientist who were studying the subject in the 19th century. They, with the culminating work by J. C. Maxwell [2], were able to beautifully condense them into four equations, Maxwell's equations (MEQS), which in frequency domain read[1] [3]

$$\nabla \cdot \mathbf{D}(\mathbf{r},\omega) = 4\pi\rho(\mathbf{r},\omega), \tag{1.1a}$$

$$\nabla \cdot \mathbf{B}(\mathbf{r},\omega) = 0, \tag{1.1b}$$

$$\nabla \times \mathbf{E}(\mathbf{r},\omega) = \mathrm{i}k\mathbf{B}(\mathbf{r},\omega), \tag{1.1c}$$

$$\nabla \times \mathbf{H}(\mathbf{r},\omega) = \frac{4\pi}{c}\mathbf{j}(\mathbf{r},\omega) - \mathrm{i}k\mathbf{D}(\mathbf{r},\omega), \tag{1.1d}$$

where we have introduced the wave vector modulus of an electromagnetic wave in free space $k = \omega/c$. In practice, Eqs. (1.1) determine the displacement field $\mathbf{D}$, the electric field $\mathbf{E}$, the magnetizing field $\mathbf{H}$ and the magnetic field $\mathbf{B}$, once the free charges ρ and currents $\mathbf{j}$ are given[2]. We highlight the fact that charges and currents depend on one another through the continuity equation

$$\nabla \cdot \mathbf{j}(\mathbf{r},\omega) = \mathrm{i}\omega\rho(\mathbf{r},\omega), \tag{1.2}$$

which can be derived from Eqs. (1.1). If we assume that all the media under consideration have a negligible nonlinear response, we can write general constitutive relations $\mathbf{D}(\mathbf{r},\omega) = \int d^3\mathbf{r}'\,\epsilon(\mathbf{r},\mathbf{r}',\omega)\mathbf{E}(\mathbf{r}',\omega)$ and $\mathbf{H}(\mathbf{r},\omega) = \int d^3\mathbf{r}'\,\mu^{-1}(\mathbf{r},\mathbf{r}',\omega)\mathbf{B}(\mathbf{r}',\omega)$, by introducing the permittivity ϵ and the permeability μ, which are the response functions encapsulating all the microscopic characteristics of the materials composing the system under study. In general, these response functions have the form of 3×3 tensors and depend both on the spatial position where the field is applied $\mathbf{r}'$ and where it is probed $\mathbf{r}$. Since they contain the details of the motion of all the material constituents, such as electrons and nuclei in solids, their accurate evaluation typically requires advanced theoretical and numerical tools, some of which we shall describe in Section 1.4.

In situations for which all the distances involved are much larger than the microscopic features, usually $\lesssim 1$ nm, as dictated by inter-atomic spacing, and the

---

[1] Throughout this work, we use the convention $f(\mathbf{r},t) = \int (d^3\mathbf{k}\,d\omega/16\pi^4)\,\mathrm{e}^{\mathrm{i}\mathbf{k}\cdot\mathbf{r}-\mathrm{i}\omega t}\,f(\mathbf{k},\omega)$ to go from space and time domain $(\mathbf{r},t)$ to Fourier space $(\mathbf{k},\omega)$. Furthermore, Gaussian Units (GU) are adopted. See Appendix A to learn how to transform electromagnetic quantities from Gaussian to SI units.

[2] With the word *free*, we mean to distinguish them from the charges and currents that are bound to a material or molecule. See, for example Ref. 4, and the discussion on surface charges and currents therein.

material isotropically polarizes along the three Cartesian directions, the so-called local isotropic approximation can be safely employed and the response tensors turn out to be proportional to the identity matrix. In this case, the relations $\epsilon(\mathbf{r},\mathbf{r}',\omega)=\epsilon(\mathbf{r},\omega)\delta(\mathbf{r}-\mathbf{r}')\mathcal{I}$ and $\mu(\mathbf{r},\mathbf{r}',\omega)=\mu(\mathbf{r},\omega)\delta(\mathbf{r}-\mathbf{r}')\mathcal{I}$ lead to

$$\mathbf{D}(\mathbf{r},\omega)=\epsilon(\mathbf{r},\omega)\mathbf{E}(\mathbf{r},\omega), \tag{1.3a}$$

$$\mathbf{H}(\mathbf{r},\omega)=\frac{1}{\mu(\mathbf{r},\omega)}\mathbf{B}(\mathbf{r},\omega), \tag{1.3b}$$

which we assume to always hold throughout this Thesis, unless otherwise specified. Furthermore, we also take all the studied systems to be nonmagnetic by setting $\mu=1$.

In order to solve Eqs. (1.1), they need to be complemented by a set of boundary conditions gluing together the solutions separately found in each material region. This can be done by making use of the integral version of MEQS, and for each interface dividing two media indexed as 1 and 2, one has[3]

$$\text{[Electric/displacement field]} \quad \begin{cases} \mathbf{E}_1^{\parallel}-\mathbf{E}_2^{\parallel}=0, \\ \mathbf{D}_1^{\perp}-\mathbf{D}_2^{\perp}=\sigma_{\mathrm{s}}, \end{cases} \tag{1.4a}$$

$$\text{[Magnetic/magnetizing field]} \quad \begin{cases} \mathbf{B}_1^{\perp}-\mathbf{B}_2^{\perp}=0, \\ \mathbf{H}_1^{\parallel}-\mathbf{H}_2^{\parallel}=\mathbf{j}_{\mathrm{s}}, \end{cases} \tag{1.4b}$$

where σ_{s} and $\mathbf{j}_{\mathrm{s}}$ denote surface free charges and currents located at the boundaries, respectively. The parallel and perpendicular superscripts refer to the parallel and perpendicular components of the fields with respect to the interface surface.

Conservation laws

Since MEQS describe the field dynamics of a closed system, in their formulation they contain the equation regulating the exchange of energy stored in the electromagnetic fields and in the charges. This can be seen by evaluating the rate of work done by the fields on the current, which by making use of Eqs. (1.1) written in their time domain version, lead to[3]

$$-\mathbf{j}(\mathbf{r},t)\cdot\mathbf{E}(\mathbf{r},t)=\partial_t u(\mathbf{r},t)+\nabla\cdot\mathbf{S}(\mathbf{r},t),$$

where

$$\text{[EM energy]} \quad u(\mathbf{r},t)=\frac{1}{8\pi}\mathbf{E}(\mathbf{r},t)\cdot\mathbf{D}(\mathbf{r},t)+\mathbf{B}(\mathbf{r},t)\cdot\mathbf{H}(\mathbf{r},t)], \tag{1.5a}$$

$$\text{[Poynting vector]} \quad \mathbf{S}(\mathbf{r},t)=\frac{c}{4\pi}[\mathbf{E}(\mathbf{r},t)\times\mathbf{H}(\mathbf{r},t)]. \tag{1.5b}$$

Equation (1.5a) represents the energy stored in the field, while the quantity in Eq. (1.5b) is known as Poynting vector and keeps track of the energy per unit time per unit area carried by the electromagnetic field.

Charge dynamics

Up to now, we discussed how sources can determine the evolution of the electromagnetic field without subjecting their motion to its influence. However, if we take a system of N classical point charges, labeled by the index i, the current $\mathbf{j}(\mathbf{r},t)=\sum_{i=1}^{N} q_i \mathbf{v}_i \delta[\mathbf{r}-\mathbf{r}_i(t)]$[3] will be determined by the position $\mathbf{r}_i(t)$ and velocity $\mathbf{v}_i(t)=\partial_t \mathbf{r}_i$ of each particle, which must be found by solving N dynamics equations (e.g., Newton's equations if they move much more slowly than light), each one including the presence of any external force at the particle position $\mathbf{F}(\mathbf{r}_i,t)$. When an electromagnetic field is present (e.g., one created by other charges and currents), the Lorentz force

$$\mathbf{F}(\mathbf{r}_i,t)=q_i\left[\mathbf{E}(\mathbf{r}_i,t)+(\mathbf{v}_i/c)\times\mathbf{B}(\mathbf{r}_i,t)\right]. \tag{1.6}$$

Therefore, Eqs. (1.1) together with Eq. (1.6) represent a set of coupled differential equations able to track both the trajectory of each particle and the evolution of the electromagnetic field also allowing for the inclusion of complex configurations in which several materials with arbitrary shapes and response functions are present. Even though for high electric and magnetic fields the Lorentz force can play an important role, for electrons interacting with nanostructures and used to study loss and cathodolumnescence spectral intensities, the trajectory perturbations introduced by Eq. (1.6) are commonly negligible.

1.1.2 Electromagnetic potentials and gauge invariance

A useful property of MEQS, especially in quantum theory, is that their mathematical structure can accept a solution which is equivalent to the one obtained through the fields $\mathbf{E}$ and $\mathbf{B}$ but given in terms of other quantities known as electromagnetic potentials. In particular, the field properties embedded in Eq. (1.1b) and Eq. (1.1c)[4] allow writing

$$\mathbf{B}(\mathbf{r},\omega)=\nabla\times\mathbf{A}(\mathbf{r},\omega), \tag{1.7a}$$

$$\mathbf{E}(\mathbf{r},\omega)=-\nabla\phi+\mathrm{i}k\mathbf{A}(\mathbf{r},\omega), \tag{1.7b}$$

where ϕ is the so-called scalar potential, of central importance in electrostatics ($c\gg 1$) as it is enough to determine the electric field, and $\mathbf{A}$ is known as vector potential. By expressing the fields as done in Eqs. (1.7), we immediately highlight an important property: they are not unique, and as a consequence, they cannot represent measurable quantities. In order to illustrate this fact, one can directly verify that for any function $\Lambda(\mathbf{r},t)$ the transformations $\mathbf{A}\rightarrow\mathbf{A}'=\mathbf{A}+\nabla\Lambda$ and $\phi\rightarrow\phi'=\phi+\mathrm{i}k\Lambda$ leave the electric and magnetic fields both unchanged. Such transformation is known as gauge transformation and the invariance under its application is called gauge invariance.

Among all the possible gauge choices, the most common ones are defined by the following conditions[3]

$$\text{[Coulomb gauge]} \qquad \nabla\cdot\mathbf{A}(\mathbf{r},\omega)=0, \tag{1.8a}$$

$$\text{[Lorentz gauge]} \qquad \nabla\cdot\mathbf{A}(\mathbf{r},\omega)-\mathrm{i}k\phi(\mathbf{r},\omega)=0,$$

$$\text{[Weyl gauge]} \qquad \phi(\mathbf{r},\omega)=0. \tag{1.8b}$$

---

[3] Here, q_i is the charge of the i-th particle, which throughout this work is taken to be $-e$ (i.e. with $e>0$).

[4] Firstly, one writes $\mathbf{B}=\nabla\times\mathbf{A}$ because of the divergenceless nature of $\mathbf{B}$, which then leads to $\nabla\times[\mathbf{E}-(\mathrm{i}\omega/c)\mathbf{A}]=0$. In addition, an irrotational field can always be written as the gradient of a scalar potential, namely $-\nabla\phi=\mathbf{E}-(\mathrm{i}\omega/c)\mathbf{A}$.

The Coulomb gauge (CG) is often used in free space, where $\epsilon = 1$ at any spatial position and frequency, as it allows us to directly express the scalar potential in terms of the charge distribution by constraining the vector potential to be transverse [see Eq. (1.1a)]. In contrast, the Lorentz gauge (LG) yields to a more symmetric form of MEQS that makes their relativistic invariance explicit[5]. Throughout this Thesis, we make use of the Weyl gauge (WG) given by the condition in Eq. (1.8b), as with this choice, and for $\rho = 0$, the vector potential satisfies the transverse condition of Eq. (1.8a) at points far from any material interface.

1.1.3 The electromagnetic Green tensor

We now proceed to solve MEQS by means of introducing a Green function. To do so, we first combine Eq. (1.1c) and Eq. (1.1d) by setting $\mu = 1$, and we make explicit use of the WG together with Eq. (1.7b) to obtain

$$\nabla \times \nabla \times \mathbf{A}(\mathbf{r}, \omega) - k^2 \epsilon(\mathbf{r}, \omega) \mathbf{A}(\mathbf{r}, \omega) = \frac{4\pi}{c} \mathbf{j}(\mathbf{r}, \omega). \tag{1.9}$$

The solution of Eq. (1.9) can be immediately written in terms of the so-called electromagnetic Green tensor $G(\mathbf{r}, \mathbf{r}', \omega)$ as

$$\mathbf{A}(\mathbf{r}, \omega) = -4\pi c \int d^3\mathbf{r}'\, G(\mathbf{r}, \mathbf{r}', \omega) \cdot \mathbf{j}(\mathbf{r}, \omega), \tag{1.10}$$

where the Green tensor is taken to satisfy

$$\nabla \times \nabla \times G(\mathbf{r}, \mathbf{r}', \omega) - k^2 \epsilon(\mathbf{r}, \omega) G(\mathbf{r}, \mathbf{r}', \omega) = -\frac{1}{c^2} \delta(\mathbf{r} - \mathbf{r}'). \tag{1.11}$$

We thus understand that the electromagnetic Green tensor contains all the information regarding both the space morphology and the material response of each element comprising a physical system. General considerations on the physical system under study makes the Green tensor to satisfy several useful properties, which are of particular importance for the following discussions. For instance, due to causality, it respects the Schwartz reflection principle[6] $G(\mathbf{r}, \mathbf{r}', \omega) = G^*(\mathbf{r}, \mathbf{r}', -\omega)$ as well as the Onsager reciprocity theorem, $G(\mathbf{r}, \mathbf{r}', \omega) = G^{\mathrm{T}}(\mathbf{r}', \mathbf{r}, \omega)$, valid for time-symmetrical systems [7].

An important step toward finding the solution of Eq. (1.11) is the separation of G into a sum of inhomogeneous and homogeneous terms. If we take our physical system to be composed by several bodies, each one defining a spatial region V_j [see Fig. (1.1)], for $\mathbf{r}, \mathbf{r}' \in V_j$, we can write

$$G(\mathbf{r}, \mathbf{r}', \omega) = G^0(\mathbf{r}, \mathbf{r}', \omega) + G^{\mathrm{s}}(\mathbf{r}, \mathbf{r}', \omega), \tag{1.12a}$$

$$\left[\nabla \times \nabla \times -k^2 \epsilon_j\right] G^0(\mathbf{r}, \mathbf{r}', \omega) = -\frac{1}{c^2} \delta(\mathbf{r} - \mathbf{r}'), \quad \text{for } \mathbf{r}, \mathbf{r}' \in V_j, \tag{1.12b}$$

$$\left[\nabla \times \nabla \times -k^2 \epsilon_j\right] G^{\mathrm{s}}(\mathbf{r}, \mathbf{r}', \omega) = 0, \tag{1.12c}$$

---

[5] The reader can find more details on the different gauge choices and their consequences in Refs. 5 and 6.

[6] We remark that this property is a direct consequence of the fact that $\epsilon(\mathbf{r}, \omega)$ is also a response function for which $\epsilon(\mathbf{r}, \omega) = \epsilon^*(\mathbf{r}, -\omega)$.

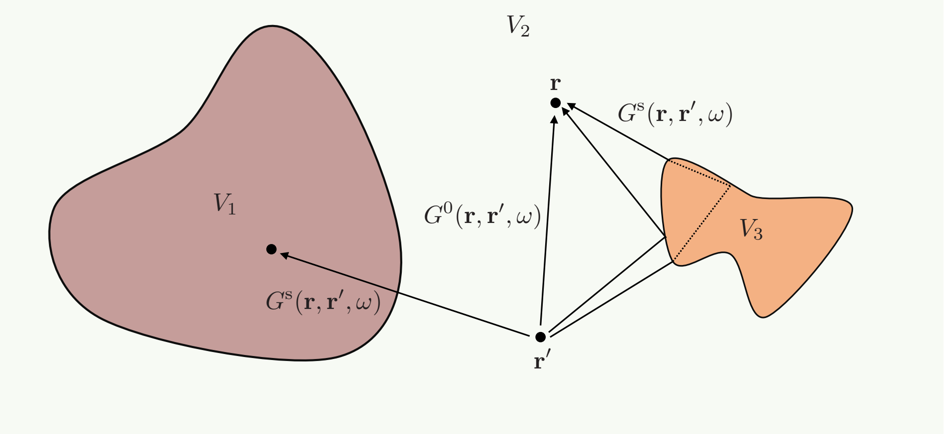

Figure 1.1: The electromagnetic Green tensor. Explanatory sketch of the separation into bulk and scattering electromagnetic Green tensors [see Eq. (1.12a)]. In an environment formed by several regions V_j, each one with a different permittivity ϵ_j, when a source, placed at $\mathbf{r}'$, induces a field at $\mathbf{r}$ with $\mathbf{r}, \mathbf{r}' \in V_j$ then both G^0 and G^{s} contribute, while, if $\mathbf{r} \in V_j$ and $\mathbf{r}' \notin V_j$, $G = G^{\mathrm{s}}$.

where we have defined the permittivity $\epsilon_j(\omega)$ of each region V_j as well as the scattering G^{s} and bulk G^0 Green tensors corresponding to the homogeneous and inhomogeneous solutions of Eq. (1.11), respectively. Whenever $\mathbf{r} \in V_j$ and $\mathbf{r}' \notin V_j$, $\mathbf{r} \neq \mathbf{r}'$ holds and therefore G^{s} represents the full solution of the differential equation as

$$G(\mathbf{r}, \mathbf{r}', \omega) = G^{\mathrm{s}}(\mathbf{r}, \mathbf{r}', \omega), \quad \text{for } \mathbf{r} \in V_j,\, \mathbf{r}' \notin V_j. \tag{1.13}$$

Finally, since the electric field has to respect the boundary conditions shown in Eqs. (1.4a), the Green tensor must satisfy similar equations[7] in order to completely solve Eq. (1.11).

The bulk Green tensor

As already anticipated, the inhomogeneous part of G corresponds to a situation in which a source current is placed in an infinite medium where the material boundaries are ignored. We thus seek the solution of Eq. (1.12b), which can be directly derived from the scalar Green function corresponding to the Helmholtz operator and reads[8]

$$G^0(\mathbf{r}, \mathbf{r}, \omega) = \frac{-1}{4\pi\omega^2\epsilon_j}\left(k_j^2\mathcal{I} + \nabla \otimes \nabla\right)\frac{\mathrm{e}^{\mathrm{i}k_j|\mathbf{r}-\mathbf{r}'|}}{|\mathbf{r}-\mathbf{r}'|}, \tag{1.14}$$

where the complex root $k_j = \sqrt{\epsilon_j}\omega/c$ needs to be chosen such as $\mathrm{Im}\{k_j\} > 0$. Given our choice of gauge, the form of G^0 accounts for charge-charge Coulomb repulsion as well as for the emission of free transverse photons, as required from MEQS. These two types of electromagnetic couplings are immediately apparent by taking the static ($c \to \infty$) and the far-field ($kr \to \infty$) limits of Eq. (1.14), respectively. The two corresponding

---

[7] They can be found, for instance, in Ref. 7.

expressions read[7]

$$G^0(\mathbf{r},\mathbf{r}',\omega) \approx \frac{-1}{4\pi\omega^2\epsilon_j}\begin{cases}\nabla\otimes\nabla|\mathbf{r}-\mathbf{r}'|^{-1} & \text{[Static limit]},\\ \mathrm{e}^{\mathrm{i}k_j(r+\hat{\mathbf{r}}\cdot\mathbf{r}')}(\hat{\mathbf{r}}\otimes\hat{\mathbf{r}}-\mathcal{I})k^2/r & \text{[Far-field limit]}.\end{cases} \tag{1.15}$$

When charges are present, the first expression in Eq. (1.15) is responsible for the interaction at short distance (e.g., for Coulomb repulsion and for the creation of the near-field: the Coulomb field produced by charges lying on the material interfaces). The second form of the bulk Green tensor accounts for the emission of spherical waves freely propagating from the sources throughout the uniform medium.

Expansion in normal modes

In situations for which the response of the system is confined within a finite spectral range, a very useful way of writing the scattering part of the Green tensor is through a combination of electromagnetic modes. Here, we analyze the scenario in which the space is composed by media with real and frequency-independent permittivity $\epsilon(\mathbf{r})$. For this case, Eq. (1.11) admits a solution of the form[9]

$$G(\mathbf{r},\mathbf{r}',\omega) = \frac{1}{2\pi}\sum_i \frac{\vec{\mathcal{E}}_i(\mathbf{r})\otimes\vec{\mathcal{E}}_i^*(\mathbf{r}')}{\hbar\omega_i[\omega^2-\omega_i^2+\mathrm{i}0^+]} + \frac{1}{4\pi\omega^2}\nabla_{\mathbf{r}}\otimes\nabla_{\mathbf{r}'}G^{\mathrm{L}}(\mathbf{r},\mathbf{r}'), \tag{1.16}$$

where 0^+ is positive infinitesimal and $\vec{\mathcal{E}}_i(\mathbf{r})$ are a set of eigenvectors, representing the mode electric field distribution, with eigenvalues ω_i satisfying the equation

$$\nabla\times\nabla\times\vec{\mathcal{E}}_i(\mathbf{r}) - \epsilon(\mathbf{r})\frac{\omega_i^2}{c^2}\vec{\mathcal{E}}_i(\mathbf{r}) = 0. \tag{1.17}$$

These modes are normalized according to $\int d^3\mathbf{r}\,\epsilon(\mathbf{r})\vec{\mathcal{E}}_i(\mathbf{r})\cdot\vec{\mathcal{E}}_{i'}^*(\mathbf{r})/2\pi = \delta_{ii'}\hbar\omega_i$ and form a complete basis set[8] satisfying the transverse completeness relation $\epsilon(\mathbf{r})\sum_i\vec{\mathcal{E}}_i(\mathbf{r})\otimes\vec{\mathcal{E}}_i^*(\mathbf{r}')/2\pi\hbar\omega_i = \delta^{\mathrm{T}}(\mathbf{r}-\mathbf{r}')$[9]. The second term of Eq. (1.16) takes care of the longitudinal interaction and therefore can be found by solving the equation

$$\epsilon(\mathbf{r})\nabla_{\mathbf{r}}\otimes\nabla_{\mathbf{r}'}G^{\mathrm{L}}(\mathbf{r},\mathbf{r}') = 4\pi\delta^{\mathrm{L}}(\mathbf{r}-\mathbf{r}'), \tag{1.18}$$

with $\delta^{\mathrm{L}}(\mathbf{r}-\mathbf{r}')$ begin the longitudinal Dirac delta function satisfying $\int d^3\mathbf{r}'\,\delta^{\mathrm{L}}(\mathbf{r}-\mathbf{r}')\mathbf{A}(\mathbf{r}') = \mathbf{A}(\mathbf{r})$ for any vector $\mathbf{A}(\mathbf{r})$ that satisfies the condition $\nabla\times\mathbf{A} = 0$.

Expansions similar to the one in Eq. (1.16) can also be formulated in the limiting case of $c \to \infty$ allowing for the incorporation of dispersion and inelastic losses in the description[10]. Furthermore, in a general situation where retardation effects are important and $\epsilon(\mathbf{r},\omega)$ represents a complex and dispersive permittivity, such expansion requires the introduction of the concept of quasinormal modes[11,12].

---

[8] This is true in the space of vectors that fulfill the generalized CG constraint $\nabla\cdot[\epsilon(\mathbf{r})\vec{\mathcal{E}}(\mathbf{r})] = 0$.

[9] The name derives from the fact that $\delta^{\mathrm{T}}(\mathbf{r}-\mathbf{r}')$ satisfies the property $\int d^3\mathbf{r}\,\delta^{\mathrm{T}}(\mathbf{r}-\mathbf{r}')\mathbf{A}^{\mathrm{T}}(\mathbf{r}') = \mathbf{A}^{\mathrm{T}}(\mathbf{r})$ for any vector for which $\nabla\cdot\mathbf{A}^{\mathrm{T}} = 0$ holds.

1.1.4 The electric field of a free electron

One of the main reasons behind the extensive use of electrons as probes to perform microscopy and spectroscopy in EMs is the promise of achieving a spatial resolution beyond the capabilities provided by similar techniques using light combined with far-field optics. Indeed, since the diffraction limit constraints the ability of focusing waves to $\sim \lambda/2$[10] (half the wavelength), the spatial resolution with visible light ($\hbar\omega \sim 1$ eV) cannot be pushed well below ~ 1 μm, while for an electron of similar energy, focusing can reach the size of a small molecule (~ 1 nm, i.e., 1000-fold smaller). We remark that the diffraction limit only refers at the minimum spatial extension that the particle wave function can assume, which does set a lower limit to spatial resolution but often takes higher values under the influence of other factors. One of them is represented by the intrinsic nature of the source of electromagnetic field, namely by the spatial extension of the electric field produced by a moving charged particle from its trajectory. By combining Eqs. (1.14) and (1.10), taking the current associated with a single electron fully focused at the center of the xy-plane and traveling at constant velocity $\mathbf{v} = v\hat{\mathbf{z}}$ (here we ignore any field backreaction on the particle), the generated vector potential reads[8]

$$\mathbf{A}^{\rm el}(\mathbf{r},\omega) = -\frac{2{\rm i}ec}{v^2\gamma_j\epsilon_j}{\rm e}^{{\rm i}\omega z/v}\left[\frac{\rm i}{\gamma_j}K_0\left(\frac{\omega R}{v\gamma_j}\right)\hat{\mathbf{z}} - K_1\left(\frac{\omega R}{v\gamma_j}\right)\hat{\mathbf{R}}\right], \tag{1.19}$$

where K_m is the modified Bessel function[13] of order m and $\gamma_j = \sqrt{1-\epsilon_j v^2/c^2}$ is the relativistic contraction factor in a dielectric of permittivity ϵ_j. Equation (1.19) highlights several properties of electrons when they are used as probes: *(i)* the divergence of the Bessel functions for points close to the beam trajectory [see Fig. (1.2)a] resembles the one of a Coulomb field containing evanescent components able to couple to any type of excitation; *(ii)* the exponential dependence on velocity and light frequency renders the spatial resolution strongly dependent both on the targeted spectral range and on the electron kinetic energy; *(iii)* the frequency in the argument of the Bessel functions leads to finite field amplitudes even in the soft x-ray range (~ 50 eV) at a distance of $R \sim 5$ nm for a 100 keV electron. We therefore conclude that a charged particle in constant motion cannot produce propagating radiation unless ϵ_j is real and the condition $v > c/\sqrt{\epsilon_j}$ is satisfied [11]. In these materials, Cherenkov radiation is indeed possible, and actually, it is commonly used as a mechanism of detection of charged particles in scintillators[14].

1.1.5 Planar interfaces and surface-plasmon polaritons

The case of a planar interface represents the simplest electromagnetic problem involving two different media of different permittivies ϵ_1 and ϵ_2 [see Fig. (1.2b)]. Despite its theoretical simplicity, surfaces and interfaces have been extensively studied especially through the use of electron beams (e-beams) to probe surface states and collective modes of conductive electrons[16–18].

As usually done in classical electrodynamics textbooks for reflection and transmission from a planar interface[3], the problem is solved by expanding the Green tensor in waves

---

[10] Here, λ is $\lambda_{\rm light} = 2\pi c/\omega$ for light, while for matter waves is the de Broglie wavelength which, for a nonrelativistic electron of kinetic energy $\hbar\varepsilon$, is $\lambda_e = \pi\sqrt{2\hbar/m_e\varepsilon}$.

[11] When this condition is satisfied, γ_j is a pure imaginary number and the Bessel functions display an oscillating behavior[13].

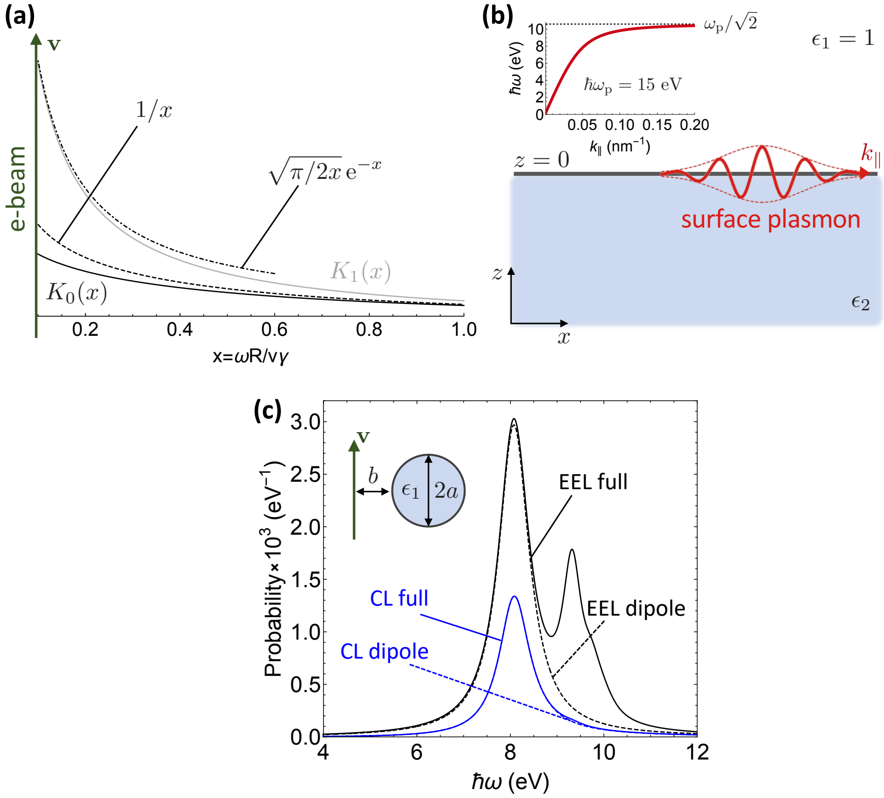

Figure 1.2: Near-field produced by free- and bound- charges. (a) Behavior of the Bessel functions describing the decay of the electron electric field in vacuum [see Eq. (1.19)] as a function of the normalized distance from its trajectory $x = \omega R/v\gamma$. (b) Sketch of a propagating surface plasmon propagating with wave vector $k_\parallel$ along the interface between a medium with permittivity ϵ_2 and vacuum ($\epsilon_1 = 1$). In the inset, we show the dispersion relation of a surface plasmon for an Al-vacuum interface with the aluminum described by a Drude permittivity [see Eq. (1.23)] with $\omega_p = 15$ eV and a vanishing inelastic decay rate γ. (c) Validity of the electric dipole approximation in the EEL (dashed black line) and CL (dashed blue line) probabilities associated to an electron interacting with an Al sphere compared with the full analytical solution, taken from Ref. 15 for both signals (see corresponding colors). All the curves are computed with $v = 0.7c$, $a = 10$ nm, and $b = 5$ nm. The sphere polrizability is computed through the Mie coefficient of Eq. (1.25) using a Drude permittivity ϵ_1 with $\omega_p = 15$ eV and $\gamma = 0.5$ eV.

having the same symmetry of the problem, therefore simplifying the application of the boundary conditions in Eqs. (1.4). By taking the interface extending over the plane $z = 0$ [see Fig. (1.2b)], two polarization vectors in the j-th medium are defined as $\hat{\mathbf{e}}_{\rm s} = (k_y\hat{\mathbf{x}} - k_x\hat{\mathbf{y}})/k_\parallel$ and $\hat{\mathbf{e}}_{\rm p}^{j\pm} = (k_\parallel\hat{\mathbf{z}} \mp k_z^j\hat{\mathbf{k}}_\parallel)/k_j$, where $k_z^{(j)} = \sqrt{k_j^2 - k_\parallel^2}$ with $\mathrm{Im}\{k_z^j\} > 0$, in order to form a right-handed triad[12]. The Green tensor $G^{\rm s}$ is then found by invoking the electromagnetic boundary conditions[7]. When both the source and the probed coordinates lie in the top layer, it reads

$$\begin{aligned} G^{\rm s,\,surf}(\mathbf{r},\mathbf{r}',\omega) = &\frac{-\mathrm{i}}{8\pi^2c^2}\int d^2\mathbf{k}_\parallel\, \mathrm{e}^{\mathrm{i}\mathbf{k}_\parallel\cdot(\mathbf{R}-\mathbf{R}')+\mathrm{i}k_z^{(1)}(z+z')} \\ &\times\left[r_{\rm s}\,\hat{\mathbf{e}}_{\rm s}\otimes\hat{\mathbf{e}}_{\rm s} + r_{\rm p}\,\hat{\mathbf{e}}_{\rm p}^{1+}\otimes\hat{\mathbf{e}}_{\rm p}^{1-}\right]/k_z^{(1)}. \end{aligned} \qquad \text{for } z, z' > 0, \tag{1.20}$$

Equation (1.20) contains all the possible electromagnetic waves sustained by the material configuration under analysis and their strength is measured by the so-called Fresnel reflection coefficients entering in the expressions:

$$[\text{p-polarization}] \qquad r_{\rm p} = \frac{\epsilon_1 k_z^{(2)} - \epsilon_2 k_z^{(1)}}{\epsilon_1 k_z^{(2)} + \epsilon_2 k_z^{(1)}}, \tag{1.21a}$$

$$[\text{s-polarization}] \qquad r_{\rm s} = \frac{k_z^{(2)} - k_z^{(1)}}{k_z^{(2)} + k_z^{(1)}}. \tag{1.21b}$$

Structural resonances are found by taking the real part of each denominator, which provides the dispersion relation of each related mode. Of particular importance are the p-polarized modes found to follow the condition

$$\frac{\omega}{c} = k_\parallel\sqrt{\frac{1}{\epsilon_1} + \frac{1}{\epsilon_2}}, \tag{1.22}$$

derived from Eq. (1.21a). They identify a set of traveling waves that are bound to the surface and cannot couple to free photons reaching the far field. For a vacuum-metal interface, we can take $\epsilon_1 = 1$ and assume ϵ_2 to be given only by the free oscillations of electrons in the conduction band of a metal or of a doped semiconductor. In this regard, a Drude dielectric function does remarkably describe their actual local response[19] and it reads

$$\epsilon_2(\omega) = 1 - \frac{\omega_{\rm p}^2}{\omega(\omega + \mathrm{i}\gamma)}, \tag{1.23}$$

where the classical bulk plasma frequency $\omega_{\rm p} = \sqrt{4\pi e^2 n_0/m_{\rm e}}$ relates to the conduction electron density n_0 and γ is a phenomenological damping rate accounting for relaxation of excited electronic states in the material[19]. By plugging Eq. (1.23) into Eq. (1.22), and by considering only subluminal solutions (i.e., satisfying $k_\parallel > \omega/c$ for $\gamma = 0$), we find the dispersion relation $\omega = (\omega_{\rm p}^2/2 + c^2k_\parallel^2 - \sqrt{\omega_{\rm p}^4/4 + c^4k_\parallel^4})^{1/2}$ of the surface-plasmon

---

[12] They indeed satisfy the completeness relation $\mathcal{I} = \hat{\mathbf{e}}_{\rm p}^{j\pm}\otimes\hat{\mathbf{e}}_{\rm p}^{j\pm} + \hat{\mathbf{e}}_{\rm s}\otimes\hat{\mathbf{e}}_{\rm s} + \hat{\mathbf{k}}^{j\pm}\otimes\hat{\mathbf{k}}^{j\pm}$, with $\hat{\mathbf{k}}^{j\pm} = \mathbf{k}_\parallel \pm k_z^{(j)}\hat{\mathbf{z}}$.

modes, which we depict in Fig. (1.2b). Because the surface-plasmon line does not cross the light cone, the field in vacuum decays exponentially as the distance from the interface plane increases, therefore allowing for a strong field confinement[13].

1.1.6 Small-particle limit: the dipole approximation

As nanophotonics deals with light-matter interaction involving scatterers of characteristic size a of the order of tens of nanometers, it often happens that we are interested in a spectral range for which $a/\lambda_{\rm light} \ll 1$. In this regime, we can assume the Green tensor G^0 to vary negligibly within the particle volume centered at position $\mathbf{r}_0$, and therefore, by only retaining the 0-th order Taylor expansion of the scattered field in terms of the $a/\lambda_{\rm light}$ parameter, from Eq. (1.10), we immediately obtain the vector potential produced in an uniform medium

$$\mathbf{A}^{\rm dip}(\mathbf{r},\omega) = 4\pi{\rm i}\omega c\, G^0(\mathbf{r},\mathbf{r}_0,\omega)\mathbf{p}(\omega),$$

where we have defined the dipole moment as $\mathbf{p}(\omega) = ({\rm i}/\omega)\int d^3\mathbf{r}\, \mathbf{j}(\mathbf{r},\omega)$. In addition, $\mathbf{p}$ can be connected to the external field generating the current inside the particle through a polarizability tensor $\alpha(\omega)$ as $\mathbf{p}(\omega) = \alpha(\omega)\mathbf{E}^{\rm ext}(\mathbf{r}_0,\omega)$. Finally, we can link $\mathbf{E}^{\rm ext}(\mathbf{r}_0,\omega)$ to its source current, leading to the definition of the Green tensor for a dipolar scatterer

$$G^{\rm s,\,dip}(\mathbf{r},\mathbf{r}',\omega) = -4\pi\omega^2 G^0(\mathbf{r},\mathbf{r}_0,\omega)\alpha(\omega)G^0(\mathbf{r}_0,\mathbf{r}',\omega). \tag{1.24}$$

Equation (1.24), with the right choice of polarizability, has been shown to be capable of successfully model relevant aspects of the dipolar electromagnetic response. For instance, for a self-standing perfect sphere of permittivity ϵ_1 placed in vacuum, the polarizability can be approximated by $\alpha(\omega) = 3t_1^{\rm E}/2k^3$ [8] in terms of the electric Mie scattering coefficient [20]

$$t_1^{\rm E} = \frac{-j_1(x_0)[x_1 j_1(x_1)]' + \epsilon\,[x_0 j_1(x_0)]' j_1(x_0)}{h_1^{(+)}(x_0)[x_1 j_1(x_1)]' - \epsilon\,[x_1 h_1^{(+)}(x_1)]' j_1(x_0)}, \tag{1.25}$$

where j_l and $h_l^{(+)}$ are the spherical Bessel and Hankel[14] functions respectively [13], while $x_0 = ka$ and $x_1 = k_1 a$. This expression incorporates retardation corrections in the dipolar modes of the particle. In Fig. (1.2c), we observe how the dipole approximation compares to the full analytical solution for the far-field cathodoluminescence emission (CL) and the electron-energy loss (EEL) probability, which we shall encounter in the next subsection, for a small metallic sphere [15].

1.1.7 Classical electron energy-loss and cathodoluminescence probabilities

When a free charged particle, like an electron in EM, interacts with a sample through the field in Eq. (1.19), the dynamical response of the involved materials induces an electric field that acts back on the particle producing a stopping force and, thus, reducing its

---

[13] This is because $k_z^{(1)}$ becomes a purely imaginary part, which leads to a real exponential in Eq. (1.20).

[14] Here, we adopt the notation of Messiah, which can be found in Ref. 21.

kinetic energy. Far from the specimen, the total energy lost by the electron is simply given by the work done by such field on the classical current associated with the moving charge $\mathbf{j}(\mathbf{r},t) = -e\mathbf{v}\delta[\mathbf{r}-\mathbf{r}_e(t)]$ integrated over the entire trajectory, which one can write as

$$\Delta E = e\int_{-\infty}^{\infty} dt\, \mathbf{v}\cdot\mathbf{E}[\mathbf{r}_e(t),t].$$

By taking the electron trajectory to be $\mathbf{r}_e(t) = (\mathbf{R}_0, vt)$ and by dividing the average energy in frequency components as $\Delta E = \int_0^\infty d\omega\, \hbar\omega\, \Gamma_{\rm EEL}(\mathbf{R}_0,\omega)$, one can exploit the definition of the field in terms of the full Green tensor leading to the well-known classical formula for the EEL probability[8]

$$\Gamma_{\rm EEL}(\mathbf{R}_0,\omega) = \frac{4e^2}{\hbar}\int_{-\infty}^{\infty} dz\, dz'\, \cos\left[\frac{\omega}{v}(z-z')\right] {\rm Im}\left\{-G_{zz}(\mathbf{R}_0,z,\mathbf{R}_0,z',\omega)\right\}. \quad (1.26)$$

Equation (1.26) represents a powerful result to compute the coupling between an e-beam and the optical modes supported by a sample (e.g., a nanoparticle), which remarkably matches experimental results measured for several different metallic and dielectric nanostructures[22]. Interestingly, the separation in Eq. (1.12a) naturally allows for the division of the energy loss probability into two contributions as $\Gamma_{\rm EEL} = \Gamma^{\rm bulk} + \Gamma^{\rm s}$, with $\Gamma^{\rm bulk}$ corresponding to G^0 and $\Gamma^{\rm s}$ to $G^{\rm s}$. Since free electrons cannot emit or absorb photons in vacuum[15], $\Gamma^{\rm bulk} = 0$ unless $\epsilon_j \neq 1$[8].

Because during the interaction not all the field scattered by the sample is reabsorbed by the electron, there is a nonzero probability to measure a photon at a detector far from the specimen. Such probability can be calculated by resorting to the Poynting vector of Eq. (1.5b) in order to evaluate the total energy flowing out of a spherical surface of infinite radius:

$$\Delta E = \lim_{kr\to\infty}\int_{-\infty}^{\infty} dt \int d\Omega_{\hat{\mathbf{r}}}\, r^2\, \mathbf{S}(\mathbf{r},t)\cdot\hat{\mathbf{r}}. \quad (1.27)$$

Then, by following similar steps as done for the calculation of the electron energy loss, we obtain the angle-resolved differential photon emission probability

$$\frac{d\Gamma_{\rm CL}}{d\omega d\Omega_{\hat{\mathbf{r}}}} = \lim_{kr\to\infty}\frac{r^2}{4\pi^2 k}{\rm Re}\{\mathbf{E}(\mathbf{r},\omega)\times\mathbf{B}^*(\mathbf{r},\omega)\}\cdot\hat{\mathbf{r}}. \quad (1.28)$$

By means of this expression, the probability of coherent cathodoluminescence[16] can be computed, predicting with good accuracy experimental results aimed at mapping optical excitations such as surface plasmons propagating on metallic surfaces[23]. Intuitively, Eqs. (1.26) and (1.28) lead to the same value for an electron interacting with samples having negligible inelastic losses (i.e., for real ϵ).

---

[15] For a classical electron, the energy dispersion along the particle propagation direction is $\omega = vk < ck$ [see Eq. (1.19)]. Such a line never crosses the projection of the light cone, thus preventing the coupling to free space light.

[16] Here, the word *coherent* is used to discern from different processes yielding the emission of a photon with energy different from the energy lost by the electron[8].

1.2 Quantum charges and classical fields

We shall now turn our attention to the description of effects that can be explained only if the quantum nature of charged particles is taken into account. Indeed, concepts such as interference of matter waves, quantum nonlinearity, and decoherence cannot be captured by the classical theoretical analysis conducted so far. Furthermore, since we want to deal with particles traveling at a considerable fraction of the speed of light, we will also need a relativistic description of the quantum mechanical interaction between charges and electromagnetic fields.

1.2.1 Relativistic and nonrelativistic dynamics

A theoretical framework capable of dealing with all the previously mentioned ingredients is quantum electrodynamics (QED), which was mostly developed during the first half of the 20th century. Its cardinal building element is represented by the Dirac equation, given by[21,24,25]

$$\left\{m_{\rm e}c^2\beta + c\vec{\alpha}\cdot\left[\mathbf{p}+\frac{e}{c}\mathbf{A}(\mathbf{r},t)\right]\right\}\Psi(\mathbf{r},t) = {\rm i}\hbar\partial_t\Psi(\mathbf{r},t), \tag{1.29}$$

where $\mathbf{p} = -{\rm i}\hbar\nabla$ is the momentum operator and

$$\beta = \begin{bmatrix} \mathcal{I}_2 & 0 \\ 0 & -\mathcal{I}_2 \end{bmatrix}, \qquad \vec{\alpha} = \begin{bmatrix} 0 & \vec{\sigma} \\ \vec{\sigma} & 0 \end{bmatrix}$$

are matrices defined in terms of the 2×2 identity and the Pauli matrices $\mathcal{I}_2$ and $\vec{\sigma}$, respectively. Equation (1.29) describes the interaction between a $1/2$-spin charged particle (in Eq. (1.29) for an electron) and a classical vector potential $\mathbf{A}(\mathbf{r},t)$ through the 4-component spinors $\Psi(\mathbf{r},t)$ by taking into account the relativistic dispersion relation $\hbar\varepsilon_k = c\sqrt{m_{\rm e}^2c^2+\hbar^2k^2}$ for the electron energy as well as spin effects embedded in the multidimensional nature of the wave function. The time dependent spinor in Eq. (1.29) is usually written as a linear combination of the noninteracting eigensolutions[17] with positive and negative energies:

$$\Psi^+_{\mathbf{k}s}(\mathbf{r},t) = A_k\begin{bmatrix}\hat{\mathbf{s}} \\ B_k\left(\vec{\sigma}\cdot\mathbf{k}\right)\hat{\mathbf{s}}\end{bmatrix}{\rm e}^{-{\rm i}\varepsilon_k t+{\rm i}\mathbf{k}\cdot\mathbf{r}},$$
$$\Psi^-_{\mathbf{k}s}(\mathbf{r},t) = A_k\begin{bmatrix}-B_k(\vec{\sigma}\cdot\mathbf{k})\hat{\mathbf{s}} \\ \hat{\mathbf{s}}\end{bmatrix}{\rm e}^{{\rm i}\varepsilon_k t+{\rm i}\mathbf{k}\cdot\mathbf{r}},$$

where $A_k = \sqrt{(\varepsilon_k + m_{\rm e}c^2/\hbar)/2\varepsilon_k V}$, $B_k = c/(\varepsilon_k + m_{\rm e}c^2/\hbar)$, V is the quantization volume used as a normalization factor and $\hat{\mathbf{s}}$ denotes one of the two orthonormalized 2-dimensional unit spin vectors[18] indexed by s as $\Psi(\mathbf{r},t) = \sum_\pm\sum_{\mathbf{k}s}\alpha^\pm_{\mathbf{k}s}(t)\Psi^\pm_{\mathbf{k}s}(\mathbf{r},t)$.

When the coefficients of the expansion take non-negligible values up to wave vectors satisfying $kc/\varepsilon_k \ll 1$, it is well known that the Dirac equation can be transformed into

---

[17] Solutions found from Eq. (1.29) by setting $\mathbf{A} = 0$.

[18] A possible choice of vectors would be the two independent eigenvectors of the Pauli matrix satisfying the equation $\sigma_z\hat{\mathbf{s}} = \pm\hat{\mathbf{s}}$.

the nonrelativistic Schrödinger equation $\mathrm{i}\hbar\partial_t\chi(\mathbf{r},t) = \mathcal{H}\chi(\mathbf{r},t)$ with a Hamiltonian formed by the sum $\mathcal{H} = \mathcal{H}_0 + \mathcal{H}_1 + \mathcal{H}_2 + \mathcal{H}_3$ [25], where

$$\mathcal{H}_1 = -\frac{\mathrm{i}\hbar e}{2m_\mathrm{e}c}\left[\nabla\cdot\mathbf{A}(\mathbf{r},t) + \mathbf{A}(\mathbf{r},t)\cdot\nabla\right], \tag{1.31a}$$

$$\mathcal{H}_2 = \frac{e^2}{2m_\mathrm{e}c^2}A^2(\mathbf{r},t), \tag{1.31b}$$

$$\mathcal{H}_3 = \frac{e\hbar}{2m_\mathrm{e}c}\,\vec{\sigma}\cdot\mathbf{B}(\mathbf{r},t), \tag{1.31c}$$

and $\mathcal{H}_0 = -\hbar^2\nabla^2/2m_\mathrm{e}$. Now, the wave function χ is a 2-dimensional spinor. The contribution $\mathcal{H}_1$ represents the linear light-matter coupling, $\mathcal{H}_2$ accounts for the ponderomotive force, and $\mathcal{H}_2$ yields a nonzero probability to spin flip events.

We can estimate the relative importance of the each term by assuming an electron with wavelength λ_e and an electric field of amplitude $\mathcal{E}$ with photon energy $\hbar\omega$ varying over a distance L. Doing so, the relative magnitude of the different contributions is $|\mathcal{H}_2/\mathcal{H}_1| \sim e\,\mathcal{E}\lambda_e/2\pi\hbar\omega$, $|\mathcal{H}_2/\mathcal{H}_3| \sim e\,\mathcal{E}L/\hbar\omega$, and $|\mathcal{H}_1/\mathcal{H}_3| \sim 2\pi eL/\lambda_e$. We immediately notice that, for an electron moving at a significant fraction of the speed of light and for light in the optical spectral region, the term linear in the vector potential dominates the dynamics over the ponderomotive and spin couplings. In contrast, the term in Eq. (1.31b) and the one in Eq. (1.31c) can take similar values under certain circumstances. However, in this Thesis we focus on situations in which either a high amplitude field ($\mathcal{E} > 10^8$ V/m) is considered or the targeted excitation energies belong to the infrared spectrum, therefore always disregarding the influence of $\mathcal{H}_3$ as a safe approximation.

1.2.2 Paraxial beams and nonrecoil approximation

According to the previous discussion, we can solve the Schrödinger equation dismissing the spin degrees of freedom. Therefore, the general scalar solution ψ must admit the expansion $\psi(\mathbf{r},t) = \sum_\mathbf{k}\alpha_\mathbf{k}(t)\mathrm{e}^{\mathrm{i}\mathbf{k}\cdot\mathbf{r}-\mathrm{i}\varepsilon_k t}/\sqrt{V}$.

In the experimental scenarios on which we are interested, an electron interacts with excitations of energies $\hbar\omega$ several orders of magnitude smaller than its kinetic energy and, in state-of-the art TEM and SEM, reaches the specimen with initial components $\alpha^0_\mathbf{k}$ describing a well-collimated[19] e-beam, with a central wave vector $\mathbf{k}_0$ defining the frequency $\varepsilon_0 = \varepsilon_{k_0}$ and the velocity $\mathbf{v} = \mathbf{k}_0c^2/\varepsilon_0$. In this regime, the so-called *nonrecoil* approximation, which is equivalent at linearizing the electron energy around $\mathbf{k}_0$ as

$$\varepsilon_k \approx \varepsilon_0 + \mathbf{v}\cdot(\mathbf{k}-\mathbf{k}_0), \quad \text{[Nonrecoil approximation]} \tag{1.32}$$

can be adopted, and the Dirac equation can be transformed into a scalar Schrödinger equation $\mathrm{i}\hbar\partial_t\psi(\mathbf{r},t) = \left(\mathcal{H}_0^\mathrm{par} + \mathcal{H}_1^\mathrm{par} + \mathcal{H}_2^\mathrm{par}\right)\psi(\mathbf{r},t)$ with [see Appendix B for a

---

[19] Here, with the word *collimated* we mean that $\alpha^0_\mathbf{k}$ takes negligible values when the transverse components of $\mathbf{k}$ (relative to the electron velocity $\mathbf{v}$) are not very small compared to the longitudinal component.

detailed proof]

$$\mathcal{H}_0^{\rm par} = \hbar\varepsilon_0 - \hbar\mathbf{v}\cdot(\mathrm{i}\nabla + \mathbf{k}_0), \tag{1.33a}$$

$$\mathcal{H}_1^{\rm par} = (e\mathbf{v}/c)\cdot\mathbf{A}(\mathbf{r},t), \tag{1.33b}$$

$$\mathcal{H}_2^{\rm par} = \frac{e^2}{2m_{\rm e}c^2\gamma}\left[A_x^2(\mathbf{r},t) + A_y^2(\mathbf{r},t) + \frac{1}{\gamma^2}A_z^2(\mathbf{r},t)\right]. \tag{1.33c}$$

Interestingly, we notice that, once the nonrecoil approximation is assumed any initial wave function $\psi_0(\mathbf{r},t)$ of an impinging electron can be written in the form $\psi_0(\mathbf{r},t) = \mathrm{e}^{\mathrm{i}\mathbf{k}_0\cdot\mathbf{r}-\mathrm{i}\varepsilon_0 t}\phi_0(\mathbf{r}-\mathbf{v}t)$, where $\phi_0(\mathbf{r}-\mathbf{v}t) = \sum_{\mathbf{k}}\alpha^0_{\mathbf{k}_0+\mathbf{k}}\,\mathrm{e}^{\mathrm{i}\mathbf{k}\cdot(\mathbf{r}-\mathbf{v}t)}/\sqrt{V}$ represents a slowly varying envelope.

We identify Eqs. (1.33) as the basic starting point in the development of the theoretical framework describing the interaction between light and fast free electrons in EMs. Indeed, as we shall see in the next subsection, they are able to successfully model a plethora of phenomena connected to the interaction of synchronized e-beams and light at a specimen.

1.2.3 Classical photon-induced near-field electron microscopy (PINEM)

We now consider a situation in which an electron reaches a specimen while it is irradiated by an intense laser pulse. Here, the electron dynamics is dominated by a high number of inelastic scattering events induced by its interaction with the external vector potential $\mathbf{A}$. Even though the electron cannot couple to free light for the reasons mentioned in Section 1.1.3, modes having subliminal dispersion like the ones shown in Fig. (1.2b) can overcome the energy-momentum mismatch and produce high interaction strengths. As a consequence, a fast dynamics is generated in which many quanta are exchanged between the electron and light, a process that goes under the name of photon-induced near-field electron microscopy (PINEM) interaction[26] given the fact that it was firstly proposed as a way to obtain time-resolved images of nanostructures. Assuming that the Hamiltonian in Eq. (1.33) describes well the physics during the entire duration of the interaction, the Schrödinger equation admits the analytical solution[20] [27–30]

$$\psi(\mathbf{r},t) = \psi_0(\mathbf{r},t)\,\exp\left[-\frac{\mathrm{i}}{\hbar}\int_{-\infty}^{t} dt'\,\mathcal{H}_{\rm int}^{\rm par}(\mathbf{r}-\mathbf{v}t+\mathbf{v}t',t')\right], \tag{1.34}$$

where we have defined the paraxial interaction Hamiltonian $\mathcal{H}_{\rm int}^{\rm par} = \mathcal{H}_1^{\rm par} + \mathcal{H}_2^{\rm par}$.

In most cases of practical interest, the laser pulse illuminating the scattering structure can be considered to carry a single frequency ω[21]. In such situations, time and spatial dependence in the vector potential can be separated by writing it as $\mathbf{A}(\mathbf{r},t) = (2c/\omega)\mathrm{Im}\{\vec{\mathcal{E}}(\mathbf{r})\,\mathrm{e}^{-\mathrm{i}\omega t}\}$, where $\vec{\mathcal{E}}(\mathbf{r})$ is the electric field amplitude resulting from the sum of the external laser and scattered amplitudes. Since we are interested in the electron wave function far from the sample, we evaluate Eq. (1.34) at long times such

---

[20] One shall try to plug this ansatz into the Schrödinger equation to verify its correctness.

[21] For works in which several light colors induce a PINEM interaction, we point the reader to Ref. 31, where $\mathbf{A}$ carries several harmonics generated by the nonlinear response of the sample, and to Ref. 32, where the electron undergoes stimulated Compton scattering in free space.

that ψ^0 vanishes in the interaction region. Doing so, and by taking $\mathbf{v} = v\hat{\mathbf{z}}$, the previous expression can be rewritten as[33]

$$\psi(\mathbf{r},t) = \psi_0(\mathbf{r},t)\,\mathrm{e}^{\mathrm{i}\varphi(\mathbf{R})} \times \mathcal{P}_0[\beta_1(\mathbf{R}),\omega,z-vt]\mathcal{P}_0[\beta_2(\mathbf{R}),2\omega,z-vt], \tag{1.35a}$$

with

$$\begin{aligned}\mathcal{P}_0[\beta,\omega,z] &= \exp\left(-\beta \mathrm{e}^{\mathrm{i}\omega z/v} + \beta^* \mathrm{e}^{-\mathrm{i}\omega z/v}\right)\\ &= \sum_{\ell=-\infty}^{\infty} J_\ell(2|\beta|)\,\mathrm{e}^{\mathrm{i}\ell \arg\{-\beta\}}\mathrm{e}^{\mathrm{i}\ell\omega z/v},\end{aligned} \tag{1.35b}$$

where J_ℓ is the ℓ-th Bessel function and $\mathcal{P}_0$ encapsulates the energy reshaping that the electron undergoes during its interaction with the field, whose coupling strength is measured by the parameters

$$\beta_1(\mathbf{R}) = \frac{e}{\hbar\omega}\int_{-\infty}^{\infty} dz\,\mathcal{E}_z(\mathbf{r})\,\mathrm{e}^{-\mathrm{i}\omega z/v}, \tag{1.36a}$$

$$\beta_2(\mathbf{R}) = -\frac{\mathrm{i}}{2\mathcal{M}\omega^2}\int_{-\infty}^{\infty} dz\,\left[\mathcal{E}_x^2(\mathbf{r}) + \mathcal{E}_y^2(\mathbf{r}) + \frac{1}{\gamma^2}\mathcal{E}_z^2(\mathbf{r})\right]\mathrm{e}^{-2\mathrm{i}\omega z/v}, \tag{1.36b}$$

and by the elastic phase

$$\varphi(\mathbf{R}) = -\frac{1}{\mathcal{M}\omega^2}\int_{-\infty}^{\infty} dz\,\left[|\mathcal{E}_x(\mathbf{r})|^2 + |\mathcal{E}_y(\mathbf{r})|^2 + \frac{1}{\gamma^2}|\mathcal{E}_z(\mathbf{r})|^2\right]. \tag{1.37}$$

We note that to obtain Eq. (1.35b) from the previous line, the Jacobi-expansion $\mathrm{e}^{\mathrm{i}u\sin\theta} = \sum_\ell J_\ell(u)\mathrm{e}^{\mathrm{i}\ell\theta}$ needs to be applied with $u = 2|\beta|$ and $\theta = \arg\{-\beta\} + \omega z/v$[22]. The factor $\mathcal{M} = m_\mathrm{e}\gamma v/c\alpha$ is an effective mass and $\alpha \approx 1/137$ is the fine-structure constant.

In Eq. (1.35b), the index ℓ counts the number of photons absorbed ($\ell > 0$) and emitted ($\ell < 0$) by the electron, which, as we have already anticipated, reshapes its wave function according to Eq. (1.35a). The factor β_1 is called the PINEM coupling coefficient[23] and it is usually orders of magnitude larger than the ponderomotive coupling β_2 for field amplitudes that do not degrade the sample. In particular, the relative strength $|\beta_2/\beta_1| \sim |\vec{\mathcal{E}}|/\mathcal{E}_\mathrm{thres}$ with $\mathcal{E}_\mathrm{thres} = 2m_\mathrm{e}\gamma v\omega/e$ ($\approx 5\times10^{12}$ V/m for $\hbar\omega = 1.5$ eV and 100 keV electrons) sets a threshold field amplitude that is ~ 4 orders of magnitude greater than the typical values used so far in PINEM experiments[36]. When $\vec{\mathcal{E}}(\mathbf{r})$ does not carry evanescent components, like in a laser pulse in free space, the energy-momentum mismatch yields $\beta_1 = \beta_2 = 0$, which in turn implies zero inelastic scattering events signaled by the fact that $\mathcal{P}_0 = 1$. Here, the phase φ [see Eq. (1.37)] remains the only trace of the interaction and it gives rise to elastic diffraction analogous to the Kaptiza-Dirac effect[37,38].

---

[22] See, for example, Eq. (9.1.41) of Ref. 13

[23] In other works (see, for example, Refs. 34 and 35), this coefficient is indicated with the letter g and sometimes it brings an additional factor of 2 in the denominator that comes from a different definition of the field amplitude taken as $\mathbf{A}(\mathbf{r},t) = (c/\omega)\mathrm{Im}\{\vec{\mathcal{E}}(\mathbf{r})\,\mathrm{e}^{-\mathrm{i}\omega t}\}$.

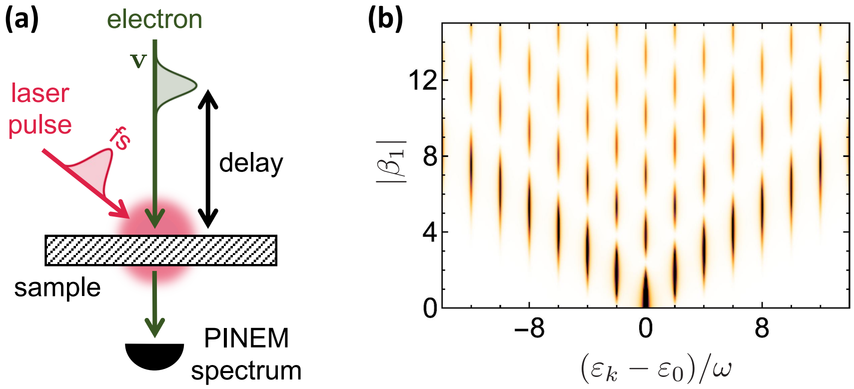

Figure 1.3: Classical PINEM interaction. (a) Schematic of the experimental realization of a PINEM interaction in which a fs laser pulse is synchronized with a an electron pulse at the sample. After leaving the interaction region the electron is collected into a spectrometer and then analyzed. (b) The resulting electron energy loss spectrum resulting from a PINEM interaction as a function of the coupling parameter $|\beta_1|$ according to the peak intensities given by Eq. (1.38). For illustrative purposes the peaks have been broadened by means of a Lorentzian function with FWHM$= 0.12$.

Coming back to the presence of a material interface ($\beta_1 \neq 0$), the linear energy superposition shown in Eq. (1.35a) can be easily observed by looking at the spectrum of the transmitted electrons, as shown in Fig. (1.3a) for $\beta_2 = 0$. According to the rules of quantum mechanics, the peak intensities are directly obtained by squaring the plane wave amplitudes in Eq. (1.35b), yielding

$$P_\ell = J_\ell^2(2|\beta_1|). \tag{1.38}$$

The average net number of quanta exchange is $\langle \ell \rangle \propto |\beta_1|$, thus growing linearly with the field amplitude, together with the presence of coherent oscillations in the scattering order ℓ.

We conclude this subsection by noticing that, neglecting the ponderomotive coupling, since the relation $\mathcal{P}_0(\beta_1, \omega, z)\mathcal{P}_0(\tilde{\beta}_1, \omega, z) = \mathcal{P}_0(\beta_1 + \tilde{\beta}_1, \omega, z)$ holds, the effect of two consecutive PINEM interactions happening under the effect of two synchronized laser pulses with the same frequency can be reduced to a single interaction with a coupling given by the sum of the respective coefficients corresponding to each isolated stage, as experimentally observed in Ref. 39.

1.2.4 Multiple free charges: second quantization

When dealing with systems including many free charges, such as in an e-beam composed by several correlated electrons, it is useful to introduce the formalism of second quantization[40]. Indeed, this formalism allows for a more compact and elegant way of writing equations having the property of maintaining their meaning even when the exact number of particles is not specified. In such framework, every single particle Hamiltonian written in first quantization is transformed into its second-quantized version via the prescription

$$\mathcal{H}(\mathbf{r}) \rightarrow \hat{\mathcal{H}} = \int d^3\mathbf{r}\, \hat{\psi}^\dagger(\mathbf{r})\mathcal{H}(\mathbf{r})\hat{\psi}(\mathbf{r}),$$

where, in the nonrelativistic limit[24], $\hat{\psi}(\mathbf{r}) = \sum_i \varphi_i(\mathbf{r})\hat{c}_i$ is the fermionic field operator, $\hat{c}_i$ are the annihilation operators respecting the anticommutation relations $\{\hat{c}_i, \hat{c}_j^\dagger\} = \delta_{ij}$ and $\{\hat{c}_i, \hat{c}_j\} = 0$, while the functions $\varphi_i(\mathbf{r})$ form a complete set of single-particle eigenstates.

For instance, by again disregarding spin, the QED Hamiltonian of Eqs. (1.31) reduces to

$$\hat{\mathcal{H}}_0 = -\frac{\hbar^2}{2m_\mathrm{e}} \int d^3\mathbf{r}\, \hat{\psi}^\dagger(\mathbf{r})\nabla^2\hat{\psi}(\mathbf{r}), \tag{1.39a}$$

$$\hat{\mathcal{H}}_\mathrm{int}(t) = -\frac{1}{c} \int d^3\mathbf{r}\, \hat{\mathbf{j}}(\mathbf{r},t)\cdot\mathbf{A}(\mathbf{r},t), \tag{1.39b}$$

where we have defined the current operator

$$\hat{\mathbf{j}}(\mathbf{r},t) = \frac{i\hbar e}{2m_\mathrm{e}}\left[\hat{\psi}^\dagger(\mathbf{r})\nabla\hat{\psi}(\mathbf{r}) - \nabla\hat{\psi}^\dagger(\mathbf{r})\hat{\psi}(\mathbf{r})\right] + \frac{e}{2m_\mathrm{e}c}\hat{\rho}(\mathbf{r})\mathbf{A}(\mathbf{r},t), \tag{1.40}$$

together with the charge operator $\hat{\rho}(\mathbf{r}) = -e\hat{\psi}^\dagger(\mathbf{r})\hat{\psi}(\mathbf{r})$. The advantage of expressing the light-matter Hamiltonian as done in Eq, (1.39b) is to explicitly present the quantum current $\hat{\mathbf{j}}$ thus allowing us to easily go from a full quantum-mechanical description of charges, to its classical version. However, we remark that, due to the lack of gauge invariance, the current in Eq. (1.40) cannot be identified as the real measurable current appearing in Eqs. (1.1), but it can be calculated from it as $\hat{\mathbf{j}}^\mathrm{g} = \hat{\mathbf{j}} + e\hat{\rho}\mathbf{A}/2m_\mathrm{e}c$.

1.3 Quantum charges and fields

By taking a closer look at the electron wave function after a PINEM interaction with a classical vector potential $\mathbf{A}(\mathbf{r},t)$ [see Eq. (1.35a)], someone could have noticed that, by extending it from $-\infty$ to ∞, the summation over the net number of exchanged quanta must implicitly assume a field able to supply an unlimited amount of photons. However, if one could dim it enough, the laser should in principle be able to inject a finite amount of quanta in the sample, such that an electron with sufficiently strong coupling could absorb them all. In what follows, we introduce the quantum theory of light necessary to incorporate these types of effects, including the possibility of dealing with scarcely populated cavities.

1.3.1 Light quantization

In order to account for the aforementioned effects, the theoretical framework of QED presented so far requires another ingredient aiming at the inclusion of the light degrees of

---

[24] In relativistic QED, the second-quantized version of the Dirac equation [Eq. (1.29)] must also incorporate the creation and annihilation of positrons represented in first quantization by the negative energy solutions (see Chapter 7).

freedom into a dynamical description: light quantization. Even though, light quantization in free space is a task addressed in almost all ordinary textbooks of quantum mechanics[41], the definition of elementary excitations in complex media is a subject that presents many difficulties and it is still a subject of research. The main problem arises from the fact that every medium different from vacuum, comprising a large number of sub-components such as atoms and molecules, is characterized by its own microscopic dynamics, therefore building complicated electromagnetic responses. However, if one is not interested in the fast processes taking place in the material, but only in the transitions between its collective light-matter states, we can still assume the macroscopic MEQS to hold at an operatorial level, namely upgrading the vector potential function to a field operator

$$\mathbf{A}(\mathbf{r},t) \to \hat{\mathbf{A}}(\mathbf{r},t),$$

where now the time dependence is introduced through a Hamiltonian $\hat{\mathcal{H}} = \hat{\mathcal{H}}_0 + \hat{\mathcal{H}}_{\rm int}$ as $\hat{\mathbf{A}}(\mathbf{r},t) = \mathrm{e}^{\mathrm{i}\hat{\mathcal{H}}t/\hbar}\hat{\mathbf{A}}(\mathbf{r})\mathrm{e}^{-\mathrm{i}\hat{\mathcal{H}}t/\hbar}$. Here, $\hat{\mathcal{H}}_0 = \hat{\mathcal{H}}_0^{\rm f} + \hat{\mathcal{H}}_0^{j}$ accounts for the coupled dynamics of all the components of matter and photons through $\hat{\mathcal{H}}_0^{\rm f}$ as well as the free dynamics of any external source defining a current $\hat{\mathbf{j}}$ via $\hat{\mathcal{H}}_0^{j}$, while $\hat{\mathcal{H}}_{\rm int}$ is given by Eq. (1.39b).

A first step connecting classical and quantum worlds can consist in calculating, in first Born approximation, the average of the quantum vector potential over the state $|\psi(t)\rangle = \mathrm{e}^{-\mathrm{i}\hat{\mathcal{H}}(t-t_0)}|\psi(t_0)\rangle$. In order to do so, we rewrite the state as $|\psi(t)\rangle = \mathrm{e}^{-\mathrm{i}\hat{\mathcal{H}}_0 t/\hbar}\hat{\mathcal{S}}(t)|\psi(-\infty)\rangle$ by means of the scattering operator[40]

$$\hat{\mathcal{S}}(t) = \mathrm{T}\exp\left\{(-\mathrm{i}/\hbar)\int_{-\infty}^{t} dt'\hat{\mathcal{H}}_{\rm int}(t')\right\}, \tag{1.41}$$

where T denotes the time-ordering operator and $\hat{\mathcal{H}}_{\rm int}(t) = \mathrm{e}^{\mathrm{i}\hat{\mathcal{H}}_0 t/\hbar}\hat{\mathcal{H}}_{\rm int}\mathrm{e}^{-\mathrm{i}\hat{\mathcal{H}}_0 t/\hbar}$ is the Hamiltonian of interaction written in the interaction picture. Here, we choose $|\psi_{\rm I}(-\infty)\rangle = |g\rangle$[25] to be the lowest energy state satisfying the equation $\hat{\mathcal{H}}_0|n\rangle = \hbar\varepsilon_n|n\rangle$, where $|n\rangle$ runs over a complete set of states of the entire system. By putting all of these elements together, and by using a classical current $\mathbf{j}$ as a source in $\hat{\mathcal{H}}_{\rm int}$, we obtain the relation[40]

$$\langle\hat{\mathbf{A}}(\mathbf{r},t)\rangle \approx -4\pi c\int_{-\infty}^{\infty} dt' \int d^3\mathbf{r}'\, G^{\rm R}(\mathbf{r},\mathbf{r}',t-t')\mathbf{j}(\mathbf{r}',t'), \tag{1.42}$$

where we have introduced the retarded response function

$$G^{\rm R}(\mathbf{r},\mathbf{r}',t-t') = -\frac{\mathrm{i}}{4\pi\hbar c^2}\langle g|\left[\hat{\mathbf{A}}^{\rm I}(\mathbf{r},t),\hat{\mathbf{A}}^{\rm I}(\mathbf{r}',t')\right]|g\rangle\,\theta(t-t'), \tag{1.43}$$

in which the superscript I stands now for a time dependence given by the interaction picture, namely $\hat{\mathbf{A}}^{\rm I}(\mathbf{r},t) = \mathrm{e}^{\mathrm{i}\hat{\mathcal{H}}_0^{\rm f}t/\hbar}\hat{\mathbf{A}}(\mathbf{r})\mathrm{e}^{-\mathrm{i}\hat{\mathcal{H}}_0^{\rm f}t/\hbar}$. From Eq. (1.42), moving to the frequency domain, we obtain an equation equivalent to Eq. (1.10), which therefore implies the strong equivalence between quantum and classical worlds set by the correspondence $G^{\rm R} = G$. For systems that are invariant under time reversal, this analogy allows one

---

[25] We consider all the media to be a $T = 0$ K (zero temperature), but the generalization to finite T is straightforward.

to deduce another fundamental relation on the average of the field fluctuations [see Appendix C for a self-contained proof]

$$\frac{1}{2}\langle g|\left\{\hat{\mathbf{A}}^{\mathrm{I}}(\mathbf{r},\omega),\hat{\mathbf{A}}^{\mathrm{I}\dagger}(\mathbf{r}',\omega')\right\}|g\rangle=-8\pi^2c^2\hbar\,\mathrm{Im}\{G(\mathbf{r},\mathbf{r}',\omega)\}\,\delta(\omega-\omega'). \tag{1.44}$$

In particular, the previous expression sets a constraint on the form that the quantized vector potential $\hat{\mathbf{A}}$ can take in order to describe the dressed excitations of matter and photons that we wish to model through a single operator.

1.3.2 The macroscopic quantum electrodynamics framework (MQED)

We shall now proceed to present one of the existent theoretical frameworks to describe quantum states of light in the presence of absorbing and dispersive materials, commonly known as macroscopic quantum electrodynamics (MQED) and consisting in quantizing the electromagnetic field while respecting the electromagnetic Green tensor correspondence and the fluctuation-dissipation relation of Eq. (1.44). In particular, MQED has been used for several different developments such as the description of van der Waals[42] and Casimir-Polder forces[43,44], electron scattering generating x-rays and plasmon polaritons[45], and to develop part of the research contained in this Thesis. A full description of such framework can be found in Ref. 7 in the CG, while here we adapt it to the WG.

MQED relies on the introduction of a quantum noise current operator $\hat{\mathbf{j}}^{\mathrm{noise}}(\mathbf{r},\omega)$, satisfying the continuity equation $\nabla\cdot\hat{\mathbf{j}}^{\mathrm{noise}}(\mathbf{r},\omega)=\mathrm{i}\omega\hat{\rho}^{\mathrm{noise}}(\mathbf{r},\omega)$, as an additional contribution to the real material currents appearing in the usual definition of the displacement field that now reads

$$\hat{\mathbf{D}}^{\mathrm{I}}(\mathbf{r},\omega)=\epsilon(\mathbf{r},\omega)\hat{\mathbf{E}}^{\mathrm{I}}(\mathbf{r},\omega)+\frac{4\pi\mathrm{i}}{\omega}\hat{\mathbf{j}}^{\mathrm{noise}}(\mathbf{r},\omega). \tag{1.45}$$

Since we want the operators $\hat{\mathbf{H}}^{\mathrm{I}}$, $\hat{\mathbf{B}}^{\mathrm{I}}$, $\hat{\mathbf{D}}^{\mathrm{I}}$, and $\hat{\mathbf{E}}^{\mathrm{I}}$ to satisfy the operatorial version of Eqs. (1.1) with no external sources, the vector potential operator can be directly written in terms of the noise current as

$$\hat{\mathbf{A}}^{\mathrm{I}}(\mathbf{r},\omega)=-4\pi c\int d^3\mathbf{r}'G(\mathbf{r},\mathbf{r}',\omega)\hat{\mathbf{j}}^{\mathrm{noise}}(\mathbf{r}',\omega). \tag{1.46}$$

By plugging Eq. (1.46) into Eq. (1.44), a relation for the noise currents is obtained. MQED is based on a specific form of the currents which, for a non-magnetic, local, and linearly responding environment are written as[7]

$$\hat{\mathbf{j}}^{\mathrm{noise}}(\mathbf{r},\omega)=\omega\sqrt{\hbar\,\mathrm{Im}\{\epsilon(\mathbf{r},\omega)\}}\,\hat{\mathbf{f}}(\mathbf{r},\omega), \tag{1.47}$$

where $\hat{\mathbf{f}}(\mathbf{r},\omega)$ are a continuous set of bosonic ladder operators satisfying the commutation relations $\left[\hat{\mathbf{f}}(\mathbf{r},\omega),\hat{\mathbf{f}}^\dagger(\mathbf{r}',\omega')\right]=\mathcal{I}\delta(\mathbf{r}-\mathbf{r}')\delta(\omega-\omega')$, and $\left[\hat{\mathbf{f}}(\mathbf{r},\omega),\hat{\mathbf{f}}(\mathbf{r}',\omega')\right]=0$, which create and annihilate photon-matter dressed excitations. By identifying the ground state $|g\rangle$ as the vacuum state such that $\hat{\mathbf{f}}(\mathbf{r},\omega)|0\rangle=0$ and by using the relation

$$\int d^3\mathbf{r}''\mathrm{Im}\{\epsilon(\mathbf{r}'',\omega)\}G(\mathbf{r},\mathbf{r}'',\omega)G^*(\mathbf{r}'',\mathbf{r}',\omega)=-\frac{1}{\omega^2}\mathrm{Im}\{G(\mathbf{r},\mathbf{r}',\omega)\} \tag{1.48}$$

[direct consequence of Eq. (1.11)[7]], one can verify that Eq. (1.44) holds true. In addition, we require the Fourier transform of the field $\hat{\mathbf{A}}^{\mathrm{I}}(\mathbf{r},t) = \int_0^\infty d\omega\, \hat{\mathbf{A}}^{\mathrm{I}}(\mathbf{r},\omega)\mathrm{e}^{-\mathrm{i}\omega t}/2\pi + \int_0^\infty d\omega\, \hat{\mathbf{A}}^{\mathrm{I}\dagger}(\mathbf{r},\omega)\mathrm{e}^{\mathrm{i}\omega t}/2\pi$ to match the time-evolved operator $\mathrm{e}^{\mathrm{i}\hat{\mathcal{H}}_0^{\mathrm{f}}t/\hbar}\hat{\mathbf{A}}(\mathbf{r})\mathrm{e}^{-\mathrm{i}\hat{\mathcal{H}}_0^{\mathrm{f}}t/\hbar}$. This is achieved by choosing the free Hamiltonian to be diagonal in the ladder operators, namely

$$\hat{\mathcal{H}}_0^{\mathrm{f}} = \int_0^\infty d\omega \int d^3\mathbf{r}\, \hbar\omega\, \hat{\mathbf{f}}^\dagger(\mathbf{r},\omega)\cdot\hat{\mathbf{f}}(\mathbf{r},\omega). \tag{1.49}$$

We are now ready to introduce external charges coupling to the quantized field-matter modes. This is accomplished by coupling the field degrees of freedom to the free sources via $\hat{\mathcal{H}}_{\mathrm{int}}$ in Eq. (1.39b). With the help of the commutators reported in Appendix C, the Heisenberg equations for the field operators lead to the last three MEQS for the quantized fields and currents, specifically

$$\begin{aligned}
\partial_t\hat{\mathbf{A}}(\mathbf{r},t) &= \frac{\mathrm{i}}{\hbar}\left[\hat{\mathcal{H}},\hat{\mathbf{A}}(\mathbf{r},t)\right] \to \nabla\times\hat{\mathbf{E}}(\mathbf{r},t) = -\frac{1}{c}\partial_t\hat{\mathbf{B}}(\mathbf{r},t),\\
\partial_t\hat{\mathbf{D}}(\mathbf{r},t) &= \frac{\mathrm{i}}{\hbar}\left[\hat{\mathcal{H}},\hat{\mathbf{D}}(\mathbf{r},t)\right] \to \nabla\times\hat{\mathbf{H}}(\mathbf{r},t) = \frac{1}{c}\partial_t\hat{\mathbf{D}}(\mathbf{r},t) + \frac{4\pi}{c}\hat{\mathbf{j}}^{\mathrm{g}}(\mathbf{r},t),
\end{aligned}$$

If the continuity equation $\nabla\cdot\hat{\mathbf{j}}^{\mathrm{g}}(\mathbf{r},t) = -\partial_t\hat{\rho}(\mathbf{r},t)$ holds[26], we also have $\nabla\cdot\hat{\mathbf{D}}(\mathbf{r},t) = 4\pi\hat{\rho}(\mathbf{r},t)$, thus completing the entire set of macroscopic MEQS.

As a final remark, we note that, since the operator $\hat{\mathbf{A}}^{\mathrm{I}}$ is proportional to the commuting ladder operators, the commutator of two vector potentials $\hat{\mathbf{A}}^{\mathrm{I}}$ turns out to be always a c-number (see, for example, Appendix C), that is a scalar multiplied by the identity in operator space. We shall see that this result has strong implications in solving the dynamics of different configurations, especially in the interaction between an electron and a cavity.

1.3.3 The limit of discrete modes

Despite the generality of the MQED framework, the fact that it is based on the possibility of creating an destroying a infinite continuum of excitations renders it hard to be applied when one is interested in studying the exact state produced by the interaction with one of the bosonic modes (a dominant one). In addition, as we have seen in the context of the dipole approximation [see Fig. (1.2c)], there are cases in which the response of the electromagnetic response of a system in a specific range of frequencies can be well modeled by explicitly considering just one or a few modes.

By following a quantum-optics approach[46,47], and in analogy to the expansion in Eq. (1.46), we write the vector potential operator as a discrete sum of modes

$$\hat{\mathbf{A}}(\mathbf{r}) = \sum_i (-\mathrm{i}c/\omega_i)\left[\vec{\mathcal{E}}_i(\mathbf{r})\hat{a}_i - \vec{\mathcal{E}}_i^*(\mathbf{r})\hat{a}_i^\dagger\right], \tag{1.50}$$

---

[26] This can be shown to hold for any system with a non-interacting Hamiltonian $\hat{\mathcal{H}}_0^j$ commuting with the density operator (i.e., $[\hat{\mathcal{H}}_0^j,\hat{\rho}(\mathbf{r})] = 0$). For instance, it is valid when a scalar and local potential $V(\mathbf{r})$ acts on the particle motion yielding $\hat{\mathcal{H}}_0^j = \int d^3\mathbf{r}\,\hat{\psi}^\dagger(\mathbf{r})[-\hbar^2\nabla^2/2m_{\mathrm{e}} + V(\mathbf{r})]\hat{\psi}(\mathbf{r})$.

where we have introduced a set of bosonic ladder operators $\hat{a}_i$ fulfilling the commutation relations $[\hat{a}_i, \hat{a}_{i'}] = 0$, $[\hat{a}_i, \hat{a}^\dagger_{i'}] = \delta_{ii'}$ as well as the electric field amplitude distributions $\vec{\mathcal{E}}_i(\mathbf{r})$ and frequencies ω_i corresponding to each mode, which still need to be defined. Again, in analogy to Eq. (1.49), when the previous expansion is taken to be valid, we write the free field Hamiltonian as

$$\hat{\mathcal{H}}^{\rm f}_0 = \sum_i \hbar\omega_i \hat{a}^\dagger_i \hat{a}_i, \tag{1.51}$$

and we append a factor $\mathrm{e}^{-\mathrm{i}\omega_i t}$ to $\hat{a}_i$ when writing $\hat{\mathbf{A}}^{\rm I}(\mathbf{r}, t)$.

While we can always expand the vector potential in the general form presented in Eq. (1.50), both the form of the vectors $\vec{\mathcal{E}}(\mathbf{r})$ and the type of evolution associated with the electromagnetic modes can vary depending on the quantization procedure that is employed. For instance, in a system composed of only dielectric structures, the modes can be defined in the same way as done in Eq. (1.16) and the time evolution can be directly introduced through a Schrödinger equation with a Hamiltonian $\hat{\mathcal{H}}^{\rm f}_0 + \hat{\mathcal{H}}^{j}_0 + \hat{\mathcal{H}}_{\rm int}$ supplemented by an additional term $\hat{\mathcal{H}}_{\rm c}$ that takes care of the Coulomb interaction modified by the dielectric environment:

$$\hat{\mathcal{H}}_{\rm c} = \frac{1}{2} \int d^3\mathbf{r}\, d^3\mathbf{r}'\, \hat{\rho}(\mathbf{r}) G^{\rm L}(\mathbf{r}, \mathbf{r}') \hat{\rho}(\mathbf{r}'). \tag{1.52}$$

In general, this term can be disregarded when looking at the interaction of a single free electron with a cavity, as long as the longitudinal self-image attraction can be considered to be negligible [see Section 4].

A more general quantization procedure that includes the possibility of dealing with leaky cavities is provided by quasinormal modes[48]. However, this approach requires the use of the density matrix $\hat{\rho}$ in order to correctly describe the evolution of the state of the quantized excitation, which in the single-mode limit is governed by the Lindblad master equation[48,49]

$$\partial_t \hat{\rho} = \frac{\mathrm{i}}{\hbar} \left[\hat{\mathcal{H}}^{\rm f}_0 + \hat{\mathcal{H}}^{j}_0 + \hat{\mathcal{H}}_{\rm int} + \hat{\mathcal{H}}_{\rm c}, \hat{\rho}\right] + \mathcal{L}[\hat{\rho}], \tag{1.53}$$

with $\mathcal{L}[\hat{\rho}] = (\gamma/2)[2\hat{a}\hat{\rho}\hat{a}^\dagger - \hat{a}^\dagger\hat{a}\hat{\rho} - \hat{\rho}\hat{a}^\dagger\hat{a}]$ standing for the Lindblad operator that phenomenologically accounts for cavity losses at a rate γ. For long-lived cavity modes having lifetimes $\tau = 1/\gamma$ of the order of ~ 1 ps, the operator $\mathcal{L}$ can be safely omitted when interacting with a fast e-beam because the interaction time is $\sim 1000 \times \tau$ for an electron kinetic energy of ~ 1 keV and a cavity of ~ 100 nm in size.

1.3.4 Brief introduction to quantum optics

One of the main consequences of light quantization is that, in order to describe the time evolution of the field and predict the result of an eventual measurement of its phase and intensity, the classical vector amplitude $\mathbf{A}(\mathbf{r}, t)$ used in Section 1.1 is not sufficient anymore, as it only contains part of the information describing the photonic state. Now, the full definition of the field can only be given upon provision of both the form of the vector potential operator $\hat{\mathbf{A}}$ and the field quantum state $|\psi\rangle$. In a single-mode system and for a pure-state evolution, such state can be written as a sum of Fock states $|n\rangle$ in the form

$$|\psi\rangle = \sum_n c_n |n\rangle, \tag{1.54}$$

where c_n are expansion coefficients. The possibility of engineering this linear combination to improve measurements as well as to tune the properties of light-based processes is the main objective of quantum optics (QO)[50]. Here, we quickly review just a few examples of quantum states of light such as single-mode coherent, squeezed, and thermal states, which will be used in the next chapters, putting more emphasis on their particular statistical properties.

Single-mode coherent state

The light state that makes the behavior of a quantum electromagnetic field the closest to its classical version is called coherent state. Its discovery can be traced back to the work of Schrödinger, who was seeking situations in which the quantum and classical descriptions coincided[51], but which were later used in a more systematic way to tackle quantum electrodynamics problems by R. J. Glauber in 1963[52]. In particular, it is defined by the relation

$$|\alpha\rangle = \hat{D}(\alpha)|0\rangle, \tag{1.55}$$

where we have introduced the so-called displacement operator $\hat{D}(\alpha) = \mathrm{e}^{\alpha\hat{a}^\dagger - \alpha^*\hat{a}}$. By projecting onto a Fock state, we can compute the expansion coefficients in Eq. (1.54) for a coherent state:

$$c_n^{\mathrm{ch}} = \mathrm{e}^{-|\alpha|^2/2}\frac{\alpha^n}{\sqrt{n!}}.$$

One immediately notices that the probability of measuring n photons in a coherent state is given by a Poissonian distribution of mean value $\langle\hat{n}\rangle_{\mathrm{ch}} = \sum_{n=0}^{\infty} n|c_n^{\mathrm{ch}}|^2 = |\alpha|^2$, and equal variance $\langle\Delta\hat{n}^2\rangle_{\mathrm{ch}} = \langle\hat{n}^2\rangle - \langle\hat{n}\rangle^2 = |\alpha|^2$, where $\hat{n} = \hat{a}^\dagger\hat{a}$. The connection between a coherent state and the classical field amplitude come from the fact that, by using the property $\hat{D}^\dagger(\alpha)\hat{a}\hat{D}(\alpha) = \hat{a} + \alpha$[46], one can show that a coherent state is an eigenstate of the lowering operator, namely $\hat{a}|\alpha\rangle = \alpha|\alpha\rangle$, therefore transforming part of the operator in Eq. (1.50) into a number. However, $|\alpha\rangle$ is not an eigenstate of the rising operator $\hat{a}^\dagger$, and therefore, it preserves some quantum properties for a low number of photons. The full quantum-classical equivalence is only met for $n \gg 1$, especially when $\hat{a}^\dagger|n\rangle \approx \hat{a}|n\rangle$ as $\sqrt{n+1} \approx \sqrt{n}$ in this limit.

We now introduce the quadrature operators $\hat{X} = (\hat{a} + \hat{a}^\dagger)/2$ and $\hat{Y} = (\hat{a} - \hat{a}^\dagger)/2\mathrm{i}$ as they become particularly important in QO because they are proportional to the position and momentum operators, respectively. In particular, their variances are bounded by the relation $\langle\Delta\hat{X}^2\rangle\langle\Delta\hat{Y}^2\rangle \geq 1/16$, and therefore, the coherent state constitutes a minimum uncertainty state that saturates the inequality through $\langle\Delta\hat{X}^2\rangle_{\mathrm{ch}} = \langle\Delta\hat{Y}^2\rangle_{\mathrm{ch}} = 1/4$.

Another important quantity in the characterization of a quantum state of light is given by the corresponding intensity fluctuations measured by a single detector sensitive to the i-th field polarization and placed at position $\mathbf{r}$. This is given by the zero-delay second-order Glauber correlation function[53]

$$G^{(2)}(0) = \langle \hat{E}_i^{\mathrm{I}-}(\mathbf{r},t)\hat{E}_i^{\mathrm{I}-}(\mathbf{r},t)\hat{E}_i^{\mathrm{I}+}(\mathbf{r},t)\hat{E}_i^{\mathrm{I}+}(\mathbf{r},t)\rangle,$$

where we separated the single-mode version of $\hat{\mathbf{E}}^{\mathrm{I}}(\mathbf{r},t)$ derived from Eq. (1.50) into a sum of two components such that $\hat{\mathbf{E}}^{-}(\mathbf{r},t) \propto \mathrm{e}^{\mathrm{i}\omega t}$ and $\hat{\mathbf{E}}^{+}(\mathbf{r},t) \propto \mathrm{e}^{-\mathrm{i}\omega t}$ [27]. Normalized by the square of the average intensity, it becomes

$$g^{(2)}(0) = \frac{\langle \hat{n}(\hat{n}-1)\rangle}{\langle \hat{n}\rangle^2}. \tag{1.56}$$

By plugging Eq. (1.55) into Eq. (1.56), we obtain $g^{(2)}_{\mathrm{ch}}(0) = 1$. For this reason, when a quantum state of light provides values of $g^{(2)}_{\mathrm{ch}}(0) > 1$, it is said to have super-Poissonian statistics, while in the opposite limit, it is referred to as sub-Poissonian. The measurement of $g^{(2)}(0)$ is therefore of primal importance in understanding the statistics of an unknown light source. For instance, it is widely used to certify single-photon sources, as Eq. (1.56) vanishes when computed for the Fock state $|1\rangle$ [54].

Single-mode coherent-squeezed state

Even though the coherent state is a minimum uncertainty state, other states can also saturate the Heisenberg uncertainty principle by simply decreasing the fluctuations of one of the two operators at the expense of the other. These states are called vacuum squeezed states[55] and they are defined as

$$|\zeta\rangle = \hat{S}(\zeta)|0\rangle, \tag{1.57}$$

with $\hat{S}(\zeta) = \mathrm{e}^{\zeta^* \hat{a}^2/2 - \zeta \hat{a}^{\dagger 2}/2}$ being the unitary squeezing operator. Performing the average on the state in Eq. (1.57) and setting $\zeta = s\,\mathrm{e}^{\mathrm{i}\theta}$, we see that the quadratures take the form $\langle \Delta \hat{X}^2\rangle_{\mathrm{s}} = \mathrm{e}^{-2s}/4$ and $\langle \Delta \hat{Y}^2\rangle_{\mathrm{s}} = \mathrm{e}^{2s}/4$. Therefore, the magnitude of s defines the precision with which a measurement on the position or momentum associated with the electromagnetic mode can be performed. In addition, the second-order correlation function $g^{(2)}_{\mathrm{s}}(0) = 3 + 1/\langle \hat{n}\rangle_{\mathrm{s}}$ predicts a vacuum-squeezed state to display super-Poissonian statistics because $\langle \hat{n}\rangle_{\mathrm{s}} > 0$.

In most realistic systems, the nonlinear generation of squeezed states is usually also accompanied by a linear coupling in the dynamics, such that the final state in the mode is given by a squeezed-coherent state of the form

$$|\alpha,\zeta\rangle = \hat{D}(\alpha)\hat{S}(\zeta)|0\rangle, \tag{1.58}$$

which, when projected onto Fock states, reads

$$c_n^{\mathrm{sch}} = \frac{(\xi/2)^{n/2}}{\sqrt{n!\cosh(s)}}\mathrm{e}^{-(|\alpha|^2+\alpha^{*2}\xi)/2} H_n\left[\frac{\alpha+\alpha^*\xi}{\sqrt{2\xi}}\right], \tag{1.59}$$

---

[27] The ordering of the operators in the correlation function is called normal ordering and its meaning can be found in the actual physical realization of photon detection [see, for example, Ref. 46].

where H_n is the n-th Hermite polynomial[13] and $\xi = \mathrm{e}^{\mathrm{i}\theta} \tanh s$. The corresponding average of the number of photons and variance can be directly computed as

$$\langle \hat{n} \rangle_{\mathrm{sch}} = |\alpha|^2 + \sinh^2(s), \tag{1.60a}$$

$$\langle \Delta \hat{n}^2 \rangle_{\mathrm{sch}} = |\alpha|^2 \left[\mathrm{e}^{-2s} \cos^2(\varphi) + \mathrm{e}^{2s} \sin^2(\varphi) \right] + 2 \sinh^2(s) \cosh^2(s), \tag{1.60b}$$

where $\varphi = \theta/2 - \arg\{\alpha\}$. In particular, Eq. (1.60b) strongly depends on the phase difference φ: the variance takes minimum and maximum values for $\varphi = 0$ and $\varphi = \pi/2$. Since the number of photons represents the phase conjugate variable[46], in the former case $|\alpha, \zeta\rangle$ receives the name of an amplitude-squeezed state, while the latter is called phase-squeezed state.

Single-mode thermal state

As a last example, we consider a state that is typically found when a physical system is in thermal equilibrium with an external reservoir at a temperature T. This state is composted by an incoherent superposition of Fock states, as such it cannot be expressed in the form of Eq. (1.54), but only through the use of the density matrix. The thermal state is thus given by

$$\hat{\rho}_{\mathrm{th}} = \left[1 - \mathrm{e}^{-\theta}\right] \mathrm{e}^{-\theta \hat{n}}, \tag{1.61}$$

where $\theta = \hbar\omega / k_{\mathrm{B}} T$. The average number of photons corresponds to the Bose-Einstein distribution $\langle \hat{n} \rangle_{\mathrm{th}} = (\mathrm{e}^{\theta} - 1)^{-1}$ and the variance is $\langle \Delta \hat{n}^2 \rangle_{\mathrm{th}} = 2 \langle \hat{n} \rangle_{\mathrm{th}} [\langle \hat{n} \rangle_{\mathrm{th}} + 1]$. Finally, from these results we see that $g^{(2)}_{\mathrm{th}}(0) = 2$.

1.4 Microscopic theory of screening

In all previous sections, we assumed the functional form of the permittivity $\epsilon(\omega)$[28] to be well-know and, from it, we derived all the properties related to the electromagnetic response of an arbitrary distribution of different media. Even though in most situations, such as for noble metals, simple models like Drude [see Eq. (1.23)] are sufficient to take into account the motion of electrons in the conduction band in the optical regime, a rigorous description able to capture more exotic effects, such as nonlocality[56], the creation of excitons[57,58], and the influence of complex non-parabolic electronic bands[59], is still remaining as a subject of current investigation. From the theoretical viewpoint, a substantial fraction of this research relies on density functional theory calculations[60], which have shown a remarkable success in predicting material properties from first principles and matching experimental results[59].

Here, we introduce a standard analytical framework based on linear response theory and the RPA to describe the electronic contribution to the permittivity of a medium. Despite its simplicity, it can fully incorporate nonlocal effects and accommodate effects derived from the electronic band structure.

---

[28] Here, the missing spatial dependence derives from the fact that we have used the local approximation in the preceding sections. Indeed, under this assumption the spatial dependence only accounts for the geometrical distribution of the different media [see Fig. (1.3)].

1.4.1 Linear response theory

If we wish to obtain the linear optical properties of a system, we first need to compute the response of its components under an external electromagnetic perturbation. In particular, we restrict our analyses to electrostatic fields ($c \to \infty$), for which the disturbance is provided by a classical scalar potential $\phi^{\rm ext}(\mathbf{r},t)$ coupling to the electrons inside the material via the Hamiltonian

$$\hat{\mathcal{H}} = \hat{\mathcal{H}}_0^j + \int d^3\mathbf{r}\, \hat{\rho}(\mathbf{r})\phi^{\rm ext}(\mathbf{r},t), \tag{1.62}$$

where now $\hat{\mathcal{H}}_0^j$ contains any additional external potential such as the one generated by the ions in a solid as well as the Coulomb repulsion between electrons. By following similar steps as the ones in Section 1.3, one can compute the induced charge density in a system at thermal equilibrium at temperature T in first-order Born approximation. We find

$$\begin{aligned}\rho^{\rm ind}(\mathbf{r},\omega) &= \langle\hat{\rho}(\mathbf{r},\omega)\rangle - \rho^0 \\ &= \int d^3\mathbf{r}'\chi(\mathbf{r},\mathbf{r}',\omega)\phi^{\rm ext}(\mathbf{r}',\omega),\end{aligned} \tag{1.63}$$

which is given in terms of a susceptibility χ and where ρ^0 is the unperturbed charge density in the medium at $t = -\infty$. This response function can be conveniently expressed by introducing a set of the states $|n\rangle$[29] satisfying the eigenvalue equation $\hat{\mathcal{H}}_0^j|n\rangle = \hbar\varepsilon_n|n\rangle$. This leads to

$$\begin{aligned}\chi(\mathbf{r},\mathbf{r}',\omega) = \frac{-1}{\hbar}\sum_{nm} &\exp\left[-(\hbar\varepsilon_m - \mu N_m + \log Z)/k_{\rm B}T\right] \\ &\times\left[\frac{\rho_{mn}(\mathbf{r}')\rho_{nm}(\mathbf{r})}{\omega+\varepsilon_{nm}+{\rm i}0^+} - \frac{\rho_{mn}(\mathbf{r})\rho_{nm}(\mathbf{r}')}{\omega-\varepsilon_{nm}+{\rm i}0^+}\right],\end{aligned} \tag{1.64}$$

where we have introduced the matrix elements $\rho_{nm}(\mathbf{r}) = \langle n|\hat{\rho}(\mathbf{r})|m\rangle$, the frequency difference $\varepsilon_{nm} = \varepsilon_n - \varepsilon_m$, the partition function $Z = \sum_m \exp\left[-(\hbar\varepsilon_m - \mu N_m)/k_{\rm B}T\right]$, the number of particles N_m in the m-th eigenstate, and the chemical potential μ.

1.4.2 The random-phase approximation (RPA)

At first glance, one could think of computing Eq. (1.64) by directly inserting the eigenstates of the system in the expression. However, their evaluation cannot be performed analytically, as it would require the digonalization of $\hat{\mathcal{H}}_0^j$, which also includes the mutual Coulomb interaction among electrons. To overcome this problem, we first define another kind of susceptibility that measures the response of the system to the total scalar potential $\phi^{\rm tot} = \phi^{\rm ext} + \phi^{\rm ind}$ as

$$\rho^{\rm ind}(\mathbf{r},\omega) = \int d^3\mathbf{r}'\,\chi^0(\mathbf{r},\mathbf{r}',\omega)\phi^{\rm tot}(\mathbf{r}',\omega). \tag{1.65}$$

---

[29] This useful method to express response functions is called Lehmann spectral representation[40] and it is fundamental to understand their analytical properties without directly solving the full problem.

Due to the presence of the induced scalar potential, the evaluation of χ^0 turns out to be slightly more involved. In order to retrieve the new susceptibility, we make use of what is known as RPA [61], based on the use of a single-particle picture in which the electron feels the presence of the rest of the charges through a Hartree self-consistent term [62]

$$\mathcal{H}^{\mathrm{F}} = e^2 \int d^3\mathbf{r}'\, \frac{\delta n(\mathbf{r}')}{|\mathbf{r}-\mathbf{r}'|}, \tag{1.66}$$

where $\delta n(\mathbf{r}) = \sum_n f_n |\psi_n(\mathbf{r})|^2 - n_0$ is the variation of the density of electrons at position $\mathbf{r}$ relative to the doping density n_0 and $f_n = 1/[\mathrm{e}^{(\hbar\varepsilon_n-\mu)/k_\mathrm{B}T}+1]$ is the Fermi-Dirac distribution. By again applying linear response theory to a system governed by a new Hamiltonian $\mathcal{H}^j_\mathrm{F}$ that contains $\mathcal{H}^\mathrm{F}$ instead of the Coulomb potential, we obtain [61]

$$\chi^0(\mathbf{r},\mathbf{r}',\omega) = \frac{e^2}{\hbar}\sum_{nm}(f_m - f_n)\frac{\psi_n(\mathbf{r})\psi^*_m(\mathbf{r})\psi^*_n(\mathbf{r}')\psi_m(\mathbf{r}')}{\omega - \varepsilon_{nm} + \mathrm{i}0^+}, \tag{1.67}$$

where now the states $\psi_n(\mathbf{r})$ are solutions of the equation $\mathcal{H}^j_\mathrm{F}\psi_n(\mathbf{r}) = \hbar\varepsilon_n\psi_n(\mathbf{r})$. From Eq. (1.67), the susceptibility χ can be computed in a self-consistent fashion by writing $\rho^\mathrm{ind} = \chi\cdot\phi^\mathrm{ext}$ and then by remembering that $\phi^\mathrm{ind} = G^\mathrm{L}\cdot\rho^\mathrm{ind}$ [30], which yields the relations

$$\phi^\mathrm{ext} = (1 - G^\mathrm{L}\cdot\chi^0)\cdot\phi^\mathrm{tot} \rightarrow \begin{cases}\epsilon = 1 - G^\mathrm{L}\cdot\chi^0, \\ \chi = \chi^0\cdot(1-G^\mathrm{L}\cdot\chi^0)^{-1},\end{cases} \tag{1.68}$$

where we adopted the matrix notation $f\cdot g = \int d^3\mathbf{r}' f(\mathbf{r},\mathbf{r}')g(\mathbf{r}')$. We therefore reduced the calculation of the electromagnetic properties of a medium to the calculation of the system eigenstates $\psi_n(\mathbf{r})$. In Chapter 6, we numerically compute them for the specific case of a 2D periodic system.

The two-dimensional electron gas (2DEG)

When a metallic material is composed of a few vertically[31] assembled atomic layers, conduction electrons are confined within the material thickness $t \sim 1$ nm, which is $\ll \lambda_\mathrm{light}$ in the optical range. In this regime, the eigenfunctions can be approximated as $\psi_n(\mathbf{r}) = \psi^\parallel_n(\mathbf{R})\psi^\perp(z)$ with $|\psi^\perp(z)|^2 = \delta(z)$, therefore yielding $\chi^0(\mathbf{r},\mathbf{r}',\omega) = \tilde{\chi}^0(\mathbf{R},\mathbf{R}',\omega)\delta(z)\delta(z')$ and also implying a similar separation of coordinates for χ.

If we consider now the case of a two-dimensional free electron gas (2DEG), namely electrons in a material that are not subject to any external potential, we obtain the eigensolutions $\psi^\parallel_{\mathbf{k}_\parallel}(\mathbf{R}) = \mathrm{e}^{\mathrm{i}\mathbf{k}_\parallel\cdot\mathbf{R}}/\sqrt{A}$ associated with the eigenvalues $\varepsilon_{k_\parallel} = \hbar k^2_\parallel/2m_\mathrm{e}$, with A the sample area. Upon insertion of these solutions into Eq. (1.67) and by going to momentum space, the susceptibility at zero temperature ($T = 0$ K) reads [62]

$$\mathrm{Re}\left\{-\chi^0_\mathrm{2DEG}(q_\parallel,\omega)\right\} = \frac{m_\mathrm{e}}{\pi\hbar^2}\left\{1 + \left[f_-(q_\parallel,\omega) - f_+(q_\parallel,\omega)\right]/\tilde{q}_\parallel\right\}, \tag{1.69a}$$

$$\mathrm{Im}\left\{-\chi^0_\mathrm{2DEG}(q_\parallel,\omega)\right\} = \frac{m_\mathrm{e}}{\pi\hbar^2\tilde{q}_\parallel}\left[g_-(q_\parallel,\omega) - g_+(q_\parallel,\omega)\right], \tag{1.69b}$$

---

[30] Here, $G^\mathrm{L}(\mathbf{r},\mathbf{r}') = 1/|\mathbf{r}-\mathbf{r}'|$ because the interaction between elementary charges in a medium takes place in vacuum, where $\epsilon = 1$ everywhere.

[31] We set the atomic layers to extend over the xy plane, while extending vertically along the z axis.

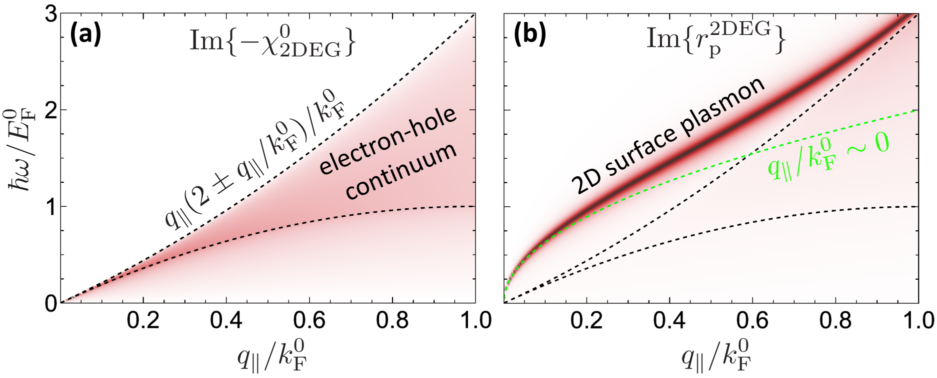

Figure 1.4: Single-particle and collective excitations in a two-dimensional electron gas (2DEG). (a) Imaginary part of the susceptibility χ^0 for a 2DEG as a function of the normalized photon energy $\hbar\omega/E_{\mathrm{F}}^0$ and parallel wave vector $q_\parallel/k_{\mathrm{F}}^0$. The black dashed lines mark the kinematically allowed region for electron-hole pairs creation. (b) Loss function associated with the susceptibility $\chi^0_{\mathrm{2DEG}}(q_\parallel,\omega)$ and calculated from Eq. (1.70), as a function of normalized parallel wave vector and photon frequency. The bright black line shows the dispersion relation of the bulk plasmon in a 2DEG, which is approximated by the curve $\hbar\omega/E_{\mathrm{F}}^0 = e\sqrt{q_\parallel/k_{\mathrm{F}}^0 m_{\mathrm{e}}}$.

where $f_\pm(q_\parallel,\omega) = \mathrm{sign}(\nu_\pm)\theta(\nu_\pm^2 - 1)\sqrt{\nu_\pm^2 - 1}$, $g_\pm(q_\parallel,\omega) = \theta(1-\nu_\pm^2)\sqrt{1-\nu_\pm^2}$, $\nu_\pm = (\hbar\omega/\tilde{q}_\parallel E_{\mathrm{F}}^0 \pm \tilde{q}_\parallel)/2$, $\tilde{q}_\parallel = q_\parallel/k_{\mathrm{F}}^0$, and we have introduced the Fermi energy and wave vector E_{F}^0 and k_{F}^0, respectively. The imaginary part of the susceptibility in Eq. (1.69b) represents a resonant single-particle excitation in which an electron is promoted to a higher energy state by the absorption of a photon [see Fig. (1.4)a]. As we previously mentioned, once $\tilde{\chi}^0$ is computed, the permittivity directly follows from the application of Eq. (1.68). In particular, the collective oscillations of electrons in the material, which are surface plasmons of an extended 2D layer, can be visualized through the so-called loss function $\mathrm{Im}\{r_{\mathrm{p}}^{\mathrm{2DEG}}(q_\parallel,\omega)\}$ defined in terms of the p-polarized Fresnel reflection coefficient [32]

$$r_{\mathrm{p}}^{\mathrm{2DEG}}(q_\parallel,\omega) = \frac{1}{1-\left[\frac{2\pi}{q_\parallel}\chi^0_{\mathrm{2DEG}}(q_\parallel,\omega)\right]^{-1}}, \tag{1.70}$$

as shown in Fig. (1.4b). We notice that the plasmon dispersion for $q_\parallel/k_{\mathrm{F}}^0 \ll 1$ follows the curve $\omega = e\sqrt{2\pi n_0 q_\parallel/m_{\mathrm{e}}}$ [see the green dashed line in Fig. (1.4b)], where $n_0 = k_{\mathrm{F}}^{0\,2}/2\pi$ in a 2DEG.

Two-dimensional periodic systems

When the wave vectors entering in Eq. (1.67) reach values of the characteristic length along which the potential varies in $\mathcal{H}_{\mathrm{F}}^{j}$, such as the interatomic spacing (~ 0.1 nm) in

---

[32] Equation (1.70) can be obtained by using the definition of the reflection coefficient in terms of the external and induced potentials $\phi^{\mathrm{ind}}(\mathbf{q}_\parallel,0) = -r_{\mathrm{p}}^{\mathrm{2DEG}}(q_\parallel,\omega)\phi^{\mathrm{ext}}(\mathbf{q}_\parallel,0)$, with $\phi(\mathbf{q}_\parallel,z) = \int d^2\mathbf{R}\,\mathrm{e}^{-\mathrm{i}\mathbf{q}_\parallel\cdot\mathbf{R}}\phi(\mathbf{r})$, and then by making use of Eq. (1.68).

solids, electrons cannot anymore be regarded as free because the presence of the external disturbance can yield strong anharmonicities in their motion.

If the potential $V(\mathbf{R})$ acting on the 2DEG produces a 2D real space lattice such that $V(\mathbf{R}+\mathbf{R}_i) = V(\mathbf{R})$ with $\mathbf{R}_i$ being any vector connecting two lattice sites, Bloch's theorem[19] ensures that all eigenfunctions can be written as $\psi_{\mathbf{k}_\parallel n}(\mathbf{R}) = \mathrm{e}^{\mathrm{i}\mathbf{k}_\parallel\cdot\mathbf{R}} u_{\mathbf{k}_\parallel n}(\mathbf{R})/\sqrt{A}$, where n is a band index and the in-plane wave vector $\mathbf{k}_\parallel$ is now restricted to the first Brillouin zone (1BZ). In particular, the functions $u_{\mathbf{k}_\parallel n}(\mathbf{R})$ must respect the same symmetry as the potential, namely $u_{\mathbf{k}_\parallel n}(\mathbf{R}) = u_{\mathbf{k}_\parallel n}(\mathbf{R}+\mathbf{R}_i)$. This fact implies that they can be decomposed into a Fourier sum given by

$$u_{\mathbf{k}_\parallel n}(\mathbf{R}) = \sum_{\mathbf{G}} \mathrm{e}^{\mathrm{i}\mathbf{G}\cdot\mathbf{R}} u_{\mathbf{k}_\parallel n\mathbf{G}},$$

with $\mathbf{G}$ running over the reciprocal lattice vectors, $u_{\mathbf{k}_\parallel n\mathbf{G}} = \int_{\mathrm{UC}} d^2\mathbf{R}\, \mathrm{e}^{-\mathrm{i}\mathbf{G}\cdot\mathbf{R}} u_{\mathbf{k}_\parallel n}(\mathbf{R})/A_{\mathrm{UC}}$ and $A_{\mathrm{UC}} = A/N$ is the area of one of the N unit cells (UCs) composing the 2D material[19]. As a consequence, the susceptibility has to satisfy the equation

$$\tilde{\chi}^0(\mathbf{R}, \mathbf{R}', \omega) = \tilde{\chi}^0(\mathbf{R}+\mathbf{R}_i, \mathbf{R}'+\mathbf{R}_i, \omega),$$

which is readily verified upon insertion of $\psi_{\mathbf{k}_\parallel n}$ into Eq. (1.67). Even though the missing continuous translational invariance prevents the analysis of single excitations in the Fourier domain, one can still express $\tilde{\chi}^0$ as a matrix by noticing that any plane wave can be decomposed as $\mathrm{e}^{\mathrm{i}(\mathbf{q}_\parallel+\mathbf{G})\cdot\mathbf{R}}$, with $\mathbf{q}_\parallel$ restricted to the 1BZ. As a consequence, the susceptibility matrix elements read[33]

$$\tilde{\chi}^0_{\mathbf{G}\mathbf{G}'}(\mathbf{q}_\parallel, \omega) = \frac{1}{A}\int d^2\mathbf{R} \int d^2\mathbf{R}'\, \mathrm{e}^{-\mathrm{i}\mathbf{G}\cdot\mathbf{R}+\mathrm{i}\mathbf{G}'\cdot\mathbf{R}'} \mathrm{e}^{-\mathrm{i}\mathbf{q}_\parallel\cdot(\mathbf{R}-\mathbf{R}')} \tilde{\chi}^0(\mathbf{R}, \mathbf{R}', \omega). \quad (1.71)$$

In Eq. (1.71), the components with $\mathbf{G} = \mathbf{G}' \neq 0$ introduce the so-called local-field corrections[63] taking into account fast variations of the total microscopic potential ϕ^{tot} inside the UC. Because of the self-consistent origin of the collective response of a system, local-field corrections may play a fundamental role in its description even if the external potential ϕ^{ext} is composed of wavelengths larger than the interatomic distance, as it is strongly influenced by the local potential landscape.

---

[33] The inverse transform can be computed by evaluating the expression $\tilde{\chi}^0(\mathbf{R}, \mathbf{R}_0, \omega) = \sum_{\mathbf{G}\mathbf{G}'} \mathrm{e}^{\mathrm{i}\mathbf{G}\cdot\mathbf{R}-\mathrm{i}\mathbf{G}'\cdot\mathbf{R}'} \int_{1\mathrm{BZ}} \frac{d^2\mathbf{q}_\parallel}{(2\pi)^2} \mathrm{e}^{\mathrm{i}\mathbf{q}_\parallel\cdot(\mathbf{R}-\mathbf{R}')} \tilde{\chi}^0_{\mathbf{G}\mathbf{G}'}(\mathbf{q}_\parallel, \omega)$.

2

Quantum photon-induced near-field electron microscopy

May the force be with you.
Star Wars

In this chapter, we present a study aimed at extending the classical theory of PINEM presented in Section 1.2 to cases in which the synchronized light cannot be described by a highly populated coherent state, but a quantum description is needed. In particular, what follows is based on the published work, Ref. 64.

2.1 Introduction

EELS performed in electron microscopes is a fertile source of information on the dielectric properties of materials down to the nanometer scale[65–67]. This technique is widely used to identify chemical species with atomic resolution through their characteristic high-energy core losses[68,69]. Additionally, low-loss EELS provides insight into the spatial and spectral distributions of plasmons in metallic nanostructures[8,70–73] and, more recently, also of phonons in polaritonic materials[67] thanks to remarkable advances in instrument resolution. In a parallel effort, the ultrafast dynamics of nanostructured materials and their influence on optical near-fields can be studied by synchronizing the arrivals of fs light and electron pulses at the sample[26,74,75]. Indeed, although photons and electrons interact extremely weakly in free space due to the lack of energy-momentum matching, the evanescent field components produced upon light scattering by material structures breaks the mismatch, giving rise to efficient light-electron interaction, and effectively producing exchanges of multiple quanta between the electron and the optical field, accompanied by a complex sub-fs dynamics[26–29,36,39,76–83]. Based on this principle, PINEM is performed by analyzing the resulting multiple gain and loss features in the electron spectra.

PINEM experiments have so far relied on coherent light sources (i.e., lasers), for which the measured spectra are well reproduced by assuming sample bosonic excitations that are coherently populated with a large number of quanta. The probability of each electron spectral peak associated with a net exchange of ℓ quanta is then simply given by the squared Bessel function $J_\ell^2(2|\beta_1|)$, where a single parameter $\beta_1 = (e/\hbar\omega)\int dz\,\mathcal{E}_z(z)\mathrm{e}^{-\mathrm{i}\omega z/v}$ captures the strength of the electron-light interaction, mediated by the optical electric field component $\mathcal{E}_z(z)$ along the direction of electron propagation z for an electron velocity v and photon frequency ω[36] (see Section 1.2). For nanometer-sized samples (e.g., $\Delta z \sim 100\,$nm) illuminated at optical frequencies ($\hbar\omega \sim 1\,$eV), a field amplitude $\mathcal{E} \sim 10^7\,$V/m renders $|\beta_1| \sim e\Delta z\mathcal{E}/\hbar\omega \sim 1$. Eventually, even the zero loss peak (ZLP, corresponding to $\ell = 0$) is fully depleted for $|\beta_1| \approx 1.2$. The underlying physics is thus described in terms of a classical optical field interacting with the electron through sample-mediated harmonic evanescent fields. However, we expect new physics to arise when departing from this regime by considering anharmonic states of the illuminated sample, such as those associated with fermionic excitations[84–86] or when the external light source is not in a coherent state such as that provided by a laser. As an interesting avenue in this direction, electron-photon entanglement has been recently predicted to influence the interaction with an electron when the sample is previously excited by a trailing electron[87]. In a related context, quantum aspects of fermionic two-level excitations have been probed in the cathodoluminescence signal emitted from single atomic defects[84–86]. In combination with external illumination, efficient excitation of bosonic and fermionic systems could be achieved in order to investigate the difference in quantum behavior between them and how this affects their interaction with electron beams.

In what follows, we discuss the interaction of electron beams with individual optical modes and predict nontrivial characteristics of this interaction when the modes are excited through external illumination depending on the mode nature and population statistics. Specifically, the electron spectra resulting from the interaction with bosonic

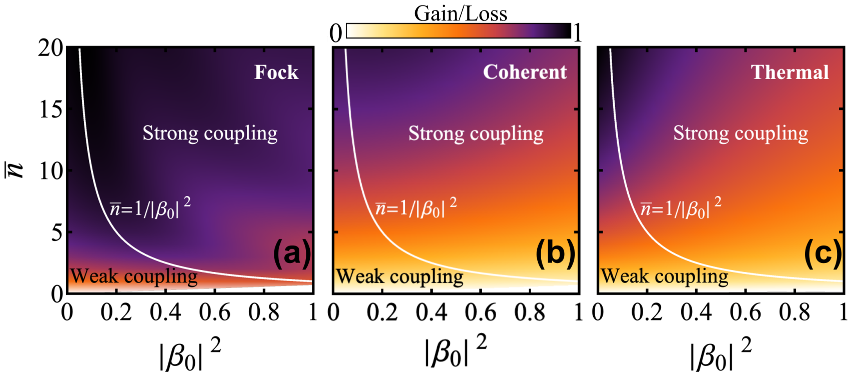

Figure 2.1: Coupling regimes in the interaction of a beam electron with an optical mode. Weak and strong coupling corresponds to the regions roughly separated by the contour $\bar{n}|\beta_0|^2 \sim 1$ (white line), where $\bar{n}$ is the average mode population and β_0 is the single-mode interaction coefficient [Eq. (2.5)]. The density plot shows the ratio of integrated gains and losses in the electron spectra for Fock (a), coherent (b), and thermal (c) populations.

and fermionic excitations exhibit a radically different dependence on the external light intensity. Additionally, the electron spectra for bosonic modes depend dramatically on the photon statistics, giving rise to a varied phenomenology of asymmetric gain and loss peaks at low fluences and distinct intensity dependences under strong pumping. Interestingly, the autocorrelation functions can be directly retrieved from ratios of measured electron gain intensities. We further propose a feasible experimental realization of these ideas based on a sample consisting of an optical cavity that is fed by optically pumped three-level quantum emitters (QEs).

2.2 Interaction between a nonrecoil electron and a quantum optical excitation

We start by considering a sample characterized by a single boson mode[1] of frequency ω_0 interacting with a focused beam electron of momentum and kinetic energy tightly peaked around $\hbar\mathbf{k}_0$ and $\hbar\varepsilon_0$, respectively. Assuming the sample to have an extension along the beam direction sufficiently small as to preserve the transversal beam profile in the sample region, we can write the incident electron wave function as $\psi_0(\mathbf{r},t) = \mathrm{e}^{\mathrm{i}(\mathbf{k}_0\cdot\mathbf{r}-\varepsilon_0 t)}\phi_0(\mathbf{r}-\mathbf{v}t)$, where ϕ_0 is a slowly varying function of the moving-frame position $\mathbf{r}-\mathbf{v}t$. Further adopting the nonrecoil approximation [see Eq. (1.32)] and neglecting inelastic boson losses (>ps lifetimes) during the interaction time (in the fs range), the components of the system Hamiltonian $\hat{\mathcal{H}} = \hat{\mathcal{H}}_0^{\rm par} + \hat{\mathcal{H}}_1^{\rm par}$ correctly approximating the dynamics can be taken from Eqs. (1.33), which by neglecting the ponderomotive term

---

[1] The case of a fermionic system is analyzed later only in the weak-coupling regime. We redirect the reader to Ref. 88 for more information on the non-perturbative interaction between a free electron and a two-level system.

and upgrading the vector potential to an operator, reads

$$\hat{\mathcal{H}}_0^{\rm par} = \hbar\omega_0 \hat{a}^\dagger \hat{a} + \hbar\varepsilon_0 - \hbar\mathbf{v}\cdot(\mathrm{i}\nabla + \mathbf{k}_0),$$
$$\hat{\mathcal{H}}_1^{\rm par} = (e\mathbf{v}/c)\cdot\hat{\mathbf{A}}(\mathbf{r}).$$

Upon inspection, taking $\mathbf{v}$ along z, we find the wave function of the sample-electron system to admit the solution

$$|\psi(\mathbf{r},t)\rangle = \psi_0(\mathbf{r},t)\sum_{\ell=-\infty}^{\infty}\sum_{n=0}^{\infty} \mathrm{e}^{\mathrm{i}\omega_0[\ell(z/v-t)-nt]} f_\ell^n(\mathbf{r})|n\rangle, \qquad (2.1)$$

where f_ℓ^n represents the amplitude of the boson Fock state $|n\rangle$ combined with a change $\ell\hbar\omega_0$ in electron energy. Inserting Eq. (2.1) into the Schrödinger equation $\hat{\mathcal{H}}|\psi\rangle = \mathrm{i}\hbar\partial_t|\psi\rangle$, we find that it is indeed a solution, provided the amplitudes satisfy the equation

$$\frac{df_\ell^n}{dz} = \sqrt{n}\,u^*\, f_{\ell+1}^{n-1} - \sqrt{n+1}\,u\, f_{\ell-1}^{n+1}, \qquad (2.2)$$

where $u(z) = (e/\hbar\omega_0)\mathcal{E}_{0z}(z)\mathrm{e}^{-\mathrm{i}\omega_0 z/v}$. Interestingly, this expression guarantees that $n+\ell$ is conserved along the interaction (i.e., the number of excitations in the electron-boson system is preserved), which in turn allows us to treat each initial population p_n of the boson state $|n\rangle$ as an independent subsystem (i.e., the subset of states in which $n+\ell$ equals the initial value of n before any electron interaction takes place, that is, when $\ell = 0$). However, if we are just interested in the transmitted electron spectrum, we can dismiss the relative phases of these subsystems and initialize the amplitudes as $f_\ell^n(-\infty) = \delta_{\ell 0}\sqrt{p_n}$, with the electron prepared in the incident state $\ell = 0$. After propagation according to Eq. (2.2), the transmitted EELS probability reduces to $\Gamma(\omega) = \sum_{\ell=-\infty}^{\infty} P_\ell\,\delta(\omega+\ell\omega_0)$, where

$$P_\ell = \sum_{n=\max\{0,-\ell\}}^{\infty} |f_\ell^n(\infty)|^2 \qquad (2.3)$$

is the probability for the electron to change its energy by $\ell\hbar\omega_0$. As explained in details in Appendix D, the solution of Eq. (2.2) is formally equivalent to the Schrödinger equation for a classically driven quantum harmonic oscillator for which it exists the analytical solution[89,90]

$$f_\ell^n(\infty) = \sqrt{p_{n+\ell}}\,\mathrm{e}^{\mathrm{i}\chi}\sqrt{(n+\ell)!n!}\;\mathrm{e}^{-|\beta_0|^2/2}(-\beta_0)^\ell \times \sum_{n'} \frac{\left(-|\beta_0|^2\right)^{n'}}{n'!(\ell+n')!(n-n')!}, \qquad (2.4)$$

where the sum is limited to the range $\max\{0,-\ell\} \le n' \le n$, χ is a global phase that describes the image potential felt by the electron during the interaction and results to be irrelevant for this analysis[2], and

$$\beta_0 = \frac{e}{\hbar\omega_0}\int_{-\infty}^{\infty} dz\,\mathcal{E}_{0z}(\mathbf{r})\,\mathrm{e}^{-\mathrm{i}\omega_0 z/v} \qquad (2.5)$$

---

[2] The reader is invited to jump directly to Chapter 4 if interested in the role of χ.

is an electron-boson coupling coefficient (like the PINEM β_0 coefficient, but with the electric field normalized to one quantum); this result, which is in excellent agreement with direct numerical integration of Eq. (2.2), shows that the interaction depends exclusively on the initial mode population p_n and the parameter β_0 defined by Eq. (2.5) (i.e., the details of the $\vec{\mathcal{E}}_0$ field are irrelevant; for instance in the case of dielectric media, they are defined by Eq. (1.17) and well-established procedures exist to obtain such fields[48]).

2.2.1 Weak-coupling limit

Bosonic excitations

A perturbative solution can be produced for Eq. (2.2) in the weak-coupling limit, provided the variations of all amplitudes f_ℓ^n are small during electron-boson interaction. When preparing the incident electron in $\ell = 0$ and the boson in state $|n\rangle$, the nonvanishing elements of the perturbation series $f_\ell^n = \sum_{s=0}^{\infty} f_\ell^{n,s}$ satisfy the equations

$$\begin{aligned}
\frac{df_{-1}^{n+1,1}}{dz} &= \sqrt{n+1}\, u^*, \\
\frac{df_{1}^{n-1,1}}{dz} &= -\sqrt{n}\, u, \\
\frac{df_{-2}^{n+2,2}}{dz} &= \sqrt{n+2}\, u^*\, f_{-1}^{n+1,1}, \\
\frac{df_{0}^{n,2}}{dz} &= \sqrt{n}\, u^*\, f_{1}^{n-1,1} - \sqrt{n+1}\, u\, f_{-1}^{n+1,1}, \\
\frac{df_{2}^{n-2,2}}{dz} &= -\sqrt{n-1}\, u\, f_{1}^{n-1,1}, \\
&\dots,
\end{aligned}$$

where $u(z) = (e/\hbar\omega_0)\mathcal{E}_{0z}(z)\mathrm{e}^{-\mathrm{i}\omega_0 z/v}$. After interaction, the first-order ($s = 1$) amplitudes reduce to $f_{-1}^{n+1,1}(\infty) = \sqrt{n+1}\,\beta_0$ and $f_{1}^{n-1,1}(\infty) = -\sqrt{n}\,\beta_0$, which upon insertion into Eq. (2.3) lead to

$$P_{-1} = (1+\bar{n})|\beta_0|^2, \tag{2.6a}$$

$$P_{1} = \bar{n}|\beta_0|^2, \tag{2.6b}$$

where $\beta_0 = \int_{-\infty}^{\infty} dz\, u(z)$ [see Eq. (2.5)] and $\bar{n} = \sum_{n=0}^{\infty} n\, p_n$ is the average population corresponding to the boson occupation distribution p_n. These expressions allow us to identify the weak-coupling limit condition as $\sqrt{\bar{n}}|\beta_0| \ll 1$. We then find that both loss and gain peaks increase in strength with $|\beta_0|^2$, but their difference is independent of $\bar{n}$. In fact, the electron-boson interaction strength is determined by $\bar{n}|\beta_0|^2$, which allows us to separate the regimes of weak and strong coupling depending on $|\beta_0|^2$ and $\bar{n}$, as shown in Fig. (2.1). We remark that this separation between weak and strong coupling regimes is consistent with the commonly used criterium based on the existence of a perturbative solution to the dynamics of the system, which in the present case depends on the combined value of the mode population $\bar{n}$ and coupling parameter $|\beta_0|$. Additionally, we observe that the ratio of gains to losses approaches 1 in the $\bar{n} \gg 1$ limit, which is consistent with the behavior of the weak-coupling ratio $\bar{n}/(\bar{n}+1)$.

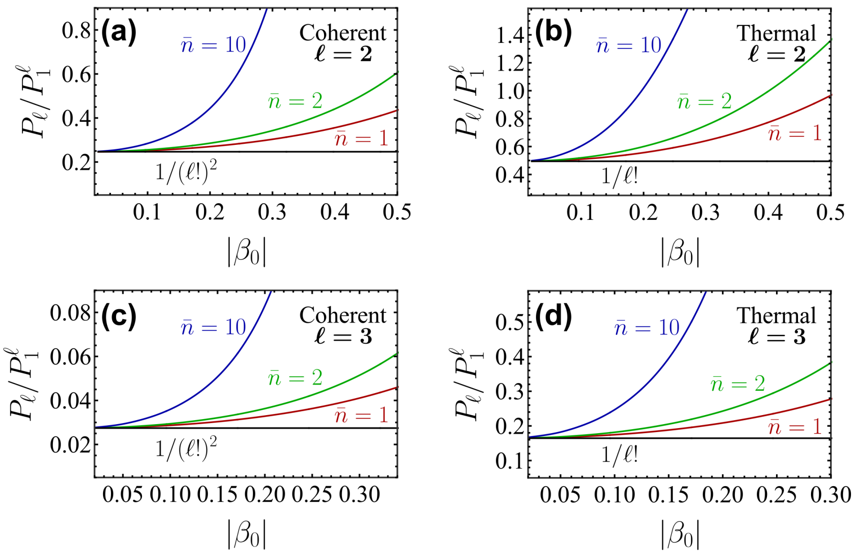

Figure 2.2: Photonic correlation functions in the weak electron-mode coupling regime. (a,b) Ratio of the $\ell = 2$ gain peak intensities for different average numbers of excitations (see color-coordinated labels) with coherent (a) and thermal (b) populations. (c,d) Same as (a,b) for $\ell = 3$. Black horizontal lines correspond to the analytical weak-coupling limit.

In the above series expansion, the lowest-order contribution to the $\ell > 0$ gain peak corresponds to the amplitude $f_\ell^{n-\ell,\ell}$, which satisfies the equation

$$\frac{df_\ell^{n-\ell,\ell}}{dz} = -\sqrt{n-\ell+1}\, u\, f_{\ell-1}^{n-\ell+1,\ell-1}.$$

By iteratively solving this concatenated series of equations, we find the post-interaction solution

$$\begin{aligned} f_\ell^{n-\ell,\ell}(\infty) &= (-1)^\ell \sqrt{n(n-1)\dots(n-\ell+1)} \int_{-\infty}^{\infty} dz_1 \int_{-\infty}^{z_1} dz_2 \\ &\quad \cdots \int_{-\infty}^{z_{\ell-1}} dz_\ell\; u(z_1)u(z_2)\cdots u(z_\ell) \\ &= \frac{1}{\ell!}\sqrt{n(n-1)\dots(n-\ell+1)}\,(-\beta_0)^\ell, \end{aligned}$$

where the rightmost expression is derived upon examination of the symmetry of the ℓ-dimensional integrand upon permutation of its ℓ arguments[40], which allows us to push the upper integration limits to ∞ by creating $\ell!$ copies of it. The intensity of the $\ell > 1$ gain peak thus becomes $P_\ell = |\beta_0|^{2\ell}\left\langle n(n-1)\cdots(n-\ell+1)\right\rangle/(\ell!)^2$, where $\langle\rangle$ denotes the average over the mode population. This leads to the powerful result

$$\frac{P_\ell}{P_1^\ell} = \frac{\mathrm{g}^{(\ell)}(0)}{(\ell!)^2}, \tag{2.7}$$

where $g^{(\ell)}(0) = \langle n(n-1)\cdots(n-\ell+1)\rangle/\bar{n}^\ell$ is the ℓ-th order correlation function at zero delay, which can then be directly inferred from a ratio of peak intensities measured in the transmitted electron spectrum. We present some illustrative examples in Fig. (2.2). For coherent states (i.e., a Poissonian distribution), we have $g^{(\ell)}(0) = 1$ (with $\ell > 0$)[46], leading to gain peak intensity ratios $P_\ell/P_1^\ell = (1/\ell!)^2$. In contrast, for a thermal distribution one has $g^{(\ell)}(0) = \ell!$[46], which produces more intense gain peaks with $P_\ell/P_1^\ell = 1/\ell!$ We stress that these results are valid only for weak interactions, as we are assuming that $|\beta| = \sqrt{\bar{n}}|\beta_0| \ll 1$.

A case of practical interest is represented by a situation in which the bosonic mode has been previously pumped by an external laser source. In this scenario, the boson density matrix admits a rigorous analytical solution[89,91]: $\hat{\rho} = |\xi(t)\rangle\langle\xi(t)|$, where $|\xi\rangle = \mathrm{e}^{-|\xi|^2/2}\sum_{n=0}^{\infty}\left(\xi^n/\sqrt{n!}\right)\mathrm{e}^{-\mathrm{i}n\omega_0 t}|n\rangle$ is a coherent state of amplitude ξ (in the interaction picture) satisfying $a|\xi\rangle = \mathrm{e}^{-\mathrm{i}\omega_0 t}\xi|\xi\rangle$[52] and describing a Poissonian distribution with occupation probabilities $p_n = \langle n|\hat{\rho}|n\rangle = \mathrm{e}^{-|\xi|^2}|\xi|^{2n}/n!$ and average population $\bar{n} = |\xi|^2$. By inserting this expression of $\hat{\rho}$ into the equation of motion, one finds the solution $\xi(t) = (-\mathrm{i}/\hbar)\int_{-\infty}^{t} dt' g(t')\mathrm{e}^{\mathrm{i}\omega_0 t' - (t-t')\kappa/2}$ for the mode amplitude driven by and external classical perturbation $g(t)$. In particular, for the monochromatic light field considered above, this integral leads to

$$\xi(t) = \frac{E_0 p}{\hbar}\left[\frac{\mathrm{e}^{\mathrm{i}(\omega_0-\omega)t}}{(\omega_0-\omega-\mathrm{i}\kappa/2)} + \frac{\mathrm{e}^{\mathrm{i}(\omega_0+\omega)t}}{(\omega_0+\omega-\mathrm{i}\kappa/2)}\right].$$

Assuming again resonant illumination ($\omega = \omega_0$) and neglecting the off-resonance term $\propto \mathrm{e}^{2\mathrm{i}\omega_0 t}$, the average population reduces to $\bar{n} = |\xi|^2 \approx (2E_0 p/\hbar\kappa)^2 = I/2I_\mathrm{s}$. The interaction with an electron in the weak coupling regime is then given by Eqs. (2.6) with the mode occupation written as $\bar{n} = I/2I_\mathrm{s}$.

Fermionic excitations

The interaction with a fast electron can be described following exactly the same formalism as previously done for a bosonic mode, but replacing the commutating bosonic operator $\hat{a}$ by the anticommutating fermionic operator $\hat{\sigma}$. This prescription leads to Eq. (2.2) with f_ℓ^n vanishing unless $n = 0$ or 1. In the weak electron-fermion coupling regime, this results in loss and gain probabilities

$$\begin{aligned} P_{-1} &= p_0|\beta_0|^2 = (1-\bar{n})|\beta_0|^2, \\ P_1 &= p_1|\beta_0|^2 = \bar{n}|\beta_0|^2, \end{aligned}$$

where $|\beta_0|^2$ accounts for the electron-mode coupling strength [see Eq. (2.5)] and $\bar{n}$ must be determined from the the analysis of any previous excitation process the two-level system has experienced prior interaction with the electron.

For instance, a two-level system (states j = 0,1 of energies $\hbar\varepsilon_j$) coupled to a monochromatic light field $\mathbf{E}(t) = \mathbf{E}_0\mathrm{e}^{-\mathrm{i}\omega t} + \mathbf{E}_0^*\mathrm{e}^{\mathrm{i}\omega t}$ constitutes a textbook example of light-matter interactions, commonly described through the optical Bloch equations[92]. The density matrix of the system satisfies the equation of motion

$$\frac{d\hat{\rho}}{dt} = \frac{\mathrm{i}}{\hbar}[\hat{\rho},\hat{\mathcal{H}}] + \frac{\gamma}{2}(2\hat{\sigma}\hat{\rho}\hat{\sigma}^\dagger - \hat{\sigma}^\dagger\hat{\sigma}\hat{\rho} - \hat{\rho}\hat{\sigma}^\dagger\hat{\sigma}), \tag{2.8}$$

where the Hamiltonian $\hat{\mathcal{H}} = \sum_j \hbar\varepsilon_j |j\rangle\langle j| + g(t)\left(\hat{\sigma}^\dagger + \hat{\sigma}\right)$ incorporates the interaction with the transition dipole p through the coupling energy $g(t) = -E(t)p$ (we assume $E_0 p$ to be real and the field aligned with the dipole), and we define $\hat{\sigma} = |0\rangle\langle 1|$ and $\hat{\sigma}^\dagger = |1\rangle\langle 0|$. Additionally, we account for inelastic $1 \rightarrow 0$ transition losses at a rate κ through a Lindbladian term in Eq. (2.8). Writing the density matrix in the interaction picture as $\hat{\rho} = \sum_{j,j'} \rho_{jj'} \mathrm{e}^{\mathrm{i}(\varepsilon_{j'} - \varepsilon_j)t} |j\rangle\langle j'|$, Eq. (2.8) reduces to the Bloch equations

$$\begin{aligned}
\dot{\bar{n}} &= (-2/\hbar)\mathrm{Im}\{\rho_{10}\, g\mathrm{e}^{-\mathrm{i}\omega_0 t}\} - \kappa\bar{n},\\
\dot{\rho}_{10} &= (-\mathrm{i}/\hbar)(1-2\bar{n})\, g\mathrm{e}^{\mathrm{i}\omega_0 t} - \kappa\rho_{10}/2
\end{aligned}$$

for the average population $\bar{n} = \rho_{11} \equiv p_1$ and the coherence ρ_{10}; the other two elements of the density matrix are given by $\rho_{00} \equiv p_1 = 1 - \bar{n}$ and $\rho_{01} = \rho_{10}^*$. At resonance ($\omega = \omega_0$), adopting the rotating-wave approximation (RWA), we have $g\mathrm{e}^{\pm\mathrm{i}\omega_0 t} \approx -E_0 p$, leading to the steady-state solution ($\dot{\bar{n}} = \dot{\rho}_{10} = 0$)

$$\bar{n} = \frac{1}{2}\frac{1}{1 + I_\mathrm{s}/I}, \tag{2.9}$$

which depends on the ratio of the light intensity $I = (c/2\pi)|E_0|^2$ to the saturation intensity of the system $I_\mathrm{s} = c(\hbar\kappa)^2/16\pi p^2$. Therefore from Eq. (2.9), we find $\bar{n} = 1/2$ in the high light-intensity limit.

2.2.2 The high-fluence limit

When the optical mode is strongly pumped prior interaction with the electron, its average photon number can be assumed to overcome the number of exchanged quanta ℓ, condition which formally corresponds in taking the $\bar{n} \gg 1$ limit in Eq. (2.2). In this scenario, the bulk of the electron-boson interaction involves high n's, which we consider to be much larger than the net number of quanta exchanges ℓ. This condition is satisfied if the interaction-strength parameter is small ($|\beta_0| \ll 1$), which is still compatible with a high total effective interaction $\bar{n}|\beta_0|^2 \sim 1$ for sufficiently large $\bar{n}$. We can then approximate both $\sqrt{n}$ and $\sqrt{n+1}$ by $\sqrt{n+\ell}$ in Eq. (2.2); for each value of $n+\ell$, which is conserved during propagation of the electron amplitudes f_ℓ^n along z, the resulting equation coincides with Eq. (2.3) of Ref. 93 for the PINEM interaction with an optical field $\mathcal{E}_z = \mathcal{E}_{0z}\sqrt{n+\ell}$, and therefore, we take from that reference the solution $f_\ell^n(\infty) = \sqrt{p_{n+\ell}}\mathrm{e}^{\mathrm{i}\ell\arg\{-\beta_0\}} J_\ell(2\sqrt{n+\ell}|\beta_0|)$, where β_0 is the electron-mode interaction parameter defined by Eq. (2.5) and $p_{n+\ell}$ is the population distribution of the mode Fock state $|n+\ell\rangle$ before interaction with the electron. Because $n \gg |\ell|$, we can further approximate $n + \ell \approx n$ and write the probability associated with a net number ℓ of quanta exchanges [see Eq. (2.3)] as

$$P_\ell \approx \sum_{n=0}^{\infty} p_n J_\ell^2(2\sqrt{n}|\beta_0|). \tag{2.10}$$

For a boson prepared in the Fock state $|n\rangle$, the interaction probabilities reduce to $P_\ell = J_\ell^2(2|\beta_0|)$, where $\beta = \sqrt{\bar{n}}\beta_0$ and obviously the average mode population is $\bar{n} = n$. Likewise, for a coherent state the population distribution approaches a Gaussian

$p_n \approx \mathrm{e}^{-(n-\bar{n})^2/2\bar{n}}/\sqrt{2\pi\bar{n}}$ in the $\bar{n} \gg 1$ limit[94], the width of which ($\sim \sqrt{\bar{n}}$) becomes increasingly small compared with the average population $\bar{n}$ as this one increases; we can thus approximate $n \approx \bar{n}$ inside the Bessel function of Eq. (2.10), which leads to the result valid both for Fock and coherent states

$$P_\ell = J_\ell^2(2|\beta|), \quad [\text{Fock, coherent}] \tag{2.11}$$

We thus conclude that in the large average population limit both Fock and coherent states of the boson mode produce the same types of electron spectra as observed in PINEM experiments.

The situation is however different for a chaotic thermal distribution $p_n = (1 - \mathrm{e}^{-\theta})\,\mathrm{e}^{-n\theta}$ with average population $\bar{n} = 1/(\mathrm{e}^{\theta} - 1)$, where $\theta = \hbar\omega_0/k_{\mathrm{B}}T$ and T is the mode temperature. We approach the $\bar{n} \gg 1$ limit at high temperatures, for which $\theta \ll 1$, and consequently, $\theta \approx 1/\bar{n}$ and $p_n \approx \mathrm{e}^{-n/\bar{n}}/\bar{n}$. Inserting these expressions into Eq. (2.10) and approximating the sum as an integral with the change of variable $n/\bar{n} = x^2$, we find $P_\ell \approx \int_0^\infty x\,dx\,\mathrm{e}^{-x^2} J_\ell^2(2x|\beta|)$ which reduces to

$$P_\ell = \mathrm{e}^{-2|\beta|^2} I_\ell(2|\beta|^2), \quad [\text{thermal}] \tag{2.12}$$

where again $\beta = \sqrt{\bar{n}}\beta_0$, and the rightmost analytical equality (Eq. (6.633-2) of Ref. 95) allows us to express the result in terms of the modified Bessel function I_ℓ. Reassuringly, we can use the analytical results of Eq. (2.11) and Eq. (2.12) in combination with the small argument approximation $\approx (z/2)^\ell/\ell!$ of both $J_\ell(z)$ and $I_\ell(z)$ with $\ell \geq 0$[13], to find $P_\ell \approx |\beta|^{2\ell}/(\ell!)^2$ and $P_\ell \approx |\beta|^{2\ell}/\ell!$, respectively, therefore directly recovering the above results for the P_ℓ/P_1^ℓ ratio. Additionally, we note that Fock states lead to the same ratio as coherent states in the $\bar{n} \gg 1$ limit because they are characterized by $\mathrm{g}^{(\ell)} = \bar{n}(\bar{n}-1)\dots(\bar{n}-\ell+1)/\bar{n}^\ell \approx 1$ (with $\ell > 0$).

2.3 The coupling to a dipolar excitation

As already mentioned in Section 1.1, reducing the response of a system to its dipolar resonance can be considered an excellent approximation for plasmonic particles and Mie resonators in certain spectral regions [see Fig. (1.2)]. In view of this, we consider a dipolar mode of frequency ω_0 characterized by a transition electric dipole moment $\mathbf{p}$ placed at the origin. We write the single-mode electric field as the one produced by this dipole, by means of the ansatz

$$\vec{\mathcal{E}}_0(\mathbf{r}) = [k_0^2\mathbf{p} + (\mathbf{p}\cdot\nabla)\nabla]\frac{\mathrm{e}^{\mathrm{i}k_0 r}}{r}$$

where $k_0 = \omega_0/c$. The interaction parameter β_0 can be now calculated upon insertion of this field into Eq. (2.5). Integrating by parts, we find that each of the z derivatives in the expression for $\vec{\mathcal{E}}_0$ can be replaced by $\mathrm{i}\omega_0/v$. Finally, assuming a distance b from the electron beam to the dipole and using the integral $\int dz\,\mathrm{e}^{\mathrm{i}k_0 r - \mathrm{i}\omega_0 z/v}/r = 2K_0(\zeta)$, where $r = \sqrt{b^2+z^2}$, $\zeta = \omega_0 b/v\gamma$, and $\gamma = 1/\sqrt{1-v^2/c^2}$ [see Eq. (3.914-4) in Ref. 95, which we use here under the assumption that k_0 has an infinitesimal positive imaginary part],

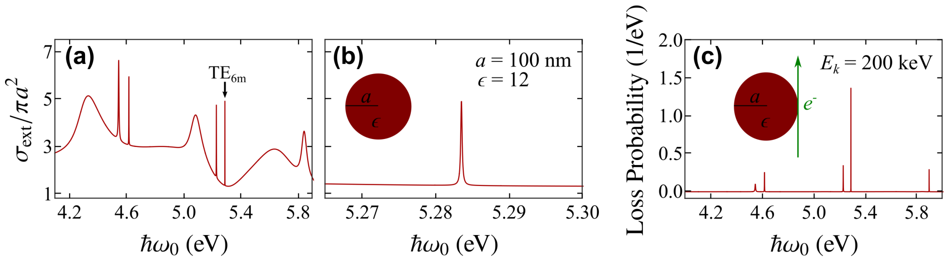

Figure 2.3: Coupling of an electron beam to a dielectric sphere. (a,b) Optical extinction cross-section normalized to projected area for a silicon sphere ($\epsilon = 12$) of radius $a = 100\,$nm. Panel (b) shows a zoom around a TE mode with orbital angular number $l = 6$ [see arrow in (a)]. (c) EELS probability for a 200 keV electron under grazing incidence with respect to the sphere in (a,b).

we readily find the expression

$$\beta_0 = \frac{-2e\omega_0}{\hbar v^2\gamma}\left[{\rm i}p_x K_1(\zeta) + \frac{p_z}{\gamma}K_0(\zeta)\right],$$

In the weak-coupling regime (see Section 2.2.1), the integral of the EELS probability over the mode spectral peak when the mode is initially depleted ($\bar{n} = 0$) reduces to $P_{-1} = |\beta_0|^2 = (2e\omega_0/\hbar v^2\gamma)^2\left[|p_x|^2K_1^2(\zeta) + (|p_z|/\gamma)^2K_0^2(\zeta)\right]$. For an isotropic particle characterized by a triply-degenerate mode of electric dipoles along the Cartesian directions, the probability is given by the sum over the three polarization directions, which amounts to setting $p_x = p_y = p_z = p$; this leads to

$$P_{-1}^{\rm isotropic} = |\beta_0|^2 = |2e\omega_0 p/\hbar v^2\gamma|^2 f(\omega_0 b/v\gamma), \tag{2.13}$$

where $f(\zeta) = K_1^2(\zeta) + K_0^2(\zeta)/\gamma^2$.

In order to corroborate the correctness of the normalization of $\vec{\mathcal{E}}_0$ in the above ansatz, we compare $P_{-1}^{\rm isotropic}$ with the result derived from the classical EELS probability for an isotropic dipolar particle[8], $\Gamma_{\rm EELS,dip}(\omega) = (1/\hbar\pi)(2e\omega/v^2\gamma)^2 f(\omega b/v\gamma)\,{\rm Im}\{\alpha(\omega)\}$, where $\alpha(\omega)$ is the polarizability. Linear response theory allows us to write the latter as[96] $\alpha(\omega) = (|p|^2/\hbar)\left[1/(\omega_0 - \omega - {\rm i}0^+) + 1/(\omega_0 + \omega + {\rm i}0^+)\right]$ in terms of the mode dipole p and frequency ω_0, which upon insertion into the spectral integral $P_{-1} = \int_0^\infty d\omega\,\Gamma_{\rm EELS,dip}(\omega)$ reproduces Eq. (2.13), therefore confirming the ansatz.

2.3.1 Coupling strength for plasmonic cavities

Plasmons in metallic nanoparticles constitute excellent candidates to explore the interaction between electrons and optical cavities. Here, we estimate the coupling parameter $|\beta_0|$ [see leading factor in Eq. (2.13)] for two types of metallic nanoparticles in which the aspect ratio allows one to tune their frequency, also affecting the values of $|\beta_0|$; in particular, we consider prolate ellipsoids and spherical shells made of silver (permittivity $\epsilon(\omega) \approx \epsilon_{\rm b} - \omega_{\rm p}^2/\omega(\omega + {\rm i}/\tau)$ with $\epsilon_{\rm b} \approx 4$, $\hbar\omega_{\rm p} = 9.17\,$eV, and $\hbar/\tau = 21\,$meV[97]). Following similar methods as those of Ref. 98, a prolate ellipsoid of volume V is found to exhibit a normal-to-the-symmetry-axis resonance frequency

$\omega_0 = \omega_\mathrm{p}/\sqrt{\epsilon_\mathrm{b} - \epsilon_0}$ and an effective transition dipole $p \approx (1 - \epsilon_0)\sqrt{\hbar\omega_0 V/8\pi(\epsilon_\mathrm{b} - \epsilon_0)}$, where $\epsilon_0 = 1 - 1/L$, $L = (r^2/2)\Delta^{-3}\left[\pi/2 - \arctan(1/\Delta) - \Delta/r^2\right]$ is the depolarization factor for a height-to-diameter aspect ratio $r > 1$, and $\Delta = \sqrt{r^2 - 1}$. For a spherical metal shell of small thickness t compared with the radius a, filled with a core dielectric ϵ_c, and treated in the $t \ll a$ limit, we find $\omega_0 \approx \left(\omega_\mathrm{p}/\sqrt{\epsilon_\mathrm{c} + 2}\right)\sqrt{2t/a}$ and $p \approx \sqrt{3\hbar\omega_0 a^3/2(\epsilon_\mathrm{c} + 2)}$. Numerical inspection of these two types particles yields optimum coupling values that can reach $|\beta_0| \sim 0.1$ with plasmon energies in the 1 eV region, particle diameters of ~ 20 nm, and electron energies ~ 10 keV when considering either disk-like prolate ellipsoids (aspect ratio $r \sim 5$) or thin shells ($t/a \sim 0.2$) filled with silica ($\epsilon_\mathrm{c} = 2$). The values that we adopt in what follows are commensurate with these parameters.

2.4 Interaction strength of quantum emitters and beam electrons with dielectric optical cavities

High-index dielectric nanostructures can trap light with small radiative leakage. For example, a Si sphere of radius a modeled with a permittivity $\epsilon = 12$ exhibits a narrow resonance at a size parameter $\rho_0 = \omega_0 a/c \approx 2.6775$ with a quality factor (frequency divided by width) $Q = \omega_0/\kappa \sim 10^4$. Analytical EELS calculations based on a previously published formula[8] predict a peak-integrated excitation probability $\sim 10^{-3}$ (i.e., $|\beta_0| \sim 0.03$) for grazingly passing electrons of 100-200 keV kinetic energy [see illustrative calculation in Fig. (2.3)]. Besides this relatively high probability, the large Q value of the Mie resonance under consideration produces a high Purcell enhancement in quantum emitters (QEs) when they are embedded inside the structure, implying nearly perfect QE-cavity coupling and negligible radiative losses. Indeed, following a quantum optics formalism for dispersionless and lossless dielectrics[9], we can express the electromagnetic Green tensor as done in Eq. (1.16); we now argue that the modes contributing to the Mie resonance ω_0 should have similar spatial profiles inside the cavity, so we approximate the transverse part $G(\mathbf{r}, \mathbf{r}', \omega) \approx \mathbf{f}_0(\mathbf{r}) \otimes \mathbf{f}_0^*(\mathbf{r}')/(\omega(\omega + \mathrm{i}\kappa) - \omega_0^2)$ by phenomenologically introducing the resonance width κ and where we have introduced $\mathbf{f}_0 = (-\mathrm{i}/\sqrt{2\pi\hbar\omega_0})\vec{\mathcal{E}}_0$; the Purcell enhancement factor (EF) is then proportional to the local-density of optical states (LDOS) normalized to the vacuum value[99], which can be calculated from G as EF $\approx (-6\pi c^3/\omega)\mathrm{Im}\{\hat{\mathbf{n}} \cdot G(\mathbf{r}, \mathbf{r}, \omega) \cdot \hat{\mathbf{n}}\}$, with $\mathbf{r} = \mathbf{r}'$ corresponding to the position of the QE; for resonant coupling $\omega = \omega_0$, arguing from the normalization condition that $|\mathbf{f}_0|^2 \sim 1/\epsilon V$, where $V = 4\pi a^3/3$ is the cavity volume, we find EF $\sim 9Q/2\epsilon\rho_0^3 \sim 250$ for the cavity under consideration. We now envision QEs with a natural decay rate $g_0 \sim$ GHz, whose coupling rate increases to $g =$ EF $\times\, g_0 \sim 10^2$ GHz; for an optical frequency in the $\omega_0 \sim 100$ THz range, the cavity damping rate is $\kappa \sim \omega_0/Q \sim 10$ GHz, thus leading to small values of $\kappa/g \sim 0.1$ similar to those used in this study.

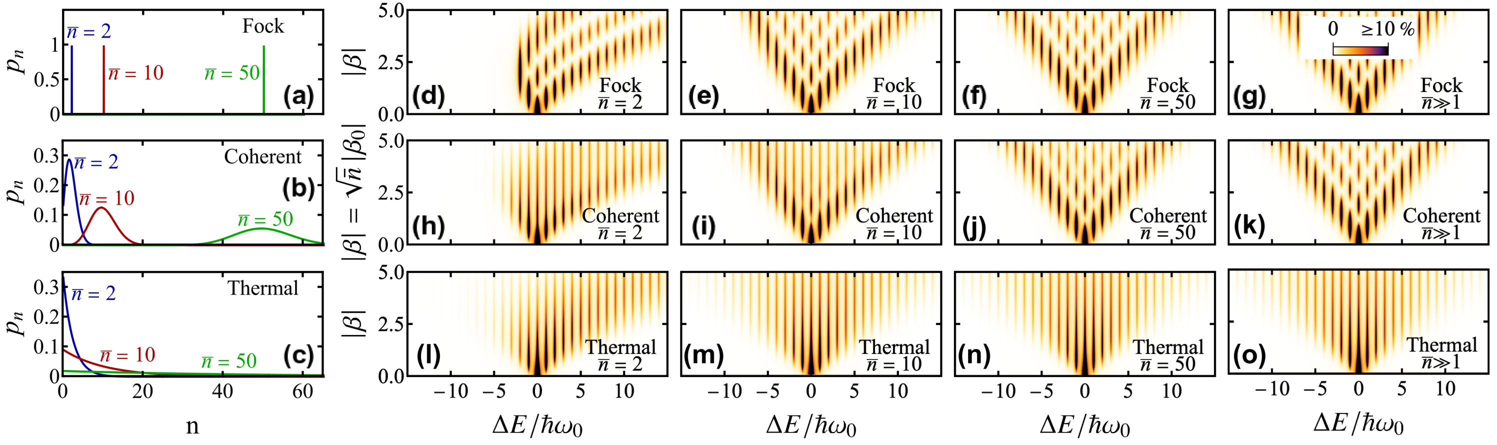

Figure 2.4: Dependence on boson population distribution in the interaction with an electron beam. (a-c) Distribution of the probability p_n for occupation of each state $|n\rangle$ in the three types of population statistics considered at the moment of electron interaction: Fock (a), coherent (b), and thermal (c), with average values $\bar{n}$ =2, 10, and 50. (d-o) Electron spectra after interaction with a dipolar mode with the initial populations of (a-c) as a function of the electron-mode coupling parameter $\sqrt{\bar{n}}|\beta_0|$. The energy loss ΔE is normalized to the boson energy $\hbar\omega_0$ and a peak Lorentzian broadening of $0.1\,\omega_0$ is introduced for clarity.

2.5 General dependence on boson population statistics

As we have already seen from the previous sections, the electron spectra strongly depends on the quantum state of light. Figure (2.1) shows a clear influence on boson population statistics by examining the gain-to-loss ratio $\left(\sum_{\ell>0} P_\ell\right) / \left(\sum_{\ell<0} P_\ell\right)$. In particular, this quantity displays oscillations for a Fock state when either $\bar{n}$ or $|\beta_0|$ is varied, presumably as a remnant of similar oscillations observed in the associated electron spectra (see below). In contrast, averaging over the different Fock states involved in coherent and thermal distributions produces more monotonic ratios. Interestingly, Fock states lead to ratios closer to 1 within the range of parameters explored in the figure, indicating that the probabilities for climbing or descending the n ladder (i.e., $\propto n+1$ and n) quickly approach similar values as n increases compared with coherent and thermal distributions, which involve a substantial contribution from low n's up to relatively large $\bar{n}$.

We further present in Fig. (2.4d-o) the evolution of the transmitted electron spectra for each of the distributions as a function of the coupling parameter $\sqrt{\bar{n}}|\beta_0|$ (vertical scales). The spectra become more asymmetric for smaller $\bar{n}$ because the number of gains cannot substantially exceed $\bar{n}$ (i.e., the electrons cannot absorb more bosons than present already in the sample; see also Fig. (2.1), as observed in recent experiments[100], while the number of losses increases indefinitely with $|\beta_0|$. Incidentally, the similarity between spectra obtained for coherent and thermal states for low $\bar{n}$ stems from the fact that their respective mode populations p_n, although different, also bear some similarity in that limit, and the resulting spectra are fully determined by p_n, as shown by Eqs. (2.3) and (2.4).

In contrast, in the $\bar{n} \gg 1$ limit, as expected from Eq. (2.11) and Eq. (2.12) the electron spectra become symmetric with respect to $\ell = 0$ [Fig. (2.4g,k,o)] when $|\ell| \ll \bar{n}$. In particular, for Fock and coherent distributions, this expression coincides with the well-known PINEM probability[27,36,93] for an optical field amplitude $\mathcal{E}_z = \sqrt{\bar{n}}\mathcal{E}_{0z}$; the resulting spectra [Fig. (2.4g,k)] present the predicted[28] and subsequently measured[29] quantum-billiard oscillatory structure as a function of both ℓ and field strength, as previously studied for model multilevel atoms[101]. In contrast, a thermal boson distribution leads to a monotonic decrease with increasing ℓ and $|\mathcal{E}_z|$ [Fig. (2.4n,o)]. In all cases, we find an average $\langle|\ell|\rangle \sim |\beta|$. The theoretical $\bar{n} \gg 1$ limit is nearly reached under the conditions of Fig. (2.4) for $\bar{n} = 50$ (cf. two rightmost panel columns).

2.6 Interaction with an optical cavity populated through pumped QEs

As a feasible system to explore the above ideas, we consider an optical cavity (e.g., a Mie resonator, similar to those already probed by EELS[102]) hosting a spectrally isolated mode (frequency ω_0, inelastic damping rate κ) fed by a number N of 3-level QEs, as illustrated in Fig. (2.5a). A similar scheme applies to 4-level systems, which are also extensively used in experimental realizations of QEs coupled to optical cavities[103]. We note that optical cavities hosting quantum emitters are customarily used as gain media, for example in infiltrated silica nanoparticles[104] and photonic crystals[105]. The emitters are initialized in their excited state at $t = 0$ (e.g., by optical pumping with a π pulse, typically requiring moderate laser fluences that depend on the kind of QE), from which they decay to an intermediate state by coupling to the cavity at a rate g (same for all QEs for simplicity) with a resonant transition frequency ω_0. We further assume fast internal decay from the intermediate to the ground state, so that each QE interacts with the cavity only once. Incidentally, if inhomogeneous irradiation of the emitters takes place, so that only a fraction of them are excited, the system can then be understood as consisting of a smaller effective number of QEs. The combined probability p_n^m for a cavity Fock state $|n\rangle$ with m remaining excited emitters follows the equation of motion

$$dp_n^m/dt = g\left[n(m+1)p_{n-1}^{m+1} - (n+1)mp_n^m\right] + \kappa\left[(n+1)p_{n+1}^m - np_n^m\right],$$

which we solve numerically to obtain the time-dependent distribution $p_n = \sum_{m=0}^{N} p_n^m$.

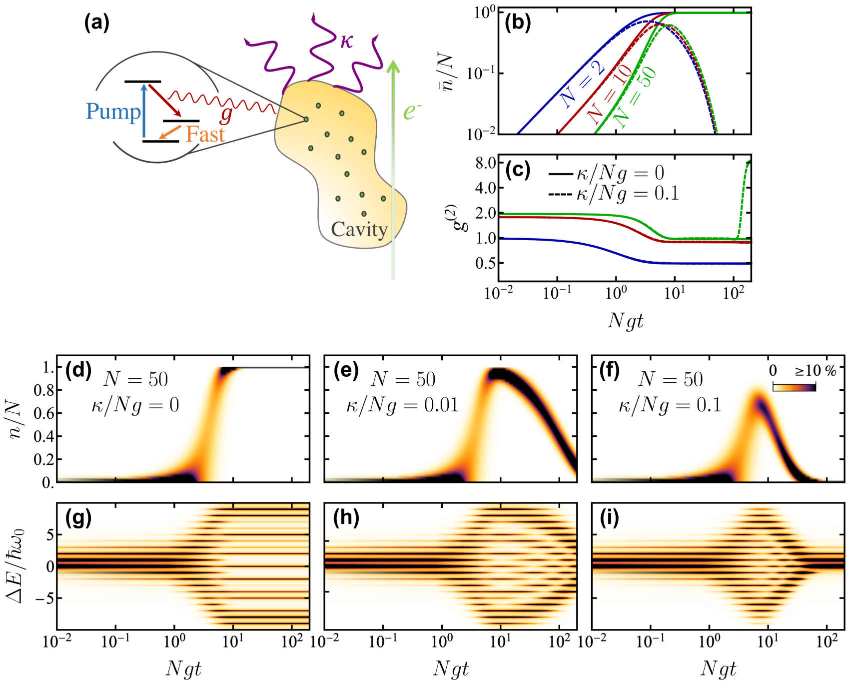

Figure 2.5: Interaction with an optical cavity coupled to pumped quantum emitters (QEs). (a) We consider a bosonic optical cavity (e.g., a Mie resonator) sustaining a single mode (frequency ω_0, inelastic decay rate κ) and infiltrated with N three-level QEs. Optical pumping prepares the emitters in their upper energy state at time $t = 0$, from which they decay to an intermediate level by resonant coupling to the cavity mode at a rate g. (b,c) Temporal evolution of the average cavity mode population $\bar{n}$ (b) and second-order autocorrelation function at zero delay $\mathrm{g}^{(2)}$ (c) for $N = 2$, 10, and 50 with $\kappa = 0$ (solid curves) and $\kappa/Ng = 0.1$ (dashed curves). (d-i) Evolution of the populations p_n (d-f) and the electron spectra (g-i) as a function of the delay time for $N = 50$ and different cavity decay rates: $\kappa/Ng = 0$ (d,g), 0.01 (e,h) and 0.1 (f,i). We assume an electron-mode coupling $|\beta_0| = 0.7$.

Examples of the evolution of the resulting average mode population $\bar{n}$ and second-order autocorrelation $\mathrm{g}^{(2)}(0)$ are shown in Fig. (2.5b,c). The latter starts at $\mathrm{g}^{(2)}(0) = 2(1-1/N)$ at $t=0$ and in the absence of damping evolves toward $1-1/N$ at long times, as expected for an assembly of N single-photon emitters. For finite cavity damping, $\bar{n}$ reaches a maximum $< N$, from which it exhibits an exponential decay, while $\mathrm{g}^{(2)}(0)$ eventually jumps to large values when $\bar{n}$ becomes very small. For a sufficiently large number of QEs, we find a substantial average population while $\mathrm{g}^{(2)}(0)$ varies from nearly 2 down to a quantum regimes characterized by < 1. This evolution strongly affects the resulting electron spectra as a function of the time t at which the electron-boson interaction occurs after pumping the QEs, shown in Fig. (2.5g-i) under the assumption that the interaction time is small compared with both $1/g$ and $1/\kappa$. The spectra initially resemble those of the thermal distributions of Fig. (2.4), as expected from the $\mathrm{g}^{(2)}(0) \approx 2$ values, and gradually become similar to those of Fock states; for finite cavity damping, they undergo an attenuation similar to Fig. (2.4g) as $\sqrt{\bar{n}}|\beta_0|$ decreases [right part of Figs. (2.5h,i)]. In particular, as the average number of photons in the cavity goes down with time, gain and loss peaks concentrate at increasingly lower orders ℓ. Incidentally, under the conditions of Fig. (2.5i), the oscillations in the spectra as a function of ℓ are attenuated compared with those of less lossy cavities [Figs. (2.5g,h)], and additionally, an oscillation-free regime is reached at long times when the population is severely reduced and $\mathrm{g}^{(2)}(0)$ takes high values [see also dashed green curves in Figs. (2.5b,c)].

2.7 Concluding remarks

In summary, in this chapter we have shown that the interaction of electron beams with near optical fields depends on both the quantum nature of the sample excitations (fermionic vs bosonic) and the statistics of their populations. For bosonic modes, the spectral distribution of losses and gains varies dramatically when comparing Fock, coherent, and thermal distributions. Our simulations reveal that these regimes can be explored by populating an optical cavity through optically pumped quantum emitters, for which we have elaborated a model based on realistic optical cavities (e.g., Mie resonators, such as those used in a recent PINEM experiment[106]) infiltrated with optically pumped quantum emitters (e.g., gain atoms or molecules like rhodamine). We predict that the autocorrelation functions of the population distributions are directly retrievable from the peak intensities in the electron spectra. An implementation of this idea to probe the statistics of light with electron beams might be facilitated by schemes in which light-electron coupling is enhanced, for example by using mirrors[36], photonic cavities[106,107], or aloof interaction with total internally reflected light in a prism[35]. Our results hold strong potential for resolving the nature of many-body excitations supported by complex materials, including strongly correlated systems, and open an unexplored avenue for the study of ultrafast plasmon, hot-electron, and phonon dynamics in optically pumped nanostructures using time-resolved electron microscope spectroscopy.

3

Free-electron shaping using quantum light

The most exciting phrase to hear in science, the one that heralds new discoveries, is not "Eureka!" but "That's funny...".
Isaac Asimov

In this chapter, we present a study exploiting the analytical solution for the interaction between a cavity and an electron beam previously found. Specifically, we investigate the role of different quantum light states in tailoring the longitudinal component of the wave function. We pay particular attention to electron density compression after free-space propagation takes place over a macroscopic distance. These results are based on a published work, Ref. 108.

3.1 Introduction

The exploration of ultrafast phenomena generally relies on the use of short probe pulses, such as those provided by femtosecond visible-infrared lasers and attosecond x-ray sources[109–111]. Electrons can potentially reach much shorter durations than light for typical beam energies in the 10^2-10^5 eV range, as they are characterized by oscillation periods of 20-0.02 as. Electron pulse compression is also capital for free-electron lasers[112], relying on the $\propto N^2$ superradiance emission produced by N electrons when acting as a single point charge. With applications such as imaging, spectroscopy, and light generation in view, strong interest has arisen in manipulating the free electron density matrix using light.

With the advent of PINEM, several experimental[26,29,35,36,39,74–78,81,83,106,107,113–115] and theoretical[27,28,31,82,87,93,116–118] studies have demonstrated that interaction with the optical near fields scattered from illuminated nanostructures provides an efficient way to manipulate the temporal and spatial distribution of free electrons. In PINEM, electron and light pulses are made to interact in the presence of a sample, giving rise to multiple photon exchanges between the optical field and the electron, and leading to comb-like energy spectra characterized by sidebands that are associated with different numbers of exchanged photons and separated from the incident electron energy by a multiple of the photon energy. Recent experiments have measured hundreds of such sidebands produced through suitable combinations of sample geometry and illumination conditions[35,106]. Additionally, electron pulse compression has been observed by free propagation of PINEM-modulated electrons over a sufficiently long distance[75,80,83,119]. The electron transforms into a series of pulses with duration down to the attosecond regime[75,80], which can be made even smaller by increasing the strength of the PINEM light[117].

While this type of electron-light interaction affects only the longitudinal part of the electron wave function, lateral control can be achieved either by the use of electron phase masks[120–123] or through modulating the optical field with a transverse spatial resolution limited by the light wavelength, and more generally, by the polariton wavelength when relying on the excitation of optical modes in material surfaces. By analogy to elastic electron diffraction by light gratings in free space (the Kapitza-Dirac effect[37,38,124]), which has been shown to also enable the formation of vortex beams[125], surface-plasmon standing waves can produce intense inelastic electron diffraction[93], as confirmed by the observation of discrete electron beam deflection upon absorption or emission of a given number of photons reflected from a thin metal plate[36]. Similarly, optical near fields can transfer orbital angular momentum[82], also demonstrated through the synthesis and observation of vortex electron beams produced by inelastic interaction with chiral near fields[115]. As a practical application of these phenomena, lateral phase imprinting on electron beams through optical fields has been recently proposed to provide a viable approach to aberration correction and lateral electron beam profiling[126].

By sweeping the photon energy of the light used for PINEM interaction, the near field experienced by the electrons undergoes amplitude modulations that map the optical response of the sample. This strategy has been proposed as a form of spectrally-resolved microscopy that can combine the subnanometer spatial focusing of electron beams[127] with an excellent energy resolution limited by the spectral width of the light source[128,129]. A first demonstration of this possibility has enabled spatial mapping of plasmons in silver nanowires with $\sim$ 20 meV energy resolution without any need for electron monochromators[81], a result that is rivalling the energy resolution achieved through state-of-the art electron energy-loss spectroscopy[67].

The above studies rely on coherent light, such as that generated by laser sources, while an extension to quantum optical fields has been recently predicted to introduce quantum effects in the electron spectra[64]. Quantum light thus presents an opportunity to further manipulate the electron wave function in applications such as pulse compression and modulation of the electron statistics.

Here, we show that a wide range of electron statistics can be reached through interaction of free electrons with quantum light. Besides changing the focusing properties of the optically-modulated electrons, this interaction reveals a strong dependence of the electron density matrix on the statistics of the light field, which can be observed in a self-interference configuration setup. Specifically, we show that interaction with phase-squeezed and minimum-phase-uncertainty light sources produce faster compression of the electron, while amplitude-squeezed light gives rise ultrashort double-pulse electron profiles. Additionally, we find that the interaction of the modulated electron with a target produces a Poissonian distribution of sample excitations with off-diagonal coherences that are strongly dependent on the statistics of the light used to modulate the electron. Besides the fundamental interest of this wealth of phenomena, we envision applications in the control of electron compression and in the generation of light with nontrivial statistics.

3.2 Electron density matrix produced upon PINEM interaction

3.2.1 The quantum PINEM interaction

Free electron-light interaction has been extensively studied under the assumption of classical illumination[27,28]. An extension to describe the quantum evolution of the joint electron-light state has been recently presented[64], which we use here to investigate the modification produced in the electron density profile following propagation after PINEM interaction with nonclassical light. We first provide a succinct summary of this quantum formalism.

We consider the sample response to be dominated by a single bosonic optical mode oscillating at frequency ω_0 and characterized by an electric-field distribution $\vec{\mathcal{E}}_0(\mathbf{r})$ defined as either a normal[9] or a quasi-normal[48] bosonic mode. In addition, we assume that the electron always consists of a superposition of states with relativistic momentum and energy tightly focused around $\hbar\mathbf{k}_0$ and $\hbar\varepsilon_0$ (i.e., having small uncertainties compared with $\hbar\omega_0/v$ and $\hbar\omega_0$, respectively, where v is the electron velocity). Also, we ignore nonunitary elements in the dynamics by considering that the electron-light interaction happens on a fast time scale compared with the decay of the bosonic mode. These assumptions allow us to linearize the electron kinetic energy operator (nonrecoil approximation). Therefore, as shown in the previous chapter, the effective Hamiltonian of the system can be approximated by the noninteraction and interaction pieces[64]

$$\hat{\mathcal{H}}_0^{\rm par} = \hbar\omega_0\hat{a}^\dagger\hat{a} + \hbar\varepsilon_0 - \hbar\mathbf{v}\cdot(\mathrm{i}\nabla + \mathbf{k}_0), \tag{3.1a}$$

$$\hat{\mathcal{H}}_1^{\rm par} = -\mathrm{i}(e\mathbf{v}/\omega_0)\cdot\left[\vec{\mathcal{E}}_0(\mathbf{r})\hat{a} - \vec{\mathcal{E}}_0^*(\mathbf{r})\hat{a}^\dagger\right], \tag{3.1b}$$

respectively, where a and $a^\dagger$ are annihilation and creation operators of the bosonic optical mode, and $\mathbf{v} = \mathbf{k}_0/\varepsilon_0 = v\hat{\mathbf{z}}$ is the electron velocity vector, taken to be along $\hat{\mathbf{z}}$. We remark that the aforementioned QED model accurately reproduces the electron-field dynamics when spin-flips, ponderomotive forces, and electron recoil can be safely disregarded. However, in situations departing from these conditions, the full minimal-coupling Hamiltonian has to be considered, and thus, numerical integration provides a more suitable method to explore the resulting physics[130–132]. We can then write the solution for the electron-optical mode wave function as a sum of energy sidebands, each of them describing the amplitude associated with a net exchange of ℓ quanta with the optical mode ($\ell > 0$ for electron energy gain and $\ell < 0$ for loss). More precisely, we have (see Chapter 2 or Appendix D)

$$|\psi(\mathbf{r},t)\rangle = \psi_0(\mathbf{r},t)\sum_{\ell=-\infty}^{\infty}\sum_{n=0}^{\infty} \mathrm{e}^{\mathrm{i}\omega_0[\ell(z/v-t)-nt]} f_\ell^n(\mathbf{r})|n\rangle, \tag{3.2}$$

where $\mathbf{r}$ denotes the electron coordinate, $|n\rangle$ runs over Fock states of the optical field, $\psi_0(\mathbf{r},t)$ is the incident electron wave function, and the amplitude coefficients admit the closed-form expression

$$\begin{aligned} f_\ell^n =& \mathrm{e}^{\mathrm{i}(\chi+\ell\arg\{-\beta_0\})}\, c_{n+\ell}\, F_\ell^n \\ F_\ell^n =& |\beta_0|^\ell \mathrm{e}^{-|\beta_0|^2/2}\sqrt{(n+\ell)!n!}\sum_{n'=\max\{0,-\ell\}}^{n}\frac{(-|\beta_0|^2)^{n'}}{n'!(\ell+n')!(n-n')!}, \end{aligned} \tag{3.3}$$

with

$$\beta_0(\mathbf{R},z) = \frac{e}{\hbar\omega_0}\int_{-\infty}^{z} dz'\,\mathcal{E}_{0,z}(\mathbf{R},z')\mathrm{e}^{-\mathrm{i}\omega_0 z'/v}$$

acting as a single-mode coupling coefficient and

$$\chi = (-e/\hbar\omega_0)\int_{-\infty}^{z} dz'\,\mathrm{Im}\{\beta_0^*(\mathbf{R},z')\mathcal{E}_{0,z}(\mathbf{R},z')\mathrm{e}^{-\mathrm{i}\omega_0 z'/v}\}$$

representing a global phase that is irrelevant in the present study (see Chapter 4 for more details). A dependence on lateral coordinates $\mathbf{R} = (x,y)$ is imprinted by the spatial distribution of the optical mode field. In the initial state (i.e., before quanta exchanges), only $\ell = 0$ terms are present, so we can write $f_\ell^n(z \to -\infty) = \delta_{\ell 0}c_n$, where the amplitudes c_n define the starting optical boson field, which must satisfy the normalization condition

$$\sum_n |c_n|^2 = 1. \tag{3.4}$$

Interestingly, the number of excitations $n' = n + \ell$ is conserved along the temporal evolution of the system[64], thus allowing us to propagate each initial n' component separately and multiply it by the initial boson amplitude $c_{n+\ell}$ when writing Eq. (3.3). Because the expansion coefficients defined in this equation are obtained from the evolution operator[64], they satisfy the normalization condition $\sum_{\ell n} |f_\ell^n|^2 = \sum_{\ell n'} |c_{n'} F_\ell^{n'-\ell}|^2 = 1$ for any optical field, which leads to the condition

$$\sum_\ell (F_\ell^{n-\ell})^2 = 1 \tag{3.5}$$

satisfied for any n.

Electron propagation prior to interaction is described through the linearized Hamiltonian $\hat{\mathcal{H}}_0$, which essentially assumes that the electron beam is well collimated and energy dispersion is negligible in the PINEM interaction region, such that we can write

$$\psi_0(\mathbf{r}, t) = \mathrm{e}^{\mathrm{i}\mathbf{k}_0\cdot\mathbf{r} - \mathrm{i}\varepsilon_0 t} \phi_0(\mathbf{r} - \mathbf{v}t),$$

where ϕ_0 is a slowly varying function of relative position $\mathbf{r} - \mathbf{v}t$. Importantly, Eq. (3.3) prescribes that the evolution of the electron-boson system is uniquely determined by the nondimensional coupling parameter β_0 in combination with the amplitudes α_n defining the initial optical wave function. In what follows, we assume no dependence on $\mathbf{R}$ (see below) and set $\beta_0 \equiv \beta_0(z \to \infty)$ because we are interested in studying free-electron propagation after PINEM interaction has taken place, even though this dependence plays a fundamental role in the observed transfer of orbital angular momentum between photons and electrons[115], and in addition, it could be useful to correct electron beam aberrations[126]. Nevertheless, the coefficients of the quantum light state in Eq. (3.3) could provide an additional knob to further intertwine longitudinal and transverse electron degrees of freedom beyond what is possible using classical light. Additionally, they could affect the maximum achievable probability associated with specific PINEM sidebands, as well as the dependence on pulse duration, which also deserve further study.

3.2.2 Effect of free propagation

Our purpose is to investigate the electron characteristics after free propagation over a macroscopic distance of several mm from the PINEM interaction region [see Fig. (3.1a)]. We identify in Eq. (3.2) a propagation phase $\mathrm{e}^{\mathrm{i}k_\ell z}$ associated with each ℓ sideband, in which the electron wave vector is replaced by its linearized nonrecoil version $k_\ell \approx k_0 + \ell\omega_0/v$. While this approximation does accurately describe propagation over the relatively small extension of the PINEM interaction region, the exact expression

$$\begin{aligned} k_\ell &= \hbar^{-1}\sqrt{E_\ell^2/c^2 - m_\mathrm{e}^2 c^2} \\ &\approx k_0 + \ell\omega_0/v - 2\pi\ell^2/z_T + \cdots, \end{aligned} \tag{3.6}$$

needs to be used to deal with arbitrarily long propagation distances z, where the second-order correction, characterized by a distance

$$z_T = 4\pi\, m_\mathrm{e} v^3 \gamma^3 / \hbar\omega_0^2 \tag{3.7}$$

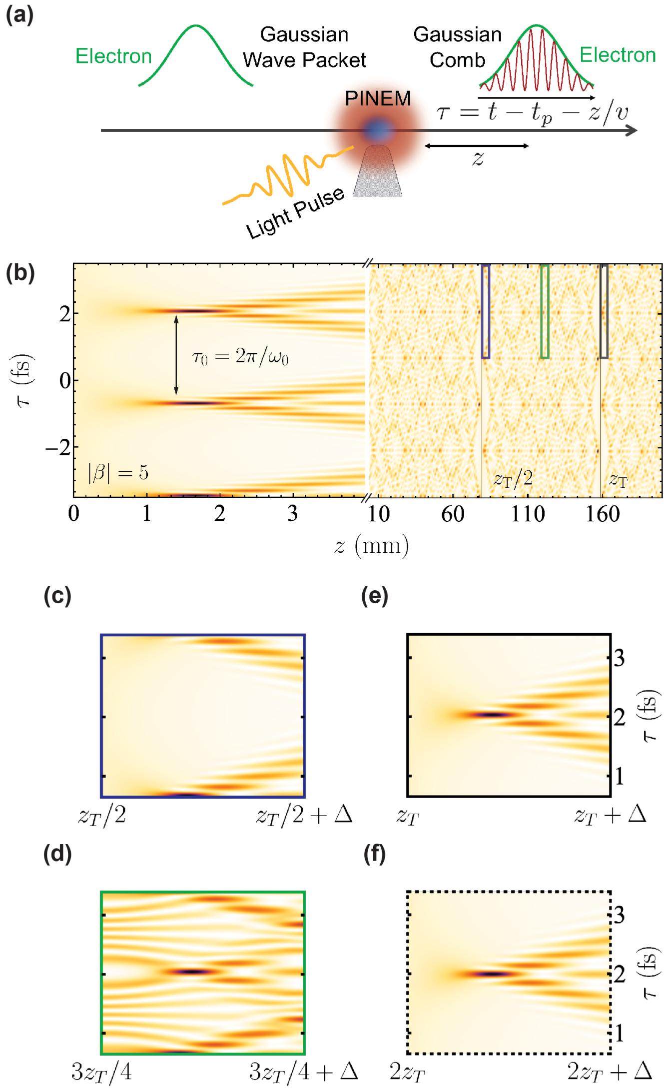

Figure 3.1: Talbot effect and electron compression with classical light. (a) An electron Gaussian wave packet (green) is transformed through PINEM interaction followed by propagation along a distance z into a substantially modified electron density profile in the propagation-distance-shifted time $\tau = t - z/v$ due to superposition of different energy components. (b) Electron density profile (vertical τ coordinate) as a function of propagation distance z (horizontal axis) after PINEM interaction with coherent light. We consider 100 keV electrons, a photon energy $\hbar\omega_0 = 1.5\,\mathrm{eV}$, and a coupling coefficient $|\beta| = 5$. Trains of compressed electron pulses are periodically observed at discrete multiple values of the Talbot propagation distance z_T. (c-e) Details of the τ-z map in (b) corresponding to the color-matched square regions of z width $\Delta = 4\,\mathrm{mm}$. (f) Same as (e), but for z near $2z_\mathrm{T}$.

(e.g., $z_T \approx 159\,\mathrm{mm}$ for $\hbar\omega_0 = 1.5\,\mathrm{eV}$ and 100 keV electrons), is sufficiently accurate under the conditions here considered, giving rise to numerical results that are indistinguishable from the full expression in the examples shown below.

Our purpose is to study electron propagating and dismiss any entanglement with the PINEM optical field. We thus consider the electron density matrix, obtained from the pure-joint-state density matrix $|\psi(z,t)\rangle\langle\psi(z',t)|$ by tracing out the optical degrees of freedom:

$$\rho(z,z',t) = \sum_{n=0}^{\infty} \psi_n(z,t)\psi_n^*(z',t), \tag{3.8}$$

with

$$\psi_n(z,t) = \phi_0(z-vt) \sum_{\ell=-\infty}^{\infty} c_{n+\ell}\, F_\ell^n \mathrm{e}^{\mathrm{i}k_\ell z - \mathrm{i}\ell\omega_0(t-t_p)},$$

where the phase of β_0 enters only through a time shift $t_p = \arg\{-\beta_0\}/\omega_0$. We remark here that the mathematical operation of tracing out the degrees of freedom associated with the photonic mode to obtain a density matrix for the electron subsystem is physically justified by the fact that this operation ensures the correct measurement statistics if one only needs to measure electron properties (i.e., without performing any measurement on the rest of the system)[133].

We note that diffraction effects involving the transverse evolution of the wave function are disregarded. Under attainable experimental conditions, an initial 100 keV electron beam with $\varphi \sim 50\,\mu$rad divergence, focused to a $2/k_0\varphi \sim 25\,\mathrm{nm}$ spot over the PINEM interaction region, becomes just a factor ~ 2 wider after free propagation over a distance $z \sim 1\,\mathrm{mm}$ due to diffraction. In addition, the results here presented are valid under the assumption that $\phi(z-vt)$ involves a sufficiently narrow wave vector decomposition to neglect corrections beyond the linear energy dependence of the wave vector during the propagation distances under consideration, so ϕ enters the electron density matrix just as a broad envelope factor. However, we note that these assumptions may break in scenarios involving slow electrons ($\hbar\varepsilon_0 \lesssim 10^2$ eV) or very strong electron-field coupling, in which the ponderomotive force can lead to a non-negligible beam spreading after interaction with the sample[132].

3.2.3 Talbot effect and periodicity of the density matrix

Retaining just up to ℓ^2 corrections in Eq. (3.6) for k_ℓ and considering relative positions $|z-z'| \ll z_T$, we can recast the electron density matrix (Eq. (3.8)) as

$$\rho(z,z',t) = \mathrm{e}^{\mathrm{i}k_0(z-z')}\phi_0(z-vt)\phi_0^*(z'-vt)\tilde{\rho}(z,\tau,\tau'),$$

where

$$\tilde{\rho}(z,\tau,\tau') = \sum_{n\ell\ell'} c_{n+\ell}c^*_{n+\ell'}\, F_\ell^n F_{\ell'}^n \times \mathrm{e}^{2\pi\mathrm{i}\left[(\ell'^2-\ell^2)z/z_T + (\ell'\tau'-\ell\tau)/\tau_0\right]}, \tag{3.9}$$

$\tau = t - t_p - z/v$, and $\tau' = t - t_p - z'/v$. Disregarding the trivial phase propagation factor $\mathrm{e}^{\mathrm{i}k_0(z-z')}$ and the slowly varying envelope introduced by ϕ, the density matrix is periodic in both of the time-shifted coordinates τ and τ' with the same period as the light optical cycle $\tau_0 = 2\pi/\omega_0$. Additionally, we find that $\tilde{\rho}(z,\tau,\tau')$ portrays a periodic pattern as a function of propagation distance z similar to the Talbot effect[134–138], with a period given by z_T in Eq. (3.7).

To illustrate this effect, we plot in Fig. (3.1b) the diagonal elements $\rho(z,z,t) = \sum_{n=0}^{\infty} |\psi_n(z,t)|^2$ normalized to the envelope density $|\phi(z-vt)|^2$ for coherent light illumination, which represent the scaled electron density profile as a function of time and propagation distance z from the PINEM interaction region, calculated in the high-fluence classical limit (see below). Incidentally, off-diagonal elements are also considered and represented below in Fig. (3.4). The plot clearly reveals a train of temporally focused electron pulses at $z \sim 1.5\,\mathrm{mm}$, followed by a series of focusing revivals at intervals of $z_T \approx 159\,\mathrm{mm}$ and accompanied by temporally shifted revivals at fractional values of the Talbot distance z_T[139].

3.3 Electron pulse compression with different optical mode statistics

Before analyzing the effect of light statistics in the evolution of the electron after PINEM interaction, we remark that the previous formalism is only valid for pure initial optical states, whose density matrix is given by $\sum_{nn'} c_n c_{n'}^* |n\rangle\langle n'|$. In contrast, for a perfect mixture (i.e., an initial optical density matrix $\sum_n |c_n|^2 |n\rangle\langle n|$ with no coherences), the outcome of interaction and propagation has to be separately calculated for each Fock state $|n\rangle$ and then averaged incoherently. Using the normalization conditions of Eqs. (3.4) and (3.5), we find an electron density matrix $\tilde{\rho}(z,\tau,\tau') = 1$, which is not altered due to interference between different energy components after PINEM interaction. We note that a well-defined optical Fock state belongs to this category and thus does not produce changes in the electron density matrix either.

3.3.1 High-fluence and classical limits

Electron coupling to a single optical mode is generally weak and therefore characterized by a small coupling coefficient $|\beta_0| \ll 1$ (e.g., we set $|\beta_0| = 0.2$ here, as a feasible value for coupling to Mie and plasmon modes in nanoparticles[64]). Still, a strong PINEM effect can be produced with a high average number of photons $\bar{n} = \sum_n n|c_n|^2$, while only sidebands $|\ell| \ll \bar{n}$ can then be efficiently populated. In this limit, the dominant contribution to the sum in F_ℓ^n comes from $n' \ll n$ terms, so we can approximate

$$F_\ell^n \approx \sum_{n'=0}^{\infty} \frac{(-1)^{n'} |\beta_0|^{2n'+\ell}}{n'!(\ell+n')!} \frac{\sqrt{(n+\ell)!n!}}{(n-n')!}.$$

We now apply the Stiling formula $n! \approx \sqrt{2\pi n}\,(n/e)^n$ to the factorials in the rightmost fraction and neglect ℓ and n' in front of n in the factors that are not affected by an exponent n. This allows us to approximate $\sqrt{(n+\ell)!n!}/(n-n')! \approx (n/e)^{n'+\ell/2}\mathrm{e}^M$, where $M = n \ln\left[\sqrt{1+\ell/n}/(1-n'/n)\right]$. We then retain only terms up to first order in the Taylor expansion of the logarithm to find $M \approx n' + \ell/2$. Upon insertion of this result into the above expression for F_ℓ^n, we find $F_\ell^n \approx \sum_{n'=0}^{\infty}(-1)^{n'}|\sqrt{n}\beta_0|^{2n'+\ell}/[n'!(\ell+n')!]$, which directly yields

$$F_\ell^n \approx J_\ell(2\sqrt{n}|\beta_0|). \tag{3.10}$$

by identifying the sum as the Taylor expansion of the Bessel function J_n with argument $2\sqrt{n}|\beta_0|$[1]. Additionally, if the optical mode is prepared in a coherent state (e.g., by exciting it with laser light), its population follows a Poissonian distribution $|c_n|^2 = \mathrm{e}^{-\bar{n}}\,\bar{n}^n/n!$, which approaches a normal distribution[94] $|c_n|^2 \approx \mathrm{e}^{-(n-\bar{n})^2/2\bar{n}}/\sqrt{2\pi\bar{n}}$ for $\bar{n} \gg 1$. Introducing this expression in Eq. (3.9), approximating $n \approx \bar{n}$ in Eq. (3.10), and using the normalization condition $\sum_n |c_n|^2 = 1$, we can write the density matrix in the high-fluence classical limit as

$$\tilde{\rho}(z,\tau,\tau') \approx \psi_{\rm cl}(z,\tau)\psi^*_{\rm cl}(z,\tau'),$$

where

$$\psi_{\rm cl}(z,\tau) = \sum_\ell J_\ell(2|\beta|)\mathrm{e}^{-2\pi\mathrm{i}(\ell^2 z/z_T + \ell\tau/\tau_0)}$$

and

$$\beta = \sqrt{\bar{n}}\beta_0 \tag{3.11}$$

is the effective coupling coefficient, which is proportional to the light intensity used to excite the optical mode. This result is consistent with previous theoretical[29,117] and experimental[80,119] studies of free propagation after high-fluence classical PINEM interaction. Electron compression and Talbot revivals in this limit are shown in Fig. (3.1b) for coherent illumination with $|\beta_0| = 0.2$ and $|\beta| = 5$, while a zoom of the focal region is presented in Fig. (3.2a).

Interestingly, for any population of the optical mode that is smooth and strongly peaked around $\bar{n} \gg 1$, we can approximate $c_{n+\ell} \approx c_n$ for $|\ell| \ll n$, so the wave function completely separates into light and electron components in Eq. (3.2), which becomes

$$\begin{aligned}|\psi(\mathbf{r},t)\rangle \approx &\sum_{n=0}^{\infty} c_n \mathrm{e}^{-\mathrm{i}n\omega_0 t}|n\rangle \\ &\times \psi_0(\mathbf{r},t)\sum_{\ell=-\infty}^{\infty} \mathrm{e}^{\mathrm{i}(\chi+\ell\arg\{-\beta\})}\, J_\ell(2|\beta|)\,\mathrm{e}^{\mathrm{i}\ell\omega_0(z/v-t)},\end{aligned}$$

in agreement with a well-known expression for PINEM with classical light[36].

---

[1] Indeed, the Taylor expansion of the Bessel J_n function reads $J_n(x) = \sum_{m=0}^{\infty}[(-1)^m/m!(m+n)!](x/2)^{2m+n}$ [13].

3.3.2 Coherent squeezed light

We now explore squeezed light as an experimentally feasible alternative to classical laser light to excite the PINEM optical mode. Single-mode coherent squeezed states $\hat{D}(g)\hat{S}(\zeta)|0\rangle$ are defined by applying the displacement and squeezing operators, $\hat{D}(g) = \exp\left(ga^\dagger - g^* a\right)$ and $\hat{S}(\zeta) = \exp\left[(\zeta^* aa - \zeta a^\dagger a^\dagger)/2\right]$, to the optical vacuum (see Section 1.3).

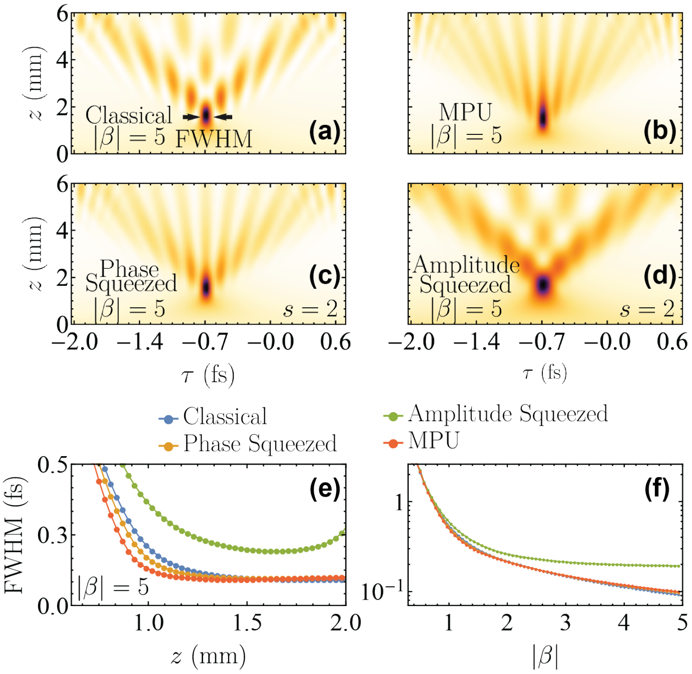

Figure 3.2: Electron compression using squeezed light. (a-d) Evolution of the electron density profile following PINEM interaction with (a) classical, (b) MPU, (c) phase-squeezed, and (d) amplitude-squeezed light using a single-mode coupling coefficient $|\beta_0| = 0.2$ and average population $\bar{n} = 625$ (i.e., $|\beta| = \sqrt{\bar{n}}|\beta_0| = 5$). (e) FWHM [see panel (a)] of the compressed electron density in (a-d) as a function of propagation distance z. (f) Minimum in the FWHM along the curves in (e) as a function of coupling coefficient $|\beta|$ (varying $|\beta_0|$ and keeping $\bar{n} = 625$). We consider 100 keV electrons and a 1.5 eV photon energy.

We consider the two extreme possibilities of PINEM interaction with purely phase- and amplitude-squeezed light in Fig. (3.2c,d), where we plot the density profile $\rho(z,z,t) = \tilde{\rho}(z,\tau,\tau)$ as a function of propagation distance z for fixed coupling strength [$|\beta| = 5$, obtained with $\bar{n} = 625$ and $|\beta_0| = 0.2$, see Eq. (3.11)]. Electron focusing takes place at a similar propagation distance $z \sim 2$ mm for all light statistics under consideration. When the illumination has classical [Fig. (3.2a)] or amplitude-squeezed [Fig. (3.2d)] statistics, the density shows oscillations as a function of relative time τ before focusing. These oscillations disappear with phase-squeezed light [Fig. (3.2c)]. Additionally, the latter produces a focal spot spanning a larger interval of propagation distances z and emerging

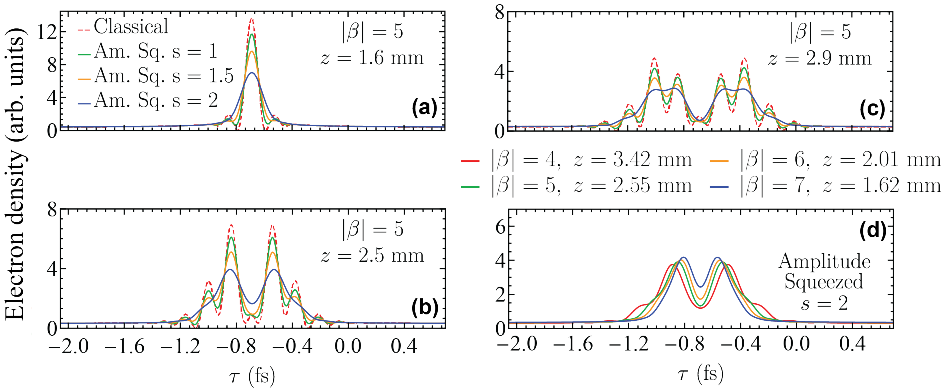

Figure 3.3: Tailoring the electron wave packet with amplitude-squeezed light. (a-c) Electron density profile produced by PINEM interaction with classical (dashed curves) and amplitude-squeezed (solid curves) light after at propagation distance z as indicated by labels. The electron-light coupling coefficient is assumed to be $|\beta| = 5$ with $|\beta_0| = 0.2$ and $\bar{n} = 625$. (d) Evolution of the density profile using amplitude-squeezed light for different coupling strengths $|\beta|$ obtained by varying $|\beta_0|$ with $\bar{n} = 625$. We consider 100 keV electrons, a photon energy 1.5 eV, and a single-mode coupling coefficient $|\beta_0| = 0.2$ in all cases.

at a shorter value of z in comparison with classical light [Fig. (3.2e)]. The behavior with amplitude-squeezed light is the opposite, and in particular, the minimum FWHM of the focal spot is approximately twice larger than the result obtained with phase-squeezed or classical light. As already discussed for classical light[117], the degree of compression increases with increasing coupling $|\beta|$ [Fig. (3.2f)].

Incidentally, upon visual inspection of the z-τ pattern for coherent-state illumination in Fig. (3.2a), smoothing along z would lead to vertical elongation of the density features, similar to those obtained using phase-squeezed light [Fig. (3.2b)]; in contrast, smoothing along τ would produce a pattern more similar to that of amplitude-squeezed illumination [Fig. (3.2d)]. This is consistent with the intuitive picture that phase-squeezing should generate sharper features in the wave function snapshots (i.e., narrower peaks as a function of τ, accompanied by broadening along z in order to preserve the total electron probability); conversely, amplitude-squeezed light should produce the opposite effect (broadening along τ and sharpening along z).

Synthesis of double-peak electron pulses

Although PINEM interaction with amplitude-squeezed light renders comparatively poorer focusing, it shows an interesting double-peak pattern for z below the focal spot. This effect, which is already observed in Fig. (3.2d), is analyzed in more detail in Fig. (3.3) for different degrees of squeezing. We also show in the same figure the profiles obtained with classical light, revealing amplitude squeezing as a better strategy to produce such double-pulse pattern. We remark that the width and distance between the two pulses can be controlled by varying the coupling strength parameter $|\beta|$ [Fig. (3.3d)]. Related to this, we note that a recent experiment[140] has shown that a single double-peak electron density profile can be achieved by exploiting classical midinfrared single-cycle laser pulses.

3.3.3 Electron compression with minimum-phase-uncertainty light

One expects that better focusing can be achieved by reducing phase uncertainty in the optical field. In the limit of large average photon number $\bar{n} \gg 1$, the state that produces a minimum phase uncertainty (MPU) has been shown to be given by[141]

$$c_n \approx \frac{C}{\sqrt{\bar{n}}} \mathrm{Ai}\left[s_1(1 - 2n/3\bar{n})\right],$$

where Ai is the Airy function, $s_1 \approx -2.3381$ is its first zero, $C = \sqrt{2|s_1|/3}/\mathrm{Ai}'(s_1) \approx 2.7805$, and $\mathrm{Ai}'(s_1)$ is the derivative of Ai. PINEM focusing with MPU light is illustrated in Fig. (3.2b). In contrast to classical light, the Rabi-like oscillations along z are now replaced by a well-defined short-period comb of electron density peaks. This is similar to what we obtain with phase-squeezed light [Fig. (3.2c)], but the pattern with MPU light becomes more pronounced. Further deviations from coherent illumination are found in the speed at which compression is achieved: among the statistics under consideration, the shortest FWHM pulse with fixed light intensity and propagation distance is obtained when using MPU light [Fig. (3.2e)]. Nevertheless, after a sufficiently large distance z, the FWHM reaches similar values with MPU, coherent, and phase-squeezed light, while amplitude-squeezed light systematically leads to lower compression, and this effect becomes more dramatic when increasing the coupling coefficient $|\beta|$ [Fig. (3.2f)].

3.3.4 Electron self-interference

We can further modify the focal properties of the electron by mixing it with a delayed version of itself, using for example a beam splitter and different lengths z and z' of the two electron paths converging at the observation region, as sketched in Fig. (3.4a). We assume that $z - z'$ is tuned to be a multiple of the electron wavelength, thus rendering $\rho \propto \tilde{\rho}$ [see Eq. (3.9)], considering for simplicity an incident electron plane wave [i.e., $\phi(z - vt) = 1/\sqrt{L}$, where L is a quantization length]. Using the notation of Eq. (3.8), the electron density profile obtained in this way then results from the superposition $(L/2)\sum_n |\psi_n(z,t) + \mathrm{e}^{\mathrm{i}\varphi}\psi_n(z',t)|^2 = \tilde{\rho}(z,\tau,\tau)/2 + \tilde{\rho}(z,\tau',\tau')/2 + \mathrm{Re}\{\mathrm{e}^{-\mathrm{i}\varphi}\tilde{\rho}(z,\tau,\tau')\}$, where an overall phase φ is introduced (e.g., by means of electrostatic elements along one of the electron arms[122]) to allow us to switch between the real and imaginary parts of $\tilde{\rho}(z,\tau,\tau')$. An example of how this quantity depends on PINEM light statistics is shown in Fig. (3.4b-i), plotted over a discrete dense sampling of τ and τ' points satisfying the condition that $v(\tau - \tau')$ are multiples of the electron wavelength. Interestingly, we observe a rotation of the focal spot feature when going from classical to amplitude-squeezed light. This is consistent with the poorer focusing properties observed for the latter. Through the proposed electron self-interference, the focal spot profile can be modified to cover a wide variety of patterns observed for different light statistics. In particular, phase-squeezed and MPU light produce a radical departure in $\tilde{\rho}(z,\tau,\tau')$ relative to classical coherent light.

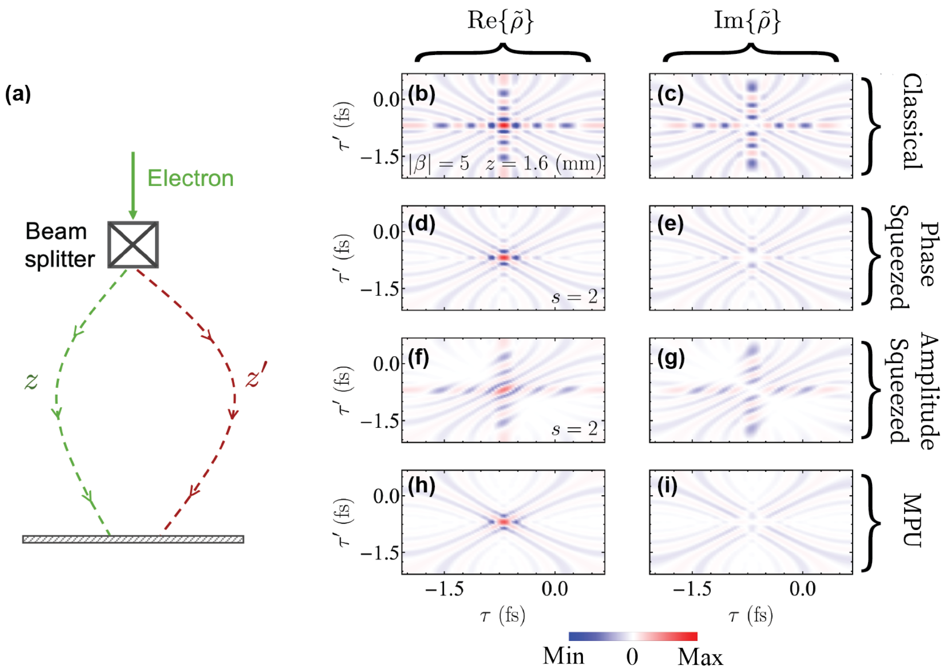

Figure 3.4: Measuring the electron density matrix through self-interference. (a) Sketch of an experimental arrangement to explore electron auto-correlation by means of a beam splitter and different lengths (z and z') along the two electron paths before recombination at the detection region. (b-i) Real (left panels) and imaginary (right panels) parts of the electron density matrix as a function of shifted times τ and τ' for $z = 1.6$ mm and different statistics of the PINEM light, as indicated by labels. We consider 100 keV electrons, 1.5 eV PINEM photons, a squeezing paramerter $s = 2$, and coupling parmameters $|\beta_0| = 0.2$ and $|\beta| = 5$.

3.4 Effect of the electron density matrix on the excitation of a sample

A commonly asked question relates to how the probability and distribution of excitations produced in a sample are affected by the profile of the beam in an electron microscope. The dependence on the transverse component of the electron wave function has been shown to reduce to a trivial average of the excitation produced by line-like beams over the lateral electron density profile[33,142]. In the present study, we concentrate instead on the longitudinal electron wave function (i.e., along the beam direction). Within first-order Born approximation, the excitation probability is known to be independent of the longitudinal electron wave function when the initial states of the sample and the electron are not phase-correlated[33,143], although a dependence has been shown to arise when the sample state is a coherent superposition of ground and excited states that is phase-locked with respect to the electron arrival time[143], and for example, this effect is actually observed in double-PINEM experiments[80]. Here, we concentrate on the common scenario of a sample prepared in its ground state before interaction with the electron. Remarkably, even when considering higher-order interactions, the number of excitations created by the electron has been shown to still remain independent of the longitudinal wave function[144], which incidentally implies that the cathodoluminescence intensity is also independent. We generalize this result below by calculating the full density matrix of the bosonic mode, which turns out to have a Poissonian diagonal part equally independent of electron wave function, although the coherences exhibit a dependence on the quantum state of light used in the PINEM interaction to modulate the electron.

For simplicity, we consider a single sample bosonic mode of frequency ω_0' interacting with an incident PINEM-modulated electron wave packet [Fig. (3.5a)]. We can then treat the electron-sample interaction using the same formalism as in Section 3.2 by just iterating Eq. (3.2). We find the expression

$$\begin{aligned}|\Psi(z,t)\rangle = {\rm e}^{{\rm i}k_0z-{\rm i}\varepsilon_0 t}\phi_0(z-vt)\sum_{\ell=-\infty}^{\infty}\sum_{n=0}^{\infty}\sum_{n'=0}^{\infty} f_\ell^n f'^{n'}_{-n'} \\ \times\, {\rm e}^{{\rm i}\omega_0[\ell(z/v-t)-nt]-2\pi{\rm i}\ell^2 d/z_T-{\rm i}n'\omega_0' z/v}|nn'\rangle \end{aligned} \tag{3.12}$$

for the wave function of the entire system, comprising the electron, as well as the PINEM and sample bosonic modes, the Fock states of which are labeled by their respective occupation numbers n and n'. Primed quantities are reserved here for the sample [i.e., f_ℓ^n refers to the first PINEM interaction, while $f'^{n'}_{\ell'}$ describes the coupling to the sample in Eq. (3.12)], and in particular the condition $\ell' = -n'$ (i.e., sample initially prepared in its ground state $|0\rangle$) is used to write the coefficients $f'^{n'}_{-n'}$. Additionally, we introduce a phase correction $\propto \ell^2$ accounting for propagation over a macroscopic distance d separating the PINEM and sample interaction regions, but we neglect this type of correction for relatively short propagation along the extension of the envelope function $\phi(z)$ and within the sample interaction region [see Fig. (3.5a)]. The density matrix of the sample mode after interaction with the electron,

$$\rho^{\rm sample} = \sum_{n_1'n_2'} \rho^{\rm sample}_{n_1'n_2'} {\rm e}^{-{\rm i}(n_1'-n_2')\omega_0' t}|n_1'\rangle\langle n_2'|,$$

is then obtained by tracing out electron (integral over z) and PINEM boson (sum over n) degrees of freedom. More precisely, we find the coefficients

$$\begin{aligned}\rho^{\rm sample}_{n_1'n_2'} &= {\rm e}^{{\rm i}(n_1'-n_2')\omega_0' t}\int dz \sum_n \langle nn_1'|\Psi(z,t)\rangle\langle\Psi(z,t)|nn_2'\rangle \\ &= f'^{n_1'}_{-n_1'} f'^{n_2'*}_{-n_2'} \sum_{\ell_1=-\infty}^{\infty}\sum_{\ell_2=-\infty}^{\infty} \phi_{\ell_1\ell_2 n_1' n_2'} \sum_{n=0}^{\infty} f_{\ell_1}^n f_{\ell_2}^{n\,*},\end{aligned} \tag{3.13}$$

where

$$\begin{aligned}\phi_{\ell_1\ell_2 n_1' n_2'} &= {\rm e}^{2\pi{\rm i}(\ell_2^2-\ell_1^2)d/z_T} \\ &\times \int dz\, |\phi_0(z)|^2\, {\rm e}^{{\rm i}[(\ell_1-\ell_2)\omega_0-(n_1'-n_2')\omega_0']z/v}.\end{aligned} \tag{3.14}$$

Incidentally, further electron propagation beyond the sample should also involve corrections to the linearized momentum $n'\omega_0'/v$, on which we are not interested here.

We remind that the momentum decomposition of ϕ involves small wave vectors compared with ω/v, so its role in the integral of Eq. (3.14) consists in introducing some broadening with respect to the perfect phase-matching condition

$$(\ell_1-\ell_2)\omega_0=(n_1'-n_2')\omega_0'. \tag{3.15}$$

Such broadening produces nonzero (but small) values of $\phi_{\ell_1\ell_2n_1'n_2'}$ even when ω_0/ω_0' is not a rational number. For simplicity, we consider ω_0/ω_0' to be a rational number and further assume the spectral width of the sample mode to also be small compared with ω_0; the coefficients of Eq. (3.14) then reduce to

$$\phi_{\ell_1\ell_2n_1'n_2'}=\mathrm{e}^{2\pi\mathrm{i}(\ell_2^2-\ell_1^2)d/z_T},$$

subject to the condition given by Eq. (3.15).

We note that the diagonal elements $\rho^{\rm sample}_{n'n'}$ involve just $\ell_1=\ell_2$ terms in virtue of Eq. (3.15), so the only nonzero coefficients in Eq. (3.13) for those elements are $\phi_{\ell\ell n'n'}=1$, and, using the normalization condition $\sum_{\ell n}|f_\ell^n|^2=1$, we find $\rho^{\rm sample}_{n'n'}=|f'^{n'}_{-n'}|^2$, which does not depend on the PINEM coefficients f_ℓ^n: we corroborate that the number of excitations created in the sample is independent of how the incident PINEM electron is prepared[144]; additionally, the distribution of those excitations is also independent. More specifically, upon inspection of Eq. (3.3), we find $f'^{n'}_{-n'}=\mathrm{e}^{\mathrm{i}\chi'}\mathrm{e}^{-|\beta_0'|^2/2}\beta_0'^{*n'}/\sqrt{n'!}$, and therefore,

$$\rho^{\rm sample}_{n'n'}=\left|f'^{n'}_{-n'}\right|^2=\mathrm{e}^{-|\beta_0'|^2}\frac{|\beta_0'|^{2n'}}{n'!}$$

reduces to a Poissonian distribution regardless of the quantum state of the incident electron, with average $|\beta_0|^2$ corresponding to the contribution of the mode under consideration to the EELS probability. This result, which was found for excitation by an electron treated as a classical probe[91,145], is now generalized to a quantum treatment of the electron. We remark that this conclusion is in essence a result of the nonrecoil approximation.

Combining the above results, the elements of the sample density matrix can be written as

$$\begin{aligned}\rho^{\rm sample}_{n_1'n_2'}=&\,\mathrm{e}^{-|\beta_0'|^2}\frac{(-\beta_0')^{n_1'*}(-\beta_0')^{n_2'}}{\sqrt{n_1'!n_2'!}}\\&\times\sum_{\ell_1\ell_2}{}'\,\mathrm{e}^{2\pi\mathrm{i}(\ell_2^2-\ell_1^2)d/z_T}\sum_{n=0}^{\infty}f_{\ell_1}^{n}f_{\ell_2}^{n*},\end{aligned}$$

where the sum is subject to the condition imposed by Eq. (3.15). The symmetry property $\rho^{\rm sample}_{n_1'n_2'}=\rho^{\rm sample*}_{n_2'n_1'}$ is easily verified from this expression. We can now calculate different observables involving the sample mode, as for example $\propto(a'^\dagger+a')$. The expectation value of this quantity, which vanishes unless the ratio of sample-to-PINEM mode frequencies $\omega_0'/\omega_0=m$ is an integer, only involves terms in which n_1' and n_2' differ by 1. A straightforward calculation leads to the result

$$\langle a'^\dagger+a'\rangle=2\mathrm{Re}\{-\beta_0'\Delta_m\mathrm{e}^{\mathrm{i}\omega_0't}\},$$

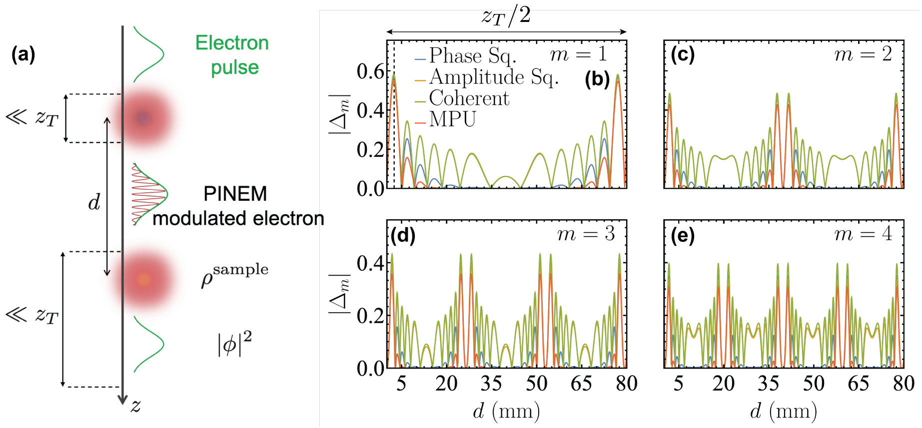

Figure 3.5: Dependence of sample polarization on electron density matrix. (a) Sketch of an electron wave packed undergoing PINEM modulation, followed by propagation along a distance d, and interaction with a single-mode sample of frequency $\omega_0' = m\omega_0$ that is a harmonic m of the PINEM photon frequency. (b-e) Amplitude Δ_m of the oscillation at frequency ω_0' displayed by the sample polarization after interaction with the electron. We plot $|\Delta_m|$ for a few values of m as a function of PINEM-sample distance d and different PINEM-light statistics. All parameters are the same as in Fig. (3.4).

where

$$\Delta_m = \mathrm{e}^{2\pi \mathrm{i} m^2 d/z_T} \sum_{\ell=-\infty}^{\infty} \mathrm{e}^{4\pi \mathrm{i} \ell m d/z_T} \sum_{n=0}^{\infty} f_\ell^n f_{\ell+m}^{n*}. \tag{3.16}$$

This polarization matrix element has been recently shown to exhibit some degree of coherence with the light used to modulate the electron in the first PINEM interaction[144]. We show in Fig. (3.5b-e) the dependence of $|\Delta_m|$ on PINEM-sample separation d for a few values of m and different PINEM statistics. This quantity is periodic in d with a period $z_T/2m$, as it is clear from the exponential inside the sum of Eq. (3.16). Dramatic differences are observed in $|\Delta_m|$ for different PINEM statistics; in particular, a clear trend is observed toward concentration of Δ_m at specific distances d when the uncertainty in the light coherence is reduced (i.e., when moving from coherent or amplitude-squeezed light to phase-squeezed light, and eventually to MPU light).

Incidentally, a similar analysis for the $N^{\rm th}$ moment $\propto (a'^{\dagger} + a')^N$ leads to a contribution oscillating at frequency $N\omega_0'$ with a coefficient Δ_{mN}. An effect at that order is produced if mN is an integer, a condition that can be met for noninteger values of the sample-PINEM frequency ratio $\omega_0'/\omega_0 = m$; for example, an oscillation with frequency ω_0 is induced in $\propto (a'^{\dagger} + a')^2$ after electron-sample interaction if the sample mode frequency is half of the PINEM photon frequency.

The time-dependent of the off-diagonal sample density matrix components under discussion could be measured through attosecond streaking[146,147], as a function of the delay between the times of arrival of the electron and an x-ray pulse, giving rise to oscillations in the energy of photoelectrons produced by the latter as a function of such delay. For low-frequency sample modes, a direct measurement could be based on time-resolved quantum tomography of the sample state; this strategy could benefit from low-frequency beatings resulting from the combination of multiple sample modes of similar frequency. More direct evidence should be provided by the nontrivial interference that has been shown to emerge when mixing the PINEM light with cathodoluminescence emission from the sample[144].

3.5 Concluding remarks

We demonstrated that the interaction of free electrons with quantum light opens a new direction for modulating the longitudinal electron profile, the degree and duration of electron pulse compression, and the statistics associated with this compression. By squeezing the interacting light in phase, the formation of electron pulses is accelerated, and this effect is maximized when using optical fields with an Airy number distribution that minimizes phase uncertainty. Interestingly, amplitude-squeezed light leads to the emergence of double-pulse electron profiles, which could be useful to investigate dynamical processes in a sample. The influence of light statistics becomes more dramatic when examining the electron density matrix after interaction, a quantity that can be accessed through our proposed self-interference experiment. Additionally, we have shown that the excitation of a sample by the electron is affected by how the latter is modulated, and in particular, by the statistics of the modulating light. Indeed, although no dependence is predicted in the probability of exciting sample modes, the temporal evolution of the electron-induced off-diagonal sample density matrix elements shows a departure from the results observed with laser-modulated electrons when considering instead electrons that have interacted with quantum light. Besides their practical interest to shape and temporally compress free electrons, the results here presented reveal a wealth of fundamental phenomena emerging from the interaction with nonclassical light. We further anticipate potential application in the creation of light sources with nontrivial statistics through electron-induced optical emission using gratings and undulators.

4

Electron diffraction by vacuum fluctuations

When a distinguished but elderly scientist states that something is possible, he is almost certainly right. When he states that something is impossible, he is very probably wrong.
Arthur C. Clarke

In this chapter, we study the decoherence and the elastic diffraction associated with the image self-interaction experienced by an electron beam when interacting with a complex material environment. In particular, we connect the latter effect to the phase χ encountered in the previous chapters and we compute its magnitude for different geometrical configurations. The following results are based on a published work, Ref. 148.

4.1 Introduction

On-demand coherent manipulation of the transverse electron wave function in electron beams is of fundamental interest to improve spatial resolution in transmission electron microscopes. The problem can be simply stated as the question of how to introduce a position-dependent phase in the electron wave function. Currently, energetic electron beams can be focused down to sub-Ångstrom spots by phase shaping their transverse wave functions using electrostatic and magnetostatic lenses, which produce macroscopic changes in the phase profile to correct aberrations in the electron optics. Recently, perforated transmission phase plates have been successfully demonstrated to create beams carrying high values of angular momentum[120], while dynamical phase patterning has been explored with the use of pixelated electrostatic plates[122]. An alternative possibility consists in exploiting photon-electron interactions, for example in the Kapitza-Dirac effect[37,38], and also in the recently demonstrated angular momentum transfer between light and electron beams[115], which has been theoretically proposed to be useful for aberration correction[126], although this approach involves the emission or absorption of real photons, therefore producing inelastic rather than elastic diffraction.

In a related context, vacuum fluctuations can also induce a phase modulation without the exchange of real photons, an effect that has been theoretically investigated in the presence of nondissipative media[149] and is still lacking experimental confirmation to the best of our knowledge. For an electron moving parallel to a perfect conductor surface, this phase has been explained as arising from the Aharonov-Bohm effect[150] produced by the electron image potential[149], while an alternative derivation has been given in terms of path integrals[151]. The presence of material excitations with which the electron may interact could add new degrees of freedom to manipulate the quantum phase, although their study would be difficult to undertake using existing theoretical approaches. It should be noted that the same type of electron phase was analysed in detail in early pioneering works, although in a different context related to electron microscopy and the understanding of elastic scattering by atomic crystal lattices for penetrating trajectories[152,153]. However, the real part of the correction to the optical potential computed in these works was found to be too small in samples with thickness smaller than the electron mean free path, and therefore, never experimentally observed to the best of our knowledge. In this context, aloof trajectories may enormously increase the interaction length, thus making this effect observable in practice.

In this chapter, we present an alternative derivation of vacuum phases produced during the interaction of electron beams with arbitrary media, enabling us to readily include the effect of material excitations for aloof electron trajectories. In Section 4.2, we show how vacuum fluctuations can induce both phase shifts and decoherence in an Aharonov-Bohm-like configuration. In Section 4.3, by analytically solving the evolution of an electron wave function at energy scales typical of electron microscope setups, we provide a demonstration that the vacuum phase shift can transversally modulate the electron beam. In Section 4.4, we discuss the phase produced on electrons moving parallel to either perfect or real planar conductor surfaces, whereas in Section 4.6 we analyze far-field diffraction induced by either a planar surface or a small particle. We anticipate that our results could be corroborated in either interference or angle-resolved experiments.

In brief, we discuss a general theory of the interaction between fast electrons and electromagnetic modes in the vicinity of material media, leading to the emergence of a quantum phase imprinted on the electron transverse wave function. For aloof interaction with a planar surface, this phase is related to the Aharonov-Bohm effect due to the image potential[149], although an accurate determination of its magnitude requires a proper quantum treatment of the electromagnetic vacuum in the presence of material boundaries. We illustrate the effect that such phase has on a free electron by investigating two different experimental scenarios: a holographic measurement in which one compares the phase of an electron wave function component passing near a sample with the phase of another component that does not interact with the sample; and a diffraction measurement in which the electron distribution in the far-field Fourier plane is modified by the dependence of the imprinted phase on transverse beam coordinates.

4.2 Vacuum phase shift induced by macroscopic media

4.2.1 Vacuum phase shift

We now obtain an expression for the elastic electron amplitude under interaction with a macroscopic quantized electromagnetic field. We consider an Aharonov-Bohm-like experiment in which the electron wave function is split into two paths (1 and 2). Before interaction with the electromagnetic field, the system density matrix is

$$\begin{aligned}\rho(t_0) = [&|\psi_1(t_0)\rangle\langle\psi_1(t_0)| + |\psi_2(t_0)\rangle\langle\psi_2(t_0)| \\ &+|\psi_2(t_0)\rangle\langle\psi_1(t_0)| + |\psi_1(t_0)\rangle\langle\psi_2(t_0)|] \otimes \sigma(t_0),\end{aligned}$$

where $\sigma(t_0)$ stands for the initial state of the photon field at time t_0, while $|\psi_1(t_0)\rangle$ and $|\psi_2(t_0)\rangle$ are the electron states in paths 1 and 2, respectively. We take the interaction between the electromagnetic field and the electron to be described by the minimal coupling Hamiltonian in the temporal gauge of Eq. (1.39b) with the vector potential being quantized within MQED framework (see Section 1.3), which in the interaction picture reads

$$\hat{\mathcal{H}}_{\rm int}(t) = -\frac{1}{c}\int d^3\mathbf{r}\ \hat{\mathbf{A}}^{\rm I}(\mathbf{r},t)\cdot\mathbf{j}(\mathbf{r},t).$$

Assuming the electron current to be well described by its classical version on each of the two electron paths[1], we can write the electron density matrix at a later time $t > t_0$, with $t_0 \to -\infty$, as

$$\begin{aligned}\rho_{\rm e}(t) =&|\psi_1(t_0)\rangle\langle\psi_1(t_0)| + |\psi_2(t_0)\rangle\langle\psi_2(t_0)| \\ &+ |\psi_2(t_0)\rangle\langle\psi_1(t_0)|\,{\rm Tr}\{\hat{\mathcal{S}}_2\sigma(t_0)\hat{\mathcal{S}}_1^\dagger\} \\ &+ |\psi_1(t_0)\rangle\langle\psi_2(t_0)|\,{\rm Tr}\{\hat{\mathcal{S}}_1\sigma(t_0)\hat{\mathcal{S}}_2^\dagger\},\end{aligned} \tag{4.1}$$

---

[1] More formally, we can think at the states $|\psi_{1/2}(t_0)\rangle$ to be eigenstates of the quantum current operator $\hat{\mathbf{j}}^{\rm I}(\mathbf{r},t)$ [see Eq. (1.40)] from which we neglect the ponderomotive contribution.

where $\hat{\mathcal{S}}_j$ is the scattering operator of Eq. (1.41) for the current along path $j = 1$ or 2, and we have traced out the photon degrees of freedom. The first two terms on the right-hand side of Eq. (4.1) represent the part of the electron wave function that is not affected by interaction with the electromagnetic field. The remaining two terms describe the coherence of the electron state. We now take the initial photon density matrix to be in a thermal state at temperature T and use the fact that the commutator between the vector potentials is a pure imaginary c-number [see Eq. (C.2)] to rewrite the scattering operator as (see Appendix D)

$$\hat{\mathcal{S}}_j = \mathrm{e}^{\mathrm{i}\chi_j}\mathrm{e}^{-\frac{\mathrm{i}}{\hbar}\int_{t_0}^{t} dt'\hat{\mathcal{H}}_j(t')} = \mathrm{e}^{\mathrm{i}\chi_j}\hat{\mathcal{U}}_j, \tag{4.2}$$

which, by going to $t = \infty$, leads to

$$\langle\hat{\mathcal{S}}_2^\dagger\hat{\mathcal{S}}_1\rangle_T = \mathrm{e}^{\mathrm{i}(\chi_1-\chi_2)}\langle\hat{\mathcal{U}}_2^\dagger\hat{\mathcal{U}}_1\rangle_T$$

with phase shifts given by

$$\chi_j = \frac{\mathrm{i}}{2\hbar^2c^2}\int_{-\infty}^{\infty} dt\,dt'\int d^3\mathbf{r}\,d^3\mathbf{r}'\,\mathbf{j}_j(\mathbf{r},t)\cdot\left[\hat{\mathbf{A}}^{\mathrm{I}}(\mathbf{r},t),\hat{\mathbf{A}}^{\mathrm{I}}(\mathbf{r}',t')\right]\cdot\mathbf{j}_j(\mathbf{r}',t'). \tag{4.3}$$

Now, we use the Baker-Campbell-Hausdorff formula to recombine the evolution of the two paths, leading to

$$\langle\hat{\mathcal{S}}_2^\dagger\hat{\mathcal{S}}_1\rangle_T = \mathrm{e}^{\mathrm{i}(\chi_1-\chi_2)}\mathrm{e}^{\mathrm{i}\varphi}\mathrm{e}^{P},$$

where we have

$$\varphi = \frac{-\mathrm{i}}{2\hbar^2c^2}\int_{-\infty}^{\infty} dt\,dt'\int d^3\mathbf{r}\,d^3\mathbf{r}'\,\mathbf{j}_2(\mathbf{r}',t')\cdot\left[\hat{\mathbf{A}}^{\mathrm{I}}(\mathbf{r}',t'),\hat{\mathbf{A}}^{\mathrm{I}}(\mathbf{r},t)\right]\cdot\mathbf{j}_1(\mathbf{r},t), \tag{4.4}$$

$$P = \frac{-1}{2\hbar^2c^2}\int_{-\infty}^{\infty} dt\,dt'\int d^3\mathbf{r}\,d^3\mathbf{r}'\,\mathbf{j}_{1,2}(\mathbf{r},t)\cdot\langle\hat{\mathbf{A}}^{\mathrm{I}}(\mathbf{r},t)\hat{\mathbf{A}}^{\mathrm{I}}(\mathbf{r}',t')\rangle_T\cdot\mathbf{j}_{1,2}(\mathbf{r}',t'), \tag{4.5}$$

and $\mathbf{j}_{1,2} = \mathbf{j}_1 - \mathbf{j}_2$. In this derivation, we have used the fact that $\hat{\mathbf{A}}^{\mathrm{I}}(\mathbf{r},t)$ is linear in the field operators, and therefore $\langle\hat{\mathbf{A}}^{\mathrm{I}}(\mathbf{r},t)\rangle_T = 0$ [see Eq. (1.46)], which leads to a cumulant expansion limited only to the second-order term[49]. The phase shift given by Eq. (4.4) relates to the interference between the two paths due to photon emission. This is clear by noticing that it appears only because of the cyclic property of the trace, which allows us to obtain the product $\hat{\mathcal{S}}_2^\dagger\hat{\mathcal{S}}_1$. In contrast, the expression in Eq. (4.5) is guaranteed to be a real number, so it represents the total decoherence experienced by the electron, which has been extensively studied from theoretical[151,154–156] and experimental[157–159] fronts. Importantly, it should be noted that, although the impressive increase of accuracy achieved in recent experiments served to rule out alternative theories, further decrease in experimental error is still needed to conclusively support a physical model[156]. The path-dependent phase and decoherence, which can affect the fringes observed in an interference experiment, was derived as a dynamical scattering correction to the electron virtual interaction with sample excitations in a pioneering work[152] that related it to the so-called optical potential[153,160,161]. A subsequent formulation of such phase was then separately given in the context of quantum field theory[149] assuming zero temperature and neglecting inelastic losses, while an extension to finite temperature was later presented[49]. However, not much attention has so far been paid to the vacuum phase shift χ_j [Eq. (4.3)] and the role played by dissipation and finite conductivity in metallic structures, on which we focus here using a macroscopic QED formalism.

We find it useful to rewrite the phase shift of Eq. (4.3) in terms of the electromagnetic Green tensor by using Eqs. (1.43) and (C.3). This allows us to write

$$\chi_j = \frac{2}{\hbar}\int_{-\infty}^{\infty} dt\,dt' \int_0^{\infty} d\omega \int d^3\mathbf{r}\,d^3\mathbf{r}'\,\cos\left[\omega(t-t')\right] \\ \times \mathbf{j}_j(\mathbf{r},t)\cdot\mathrm{Re}\{-G(\mathbf{r},\mathbf{r}',\omega)\}\cdot\mathbf{j}_j(\mathbf{r}',t'), \qquad (4.6)$$

where we have also used the Onsager reciprocity relation $G(\mathbf{r},\mathbf{r}',\omega) = G^{\mathrm{T}}(\mathbf{r}',\mathbf{r},\omega)$. Now, if we consider the electron to be a point particle traveling along the z direction with constant velocity v and fixed transverse coordinates $\mathbf{R}_j = (x_j, y_j)$ (different for each of the two paths $j = 1$ and 2), the electron current is

$$\mathbf{j}_j(\mathbf{r},t) = -ev\,\delta(z-vt)\,\delta(\mathbf{R}-\mathbf{R}_j)\,\hat{\mathbf{z}}, \qquad (4.7)$$

which upon insertion into Eq. (4.6) leads to the expression

$$\chi_j = \frac{2e^2}{\hbar}\int_0^{\infty} d\omega \int_{-\infty}^{\infty} dz\,dz'\,\cos\left[\frac{\omega}{v}(z-z')\right]\mathrm{Re}\{-G_{z,z}(\mathbf{R}_j,z,\mathbf{R}_j,z',\omega)\} \qquad (4.8)$$

for the impact-parameter-dependent electron phase shift. This result clearly emphasizes the fact that the quantum phase is the integral of a nonresonant quantity (the real part of the Green tensor), and thus it is expected to be small, although the numerical examples discussed below reveal a measurable effect. In more physical terms, the electron has to undergo an even number of virtual inelastic processes during its interaction with the sample before recovering its initial energy, so the phase change is at least a second-order process (indeed it arises from a commutator), although its effect is accumulated over an infinite number of electromagnetic modes that renders it non-negligible. We also remark that the phase does not depend on how the electromagnetic modes are populated, so it takes the same value if the sample starts from the ground state or from an excited state. For completeness, we calculate the decoherence from Eq. (4.5), which requires the evaluation of the thermal average of the vector potentials,

$$\langle \hat{A}_i(\mathbf{r},t)\hat{A}_{i'}(\mathbf{r}',t')\rangle_T = -4\hbar c^2 \int_0^{\infty} d\omega\,\mathrm{Im}\{G_{i,i'}(\mathbf{r},\mathbf{r}',\omega)\} \\ \times \left[2n_T(\omega)\cos[\omega(t-t')] + \mathrm{e}^{-\mathrm{i}\omega(t-t')}\right].$$

Upon insertion of this expression into Eq. (4.5), using again the Onsager reciprocity relation and the Bose-Einstein distribution $n_T(\omega)$ at temperature T and frequency ω [see Section 1.3], we find

$$P = \frac{2}{\hbar}\int_0^{\infty} d\omega \int_{-\infty}^{\infty} dt\,dt' \int d^3\mathbf{r}\,d^3\mathbf{r}'\,\cos[\omega(t-t')][2n_T(\omega)+1] \\ \times \mathbf{j}_{1,2}(\mathbf{r},t)\cdot\mathrm{Im}\{G(\mathbf{r},\mathbf{r}',\omega)\}\cdot\mathbf{j}_{1,2}(\mathbf{r}',t').$$

Considering now the two parallel paths described by the currents of Eq. (4.7), the decoherence takes the simple form

$$P = \frac{-1}{2}\int_0^\infty d\omega\;[2n_T(\omega)+1]\;\left[\Gamma_{\rm EEL}(\mathbf{R}_1,\mathbf{R}_1\omega)+\Gamma_{\rm EEL}(\mathbf{R}_2,\mathbf{R}_2,\omega)\right.$$
$$\left.-\Gamma_{\rm EEL}(\mathbf{R}_1,\mathbf{R}_2,\omega)-\Gamma_{\rm EEL}(\mathbf{R}_2,\mathbf{R}_1,\omega)\right], \qquad (4.9)$$

where

$$\Gamma_{\rm EEL}(\mathbf{R}_j,\mathbf{R}_{j'},\omega) = \frac{4e^2}{\hbar}\int_{-\infty}^{\infty} dz\,dz'\,\cos\left[\frac{\omega}{v}(z-z')\right]\,{\rm Im}\{-G_{z,z}(\mathbf{R}_j,z,\mathbf{R}_{j'},z',\omega)\}$$

[compare this expression with Eq. (4.8)], so the first two terms inside the ω integral of Eq. (4.9) arise from the separate-path EELS probabilities [i.e., $\Gamma_{\rm EEL}(\mathbf{R}_j,\mathbf{R}_j,\omega)$ is the EELS probability for an electron following path j of Eq. (1.26)] , whereas the last two terms stand for the inelastic path-interference contribution, all of which are weighted by a thermal factor that results from the sum of electron energy losses ($\propto n_T+1$) and gains ($\propto n_T$).

4.2.2 Quantum phase and Aharonov-Bohm effect in arbitrary geometries

As an extension of the explanation of the vacuum phase in terms of the Aharonov-Bohm effect associated with the image potential for an electron moving parallel to a perfect-conductor plate[149], we now argue that Eq. (4.8) results from the Aharonov-Bohm effect associated with a vector potential in the current temporal gauge. Indeed, direct application of Eq. (1.10) allows us to write the expectation value of the z component of the vector image potential produced by the electron current given by Eq. (4.7) as $A_z(\mathbf{r},t) = (2ec)\int_0^\infty d\omega\int_{-\infty}^{\infty} dz'{\rm Re}\{G_{zz}(\mathbf{r},\mathbf{R}_j,z',\omega)e^{{\rm i}\omega(z'/v-t)}\}$, where an overall factor of $1/2$ is introduced to reflect the fact that the potential arises from the electron self-interaction rather than from an external source, and we use causality to reduce the ω integral to the positive frequency part. We now plug this expression into the phase $(-e/\hbar c)\int_{-\infty}^{\infty} dz\,A_z(\mathbf{R}_j,z,t)$ due to the Aharonov-Bohm effect[150], which is proportional to the integral of the vector potential acting on the electron along its trajectory $t=z/v$. Combining these expressions, we readily obtain Eq. (4.8), thus demonstrating that the quantum phase under discussion can be ascribed to the Aharonov-Bohm effect produced by the electron self-image potential for any sample geometry.

4.2.3 Quantum phase in nonlocal media

We have so far considered materials characterized a frequency-dependent dielectric function $\epsilon(\mathbf{r},\omega)$ that bears a local dependence on spatial position $\mathbf{r}$. While this assumption is generally safe to describe the response of dielectric optical cavities and plasmons in noble metal nanostructures with size features larger than $\sim 10\,$nm, it becomes inaccurate in smaller particles[56,162], in strongly nonlocal materials such as graphene[163], or in the analysis of free-electron interactions with tightly bound modes near metal surfaces[164], where quantum confinement, electron spill-out[165,166], and the finite $\sim 1\,$nm screening length[56,61] contribute to make the material response nonlocal. A more complete description requires the use of a nonlocal dielectric function $\epsilon(\mathbf{r},\mathbf{r}',\omega)$, where the displacement at $\mathbf{r}$ depends on the electric field at different positions $\mathbf{r}'$. Unfortunately, a first-principles description of such function is only feasible for relatively simple geometries (e.g., planar surfaces and ultrathin films, as well as molecules and atomic clusters with up to a few hundred atoms). A classical hydrodynamic model of the conduction electron gas in metals[167–169] provides a simple description of nonlocal effects that has been extensively used to study inelastic electron interactions[170], while the specular reflection model[171] gives a general prescription to relate the nonlocal response of arbitrarily shaped nanostructures to the bulk nonlocal dielectric function[56]. In this context, the leading linear-order nonlocal correction in the surface response function captured by the Feibelman d parameters[172] has recently been revisited as a powerful tool to incorporate nonlocal effects in the electromagnetic response of metallic nanostructures[173]. Here, we do not enter into the details of the calculation of $\epsilon(\mathbf{r},\mathbf{r}',\omega)$ and simply argue that the local description of the preceding sections remains essentially unchanged when nonlocal effects are taken into consideration. Indeed, Eq. (1.46) represents again the complete solution of Maxwell's equations with the Green tensor satisfying a generalization of Eq. (1.11):

$$\nabla\times\nabla\times G(\mathbf{r},\mathbf{r}',\omega)-\frac{\omega^2}{c^2}\int d^3\mathbf{r}''\,\epsilon(\mathbf{r},\mathbf{r}'',\omega)G(\mathbf{r}'',\mathbf{r}',\omega)=-\frac{1}{c^2}\delta(\mathbf{r}-\mathbf{r}').$$

Following reference[174], we impose the commutation relations

$$\left[\hat{\mathbf{j}}^{\rm noise}(\mathbf{r},\omega),\hat{\mathbf{j}}^{\rm noise\dagger}(\mathbf{r}',\omega')\right]=\hbar\omega^2\,{\rm Im}\{\epsilon(\mathbf{r},\mathbf{r}',\omega)\}\;\delta(\omega-\omega')\mathcal{I}$$

for the noise currents and exploit the identity

$$\int d^3\mathbf{r}''\,d^3\mathbf{r}'''\;{\rm Im}\{\epsilon(\mathbf{r}'',\mathbf{r}''',\omega)\}\,G(\mathbf{r},\mathbf{r}'',\omega)\,G^*(\mathbf{r}''',\mathbf{r}',\omega)=-\frac{1}{\omega^2}{\rm Im}\{G(\mathbf{r},\mathbf{r}',\omega)\},$$

to verify that Eqs. (C.2) and (C.3) also old for nonlocal media. Finally, because Eq. (4.3) does not depend on the explicit form of the electromagnetic potentials, as long as they are linear in the bosonic ladder operators, Eqs. (4.8) and (4.9) retain its validity when including nonlocal effects in the definition of the Green tensor.

For translationally invariant samples, the dielectric response is only a function of position difference $\mathbf{r}-\mathbf{r}'$, which yields a local dielectric function in momentum space $\epsilon(\mathbf{q},\omega)$. In particular, the response of noble metals deviates from the local limit mainly for $\omega/v_{\rm F}\lesssim q$[56], where $v_{\rm F}$ is the Fermi velocity. This allows us to estimate the importance of nonlocal effects for an electron passing at a distance $\geq 10\,$nm from a gold surface, which should involve components $q\leq 0.1\,{\rm nm}^{-1}$, so we can neglect nonlocal effects for energy exchanges $\hbar\omega\gtrsim\hbar q v_{\rm F}\sim 0.1\,$eV. As we show in Section 4.4 below, the frequencies involved in the calculation of the phase for the examples considered in this work lie above this value, and therefore we can safely neglect nonlocal effects.

4.3 Elastic phase shift from explicit QED solution

We now restrict ourselves to a situation similar to the one explored in Chapter 2 and 3 in which a fast collimated e-beam interacts with a an infinite set of modes supported by a macroscopic structure. For this system, we can write the Hamiltonian describing its dynamics as

$$
\begin{aligned}
\hat{\mathcal{H}}_0^{\rm par} &= \sum_i \hbar\omega_i\, \hat{a}_i^\dagger \hat{a}_i + \hbar\varepsilon_0 - \hbar\mathbf{v}\cdot(\mathrm{i}\nabla+\mathbf{k}_0),\\
\hat{\mathcal{H}}_1^{\rm par} &= (e\mathbf{v}/c)\cdot\hat{\mathbf{A}}(\mathbf{r}),
\end{aligned}
$$

defining the solution of the Schrödinger equation $(\hat{\mathcal{H}}_0^{\rm par}+\hat{\mathcal{H}}_1^{\rm par})|\psi(\mathbf{r},t)\rangle = \mathrm{i}\hbar\partial_t|\psi(\mathbf{r},t)\rangle$. We remark that now the vector potential is constructed by an infinite summation over the modes of the system as shown in Eq. (1.50). Taking the electron beam to be oriented along the z direction, the full problem admits an analytical solution given by (see Appendix D)

$$
|\psi(\mathbf{r},t)\rangle = \psi_0(\mathbf{r},t) \sum_{\{n\},\{\ell\}} \mathrm{e}^{\mathrm{i}\sum_i \omega_i[\ell_i(z/v-t)-n_i it]} f_{\{\ell\}}^{\{n\}}(\mathbf{r})|\{n\}\rangle,
$$

with

$$
\begin{aligned}
f_{\{\ell\}}^{\{n\}}(\mathbf{r}) =& \mathrm{e}^{\mathrm{i}\chi(\mathbf{r})} c_{\{n+\ell\}} \prod_i \sqrt{(n_i+\ell_i)!n_i!}\; \mathrm{e}^{-|\beta_i(\mathbf{r})|^2/2}\\
&\times(-\beta_i(\mathbf{r}))^{\ell_i} \sum_{n_i'=\max\{0,-\ell_i\}}^{n_i} \frac{(-|\beta_i(\mathbf{r})|^2)^{n_i'}}{n_i'!(\ell_i+n_i')!(n_i-n_i')!},
\end{aligned}
\tag{4.10}
$$

where the coefficients $c_{\{n\}}$ represent the state of the photonic field right before interaction with the electron, $\beta_i(\mathbf{r}) = (e/\hbar\omega_i)\int_{-\infty}^z dz'\,\mathcal{E}_{i,z}(\mathbf{R},z')\mathrm{e}^{-\mathrm{i}\omega_i z'/v}$ and

$$
\begin{aligned}
\chi(\mathbf{r}) = -\sum_i \frac{e^2}{\hbar^2\omega_i^2}\int_{-\infty}^z & dz'\,dz''\theta(z'-z'')\\
&\times \mathrm{Im}\left\{\mathcal{E}_{i,z}^*(\mathbf{R},z'')\mathcal{E}_{i,z}(\mathbf{R},z')\mathrm{e}^{-\mathrm{i}\omega_i(z'-z'')/v}\right\}.
\end{aligned}
\tag{4.11}
$$

Equation (4.10) represents the nonperturbative solution of the scattering between a scalar relativistic electron and all optical modes of the vacuum-sample system. There is obviously a part of the joint photon-electron state that represents the contribution without net photon (emission or absorption) exchanges. From the electron point of view, this component relates to elastic transitions and can be calculated from the associated density matrix after tracing out the photon degrees of freedom and isolating the zero quanta exchange term. Additionally, we are interested in samples held at some temperature, so we need to deal with thermal electromagnetic mixtures of states, which can be treated by calculating Eq. (4.10) for Fock states (i.e., taking $c_{\{n\}} = \prod_i \delta_{n_i,n_{0,i}}$ for a given realization of Fock states $\{n_{0,j}\}$ before interaction with the electron) and averaging over thermal populations (i.e., over a Bose-Einstein distribution $p_{n_{0,i}} = \mathrm{e}^{-n_{0,i}/\bar{n}_i}/\bar{n}_i$ with average mode population $\bar{n}_i = 1/\left[\exp(\hbar\omega_i/k_{\rm B}T)-1\right]$). We find an elastic electron density matrix

$$
\begin{aligned}
\rho_{\rm elastic}(\mathbf{r},\mathbf{r}',t) &= \sum_{\{n_0\}} p_{\{n_0\}}\,\mathrm{Tr}\left\{|\psi(\mathbf{r},t)\rangle\langle\psi(\mathbf{r}',t)|\right\}_{\rm elastic}\\
&= \psi_0(\mathbf{r},t)\psi_0^*(\mathbf{r}',t)\sum_{\{n_0\}} p_{\{n_0\}}\; f_{\{0\}}^{\{n_0\}}(\mathbf{r})[f_{\{0\}}^{\{n_0\}}(\mathbf{r}')]^*\\
&= \psi_0(\mathbf{r},t)\psi_0^*(\mathbf{r}',t)\;\mathrm{e}^{\mathrm{i}[\chi(\mathbf{r})-\chi(\mathbf{r}')]}\;D_{\rm elastic}(\mathbf{r},\mathbf{r}'),
\end{aligned}
\tag{4.12}
$$

where

$$D_{\text{elastic}}(\mathbf{r},\mathbf{r}') = \prod_i \mathrm{e}^{-\left[|\beta_i(\mathbf{r})|^2 + \beta_i(\mathbf{r}')|^2\right]/2} \tag{4.13}$$
$$\times \sum_{n_{0,i}} p_{n_{0,i}} (n_{0,i}!)^2 \sum_{n_i=0}^{n_{0,i}} \frac{(-|\beta_i(\mathbf{r})|^2)^{n_i}}{(n_i!)^2 (n_{0,i}-n_i)!} \sum_{n'_i=0}^{n_{0,i}} \frac{(-|\beta_i(\mathbf{r}')|^2)^{n'_i}}{(n'_i!)^2 (n_{0,j}-n'_j)!}$$

contains the remaining factors beyond $\exp[\mathrm{i}\chi(\mathbf{r})]$ from Eq. (4.10). We note again that we are forcing the electromagnetic field to return to its initial state (i.e., we neglect emission and absorption of degenerate photonic states that leave the electron energy unaffected, although electron-mediated transfer of excitations between degenerate electromagnetic states could play a role in the elastically scattered electron signal). Interestingly, Eq. (4.12) includes both a phase shift $\chi(\mathbf{r})$ and a real decoherence amplitude $D_{\text{elastic}}(\mathbf{r},\mathbf{r}')$, which we present in a self-contained form that can be computed for any general pure quantum state, in contrast to the specific case of a thermal mixture considered in Eq. (4.5). At $T = 0$, the second line of Eq. (4.13) reduces to 1, so $D_{\text{elastic}}(\mathbf{r},\mathbf{r}') = \mathrm{e}^{P(\mathbf{r})+P(\mathbf{r}')}$, which allows us to define a position-dependent decoherence

$$P = \frac{-1}{2} \sum_i |\beta_i(\mathbf{r})|^2 \tag{4.14}$$

directly in the elastic electron wave function.

Here, we focus on the elastic phase shift, which is given by $\chi(\mathbf{r})$ of Eq. (4.11)[64]. This phase shift can be shown to be equivalent to Eq. (4.3) by directly substituting the expansion of the vector potential [Eq. (1.50)] in the commutator of Eq. (1.43), keeping in mind that the ladder operators of the electromagnetic modes evolve in time according to the free Hamiltonian $\hat{\mathcal{H}}_0^{\text{rad}}$ as

$$\hat{a}_i(t) = \hat{a}_i \mathrm{e}^{-\mathrm{i}\omega_i t}, \quad \hat{a}_i^\dagger(t) = \hat{a}_i^\dagger \mathrm{e}^{\mathrm{i}\omega_i t},$$

and considering a classical current centered at $\mathbf{R} = \mathbf{R}_j$ as in Eq. (4.7). Finally, because the retarded Green tensor satisfies the correspondence $G^{\text{R}} = G$ (see Section 1.3), we conclude that Eqs. (4.11) and (4.8) represent the same quantity.

4.4 Elastic diffraction by metallic plates

We now illustrate the vacuum-induced phase by considering electrons moving parallel to a planar conductor surface at a distance x from it [see inset in Fig. (4.1a)]. We take the conductor to span a large distance along the direction of motion compared with both x and any of the photon wavelengths effectively contributing to the electron-surface interaction. The Green tensor can then be written as the sum of free-space and scattered components $G^0 + G^{\text{s}}$. The phase shift arising from the free-space Green tensor G^0 is formally infinite, but it does not depend on the transverse coordinate of the electron, therefore becoming unobservable[149]. The remaining scattered component is given by [see Eq. (1.20)]

$$G^{\text{s}}_{z,z}(\mathbf{R},z,\mathbf{R},z',\omega) = \frac{\mathrm{i}}{2c^2} \int \frac{d^2\mathbf{k}_\parallel}{(2\pi)^2} \frac{1}{k_\parallel^2 k_x} \mathrm{e}^{\mathrm{i}k_z(z-z')+2\mathrm{i}k_x x} \left(r_{\text{p}} \frac{k_z^2 k_x^2}{k^2} - r_{\text{s}} k_y^2 \right), \tag{4.15}$$

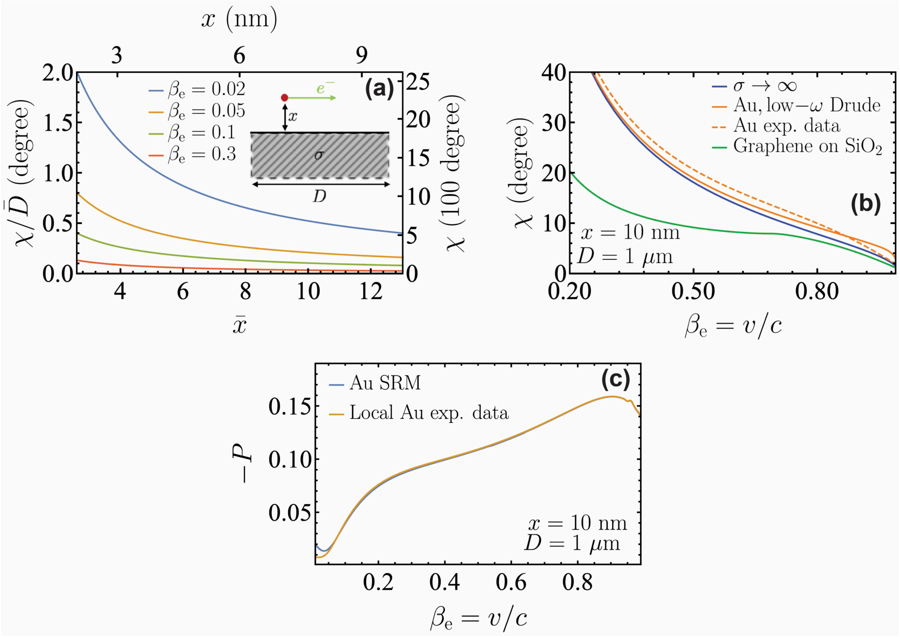

Figure 4.1: Phase shift and decoherence. (a) Vacuum phase shift induced on an electron traveling parallel to a planar surface of a metal of DC conductivity σ normalized to the scaled effective path length $\bar{D} = D\sigma/c$ as a function of the scaled electron-surface distance $\bar{x} = x\sigma/c$ for different electron velocities $\beta_e = v/c$. Upper and right scales correspond to gold ($\sigma = 257$ eV) with $D = 1\ \mu$m. (b) Velocity dependence of the vacuum phase shift for a perfect conductor (blue curve, $\sigma \to \infty$); gold described by the Drude permittivity in the low-frequency limit (solid-orange curve); gold described using its measured dielectric function in the 0.64-6.6 eV [97] and > 6.6 eV [175] photon-energy ranges, and extended by matching the Drude-like expression $\epsilon = \epsilon_b - \omega_p^2/\omega(\omega + i\gamma)$ with $\epsilon_b = 13.31 - 0.19i$, $\hbar\omega_p = 9.14$ eV, and $\hbar\gamma = 0.071$ eV at lower photon energies (dashed-orange curve); and a graphene monolayer (Fermi energy $E_F = 0.5$ eV, damping $\hbar\tau^{-1} = 10$ meV, room temperature $T = 300$ K) on top of a SiO_2 substrate (green curve) with values of x and D as shown by labels. (c) Total decoherence experienced by a single electron-path passing aloof above a gold surface, as calculated from Eq. (4.18) [156] for the same parameters as in Fig. (4.1b) at room temperature with (blue curve) and without (yellow curve) inclusion of nonlocal effects.

where $k = \omega/c$, the integral extends over wave vectors $\mathbf{k}_\parallel = (k_y, k_z)$ parallel to the surface, and $k_x = \sqrt{\omega^2/c^2 - k_\parallel^2 + \mathrm{i}0^+}$ with the square root taken to yield a positive real part.

4.4.1 Perfect conductor

For a perfect electric conductor, we have Fresnel coefficients $r_\mathrm{p} = 1$ and $r_\mathrm{s} = -1$, which permit obtaining a closed-form expression from Eq. (4.8). We first note that the in-plane translational invariance of the Green tensor component in Eq. (4.15) allows us to replace one of the spatial integrals by the effective electron path length D, which, neglecting inelastic deflections occurring during the interaction, may be approximated by the length of the plate (we refer to Ref. 176, where the deflection due Johnson noise is estimated to produce a correction of only a few hundred nanometers in the effective length for $D = 10\,\mu$m; additionally, Fig. (4.1c) shows that the fraction of inelastically scattered electrons is, for example, ~ 0.1 at 300 K for an electron passing with velocity $v = 0.1\,c$ at a distance of 10 nm from a 10-μm-long gold plate). The remaining integral over the difference $z - z'$ yields δ functions, leading to

$$\chi(x) = \frac{\alpha\pi}{c} D \int_0^\infty d\omega \int \frac{d^2\mathbf{k}_\parallel}{(2\pi)^2} \left[\delta\left(k_z - \frac{\omega}{v}\right) + \delta\left(k_z + \frac{\omega}{v}\right)\right] \frac{\mathrm{e}^{-2x\kappa_x}}{k_\parallel^2 \kappa_x} \left(\frac{k_z^2 \kappa_x^2}{k^2} - k_y^2\right),$$

where $\kappa_x = \sqrt{k_\parallel^2 - \omega^2/c^2}$ and $\alpha \approx 1/137$ is the fine structure constant. We now perform the frequency integral using the delta functions and write the remaining 2D integral in polar coordinates $(k_z, k_y) = k_\parallel(\cos\theta, \sin\theta)$. We obtain

$$\chi(x) = \frac{\alpha}{2\pi} \frac{D}{\beta_\mathrm{e}\gamma^2} \int_0^\infty dk_\parallel \int_{-\pi/2}^{\pi/2} d\theta \, \frac{\exp\left(-2k_\parallel x\sqrt{1 - \beta_\mathrm{e}^2 \cos^2\theta}\right)}{\sqrt{1 - \beta_\mathrm{e}^2 \cos^2\theta}},$$

where $\beta_\mathrm{e} = v/c$. Finally, using the integral $\int_{-\pi/2}^{\pi/2} dx\,(1 - a\cos^2 x)^{-1} = \pi/\sqrt{1-a}$ [Eq. (3.653-2) of Ref. 95], we find

$$\chi(x) = \frac{\alpha D}{4x} \frac{1}{\beta_\mathrm{e}\gamma}, \tag{4.16}$$

which coincides with the Aharonov-Bohm phase shift induced on a moving charge under the effect of its image potential, as pointed out in previous studies[149,177].

4.4.2 Real conductor

We now extend the previous result to real metals by including inelastic losses in the material, which we model through a frequency-dependent local dielectric function $\epsilon(\omega)$. Inserting Eq. (4.15) into Eq. (4.11) and following similar steps as in Section 4.4.1, we find the phase

$$\chi = \frac{\alpha D}{2\pi\beta_\mathrm{e}} \int_0^\infty dk_\parallel \int_{-\pi/2}^{\pi/2} d\theta \, \frac{\exp\left(-2xk_\parallel\sqrt{1 - \beta_\mathrm{e}^2\cos^2\theta}\right)}{\sqrt{1 - \beta_\mathrm{e}^2\cos^2\theta}} \times \mathrm{Re}\{r_\mathrm{p} - \beta_\mathrm{e}^2\left(r_\mathrm{p}\cos^2\theta - r_\mathrm{s}\sin^2\theta\right)\}, \tag{4.17}$$

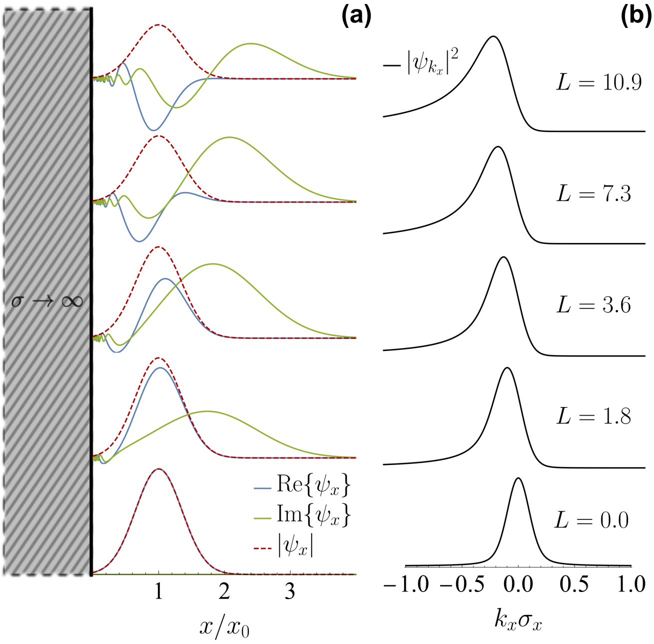

Figure 4.2: Vacuum elastic diffraction by a planar surface. Evolution of the elastic part of the transverse electron wave function in real space ψ_x (a) and in momentum space ψ_{k_x} (b) as a function of the scaled interaction length $L = \alpha D/4\gamma\beta_{\rm e}\sigma_x$ when the electron is traveling aloof and parallel to a planar perfect-conductor surface. The electron wave function is assumed to be initially prepared in a Gaussian transverse profile centered around x_0 with standard deviation $\sigma_x/x_0 = 1/4$ before interaction with the surface. The electron velocity is $v = 0.1\,c$.

where the Fresnel coefficients $r_{\rm p} = (\epsilon k_x - k_x')/(\epsilon k_x + k_x')$ and $r_{\rm s} = (k_x - k_x')/(k_x + k_x')$, with $k_x = \sqrt{\omega^2/c^2 - k_\parallel^2}$ and $k_x' = \sqrt{\epsilon\omega^2/c^2 - k_\parallel^2}$, must be evaluated at frequency $\omega = vk_\parallel \cos\theta$. Equation (4.17) confirms the validity of neglecting nonlocal effects because for an electron with $\beta_e = 0.1$ passing 10 nm above the surface we have $\hbar\omega \approx \hbar v/x \sim 2$ eV (see Section 4.2.3); the local approximation starts failing at angles that make $\cos\theta$ small, and thus contribute only negligibly to the integral, and also at low velocities. Using the Drude approximation $\epsilon = 1 + 4\pi{\rm i}\sigma/\omega$ for the metal dielectric function, where σ is the DC conductivity, we find from Eq. (4.17) the results presented in Fig. (4.1a) for an electron moving above a gold surface ($\hbar\sigma \sim 257$ eV, upper and right axes) with different velocities $v = \beta_{\rm e}c$. Finite conductivity in the real metal affects very little the decay of the phase shift as a function of electron velocity compared to Eq. (4.16), as shown in Fig. (4.1b). We further corroborate good agreement with results obtained by using the measured dielectric function of gold taken from references[97,175] [see Fig. (4.1b)], which is in agreement with the intuition that low frequencies (i.e., those that are well captured by the Drude model) contribute dominantly for the surface-electron distances under consideration.

Upon inspection of Eq. (4.17), we find that the phase depends on metal conductivity σ and geometrical parameters (separation x and path length D) as $\chi = (D/x)F(\bar{x}, \beta_{\rm e})$, where F is a function of the scaled distance $\bar{x} = x\sigma/c$ and the electron velocity $v = \beta_\mathrm{e}c$. This expression justifies the universal scaling used in Fig. (4.1a) (left and lower axes). In particular, in the $\beta_\mathrm{e} \ll 1$ limit, we can approximate $r_\mathrm{p} \approx 1 + \mathrm{i}\omega/2\pi\sigma - \omega^2/4\pi^2\sigma^2$ to obtain

$$\chi \approx \frac{\alpha D}{4\pi x\,\beta_\mathrm{e}}\left[1 - \left(\frac{\beta_\mathrm{e}}{4\pi\bar{x}}\right)^2\right], \qquad \beta_\mathrm{e} \ll 1.$$

This expression shows that the perfect conductor approximation [Eq. (4.16)] describes well the phase shift in front of gold for slow electrons, in agreement with the results of Fig. (4.1b).

The above results need to be contrasted with the effect of decoherence in order to determine whether the predicted phase shift may be observed in practice. As mentioned in Section (4.2.1), decoherence was calculated in reference[156] by assuming local response and neglecting retardation effects. Here, we calculate decoherence from Eq. (4.9) including retardation and nonlocal effects in the EELS probability. For a single electron path running parallel to a planar surface, we have[8]

$$P = -\frac{De^2}{\pi\hbar v^2}\int_0^\infty d\omega \int_0^\infty \frac{dk_y}{k_\parallel^2}\mathrm{Re}\left\{k_x e^{2\mathrm{i}k_x x}\left[\left(\frac{k_y v}{k_x c}\right)^2 r_\mathrm{s} - r_\mathrm{p}\right]\right\}, \tag{4.18}$$

where $k_\parallel = \sqrt{\omega^2/v^2 + k_y^2}$. We introduce nonlocal effects in this expression by adopting the specular-reflection model[171] and using the Feibelman d-parameters approach[172]. Only the Fresnel coefficient

$$r_\mathrm{p} = \frac{\epsilon k_x - k_x' + (\epsilon - 1)\mathrm{i}k_\parallel^2 d_\perp}{\epsilon k_x + k_x' - (\epsilon - 1)\mathrm{i}k_\parallel^2 d_\perp} \tag{4.19}$$

needs to be corrected[178], where[179]

$$d_\perp = -\frac{2}{\pi}\frac{\epsilon}{\epsilon - 1}\int_0^\infty \frac{dk}{k^2}\left[\frac{1}{\epsilon_\mathrm{NL}(k,\omega)} - \frac{1}{\epsilon(\omega)}\right] \tag{4.20}$$

is the perpendicular Feibelman parameter and $\epsilon_\mathrm{NL}(k,\omega)$ is the nonlocal metal permittivity. We approximate the latter following the prescription of Ref. 56. Fig. (4.1c) confirms that nonlocal effects contribute only at low velocities for the electron-surface distances under consideration, and additionally, decoherence takes negligible values ~ 0.1. We also find that low electron velocities are more favorable for the observation of interference fringes produced by the vacuum phase shift.

4.4.3 Graphene film

The above formalism allows us to discuss the quantum phase shift induced on a swift electron flying parallel to a graphene monolayer deposited on a semi-infinite substrate of permittivity ϵ. Describing graphene as a zero-thickness layer with local, frequency-dependent surface conductivity $\sigma_\mathrm{g}(\omega)$, the phase of Eq. (4.8) can be easily computed from

Eq. (4.17) by now writing the Fresnel coefficients as[180]

$$r_{\rm p} = \frac{\epsilon k_x - k'_x + 4\pi\sigma_{\rm g} k_x k'_x/\omega}{\epsilon k_x + k'_x + 4\pi\sigma_{\rm g} k_x k'_x/\omega},$$
$$r_{\rm s} = \frac{k_x - k'_x - 4\pi\sigma_{\rm g}\omega/c^2}{k_x + k'_x + 4\pi\sigma_{\rm g}\omega/c^2},$$

where k_x and k'_x are the out-of-plane light wave-vector components outside and inside the substrate (see expressions above), respectively. In order to numerically calculate the phase shift, we evaluate the graphene conductivity within the local-RPA model at finite temperature T using the analytical expression[181,182]

$$\sigma_{\rm g}(\omega) = \frac{e^2}{\pi\hbar^2}\frac{\rm i}{\omega + {\rm i}\tau^{-1}}\left\{\mu^{\rm D} - \int_0^\infty dE \frac{f_E - f_{-E}}{1 - 4E^2/\left[\hbar^2(\omega + {\rm i}\tau^{-1})^2\right]}\right\},$$

where $\mu^{\rm D} = \mu + 2k_{\rm B}T\log\left(1 + {\rm e}^{-\mu/k_{\rm B}T}\right)$, τ is a phenomenological relaxation time, and $f_E = \left[{\rm e}^{(E-\mu)/k_{\rm B}T} + 1\right]^{-1}$ is the Fermi-Dirac distribution depending on graphene electron energy E and chemical potential

$$\mu \approx \sqrt{\sqrt{(E_{\rm F})^4 + (2\log^2 4)^2(k_{\rm B}T)^4} - (2\log^2 4)(k_{\rm B}T)^2}$$

for a given Fermi energy $E_{\rm F}$. In Fig. (4.1b), we show the dependence of the resulting phase [Eq. (4.17)] on electron velocity for high-quality doped graphene ($E_{\rm F} = 0.5\,$eV, $\hbar\tau^{-1} = 10\,$meV) supported on a silica substrate described by a permittivity ϵ taken from Ref. 175. At high velocity, we recover the perfect-conductor limit because low frequencies are dominant in that regime.

4.5 Elastic diffraction by a small particle

We now consider a geometry lacking any translational symmetry by computing the vacuum phase for an electron interacting with a small particle, the electromagnetic response of which is described within the dipolar approximation in terms of the particle polarizability tensor α. The scattering part of the associated Green tensor admits an analytical expression in terms of the free-space Green tensor G^0 given by [see Eq. (1.24)]:

$$G^{\rm s}_{z,z}(\mathbf{R}, z, \mathbf{R}, z', \omega) = -4\pi\omega^2 \sum_{i,i'} G^0_{z,i}(\mathbf{R}, z, \mathbf{r}_0, \omega)\alpha_{i,i'}G^0_{i',z}(\mathbf{r}_0, \mathbf{R}, z', \omega), \qquad (4.21)$$

where $\mathbf{r}_0$ is the particle position ($\mathbf{r}_0 = 0$ for simplicity) and the indexes i, i' run over Cartesian directions. In what follows, we consider a diagonal polarizability tensor α of components α_x, α_y, and α_z. Now, by plugging Eq. (4.21) into Eq. (4.8) and then using the integrals $\int_{-\infty}^{\infty} dz\ {\rm e}^{{\rm i}\omega z/v}{\rm e}^{{\rm i}kr}/r = 2K_0(\zeta)$ and $\int_{-\infty}^{\infty} dz\ {\rm e}^{{\rm i}\omega z/v}\left[{\rm e}^{{\rm i}kr}/r^2 - {\rm i}{\rm e}^{{\rm i}kr}/kr^3\right] = 2{\rm i}cK_1(\zeta)/Rv\gamma$, where $r = \sqrt{R^2 + z^2}$ and $\zeta = \omega R/v\gamma$ [see Eqs. (3.914-4) and (3.914-5) in Ref. 95, where we consider that $k = \omega/c + {\rm i}0^+$ has a positive infinitesimal imaginary part], we obtain the expression

$$\chi(x, y) = \frac{2e^2}{\pi\hbar v^4\gamma^2}\int_0^\infty \omega^2 d\omega {\rm Re}\left\{\left[\frac{\alpha_x x^2 + \alpha_y y^2}{R^2}K_1^2\left(\frac{\omega R}{v\gamma}\right) + \frac{\alpha_z}{\gamma^2}K_0^2\left(\frac{\omega R}{v\gamma}\right)\right]\right\}.$$

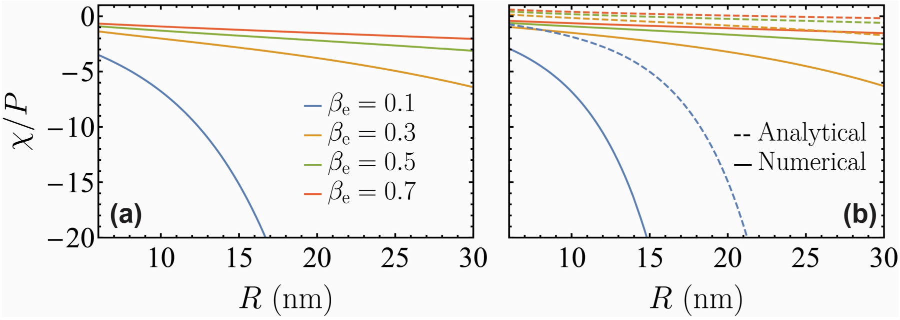

Figure 4.3: Quantum phase compared with decoherence for small particles. We present the ratio of the $T = 0$ position-dependent phase shift χ and decoherence P for (a) gold and (b) silver spheres of 6 nm radius and different electron velocities $v = \beta_e c$ (see labels). We use measured dielectric permittivities[97] to describe these materials.

For an isotropic particle ($\alpha = \alpha_x = \alpha_y = \alpha_z$), the phase depends only on radial distance R and this expression reduces to

$$\chi(R) = \frac{2e^2}{\pi\hbar v^4\gamma^2}\int_0^\infty \omega^2 d\omega \; f\left(\frac{\omega R}{v\gamma}\right) \mathrm{Re}\left\{\alpha\right\}, \tag{4.22}$$

where $f(\zeta) = K_1^2(\zeta) + K_0^2(\zeta)/\gamma^2$. We study below a small homogeneous sphere, in which the approximation $\alpha = 3c^3 t_1^E/2\omega^3$ in terms of the dipolar electric Mie coefficient t_1^E captures retardation effects and compares well with full calculations in EELS for realistic metal spheres similar to the one considered in next section[8], which leads to a position-dependent decoherence [see Eq. (4.14) and the analytical result for the coupling coefficient β_j presented in Ref. 64]

$$P(R) = \frac{-2e^2}{\pi\hbar v^4\gamma^2}\int_0^\infty \omega^2 d\omega \; f\left(\frac{\omega R}{v\gamma}\right) \mathrm{Im}\left\{\alpha\right\} \tag{4.23}$$

at $T = 0$.

Incidentally, for a particle hosting a dominant sharp mode of frequency ω_0, we can approximate $\alpha = A/(\omega_0 - \omega - \mathrm{i}0^+)$, which upon insertion in Eqs. (4.22) and (4.23) leads to

$$P(R) = \frac{-2e^2 A\omega_0^2}{\hbar v^4\gamma^2}\; f\left(\frac{\omega_0 R}{v\gamma}\right), \tag{4.24}$$

$$\chi(R) = \frac{-2e^2 A\omega_0^2}{\hbar v^4\gamma^2}\; g\left(\frac{\omega_0 R}{v\gamma}\right), \tag{4.25}$$

where

$$g(\theta) = \frac{1}{\pi}\,\mathrm{P}\int_0^\infty \frac{x^2 dx}{x-1}\; f(x\theta).$$

In EM one is interested in imaging without damaging, for which a high ratio $\chi/P = |g/f|$ becomes advantageous. We explore such ratio in Fig. (4.3) for the interaction with gold and silver spherical particles, where we find that χ takes much larger values than P (in particular, we find vacuum phase shifts $\chi \sim 3^\circ$ for the gold sphere at a distance $R = 15\,$nm, see below), thus supporting the use of holography (i.e., measurement of the quantum phase) as an advantageous route to imaging without damaging compared with bright-field electron acquisition (i.e., resolving P). We present calculations based on direct use of Eqs. (4.22) and (4.23) [solid curves in Fig. (4.3)]. For silver, which diplays a well-defined plasmon mode, these results compare well with the analytical calculation obtained from Eqs. (4.24) and (4.25) (broken curves).

4.6 Diffraction in the far-field

4.6.1 Interaction with a planar surface

Equation (4.8) shows a position-dependent phase shift that the electron wave function experiences after interaction with the electromagnetic vacuum. This phase shift may be observed through an interference experiment, as the one described in Section 4.2, consisting in splitting an electron beam in two parts and then recombining them after interaction of one of the components with the structure. The theory developed in Section 4.3 shows how this phase affects the transverse component of the electron wave function, and consequently, an alternative to beam splitting techniques may be provided by a combined energy- and angle-resolved experiment. Indeed, the elastic component of the electron beam density matrix contains the vacuum phase through $\rho_{\rm elastic}(\mathbf{r},\mathbf{r}') = \psi_0(\mathbf{r})\,\psi_0^*(\mathbf{r}')\;\exp\{{\rm i}[\chi(\mathbf{r})-\chi(\mathbf{r}')]\}\,D_{\rm elastic}(\mathbf{r},\mathbf{r}')$ (see Eq. (4.12)). We remark that, although we only study the effect of the quantum phase associated with vacuum fluctuations on elastic electron components, it also affects inelastic components, where a certain degree of coherence is preserved, which could be analyzed following the approach used to study inelastic electron holography[183]. Obviously, the elastic electron density $\rho_{\rm elastic}(\mathbf{r},\mathbf{r})$ is not modified, and therefore, it does not lead to any measurable effect if decoherence is neglected, as shown in Fig. (4.2a), where only the x-dependent part of the wave function ψ_x is plotted.

In contrast, the diagonal coefficients of the electron density matrix in momentum space, which we calculate by Fourier-transforming the electron wave function as

$$\psi_{{\rm elastic},\mathbf{Q}}(z) = \int d^2\mathbf{R}\;\psi_0(\mathbf{r})\;\exp\left[{\rm i}\chi(\mathbf{R}) + P(\mathbf{R}) - {\rm i}\mathbf{Q}\cdot\mathbf{R}\right] \tag{4.26}$$

with $\mathbf{r} = (\mathbf{R}, z)$ and $\mathbf{R} = (x, y)$, display a dependence on the imprinted position-dependent quantum phase χ and decoherence P, with the latter expressed at $T = 0$ from Eq. (4.14). For illustration, we assume the initial electron wave function along the out-of-plane direction x to be well described by a Gaussian of standard deviation σ_x centered at a distance x_0 from the metallic plate. Since the electron wave function does not experience any change along in-plane directions, these Fourier components can be factorized. The only nontrivial component is thus $\psi_{k_x} \equiv \psi_{{\rm elastic},k_x}$, the squared modulus of which presents an evolution as illustrated in Fig. (4.2b) for an electron traveling parallel to a perfect conductor, which, as shown above, provides a good approximation to gold surfaces for the large values of x_0 under consideration, and furthermore results in $P = 0$. The presence of the distance-dependent phase shift affects the out-of-plane electron wave function, which is progressively bent toward the surface, as expected from image charge attraction.

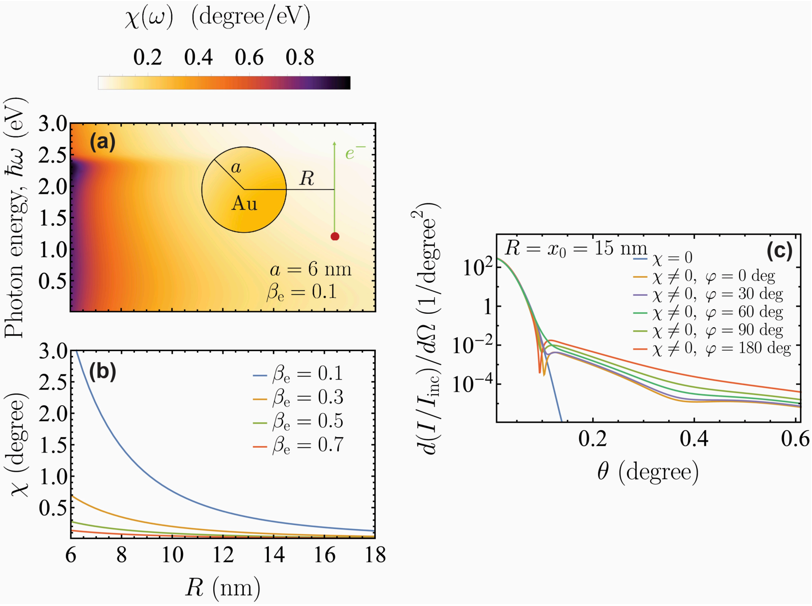

Figure 4.4: Quantum-vacuum-induced phase shift produced by a small particle. (a) Frequency-resolved contribution to the vacuum phase $\chi(\omega)$ induced on an electron moving with velocity $v = 0.1\,c$ and passing near a gold nanosphere of 6 nm radius, plotted as a function of photon energy $\hbar\omega$ and impact parameter R (see inset). We describe the particle through its electric polarizability α evaluated in turn using the measured dielectric function for this material[97]. (b) Phase shift (i.e., integral of $\chi(\omega)$ over ω) for different values of β_e. (c) Angular dependence of the electron current scattered in the far-field due to diffraction of an focused electron wave under the same conditions as in (a) as a function of polar scattering angle θ for different azimuthal angles φ (see legend) relative to the direction specified by the impact parameter $\mathbf{R}_0 \parallel \hat{\mathbf{x}}$. The incident electron beam has a transverse Gaussian profile of width $\sigma_R = 5\,$nm centered at coordinates $\mathbf{R}_0 = (15\,\text{nm}, 0)$. For reference, we show the pattern obtained without quantum phase and decoherence ($\chi = 0$ curve).

4.6.2 Interaction with a small object

Quantum-vacuum-induced diffraction can be equivalently quantified in terms of the electron current measured far from the scatterer. In particular, if we assume the interaction region to be limited to $z < z_1$, the acquired phase χ can be considered a function only of the transverse coordinates $\mathbf{R} = (x, y)$. Additionally, outside that region the elastic part of the scattered electron $\psi^{\rm e}_{\rm elastic}$ must satisfy the Helmholtz equation $(\nabla^2 + k_0^2)\psi_{\rm elastic} = 0$, where k_0 is the electron wave vector. We thus have for $z > z_1$

$$\psi_{\rm elastic}(\mathbf{r}) = \int \frac{d^2\mathbf{Q}}{(2\pi)^2}\ \psi_{{\rm elastic},\mathbf{Q}}(z_1)\ \exp\left[{\rm i}k_{z,\mathbf{Q}}(z - z_1) + {\rm i}\mathbf{Q}\cdot\mathbf{R}\right], \qquad (4.27)$$

where $k_{z,\mathbf{Q}} = \sqrt{k_0^2 - \mathbf{Q}^2 + \mathrm{i}0^+}$ and $\psi_{\text{elastic},\mathbf{Q}}(z_1)$ is defined in Eq. (4.26). Equation (4.27) guarantees the continuity of the wave function at $z = z_1$. In the far-field limit ($k_0 r \gg 1$), Eq. (4.27) can be approximated, using the stationary-phase method [2], as

$$\psi_{\text{elastic}}(\mathbf{r}) \approx -\frac{\mathrm{i}k_0 \cos\theta}{2\pi}\,\psi_{\mathbf{Q}_{\hat{\mathbf{r}}}}\,\frac{\mathrm{e}^{\mathrm{i}k_0 r}}{r},$$

where $\mathbf{Q}_{\hat{\mathbf{r}}} = k_0\,\mathbf{R}/r$ and $\cos\theta = z/r$. Taking now an incident beam with transverse Gaussian profile of width σ_R focused at $\mathbf{r} = (x_0, 0, 0)$ (i.e., an incident electron wave function $\psi_0(\mathbf{r}) \approx \mathrm{e}^{\mathrm{i}k_0 z - [(x-x_0)^2+y^2]/4\sigma_R^2}/(2\pi\sigma_R^2 L)^{1/2}$ near the region of interaction with the particle, where L is the quantization length along the beam direction), we can calculate the electron current collected within a far-field solid angle $d\Omega$ as

$$dI = (\hbar/m_{\mathrm{e}})\,\mathrm{Im}\{\psi^*\,\hat{\mathbf{r}}\cdot\nabla\psi\}\,r^2 d\Omega = I_{\mathrm{inc}}\frac{k_0^2\cos^2\theta}{4\pi^2}|\sqrt{L}\psi_{\mathbf{Q}_{\hat{\mathbf{r}}}}|^2 d\Omega, \tag{4.28}$$

where $I_{\mathrm{inc}} = \hbar k_0/m_{\mathrm{e}}L$. We use this expression to study the effect of vacuum fluctuations produced by interaction of the electron with a small particle, for which we apply the formalism of Section 4.5, so we plug Eq. (4.22) into Eq. (4.28) and focus on a nanosphere of radius a located at the origin and described by its dipolar response. We obtain

$$\frac{dI}{d\Omega} = I_{\mathrm{inc}}\frac{k_0^2\cos^2\theta}{2\pi\sigma_R^2}\mathrm{e}^{-x_0^2/2\sigma_R^2} \tag{4.29}$$

$$\times\left|\int_0^\infty R\,dR\,\mathrm{e}^{-R^2/4\sigma_R^2+\mathrm{i}\chi(R)+P(R)-\mathrm{Re}\{\sqrt{a^2-R^2}\}/\lambda_e}\,I_0\left[R\sqrt{\left(\frac{x_0}{2\sigma_R^2}-\mathrm{i}Q_x\right)^2-Q_y^2}\right]\right|^2,$$

where we use the notation $\mathbf{Q}_{\hat{\mathbf{r}}} = (Q_x, Q_y)$, the modified Bessel function I_0 is the result of applying the tabulated integral (3.937-2) in Ref. 95, and an elastic attenuation length λ_e is introduced to account for the depletion of the transmitted electron wave function due to heavy collisions inside the metal. We plot the resulting electron angular distribution calculated from Eq. (4.29) in Fig. (4.4c) ($\chi \neq 0$ curves) for a gold nanosphere of radius $a = 6\,\mathrm{nm}$ ($\ll \lambda_e$) and an electron beam of velocity $v = 0.1\,c$, width $\sigma_R = 5\,\mathrm{nm}$, and impact parameter $x_0 = 15\,\mathrm{nm}$ relative to the particle center. We further compare the scattering pattern with the one obtained in the absence of the nanoparticle (i.e., setting $\chi = 0$), which takes the analytical form (also assuming $a \ll \lambda_e$)

$$\frac{dI}{d\Omega} = I_{\mathrm{inc}}\,(2k_0^2\sigma_R^2\cos^2\theta/\pi)\,\mathrm{e}^{-2k_0^2\sigma_R^2\sin^2\theta}. \tag{4.30}$$

Reassuringly, for the large values of $k_0\sigma_R > 10^3$ under consideration, the right-hand side of Eq. (4.30) yields $I \approx I_{\mathrm{inc}}$ when integrated over solid angle Ω. Remarkably, the influence of vacuum fluctuations modifies the electron wave function, introducing in the far-field current distribution an azimuthal dependence as well as substantial scattering up to $\theta \sim 1°$, in contrast to the result otained from the direct beam without particle-mediated coupling to vacuum fluctuations [see Fig. (4.4c) and Eq. (4.30)).

---

[2] Such method provides the asymptotics of Fourier integrals of the type $f(\mathbf{r}) = \int(d^2\mathbf{Q}/4\pi^2)\exp\left[\mathrm{i}\mathbf{Q}\cdot\mathbf{R} + \mathrm{i}\sqrt{k_0^2 - Q^2}z\right]f(\mathbf{Q})$ which reduce to $f(\mathbf{r}) = (-\mathrm{i}k_0\cos\theta/2\pi r)\mathrm{e}^{\mathrm{i}k_0 r}f(\mathbf{Q} = k_0\mathbf{R}/r)$ in the limit of $k_0 r \to \infty$ (see proof in Ref. 184).

4.7 Concluding remarks

In summary, we have shown that the elastic part of an electron beam has a phase shift imprinted in its transverse wave function dependence upon interaction with the vacuum electromagnetic field in the presence of a material structure. This effect, which can be attributed to fluctuations characterizing the quantum electromagnetic field, could be experimentally measured by means of either interference or diffraction of electron beams using an electron microscope. Specifically, our calculations predict that the aloof vacuum interaction of a $\beta_e = 0.1$ ($\sim 2.5\,$keV kinetic energy) electron with a planar gold surface results in a significant phase shift for a path length $D \sim 1\,\mu$m [see Fig. (4.1)], which should produce discernible interference fringes only marginally affected by decoherence [see Fig. (4.1c) and Ref. 156]. Indeed, the recombination of the two parts of the electron wave function $\psi_j e^{i\chi_j}$ following different paths $j = 1, 2$ that are affected by their corresponding phases χ_j leads to an electron probability at the detector $\propto |\psi_1|^2 + |\psi_2|^2 + 2\mathrm{Re}\{\psi_1\psi_2^* e^{i(\chi_1-\chi_2)}\}$; when one of the paths passes near a 12 nm gold particle [Fig. (4.4)], the phase-shift difference can be as large as $|\chi_1 - \chi_2| \sim 3°$, which could be resolved in an electron holography setup. Additionally, we conclude that signatures of vacuum fluctuations should also be observed by monitoring the angular distribution of electrons after such interaction [e.g., in the Fourier plane of an electron microscope; see Fig. (4.2b) and Fig. (4.4c)]. However, the electron deflections involved in such type of diffraction experiment could be overshadowed by very-low-energy inelastic contributions associated with Johnson noise[176,185,186], so the previously noted two-path holography experiment appears to be a more plausible solution to measure the quantum vacuum phase shift. It is our hope that the present work contributes to clarify the role of vacuum fluctuations in macroscopic quantum electrodynamics and supports the fact that an experimental verification is feasible using state-of-art electron microscopes. Considering the strong effect induced on the electron wave function by the quantum vacuum phase, we anticipate further efforts oriented toward the engineering of structures capable of tailoring vacuum fluctuations as a novel route to design free-electron phase plates. Additionally, this effort can lead to optimized strategies for electron microscope imaging: indeed, from the holography configuration discussed in Section 4.2.1, taking path 2 to be far from both the sample and path 1, we have an interference term

$$\langle \hat{\mathcal{S}}_2^\dagger \hat{\mathcal{S}}_1 \rangle_T = \exp\left\{ \frac{-2ie^2}{\hbar} \int_0^\infty d\omega \int_{-\infty}^\infty dz\, dz' \cos\left[\frac{\omega}{v}(z - z')\right] G^{\rm s}_{z,z}(\mathbf{R}_1, z, \mathbf{R}_1, z', \omega) \right\}$$

at $T = 0$, clearly showing that the imaginary part of the Green tensor produces a depletion of the signal, while possibly creating excitations in the sample, whereas the real part determines the phase shift under discussion; for practical purposes in electron microscopy, it is useful to reduce the former (i.e., limit sample damage) while increasing the latter (i.e., enhance phase contrast), a task that leads to a problem of optimization in the present formalism. Our results for small noble-metal spheres [Fig. (4.3)] already indicate that measurement of the quantum phase can be advantageous compared with bright-field imaging to avoid sample damage.

5

Modulation of cathodoluminescence emission by interference with external light

Above all, don't fear difficult moments. The best comes from them.
Rita Levi-Montalcini

In this chapter, we study how light and free-electron pulses can interfere when interacting with a nanostructure, therefore giving rise to a modulation in the spectral distribution of the cathodoluminescence light emission that is strongly dependent on the electron wave function. Specifically, we show that for a temporally focused electron, cathodoluminescence can be cancelled upon illumination with a spectrally modulated dimmed laser that is phase-locked relative to the electron density profile. What follows is based on a published work, Ref. 187.

5.1 Introduction

Coherent laser light provides a standard tool to selectively create optical excitations in atoms, molecules, and nanostructures with exquisite spectral resolution[188]. Additional selectivity in the excitation process can be gained by exploiting the light polarization and the spatial distribution of the optical field to target, for example, modes with specific angular momentum in a specimen[189]. However, the diffraction limit constraints our ability to selectively act on degenerate excitation modes sustained by structures that are separated by either less than half the light wavelength when using far-field optics (unless ingenious, sample-dependent schemes are adopted[190–192]) or a few tens of nanometers when resorting to near-field enhancers such as metallic tips[193–195]. In contrast to light, electron beams, which are also capable of producing optical excitations[8], can actuate with a spatial precision roughly determined by their lateral size, currently reaching the sub-Ångstrom domain in state-of-the-art electron microscopes[67,127,196]. Indeed, the evanescent electromagnetic field accompanying a fast electron spans a broadband spectrum that mediates the transfer of energy and momentum to sample excitation modes with such degree of spatial accuracy[8]. But unfortunately, spectral selectivity is lost because of the broadband nature of this excitation source, unless post-selection is performed by energy-filtering of the electrons, as done for instance in EELS[8,71,197].

Photons and electrons team up to extract the best of both worlds in the rapidly evolving field of ultrafast transmission electron microscopy (UTEM), whereby the high spatial precision of electron microscopes is combined with the time resolution and spectral selectivity of optical spectroscopy. In this technique, ultrashort electron pulses created by photoelectron emission are used to track structural or electronic excitations with picosecond and femtosecond temporal resolution[26,29,79,198–205]. Regarding electron-photon interaction, UTEM allows us to exploit the evanescent optical field components created by light scattering at nanostructures, so that the interaction is facilitated by passing the free-electron beam through these fields, thus enabling spectrally and temporally resolved imaging with combined resolution in the nanometer–fs–meV domain via the PINEM technique[26–29,35,36,39,64,74,76–83,87,93,100,106,107,113–116,118,119,206–209]. This approach has been exploited to investigate the temporal evolution of plasmons[77,78] and optical cavity modes[106,107], as well as a way to manipulate the electron by exchanging transverse linear[34,36,93] and angular[82,115] momentum with the photon field.

Following concepts from accelerator physics[210], temporal compression of the electron beam into a train of attosecond pulses can be achieved by periodic momentum modulation and free-space propagation, using either ponderomotive forces[211–213] or PINEM-like inelastic electron-light scattering interactions[29,80,83,119,140,214]. Accompanying these advances in our ability to manipulate free electrons, recent theoretical studies have explored the use of modulated free electrons to gain control over the density matrix of excitations created in a sample[108,144,215–217]. Intriguingly, the CL emission produced by a PINEM-modulated electron has been predicted to bear coherence with the laser used to achieve such modulation, which could be revealed through correlations in an interferometer[144]. This scenario holds the potential to combine light and electrons as coherent probes acting on a sample, possibly enabling practical applications in pushing the space-time-energy levels of resolution beyond their current values. We remark that with the word *coherence*, we refer in what follows in a precise way at the interference of two phase-locked processes.

The CL intensity is extremely low in most samples ($\lesssim 10^{-5}$ photons per electron), unless we restrict ourselves to special classes of targets (e.g., those enabling phase matching between the emitted radiation and the electron[35,87,218]). When measuring far-field radiation, the visibility of the interference between CL emission and external light could be enlarged by dimming the latter to match the former. Shot noise that could potentially mask the resulting interference is avoided if photon measurements are performed at a single detector (i.e., after the amplitudes of CL and external light have been coherently superimposed). Based on this idea, we anticipate that the use of dimmed illumination in combination with CL light emission represents a practical route towards the sought-after push in space-time-energy resolution with which we can image and manipulate optical excitations at the nanoscale.

In this chapter, we show that the optical excitations produced in a structure by the combined effect of light and free electrons can add coherently, therefore providing a tool for actively manipulating sample excitations. The combination of light and electrons adds the spatial resolution of the latter to the spectral selectivity of the former in our ability to manipulate and probe nanoscale materials and their optical response. Specifically, we illustrate this possibility by showing that the CL emission produced by a free electron can be coherently manipulated by simultaneously exciting the sample with suitably modulated external light. We demonstrate that it is possible to strongly modulate the CL emission using currently existing technology, while complete cancellation of CL is physically feasible using tightly compressed electron wavepackets, which act as classical external point charges. The present work thus capitalizes on the correlation between CL from modulated electrons and synchronized external light as discussed in Ref. 144, so we propose a disruptive form of ultrafast electron microscopy based on the direct observation of interference between CL emission and dimmed light scattering at a single photon spectrometer. We anticipate the application of interference in the excitations produced by the simultaneous action of light and electrons as a route towards spectrally resolved imaging and selective excitation of sample optical modes with an improved level of space-time-energy resolution. The sensitivity provided by the measurement of the relative phases between electron and laser waves could be further enhanced through lock-in amplification schemes that isolate the interference effects to gain information on both the electron density profile and the temporal evolution of the targeted optical excitations.

5.2 First-principles description of CL interference with external light

We consider the combined action of external light and free electrons on a sampled structure, such as schematically illustrated in Fig. (5.1). Under common conditions met in electron microscopes, the electrons can be prepared with well-defined velocity, momentum, and energy, such that their wave functions consist of components that have a narrow spread relative to those values. Additionally, we adopt the nonrecoil approximation by assuming that any interaction with the specimen produces negligible departures of the electron velocity with respect to its average value (i.e., small momentum

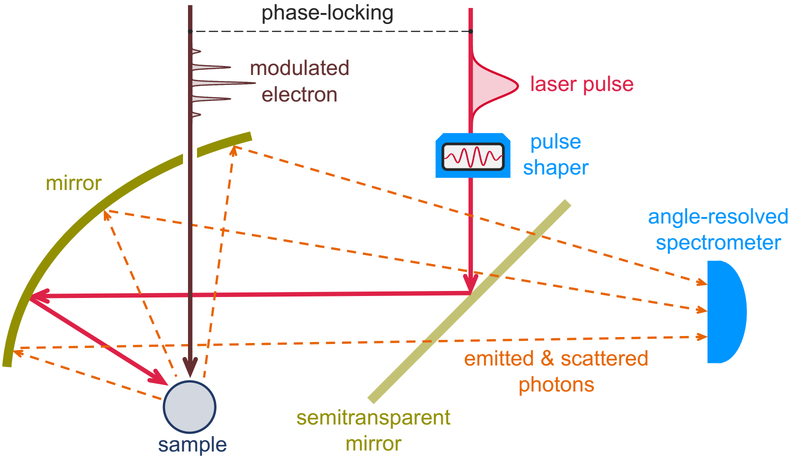

Figure 5.1: Sketch of the system under consideration. A laser pulse and a modulated electron are made to interact with a sample and produce light scattering and CL emission, respectively. The electron is synchronized with the laser pulse to maintain mutual phase coherence. The resulting emitted and scattered photons are collected by a spectrometer. A laser pulse shaper is inserted in this scheme to bring the scattered light amplitude to a level that is commensurate with the CL emission field.

transfers relative to the central electron momentum). Under these conditions, we calculate the far-field radiation intensity produced by the combined contributions of interaction with the electron and scattering from a laser, based on the far-field Poynting vector [see Eq. (1.5b)]. In a fully quantum treatment of radiation, the angle- and frequency-resolved far-field (ff) photon probability reduces to

$$\frac{d\Gamma_{\rm ff}}{d\Omega_{\hat{\mathbf{r}}}d\omega} = \lim_{kr\to\infty} \frac{r^2}{4\pi^2\hbar k}{\rm Re}\left\{\left\langle\hat{\mathcal{E}}(\mathbf{r},\omega)\times\hat{\mathcal{B}}^\dagger(\mathbf{r},\omega)\right\rangle\right\}\cdot\hat{\mathbf{r}}, \tag{5.1}$$

where $k = \omega/c$ (see detailed derivation in the Appendix E). This expression is the quantum counterpart of a classical result for CL of Eq. (1.28), now involving the position- and frequency-dependent positive-energy part of the electric and magnetic field operators $\hat{\mathcal{E}}(\mathbf{r},\omega)$ and $\hat{\mathcal{B}}(\mathbf{r},\omega)$, respectively. We use the MQED formalism to calculate this quantity for a free electron of incident wave function $\psi_0(\mathbf{r})$ and external light characterized by a spectrally resolved electric field amplitude $\mathbf{E}^{\rm ext}(\mathbf{r},\omega)$. After some analysis (see Appendix E), taking the electron velocity vector $\mathbf{v}$ along z, we find

$$\begin{aligned}\frac{d\Gamma_{\rm rad}}{d\Omega_{\hat{\mathbf{r}}}d\omega} =& \frac{1}{4\pi^2\hbar k}\bigg[\int d^2\mathbf{R}'\, M_0(\mathbf{R}')|\mathbf{f}^{\rm CL}_{\hat{\mathbf{r}}}(\mathbf{R}',\omega)|^2 \\ &+|\mathbf{f}^{\rm scat}_{\hat{\mathbf{r}}}(\omega)|^2+2\int d^2\mathbf{R}'\,{\rm Re}\left\{M_{\omega/v}(\mathbf{R}')\,\mathbf{f}^{\rm CL*}_{\hat{\mathbf{r}}}(\mathbf{R}',\omega)\cdot\mathbf{f}^{\rm scat}_{\hat{\mathbf{r}}}(\omega)\right\}\bigg],\end{aligned} \tag{5.2}$$

where

$$M_{\omega/v}(\mathbf{R}) = \int_{-\infty}^{\infty} dz\; {\rm e}^{{\rm i}\omega z/v}\,|\psi_0(\mathbf{r})|^2 \tag{5.3}$$

is the Fourier transform of the electron probability density, which acts as a coherence factor. Here, we use the notation $\mathbf{r} = (\mathbf{R}, z)$ with $\mathbf{R} = (x, y)$ and we define the electric far-field amplitudes $\mathbf{f}^{\rm CL}_{\hat{\mathbf{r}}}(\mathbf{R}', \omega)$ and $\mathbf{f}^{\rm scat}_{\hat{\mathbf{r}}}(\omega)$ through the asymptotic expressions

$$4\pi {\rm i} e\omega \int dz'\, {\rm e}^{{\rm i}\omega z'/v}\, G(\mathbf{r}, \mathbf{R}', z', \omega) \cdot \hat{\mathbf{z}} \xrightarrow[kr\to\infty]{} \frac{{\rm e}^{{\rm i}kr}}{r} \mathbf{f}^{\rm CL}_{\hat{\mathbf{r}}}(\mathbf{R}', \omega), \tag{5.4a}$$

$$\mathbf{E}^{\rm scat}(\mathbf{r}, \omega) \xrightarrow[kr\to\infty]{} \frac{{\rm e}^{{\rm i}kr}}{r} \mathbf{f}^{\rm scat}_{\hat{\mathbf{r}}}(\omega), \tag{5.4b}$$

corresponding to the classical CL and laser scattering contributions, respectively. It should be noted that we only retain the $1/r$ radiative components of the far field in $d\Gamma_{\rm rad}/d\Omega_{\hat{\mathbf{r}}} d\omega$ [see Eqs. (5.2) and (5.4)], which is a legitimate procedure when considering directions in which they do not interfere with the external illumination. Nevertheless, interference between the incident and forward $1/r$ radiative components produces an additional contribution $d\Gamma_{\rm forward}/d\Omega_{\hat{\mathbf{r}}} d\omega$ (i.e., $d\Gamma_{\rm ff}/d\Omega_{\hat{\mathbf{r}}} d\omega = (d\Gamma_{\rm rad}/d\Omega_{\hat{\mathbf{r}}} d\omega) + (d\Gamma_{\rm forward}/d\Omega_{\hat{\mathbf{r}}} d\omega)$), as we discuss below in relation to the energy pathways associated with the interaction. The specimen is assumed to be characterized by a linear and local electromagnetic response, which enters this formalism through the Green tensor, implicitly defined by Eq. (1.11). The first and second terms in Eq. (5.2) describe the separate contributions from CL and light scattering, respectively, whereas the third term accounts for interference between them. We remark that this result relies on the nonrecoil approximation for the electron, which allows us to replace its associated current operator by the average expectation value under the the assumption that $\mathbf{v}$ remains unaffected by the interaction.

Interestingly, the CL emission in the absence of external illumination (i.e., the first term in Eq. (5.2)], is constructed as an incoherent sum of contributions from different lateral positions $\mathbf{R}'$ across the electron beam[33,142] (i.e., no interference remains in this signal between the CL emission from different lateral positions of the beam). In contrast, the signal associated with the interference between CL and light scattering [third term in Eq. (5.2)] contains further interference between the contribution of different lateral electron-beam positions $\mathbf{R}'$. Interestingly, this effect is genuinely associated with interference between different lateral positions of the beam because the light scattering amplitude $\mathbf{f}^{\rm scat}_{\hat{\mathbf{r}}}(\omega)$ in that equation does not depend on $\mathbf{R}'$.

For completeness, we note that Eq. (5.2) can be written in the more compact form

$$\frac{d\Gamma_{\rm rad}}{d\Omega_{\hat{\mathbf{r}}} d\omega} = \frac{1}{4\pi^2 \hbar k} \int d^3\mathbf{r}'\, |\psi_0(\mathbf{r}')|^2 \left| {\rm e}^{-{\rm i}\omega z'/v}\, \mathbf{f}^{\rm CL}_{\hat{\mathbf{r}}}(\mathbf{R}', \omega) + \mathbf{f}^{\rm scat}_{\hat{\mathbf{r}}}(\omega) \right|^2,$$

which directly reflects the interference between CL and laser scattering. In addition, our results can easily be generalized to deal with several distinguishable electrons (labeled by superscripts j), for which we have

$$
\begin{aligned}
\frac{d\Gamma_{\rm rad}}{d\Omega_{\hat{\mathbf{r}}}d\omega} = \frac{1}{4\pi^2\hbar k}\Bigg\{ & \sum_j \int d^2\mathbf{R}'\, M_0^j(\mathbf{R}')|\mathbf{f}^{\rm CL}_{\hat{\mathbf{r}}}(\mathbf{R}',\omega)|^2 \\
& + |\mathbf{f}^{\rm scat}_{\hat{\mathbf{r}}}(\omega)|^2 + 2\sum_j \int d^2\mathbf{R}'\, {\rm Re}\left\{M^j_{\omega/v}(\mathbf{R}')\, \mathbf{f}^{\rm CL*}_{\hat{\mathbf{r}}}(\mathbf{R}',\omega)\cdot\mathbf{f}^{\rm scat}_{\hat{\mathbf{r}}}(\omega)\right\} \\
& + \sum_{j\neq j'} \left[\int d^2\mathbf{R}'\, M^j_{\omega/v}(\mathbf{R}')\mathbf{f}^{\rm CL*}_{\hat{\mathbf{r}}}(\mathbf{R}',\omega)\right] \left[\int d^2\mathbf{R}''\, M^{j'*}_{\omega/v}(\mathbf{R}'')\mathbf{f}^{\rm CL}_{\hat{\mathbf{r}}}(\mathbf{R}'',\omega)\right] \Bigg\}
\end{aligned}
\tag{5.5}
$$

(see derivation in the Appendix E), where $M^j_{\omega/v}$ is given by Eq. (5.3) with ψ_0 replaced by ψ_j (the wave function of electron j). In the absence of external light (i.e., with $\mathbf{f}^{\rm CL}_{\hat{\mathbf{r}}} = 0$), this expression converges to the multi-electron excitation probability described elsewhere[33].

While the above results are derived for electrons prepared in pure states (i.e., with well-defined wave functions), the extension to mixed electron states is readily obtained by evaluating the averages in Eqs. (E.7) as ${\rm Tr}\{\hat{\mathbf{j}}^{\rm el}(\mathbf{r}',\omega)\hat{\mathbf{j}}^{\rm el}(\mathbf{r}'',\omega)\hat\rho_j\}$ and ${\rm Tr}\{\hat{\mathbf{j}}^{\rm el}(\mathbf{r}',\omega)\hat\rho_j\}$, respectively, where $\hat\rho_j$ is the electron density matrix of electron j. This leads exactly to the same expressions as above but replacing $|\psi_j(\mathbf{r})|^2$ by the probability densities $\langle\mathbf{r}|\hat\rho_j|\mathbf{r}\rangle$, which allow us to describe electrons that have undergone decoherence processes before interacting with the sample.

We present results below for nanoparticles whose optical response can be described through an isotropic, frequency-dependent polarizability $\alpha(\omega)$. Considering a well-focused electron with impact parameter $\mathbf{R}_0$ relative to the particle position $\mathbf{r}=0$ (i.e., an electron probability density $|\psi_0(\mathbf{r})|^2 \approx \delta(\mathbf{R}-\mathbf{R}_0)|\psi_\parallel(z)|^2$), we find that Eq. (5.2) then reduces to

$$
\begin{aligned}
\frac{d\Gamma_{\rm rad}(\mathbf{R}_0)}{d\omega} = \frac{2k^3}{3\pi\hbar}|\alpha(\omega)|^2\Bigg[& \left|\mathbf{E}^{\rm ext}(0,\omega) + M^*_{\omega/v}\,\mathbf{E}^{\rm el}(\mathbf{R}_0,\omega)\right|^2 \\
& + \left(1-\left|M_{\omega/v}\right|^2\right)\,|\mathbf{E}^{\rm el}(\mathbf{R}_0,\omega)|^2\Bigg],
\end{aligned}
\tag{5.6}
$$

where

$$
\mathbf{E}^{\rm el}(\mathbf{R}_0,\omega) = \frac{2e\omega}{v^2\gamma}\left[K_1\left(\frac{\omega R_0}{v\gamma}\right)\hat{\mathbf{R}}_0 + \frac{\rm i}{\gamma}K_0\left(\frac{\omega R_0}{v\gamma}\right)\hat{\mathbf{z}}\right], \tag{5.7}
$$

is the bare electron field [see Eq. (1.19)], and we now have

$$
M_{\omega/v} = \int_{-\infty}^{\infty} dz\, {\rm e}^{{\rm i}\omega z/v}\,|\psi_\parallel(z)|^2 \tag{5.8}
$$

for the electron coherence factor. These expressions clearly reveal that, although the phase of the electron wave function is erased because only the probability density appears in Eq. (5.8), the mutual electron-light coherence is controlled by the temporal profile of that density, as well as its timing with respect to the light field, which produces a global phase in $M_{\omega/v}$ relative to the light field that in turn enters through the first term inside the square brackets in Eq. (5.6) (e.g., to partially cancell the CL emission). Obviously, without electron-laser timing, averaging over this phase difference cancels such interference.

Reassuringly, Eq. (5.6) reduces to well-known expressions for the CL emission when setting $\mathbf{E}^{\rm ext}=0$ (i.e., in the absence of external light). This result is independent of the electron wave function[33,108,143,144]. Moreover, we recover the photon scattering cross section $\propto \omega^3|\alpha|^2$ when $\mathbf{E}^{\rm el}=0$ (i.e., without the electron). An additional element of intuition is added by the fact that the expression for $\mathbf{E}^{\rm el}(\mathbf{R}_0,\omega)$ corresponds to the spectrally resolved evanescent field produced by a classical point electron[8], which decays exponentially away from the trajectory, as described by the modified Bessel functions K_0 and K_1.

The electron coherence factor $M_{\omega/v}$ in Eq. (5.8) [and similarly $M_{\omega/v}(\mathbf{R})$ in Eq. (5.3)] determines the degree of coherence (DOC) of the electron excitation (i.e., the CL emission) relative to the signal originating in the laser (i.e., light scattering). This factor enters Eq. (5.6) through terms proportional to $\mathrm{DOC}(\omega)=|M_{\omega/v}|^2$, where we use the definition of DOC introduced in Ref. 144. Indeed, for $M_{\omega/v}=0$, the scattered light field does not mix at all with the CL emission field, so they are mutually incoherent. In contrast, if $M_{\omega/v}=1$, we have a maximum of coherence, so that the external illumination can fully suppress the CL emission. Specifically, we stress that the point-particle limit of the electron (i.e., $|\psi_0(\mathbf{r})|^2\rightarrow\delta(\mathbf{r})$) produces $M_{\omega/v}=1$, thus recovering the intuitive result for a classical point charge: the radiation from the passage of the electron is a deterministic solution of the Maxwell equations, and thus, it can be suppressed by an external light field with the same frequency-dependent amplitude and an opposite phase. This is not the case in general, so for arbitrarily distributed electron wave functions, the degree of coherence is partially reduced. We also note that the phase of the electron wave function is entirely removed from the coherence factor [see Eq. (5.3)].

We have shown that the CL emission can be modulated by interference with external laser light. As a way to illustrate this effect, we discuss in what follows the maximum achievable minimization of the overall far-field (scattered+emitted) photon intensity by appropriately selecting the external far-field amplitude. If we have complete freedom to choose the external field, we readily find from Eq. (5.6) that $d\Gamma_{\rm rad}/d\omega$ is minimized by taking

$$\mathbf{E}^{\rm ext}(0,\omega)=-M^*_{\omega/v}\mathbf{E}^{\rm el}(\mathbf{R}_0,\omega). \tag{5.9}$$

Alternatively, when one adopts light pulses $\mathbf{E}^{\rm ext}(0,\omega)=f(\omega)\,\mathbf{E}_0$ with a predetermined spectral profile $f(\omega)$ (e.g., a Gaussian $f(\omega)={\rm e}^{-(\omega-\omega_0)^2\sigma_t^2/2}$), the minimization condition at a given sample resonance frequency $\omega=\omega_0$ is readily achieved by setting the field amplitude to $\mathbf{E}_0=-M^*_{\omega_0/v}\mathbf{E}^{\rm el}(\mathbf{R}_0,\omega_0)\,f^*(\omega_0)/|f(\omega_0)|^2$. As an estimate of the laser intensity needed to optimally modulate the CL emission, we take $\left|M_{\omega/v}\right|=1$ and consider the electric field amplitude from Eq. (5.7) for a 100 keV electron passing at a distance R_0 =50 nm (10 nm) away from the dipolar particle, so that, setting $\hbar\omega=1$ eV, we have $|\mathbf{E}^{\rm el}(\mathbf{R}_0,\omega)|\Delta\omega\sim 50$ kV/m (280 kV/m), assuming a depletion bandwidth $\hbar\Delta\omega=0.1$ eV; also, the corresponding laser fluence is $(c/4\pi^2)|\mathbf{E}^{\rm el}(\mathbf{R}_0,\omega)|^2\Delta\omega\sim 10$ nJ/m^2 (400 nJ/m^2).

5.3 Results and discussion

Motivated by potential application of electron beams in controlling the excitations of small elements in a sample (e.g., molecules), we consider a dipolar scatterer as that depicted in Fig. (5.2a), consisting of a 60 nm silicon sphere coated with a silver layer of 5 nm thickness (i.e., an outer radius $a = 35$ nm), which exhibits a spectrally isolated plasmon resonance at a photon energy $\hbar\omega_0 = 1.3$ eV. In practice, we calculate the dipolar polarizability of small spheres from the corresponding electric Mie scattering coefficient as $\alpha = (3/2k^3)t_1^E$ (see Section 1.1). The relatively low level of ohmic losses in silver produces a narrow resonance, with 14% of its FWHM ($\hbar\gamma = 0.013\,\hbar\omega_0 \approx 17$ meV) attributed to radiative losses, as estimated from the ratio (≈ 0.86) of peak absorption to extinction cross sections. Similar dipolar resonances can be found in other types of samples, such as metallic nanoparticles of different morphology[219,220] and dielectric cavities[221], for which we anticipate a variability in their coupling strength to light and electrons that should not however affect the qualitative conclusions of the present work.

In what follows, we consider modulated electrons, focusing on their interaction with a particle under simultaneous laser irradiation. The production of sub-fs-modulated electrons has become practical thanks to PINEM-related advances in ultrafast electron microscopy, whereby an ultrashort laser pulse is used to mould each electron into a train of pulses[75,80,83,119,213,214], from which an individual wavepacket can be extracted by applying a streaking technique[140]. Specifically, we consider either Gaussian electron wavepackets defined by the wave function

$$\psi_{\parallel}(z) = \frac{1}{(2\pi\sigma_t^2 v^2)^{1/4}} \mathrm{e}^{-z^2/4\sigma_t^2 v^2 + \mathrm{i}q_0 z}, \tag{5.10}$$

where the duration is expressed in terms of the standard deviation σ_t of the electron pulse probability density $|\psi_{\parallel}(z)|^2$ and q_0 is the central wave vector, or electrons modulated by PINEM interaction with scattered laser light followed by free-space propagation over a macroscopic distance d before reaching the sampled particle. The wave function of the so modulated electron consists of a Gaussian wavepacket envelope [i.e., Eq. (5.10)] multiplied by an overall modulation factor[33,108]

$$\mathcal{P}_d(\beta, \omega, z) = \sum_{\ell=-\infty}^{\infty} J_\ell(2|\beta|)\, \mathrm{e}^{\mathrm{i}\ell\omega_P(z-z_P)/v - 2\pi\mathrm{i}\ell^2 d/z_T}, \tag{5.11}$$

where ℓ labels a periodic array of energy sidebands separated by the laser photon energy $\hbar\omega_P$; the modulation strength is quantified by a single complex coupling parameter β that is proportional to the laser amplitude and whose phase determines the reference position z_P; and we have introduced a sideband-dependent recoil correction phase $\propto \ell^2$ to account for propagation over d, involving a Talbot distance $z_T = 4\pi m_\mathrm{e} v^3\gamma^3/\hbar\omega_P^2$. These expressions are valid under the assumption that the laser is quasi-monochromatic (i.e, its frequency spread is small compared with ω_P). Then, for an optimum value of d, the factor $\mathcal{P}_d(\beta, \omega, z)$ renders a temporal comb of periodically spaced pulses (time period $2\pi/\omega_P$) that are increasingly compressed as $|\beta|$ is made larger, eventually reaching attosecond duration[75,80,83,119,213,214]. We remark that mutual electron-laser phase coherence can be achieved by using the same laser to both modulate the electron and subsequently

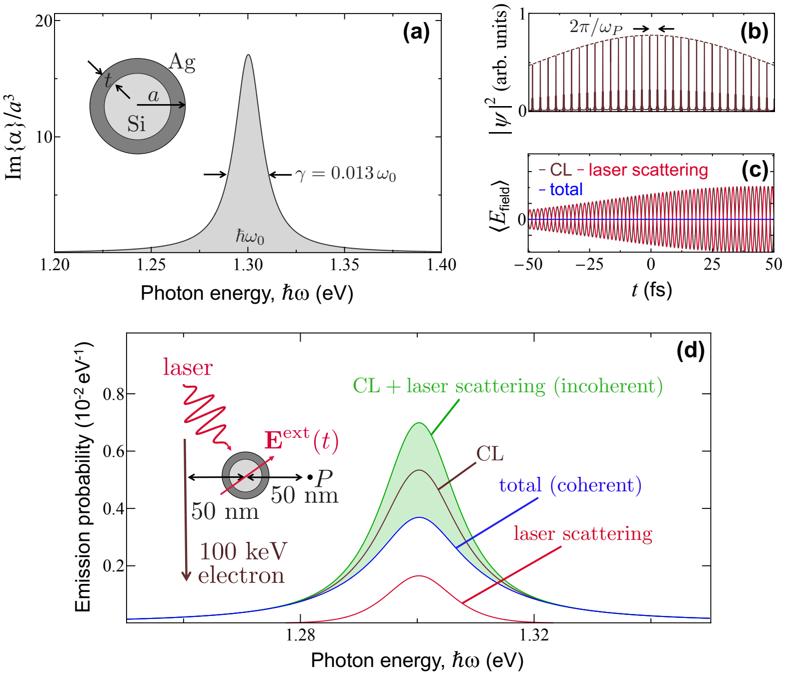

Figure 5.2: Interference between cathodoluminescence and external light scattering. (a) We consider a sample consisting of a small isotropic scatterer described through a frequency-dependent polarizability $\alpha(\omega)$ that is dominated by a single resonance of frequency ω_0 and width γ. For concreteness, we take a nanosphere (see inset) comprising a silicon core (60 nm diameter, $\epsilon = 12$ permittivity) coated with a silver layer (5 nm thickness, permittivity taken from optical data[97]), for which $\hbar\omega_0 = 1.3\,$eV and $\gamma = 0.013\,\omega_0$. In the plot, the polarizability is normalized using the outer particle radius $a = 35\,$nm. (b) Electron density profile of a 100 keV electron Gaussian wavepacket (50 fs standard-deviation duration in probability density) after modulation through PINEM interaction (coupling coefficient $|\beta| = 5$, central laser frequency tuned to $\omega_P = \omega_0$) followed by free propagation over a distance $d = 2.5\,$mm, which produces a train of temporally compressed density pulses. (c) Time dependence of the CL, laser-scattering, and total field amplitudes for the electron in (b) and a laser Gaussian pulse of 50 fs duration in amplitude. The light amplitude is optimized to deplete the CL signal at frequency ω_0. (d) Spectral dependence of the resulting angle-integrated far-field CL (maroon curve), laser-scattering (red curve), and total (blue curve) light intensity for the optimized amplitude of the Gaussian laser pulse. The incoherent sum of CL emission and laser scattering signals is shown for comparison (green curves). The shaded region corresponds to spectra obtained with partially optimized laser pulses. The inset in (d) shows details of the geometry under consideration, also indicating the position P at which the field in (c) is calculated.

interact with the sample. For concreteness, we set the electron energy to 100 keV and tune the PINEM laser frequency to the resonance of the aforementioned sample (i.e., $\hbar\omega_P = \hbar\omega_0 = 1.3\,\text{eV}$). The corresponding Talbot distance is then $z_T \approx 211\,\text{mm}$.

5.3.1 Optical modulation of CL from a dipolar scatterer

An example of PINEM-modulated electron density profile is shown in Fig. (5.2b) for $\sigma_t = 50\,\text{fs}$, $|\beta| = 5$, and $d = 2.5\,\text{mm}$. Direct application of Eq. (5.6) to this electron allows us to calculate the CL emission spectrum, along with its modulation due to interference with light scattering from a phase-locked Gaussian pulse (50 fs duration in field amplitude), as shown in Fig. (5.2d), where the inset depicts further details of the geometrical arrangement and configuration parameters. Starting from the CL spectrum in the absence of external illumination (maroon curve, which we insist is independent of electron wave function profile[33,108,143,144]), we then superimpose the phase-locked laser pulse in which we optimize the light field amplitude $\mathbf{E}_0$ as prescribed above to produce a maximum of depletion in the resulting photon intensity at the peak maximum (blue curve). The achievable depletion is not complete because we have $\text{DOC}(\omega_0) = |M_{\omega_0/v}|^2 \approx 0.31$ for the considered electron, which differs from the limit of perfect coherence (see below), so a fraction of the original CL signal given by $1 - \text{DOC}(\omega_0) \approx 69\%$ remains after complete cancellation of the coherent part. If the electron and light pulses are not phase-locked, relative phase averaging renders $M_{\omega/v} = 0$, so the resulting probability of detecting CL or scattered photons (green curve) is just the incoherent sum of the probabilities associated with these two processes (i.e., the sum of the blue and red curves).

It is instructive to compare the electric near field associated with CL versus light scattering by computing the quantum average of the corresponding field operator $\hat{\mathbf{E}}(\mathbf{r},t)$. Although this quantity is an observable, we note that its measurement is not straightforward. Following the approach explained in the Appendix E and retaining only terms that are linear in the electron current operator $\hat{\mathbf{j}}(\mathbf{r},\omega)$, we find the average field to be given by $\langle\hat{\mathbf{E}}(\mathbf{r},t)\rangle = -2\mathrm{i}\int_{-\infty}^{\infty}\omega\,d\omega\,\mathrm{e}^{-\mathrm{i}\omega t}\int d^3\mathbf{r}'\,G(\mathbf{r},\mathbf{r}',\omega)\cdot\langle\hat{\mathbf{j}}(\mathbf{r}',\omega)\rangle$, which under laser and electron exposure becomes

$$\left\langle\hat{\mathbf{E}}(\mathbf{r},t)\right\rangle = (2\pi)^{-1}\int_{-\infty}^{\infty} d\omega\,\mathrm{e}^{-\mathrm{i}\omega t}\left[\mathbf{E}^{\text{light}}(\mathbf{r},\omega) + \int d^2\mathbf{R}'\,M^*_{\omega/v}(\mathbf{R}')\,\mathbf{E}^{\text{CL}}(\mathbf{r},\mathbf{R}',\omega)\right],$$

where $\mathbf{E}^{\text{CL}}$ is defined in the Appendix E [Eq. (E.9)]. The scattered part of the resulting time-dependent field is plotted in Fig. (5.2c) as calculated from this equation at the position P indicated in the inset of Fig (5.2d). We corroborate that the optimized laser scattering field (red) can be made to cancel the CL field (blue), therefore producing a nearly vanishing total field (blue) that is consistent with the depletion of CL observed in Fig. (5.2d). It is important to stress that the average of the electric field amplitude cancels, while non-vanishing fluctuations give rise to the incoherent part of the emission, which is not suppressed.

5.3.2 CL modulation for gaussian electrons

In Fig. (5.3), we consider an electron prepared in a Gaussian wavepacket with standard-deviation duration σ_t of either 0.3 fs or 0.9 fs [Fig. (5.3a)]. These values are consistent

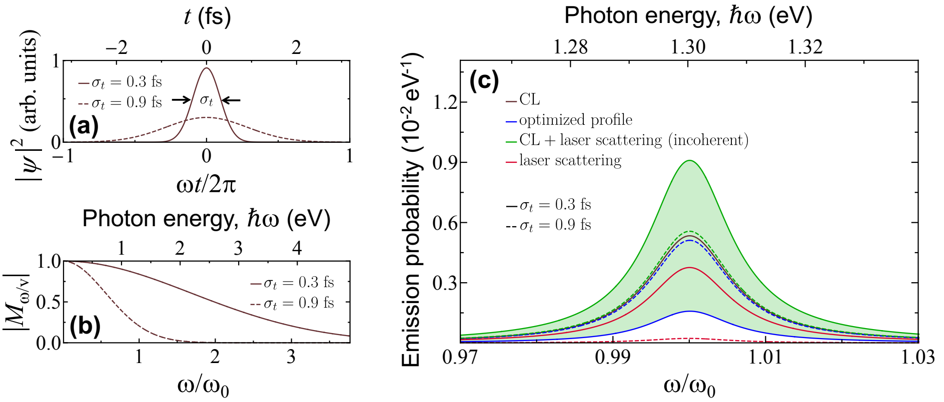

Figure 5.3: Modulation of the CL emission by Gaussian electron and laser pulses. (a) Gaussian electron wavepackets of 0.3 fs and 0.9 fs duration. (b) Frequency dependence of the electron coherence factor $M_{\omega/v}$ (Fourier transform of the profiles in (a)). (c) Angle-integrated CL, laser scattering, and total far-field photon intensity using the electron pulses in (a), the same particle and geometrical configuration as in Fig. (5.2), and an optimized spectral profile of laser field amplitude. We also show the incoherent sum of CL emission and laser scattering signals for comparison (green curve).

with those achieved in recent experiments[140]. The corresponding coherence factor $M_{\omega/v} = \mathrm{e}^{-\omega^2\sigma_t^2/2}$ [Fig. (5.3b), as calculated from Eqs. (5.8) and (5.10)] quickly dies off as the electron pulse duration exceeds the optical period $2\pi/\omega$ of the targeted excitation. In the point-electron limit ($\sigma_t \to 0$), full coherence is obtained in accordance with the intuitive picture that the electron then generates a classical field that is well described by the solution of Maxwell's equations for a classical external source. The corresponding CL emission probability [Fig. (5.3c), maroon curve] is again independent of electron wave function, while maximal depletion can be obtained upon sample irradiation with an optimum spectral profile of the external field amplitude [Eq. (5.9)], so that only a fraction $1 - |M_{\omega/v}|^2$ of the CL emission remains [see Eq. (5.6)]. Consequently, the level of depletion depends dramatically on pulse duration, as illustrated by comparing solid and dashed curves in Fig. (5.3c).

5.3.3 CL modulation for PINEM-compressed electrons

The wave function of a PINEM-modulated electron at the sample interaction region is given by the product of Eqs. (5.10) and (5.11) when using a quasi-monochromatic laser. The corresponding coherence factor can be calculated from Eq. (5.8), and reads

$$M_{\omega/v} = \sum_{\ell\ell'} \mathrm{e}^{-\frac{\sigma_t^2}{2}[(\ell-\ell')\omega_P+\omega]^2} J_\ell(2|\beta|) J_{\ell'}(2|\beta|)\, \mathrm{e}^{\mathrm{i}(\ell'-\ell)\frac{\omega_P z_P}{v}+2\pi\mathrm{i}(\ell'^2-\ell^2)\frac{d}{z_T}}, \tag{5.12}$$

which we evaluate numerically for finite σ_t. In the $\omega_P\sigma_t \gg 1$ limit, $M_{\omega/v}$ takes negligible values unless the excitation frequency is a multiple of the PINEM laser frequency (i.e.,

$\omega = m\omega_P$). Then, only $\ell' = \ell + m$ terms contribute to the above sum, which reduces to

$$M_{\omega/v} = \mathrm{e}^{\mathrm{i}m\omega_P z_P/v + 2\pi \mathrm{i}m^2 d/z_T} \sum_{\ell} J_\ell(2|\beta|) J_{\ell+m}(2|\beta|)\, \mathrm{e}^{4\pi \mathrm{i}m\ell d/z_T} \tag{5.13}$$

and using Graf's addition theorem[13], we have $|M_{\omega/v}| = |J_m[4|\beta|\sin(2\pi m d/z_T)]|$[217]. Equation (5.12) is a function of the PINEM coupling coefficient β, the free propagation distance d, the excitation frequency ω, the electron velocity v, and a slowly varying envelope profile of width σ_t. In addition, for $\omega\sigma_t \gg 1$, which is reached in practice for instance with $\sigma_t \sim 2\,$fs for sample excitations of $\hbar\omega = 1.3\,$eV energy, we can use Eq. (5.13) to generate the universal plot for $|M_{\omega/v}|$ shown in Fig. (5.4a), where the dependence on ω, d, and v is fully encapsulated in the d/z_T ratio, using the Talbot distance z_T defined above. Importantly, we find a region of maximum coherence (blue contour) in which $|M_{\omega/v}| \approx 0.582$, and therefore, the fraction of excitations produced by the electron that are coherent with respect to the external phase-locked laser is limited to $\mathrm{DOC}(\omega) = |M_{\omega/v}|^2 \leq 34\%$. This maximum value can be reached for coupling parameters $|\beta| \geq 0.46$, while the corresponding free-propagation distance d can be controlled by changing the modulating laser intensity. We note that the d position at which maximum coherence is found does not coincide with that of maximal temporal compression of the electron pulse train due to a substantial electron probability density remaining in the region between consecutive peaks[108].

In Fig. (5.4b), we consider a dipolar scatter with a broad spectral response to better illustrate the optically driven depletion of CL for PINEM-compressed electrons. In particular, we take a 160 nm Pt spherical particle, which produces a wide CL emission peak (maroon curve). For comparison, we show the depletion obtained under optimized laser irradiation [i.e., with the external light field amplitude given in Eq. (5.9)] for a Gaussian electron wavepacket of 0.3 fs duration [Fig. (5.4b), dashed curve], showing a stronger effect at lower photon energies in accordance with Fig. (5.3b). In contrast, for a nearly-optimum PINEM-modulated electron [the same as in Fig. (5.2b)], we find instead discrete depletion features, corresponding to the PINEM energy ω_P (i.e., $\hbar\omega_P = 1.3\,$eV in this case) and its harmonics $\omega = m\omega_P$ [only $m = 1$ and 2 peaks are visible in the solid and dotted curves of Fig. (5.4b)]. We note that the leftmost depletion does not reach as deep as that produced by the Gaussian wavepacket electron, whereas the second one has nearly the same magnitude. In the $\omega\sigma_t \gg 1$ limit, the depletion observed at the excitation frequencies $\omega = m\omega_P$ is equally ruled by universal behaviors of $M_{\omega/v}$ analogous to that in Fig. (5.4a), showing a similar dependence on β and d, but with an increasingly reduced magnitude as the harmonic order m is increased. When the envelope of the PINEM-modulated electron is reduced from 50 fs (solid blue curved) to 10 fs (dotted curve), the depletion features are broadened, but their depth is maintained, directly mimicking the behavior of $\mathrm{DOC}(\omega)$. In other words, shorter electron pulses allow us to suppress a larger fraction of the CL power, and of course, this suppression requires illuminating the sample with a synchronized, amplitude-optimized laser that covers the range of sampled excitation frequencies ω.

5.3.4 Temporal control of the emission

The studied CL modulation strongly depends on the timing between the laser and electron interactions with the sampled structure, as illustrated in Fig. (5.5). To elaborate on this

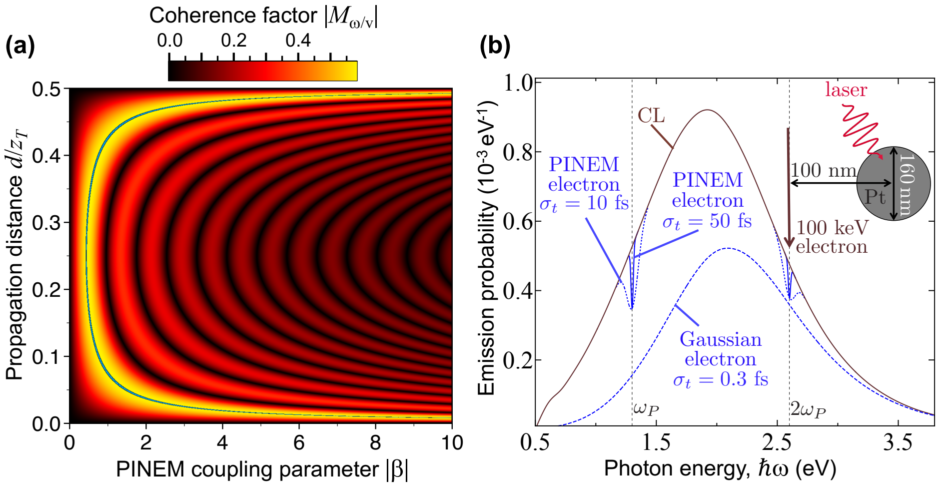

Figure 5.4: Coherence factor of PINEM-modulated electrons. (a) We show the coherence factor $|M_{\omega/v}|$ for modulated electrons in the limit of long pulse duration ($\omega\sigma_t \gg 1$) as a function of the PINEM coupling parameter β and free propagation distance d. This function is periodic along d with a period given by half the Talbot distance z_T. Additionally, $|M_{\omega/v}|$ presents an absolute maximum of $\approx\ 0.582$ along the blue contour superimposed on the density plot. (b) Unperturbed (maroon curve) and optically depleted (blue curves) CL spectra from a 160 nm Pt spherical particle and electrons prepared in Gaussian wavepacket (dashed blue curve, $\sigma_t = 0.3$ fs) or PINEM-modulated (solid and dotted blue curves obtained with $|\beta| = 5$ and either $\sigma_t = 50$ fs or $\sigma_t = 10$ fs, see labels) states. The inset shows the geometrical arrangement and parameters. The laser amplitude is taken to be optimized for all emission frequencies.

point, we reduce the number of parameters by considering electron wavepackets with a Gaussian profile (i.e., without an additional PINEM modulation) and vary their temporal delay relative to laser pulses [see sketch in Fig. (5.5a)], using the same standard deviation duration $\sigma_t = 10$ fs both for the electron probability density and for the light field amplitude. We consider the same particle as in Fig. (5.1) and integrate the CL signal over frequency to cover the resonance region. The result is plotted in Fig. (5.5b). For optimal CL suppression, the polarization induced in the particle by the electron and the laser must have overlapping envelopes with a temporal delay precision well below an optical cycle. For finite delay, we show that the interference signal oscillates as a function of τ with a period that coincides with the resonance optical period $2\pi/\omega_0$. Additionally, the amplitude of these oscillations is effectively attenuated by a factor $e^{-\gamma|\tau|/2}$ away from zero delay; this attenuation takes place at a pace that is half of the resonance decay rate γ because interference is governed by the resonance amplitude rather than the intensity.

5.3.5 Energy pathways

Within the formalism developed in Appendix E, we obtain the partial probabilities for processes associated with energy changes in the electron ($\Gamma_{\rm el}$) and emission of radiation along forward ($\Gamma_{\rm forward}$). On the contrary, the distributions associated with the accumulated excitations and subsequent decays of the particle mode ($\Gamma_{\rm decay}$) and with the inelastic absorption events ($\Gamma_{\rm abs}=\Gamma_{\rm decay}-\Gamma_{\rm rad}$) are evaluated by means of a density matrix formalism reported in Section E.5. The combination of the two analyses leads to the following expressions for the corresponding frequency-resolved probabilities:

$$\frac{d\Gamma_{\rm el}}{d\omega}=-\frac{1}{\pi\hbar}\,{\rm Im}\Big\{\alpha(\omega)\,\mathbf{E}^{\rm ext}(0,\omega)\cdot\mathbf{E}^{\rm el*}(\mathbf{R}_0,\omega)\,M_{\omega/v}\Big\} \qquad (5.14a)$$

$$-\frac{1}{\pi\hbar}\,\left|\mathbf{E}^{\rm el}(\mathbf{R}_0,\omega)\right|^2\,{\rm Im}\left\{\alpha(\omega)\right\},$$

$$\frac{d\Gamma_{\rm decay}}{d\omega}=\frac{1}{\pi\hbar}\,{\rm Im}\{\alpha(\omega)\}\,\Big[|\mathbf{E}^{\rm ext}(0,\omega)|^2+|\mathbf{E}^{\rm el}(\mathbf{R}_0,\omega)|^2 \qquad (5.14b)$$

$$+\,2\,{\rm Re}\Big\{\mathbf{E}^{\rm ext}(0,\omega)\cdot\mathbf{E}^{\rm el*}(\mathbf{R}_0,\omega)M_{\omega/v}\Big\}\Big],$$

$$\frac{d\Gamma_{\rm forward}}{d\omega}=-\frac{1}{\pi\hbar}\,{\rm Im}\Big\{\alpha(\omega)\,\mathbf{E}^{\rm ext*}(0,\omega)\cdot[\mathbf{E}^{\rm ext}(0,\omega)+\mathbf{E}^{\rm el}(\mathbf{R}_0,\omega)M^*_{\omega/v}]\Big\}. \qquad (5.14c)$$

Importantly, the probabilities in Eqs. (5.14) satisfy the energy-conservation condition

$$\frac{d\Gamma_{\rm el}}{d\omega}+\frac{d\Gamma_{\rm decay}}{d\omega}+\frac{d\Gamma_{\rm forward}}{d\omega}=0. \qquad (5.15)$$

We interpret $\Gamma_{\rm forward}$ as the change in photon forward emission (i.e., toward the direction of propagation of the incident light beam) associated with interference between emitted and externally incident photons (i.e., the type of stimulated process that is neglected in the non-forward far-field radiation probability $\Gamma_{\rm rad}$). In particular, the first term inside the squared brackets of Eq. (5.14c) agrees with the depletion of the incident light that is described by the optical theorem[3] (i.e., $(1/\pi\hbar){\rm Im}\{\alpha(\omega)\}\,|\mathbf{E}^{\rm ext}(0,\omega)|^2=\sigma_{\rm ext}(\omega)I(\omega)/\hbar\omega$, where $\sigma_{\rm ext}(\omega)=(4\pi\omega/c){\rm Im}\{\alpha(\omega)\}$ is the extinction cross section and $I(\omega)=(c/4\pi^2)|\mathbf{E}^{\rm ext}(0,\omega)|^2$ is the light intensity per unit frequency), whereas the remaining term originates in electron-light interference. The probabilities given above are derived for isotropic dipolar particles, but a similar analysis leads to expressions corresponding to a particle characterized by a polarizability tensor $\alpha(\omega)\,\hat{\mathbf{u}}\otimes\hat{\mathbf{u}}$ (i.e., linear induced polarization along a certain direction $\hat{\mathbf{u}}$), for which the partial probabilities are given by Eqs. (5.6) and (5.14) by substituting $\mathbf{E}^{\rm ext}$ and $\mathbf{E}^{\rm el}$ by $\hat{\mathbf{u}}\cdot\mathbf{E}^{\rm ext}$ and $\hat{\mathbf{u}}\cdot\mathbf{E}^{\rm el}$, respectively.

We explore the aforementioned energy pathways in Fig. (5.5b-e), where we plot the frequency-integrated probabilities $\Gamma_{\rm rad}$, $\Gamma_{\rm forward}$, $\Gamma_{\rm decay}$, and $\Gamma_{\rm el}$, respectively, as a function of electron-light pulse delay τ. We find that the decay probability follows a similar symmetric profile as the radiative emission [cf. panels (b) and (d), both of them independent of the sign of τ. In contrast, the electron energy-change probability [Fig. 5.5e)] is markedly asymmetric [and so is the forward-emission probability [Fig. 5.5c)] as a result of energy conservation via Eq. (5.15)]: we find the intuitive result that the electron energy remains nearly unmodulated if the electron arrives before the optical pulse, while the opposite is true for the forward light emission component.

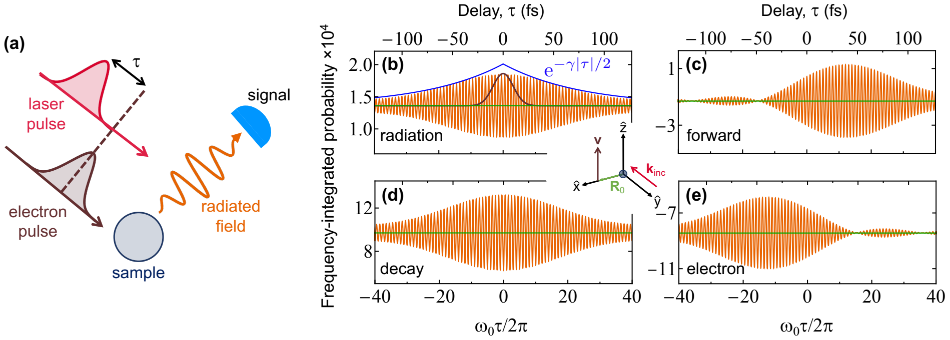

Figure 5.5: Control of the far-field photon intensity and energy pathways through the electron-laser temporal delay. (a) We consider the same configuration as in Fig. (5.2), using electron and laser Gaussian pulses that act on the sample with a relative time delay τ. (b) Angle- and frequency-integrated photon intensity (orange, in units of photons per electron), showing oscillations of period $2\pi/\omega_0$ as a function of τ, as calculated for 100 keV electrons, 10 fs Gaussian pulse durations (i.e., $f(\omega) = \mathrm{e}^{-(\omega-\omega_0)^2\sigma_t^2/2}$, see black profile for comparison, referring to the standard deviation of the electron density profile and the laser field amplitude), and the same particle as in Fig. (5.2a). The interference attenuation for $\gamma\tau \gg 1$ is indicated by the blue curve, where γ is the decay rate of the sampled resonance. The laser field amplitude is fixed to $(1.4\, e\omega_0/v^2\gamma)\, f(\omega)$ and contained within the plane of the figure. (c-e) Frequency-integrated probability associated with additional energy pathways: laser-stimulated forward scattering (c), total decay following excitation of the particle plasmon (d), and change in the electron energy (e). Calculations in (b-e) correspond to the orientations of the light (incident wave vector $\mathbf{k}_{\mathrm{inc}}$) and the electron (velocity $\mathbf{v}$) shown in the central inset.

5.4 Concluding remarks

Electron-beam-based spectroscopy techniques provide unrivalled spatial resolution for imaging sample excitations by measuring electron energy losses (EELS) or light emission (CL) associated with them. In this study, we propose the opposite approach: suppression of sample excitations produced by free electrons through combining them with mutually coherent laser irradiation. Indeed, our first-principles theory confirms that electrons and light can both be treated as mutually coherent tools for producing optical excitations. They form a synergetic team that combines optical spectral selectivity with the high spatial precision of electron beams. In contrast to EELS, where free electrons act as a broadband electromagnetic source, so that only a posteriori selection of specific mode frequencies is performed by spectrally resolving the inelastically scattered probes, the methods here explored allow us to target designated mode frequencies with sub-Ångstrom control over the excitation process. In addition, the excitation of on-demand nanoscale optical modes through the combined use of modulated electrons and tailored light pulses is amenable to the implementation of coherent control schemes[222,223] for the optimization of the desired effects on the specimen.

From a practical viewpoint, PINEM interaction provides a way of moulding the electron wave function to produce the temporally compressed pulses that are required to address specific sample frequencies. However, this method has a limited degree of achievable coherence in the electron-driven excitation process when using quasi-monochromatic light, quantified through the degree of coherence[144] $0 < \mathrm{DOC}(\omega) = |M_{\omega/v}|^2 \leq 1$; more precisely, it can produce values $\mathrm{DOC}(\omega) \lesssim 34\%$, as we show above. We remark that the frequency-dependent function $\mathrm{DOC}(\omega)$ is a property of the electron: this function is univocally determined by the probability density profile. Full coherence at a frequency ω, corresponding to the $\mathrm{DOC}(\omega) \to 1$ limit, can be delivered by δ-function-like combs of electron pulses (i.e., for an electron probability density $|\psi(z)|^2 \approx \sum_m b_m\, \delta(z - 2\pi m v/\omega)$ along the beam[33], with arbitrary coefficients b_m, including single pulses for $b_m = \delta_{m,0}$), the synthesis of which emerges as a challenge for future research.

By putting free electrons and light on a common basis as tools for creating excitations in a specimen, one could additionally envision the combined effect of multiple electron and laser pulses, which would increase the overall probability of exciting an optical mode, provided that their interactions take place within a small time interval compared with the mode lifetime. This idea capitalizes on the concept of superradiance produced by PINEM-modulated electrons[215], which our first-principles theory supports for probing and manipulating nanoscale excitations including the extra degrees of freedom brought by synchronized light and electron probes.

We remark that CL is just one instance of sample excitation, but the present study can be straightforwardly extended to optically bright modes in general (see independent analysis in Ref. 33), including two-level resonances of different multipolar character. A key ingredient of our work is the use of dimmed illumination, so that the weak probability amplitude that the electron typically imprints on the sample has a magnitude that is commensurate with the effect of the external light. Because the measurement is performed once interference between electron- and light-driven excitation amplitudes takes place (i.e., at the far-field photospectrometer in CL, or by the effect of any subsequent inelastic process following the decay of the excited sample mode in general), the studied electron-light mutual coherence is unaffected by additional sources of shot noise other than the intrinsic ones associated with the detection process (e.g., like in conventional CL).

Our prediction of unity-order effects in the modulation of electron-sample interactions through the use of external light enables applications in the manipulation of optical excitations at the atomic scale. Additionally, it suggests an alternative approach to damage-free sensing, whereby the spectral response of a specimen could be monitored through the modulation produced by the combined action of light and electrons, involving a reduced level of sample exposure to electrons because the targeted interference is proportional to the polarization amplitudes that they induce, so the outcome of a weak electron interaction could be amplified by applying a lock-in technique to the laser. This approach could be useful for imaging biomolecules, as well as strongly correlated materials in which probing without invasively perturbing the system is essential and remains a challenge in the exploration of spin and electronic ultrafast dynamics. Besides the experimental configuration proposed in Fig. (5.1), one could alternatively flip the semitransparent mirror horizontally to mix the external laser light with the CL emission at the detector instead of undergoing scattering at the specimen.

We find it interesting the possibility of adjusting the amplitude of the external light field, for example through a temporal light shaper, to determine the frequency-dependent magnitude and phase of the CL amplitude field ($\mathbf{f}^{\mathrm{CL}}_{\hat{\mathbf{r}}}(\mathbf{R},\omega)$ in our formalism), thus providing temporal resolution when probing the specimen by direct Fourier transformation of this quantity. This method could yield a time resolution limited by the width of the frequency window in the CL measurement at the spectrometer, without affecting the intrinsic temporal resolution associated with the short duration of electron and light pulses, and likewise, retaining the sub-Ågnstrom spatial resolution associated with tightly focused electron beams. In a related direction, spatial light modulation and raster scanning of the electron beam could also be employed to gain further insight into the symmetry and nanoscale spatial dependence of the sample response. Additionally, for a sample in which $\mathbf{f}_{\hat{\mathbf{r}}}^{\rm CL}(\mathbf{R},\omega)$ is well characterized (e.g., a dielectric sphere[221]), the modulation of CL by varying the external field could be used to resolve the coherence factor $M_{\omega/v}$, thus allowing us to retrieve the electron density profile from the Fourier transform of this quantity. Besides far-field optical measurements, the present analysis can also be extended to alternative ways of probing optical excitations that are coherently created by light and electrons, such as electrical or acoustic detection of the modifications produced in the specimen.

6

An image interaction approach to quantum-phase engineering of two-dimensional materials

An expert is a person who has made all the mistakes that can be made in a very narrow field.
Niels Bohr

In this chapter, we theoretically show that electrons in a semiconductor atomic monolayer acquire a quantum phase χ analogous to that studied in Chapter 4 and resulting from the image potential induced by the presence of a neighboring periodic array of conducting ribbons, which in turn modifies the optical, electrical, and thermal properties of the monolayer, expressed in terms of additional interband optical absorption, plasmon hybridization, and metal-insulator transitions. What follows is based on a published work, Ref. 224.

6.1 Introduction

At the heart of condensed-matter physics is the drive to manipulate materials in a purposeful fashion to improve or enable functionalities. To that end, the sustained advances in fabrication capabilities along with the continuous emergence of novel material platforms have together fuelled the field over the past half-century. Moreover, when suitably engineered, nanostructured materials can generally exhibit new properties beyond those found in their native, bulk form. A paradigmatic example that benefited from such approach was the development of semiconductor devices [225,226], whose electronic properties were controlled by modifying the band structure through, for example, spatially patterning their compositional or doping characteristics [226–231].

With the advent of 2D and atomically thin materials [232–235], those ideas were swiftly transferred to this arena as well, leading to the realization of 2D superlattices that incorporated not only vertical stacks, but also laterally assembled heterostructures [236–241], as well as electrically modulated graphene [242,243], artificial graphene [244,245], and optical near-field dressing through periodic patterning of the supporting dielectric substrate [246]. More recently, similar band structure engineering concepts have been explored to create moiré superlattices [236,247–250] and moiré excitons [251–253], and also to investigate topological phenomena [254–257]. However, these approaches are generally invasive, as they require physical material nanostructuring or the injection of charge carriers. Now, the question arises, can a more gentle engineering of a 2D material be realized without structural modifications or exposure to external fields?

In this chapter, we introduce a disruptive approach for tailoring the electrical, optical, and thermal properties of 2D materials based on the manipulation of their electronic band structures by means of the gate-free, noncontact image-potential interaction experienced by the material's electrons in the presence of a neutral neighboring structure [see Fig. (6.1)]. Indeed, when a charged particle (e.g., an electron in the 2D material) is placed near an interface, an image potential is induced that affects the particle dynamics. For free electrons, the image interaction is tantamount to the position-dependent Aharonov–Bohm quantum phase (Q-phase) imprinted on their wave functions by the self-induced electromagnetic fields in the vicinity of the interface (see Chapter 4) Likewise, valence and conduction electrons in a material should acquire a Q-phase that depends on the geometrical and compositional details of the environment. This phase is expected to modify the electronic energy bands and, consequently, the dynamical response and transport properties of the hosting material as well. In reference to the origin of these modifications, hereinafter we refer to such 2D-material-based configurations as Q-phase materials.

Here, we introduce a specific realization of Q-phase materials consisting of a 2D semiconductor that is modified by the presence of a one-dimensional (1D) periodic array of ribbons. Specifically, we demonstrate that the periodic image potential produced by this pattern on the semiconductor electrons gives rise to substantial modifications in its band structure that translate into changes in the optical, electrical, and thermal properties, which are controlled by purely geometrical parameters [the separation and period of the array, see Fig. (6.1)]. We present rigorous theoretical calculations of the self-consistent electronic band structure, the ensuing optical response, and the electrical and thermal conductivities, all of which reveal dramatic modulations due to the aforementioned image

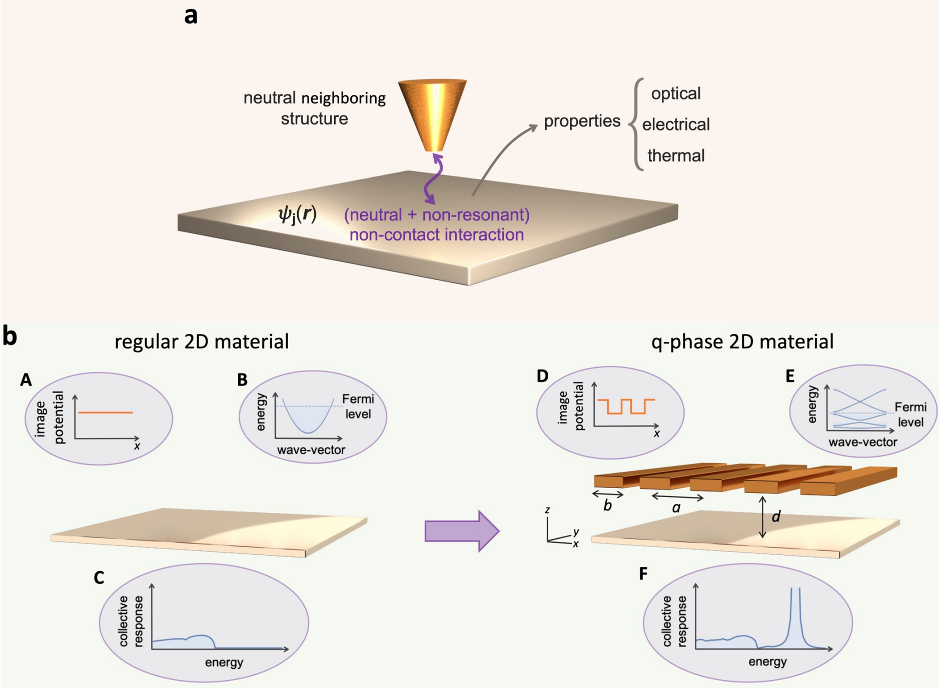

Figure 6.1: Realization of a quantum-phase (Q-phase) material. (a) Sketch of the noncontact interaction between a 2D material and a neighboring structure. The image potential experienced by conduction electrons in the material imprints a Q-phase on their wave functions $\psi_j(\mathbf{r})$ that in turn changes the optical, electrical, and thermal transport properties. (b) Possible realization of a Q-phase material. In the absence of an additional structure, there is no image interaction (A), so conduction electrons exhibit a characteristic parabolic dispersion (B), leading to a collective response function like that of a 2DEG (C). An image potential landscape (D) is produced by introducing a neighboring neutral structure (a periodic array of conducting ribbons of period a, width b, and separation d). The electron wave functions then acquire a Q-phase that reshapes the band structure, opening gaps (E) and enabling additional electronic transitions that translated into modifications of the material properties (F).

interaction. More precisely, we predict the opening of electronic gaps, which enable interband optical transitions and hybrid plasmon-interband modes that are otherwise optically forbidden in the absence of the image interaction. In addition, we observe a metal-insulator transition as the pattern is brought closer to the semiconductor and the image interaction increases, essentially reflecting a reduction in carrier propagation induced by the periodic patterning. This also affects the thermal conductivity, which we predict to undergo a corresponding conductor-insulator transition. Importantly, the image interaction is long-range and nonresonant, so this method can be generally applied to any 2D material, adding a brand new tool to design nanodevices.

6.2 Results

6.2.1 Theoretical framework

We consider an atomically thin semiconductor of area L^2, doped to a Fermi level E_{F}^0 (corresponding to a carrier density n_0 in the conduction band), and lying in the $z=0$ plane at a distance $d>0$ from a 1D periodic array of conductive ribbons [period a, width b, see Fig. 6.1b]. The latter are taken to be infinitely extended along the y direction, periodic along x, and made of a material with a high DC conductivity and low infrared absorbance (e.g., indium tin oxide[258]), so that it behaves as a perfect conductor with regards to the determination of the equilibrium configuration of the electronic structure in the semiconductor. A patterned and doped semiconductor monolayer with a partially filled conduction band could serve this purpose. We further consider the periodic array to be embedded in a medium of permittivity ϵ matching that of the ribbon material at the optical frequencies discussed below, such that the array appears to be invisible. The semiconductor electrons can however interact with the array through a image potential energy $-V_0$[259–261], which for distances $d \gtrsim 1\,\mathrm{nm}$ can be well approximated by the local electrostatic limit[262–264] (i.e., $V_0=e^2/4\epsilon d$). Incidentally, films consisting of three atomic layers of hexagonal boron nitride are now commonly used to introduce a dielectric spacing of $\sim 1\,\mathrm{nm}$ in 2D material heterostructures[265], but other materials amenable to exfoliation down to a few monolayers could also be employed for that purpose, as well as atomic layer deposition[173] methods. Neglecting ribbon edge effects by assuming $d \ll a$, we describe the image interaction of each semiconductor electron through the periodic stepwise energy function $V^{\mathrm{im}}(x)=-V_0 p(x)$, where $p(x)=1$ for x directly below a ribbon and $p(x)=0$ otherwise. In this work, we set $\epsilon=1$ for simplicity and remark that the image potential is the result of the Q-phase introduced in the electron wave functions due to their interaction with the surrounding patterned structure, as illustrated for free electrons moving near a material surface[148].

We describe the semiconductor electrons in the single-particle approximation[61], and further consider them to be strongly confined to an atomic layer of small thickness compared with the separation d from the conductive ribbons. This allows us to factorize the one-electron wave functions as $\psi_{\mathbf{k}n}(\mathbf{r}) = \psi_{\mathbf{k}_\parallel n}(\mathbf{R})\psi_\perp(z)$, with out-of-plane components yielding a probability density profile $|\psi_\perp(z)|^2 \approx \delta(z)$. The remaining in-plane components depend on $\mathbf{R}=(x,y)$ and are determined by the self-consistent equation[61]

$$\left[\mathcal{H}^0+V^{\mathrm{im}}+V^{\mathrm{H}}\right]\psi_{\mathbf{k}_\parallel n}(\mathbf{R}) = \hbar\varepsilon_{\mathbf{k}_\parallel n}\psi_{\mathbf{k}_\parallel n}(\mathbf{R}), \tag{6.1}$$

where $\mathcal{H}^0 = -\hbar^2\nabla^2_{\mathbf{R}}/2m^*$ is the unperturbed electron Hamiltonian, m^* denotes the effective mass, $V^{\rm im}$ is the aforementioned image potential, and $V^{\rm H}$ is the Hartree potential of Eq. (1.66).

The numerical solution of the eigenvalue problem

We note that Eq. (6.1) can be solved by factorizing the one-electron wave functions as $\psi_{\mathbf{k}_\parallel n}(\mathbf{R}) = \psi_{k_x n}(x)\varphi_{k_y}(y)$, leading to

$$\left(\frac{\hbar^2}{2m^*}\partial_y^2 + \hbar\varepsilon^y_{k_y n}\right)\phi_{k_y}(y) = 0, \tag{6.2a}$$

$$\left[\frac{\hbar^2}{2m^*}(k_x - {\rm i}\partial_x)^2 + V_{\rm im}(x) + V_{\rm H}(x) - \hbar\varepsilon^y_{k_x n}\right]u_{k_x n}(x) = 0, \tag{6.2b}$$

where we have used Bloch's theorem to express $\psi_{k_x n}(x) = {\rm e}^{{\rm i}k_x x}u_{k_x n}(x)/\sqrt{L}$ in terms of a periodic function $u_{k_x n}(x)$ with the same period a as the ribbon array. From Eq. (6.2a), the component along the direction of translational invariance admits plane-wave solutions $\phi_{k_y}(y) = {\rm e}^{{\rm i}k_y y}/\sqrt{L}$ with parabolic dispersion. In the remaining in-plane direction, Eq. (6.2b) transforms into an eigenvalue problem by expanding $u_{k_x n}(x) = \sum_G {\rm e}^{{\rm i}Gx}u_{k_x n,G}$ as a sum over reciprocal lattice vectors G (multiples of $2\pi/a$). More precisely, Eq. (6.2b) becomes

$$\left[\frac{\hbar^2}{2m^*}(k_x + G)^2 - \hbar\varepsilon^x_{k_x n}\right]u_{k_x n,G} + \sum_{G'}\left(V^{\rm im}_{G-G'} + V^{\rm H}_{G-G'}\right)u_{k_x n,G'} = 0, \tag{6.3}$$

where $V^{\rm im}_G = {\rm i}\left(V_0/aG\right)\left[1 - {\rm e}^{-{\rm i}Gb}\right]$ and $V^{\rm H}_G = 2\pi e^2(1-\delta_{G,0})n_G/|G|$ are the Fourier components of the image and Hartree potentials [see Appendix F for the evaluation of the Hartree potential in reciprocal space]. We solve Eq. (6.3) iteratively by calculating the components of the electron density $n_G = (2/a)\int_0^a dx\, {\rm e}^{-{\rm i}Gx}\sum_{\mathbf{k}_\parallel n} f_{\mathbf{k}_\parallel n}|\psi_{\mathbf{k}_\parallel n}(\mathbf{R})|^2$ calculated from the (spin-degerate) electron wave functions and the Fermi-Dirac distribution $f_{\mathbf{k}_\parallel n}$ (e.g., $f_{\mathbf{k}_\parallel n} = \theta(E_{\rm F} - \hbar\varepsilon_{\mathbf{k}_\parallel n})$ at $T=0$) at every step and adjusting the Fermi energy $E_{\rm F}$ to meet the condition that $n_{G=0}$ is equal to the unperturbed electron density n_0.

Summarizing, the electron eigenstates and spectrum, labeled by the in-plane wave vector $\mathbf{k}_\parallel$ and the band index n, such that $\psi_{\mathbf{k}_\parallel n}(\mathbf{R}) = {\rm e}^{{\rm i}\mathbf{k}_\parallel\cdot\mathbf{R}}u_{\mathbf{k}_\parallel n}(\mathbf{R})/L$, where $u_{\mathbf{k}_\parallel n}(\mathbf{R}) = u_{\mathbf{k}_\parallel n}(\mathbf{R} + \ell a\hat{\mathbf{x}})$ for any integer ℓ, assume the form

$$\psi_{\mathbf{k}_\parallel n}(\mathbf{R}) = {\rm e}^{{\rm i}\mathbf{k}_\parallel\cdot\mathbf{R}}u_{k_x n}(x)/L, \tag{6.4a}$$

$$\varepsilon_{\mathbf{k}_\parallel n} = \varepsilon^x_{k_x n} + \hbar k_y^2/2m^*, \tag{6.4b}$$

and are found from Eq. (6.1) by means of an iterative method. Importantly during the application of such method, we assume the semiconductor to remain electrically neutral in its environment, so that no charge imbalance is introduced by doping. Then, the charge neutrality condition $\int d^2\mathbf{R}\,\left[n(\mathbf{R}) - n_0\right] = 0$ needs to hold at every iteration step and is used to determine the Fermi energy $E_{\rm F}$, which generally deviates from the value $E^0_{\rm F}$ in the homogeneous semiconductor (i.e., in the absence of image interaction). Incidentally, we note that the parabolic band assumed to describe the unperturbed conduction band of

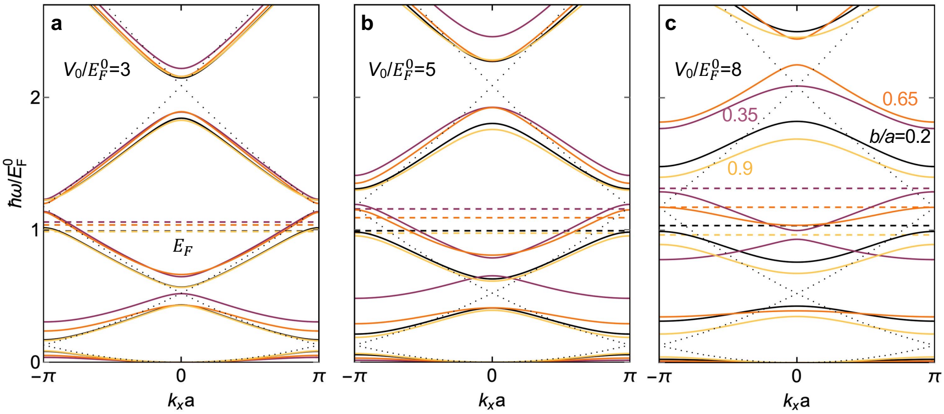

Figure 6.2: Modulation of the electronic band structure for different patterning ratios b/a. We plot the electronic bands (solid curves) in the direction of periodic patterning for different values of b/a (see color-matched labels). Results are presented for $V_0/E_\mathrm{F}^0 = 3$ (a), $V_0/E_\mathrm{F}^0 = 5$ (b), and $V_0/E_\mathrm{F}^0 = 8$ (c), along with the corresponding normalized Fermi energies (dashed lines). Dotted curves stand for the 2DEG limit.

the doped semiconductor should be an excellent approximation because the patterning period a exceeds by several orders of magnitude the interatomic distance, thus leading to a comparatively small 1D 1BZ of extension $\sim 1/a$.

6.2.2 Modulation of the electronic band structure

Once the conducting ribbons are brought close to the semiconductor, electrons in the latter are no longer free to move along the patterning direction x because they are modulated by the self-induced potential resulting from the image interaction. In particular, the electronic band structure is modified by the emergence of band gaps at the center and edges of the 1BZ [see Fig. 6.2a)], which also imply changes in the electron velocity component $\partial_{k_x}\varepsilon^x_{k_x n} \equiv v_{k_x n}$ and the effective mass. We note that the normalized band energies $\hbar\varepsilon^x_{k_x n}/E_\mathrm{F}^0$ and the dimensionless eigenvectors $a\psi_{\mathbf{k}_\parallel n}(\mathbf{R}/a)$ depend only on four independent parameters: (i) the geometrical ratio b/a [see Fig. 6.1b], which regulates the tunneling rate across barriers introduced by the image potential; (ii) the size of the 1BZ $k_\mathrm{BZ} = \pi/a$ relative to the unperturbed Fermi wave vector (i.e., $k_\mathrm{BZ}/k_\mathrm{F}^0$); (iii) the strength of the image energy relative to the unperturbed Fermi energy, V_0/E_F^0; and (iv) the normalized electron-electron Coulomb interaction energy across a unit cell $V_\mathrm{C}/E_\mathrm{F}^0$, where $V_\mathrm{C} = e^2/a$. As illustrated in the dispersion diagrams shown in Fig. (6.2a) for different values of V_0/E_F^0, when the ribbons are moved far apart, and thus V_0/E_F^0 approaches 0, we rapidly recover a folded 2DEG (dotted curves) at the center of the 1BZ, while small gaps of decreasing size remain visible at the zone edge. Reassuringly, we find that for vanishing value of $V_\mathrm{C}/E_\mathrm{F}^0$ the Hartree potential contributes negligibly to the energy of the system and the eigenvalues $\varepsilon^x_{k_x n}$ agree well with those obtained in the Krönig–Penney model[266]. In addition, when scanning the geometrical ratio b/a, we find oscillations in the magnitude of the band gap produced by the image-interaction

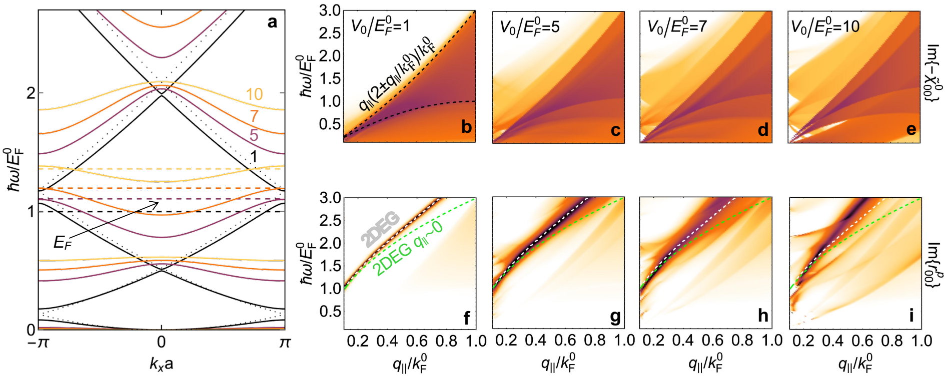

Figure 6.3: Modulation of the electronic band structure and optical response in a Q-phase material. (a) Electronic bands (solid curves) in the periodic patterning direction for different strengths of the normalized image potential V_0/E_F^0 (see color-matched labels), along with the corresponding normalized Fermi energies (dashed lines). Dotted curves stand for the 2DEG limit. (b-i) Single-particle excitations described by the 2D noninteracting susceptibility $\tilde{\chi}^0_{00}$ (b-e) and collective response resonances revealed by the loss function $\mathrm{Im}\{r^\mathrm{p}_{00}\}$ (f-i) as a function of transferred energy $\hbar\omega$ and in-plane wave vector $q_\| = |(q_x, q_y)|$, normalized to the Fermi energy E_F^0 and wave vector k_F^0, respectively, for fixed $q_x/k_\mathrm{F}^0 = 0.1$. In (b), the black-dashed curves indicate the boundaries of the continuum of electron-hole pair excitations $\hbar\omega/E_\mathrm{F}^0 = q_\|(2 \pm q_\|/k_\mathrm{F}^0)/k_\mathrm{F}^0$. The plasmon dispersion relation in a 2DEG is shown for comparison in (f-i) (white-dashed curves), along with its $q_\|/k_\mathrm{F}^0 \ll 1$ limit (green-dashed curves). All calculations are performed for $E_\mathrm{F}^0 = 0.29$ eV, $m^*/m_\mathrm{e} = 0.1$, $a = 10$ nm, and $b = 5$ nm.

modulation as a consequence of the functional dependence V_G^im, with the extreme cases of $b/a = 0$ and 1 reducing to just a rigid shift in the energy bands [see Fig. (6.2)].

Here, we are interested in a regime where the image potential strongly affects the transport properties of the material. Such a regime is reached when the total (i.e., summed for all electrons) image energy E^im dominates over the kinetic energy E^kin, as otherwise the latter would push the system towards a ballistic behavior. The ratio between these two energies scales as $E^\mathrm{im}/E^\mathrm{kin} \sim V_0/E_\mathrm{F}^0$, assuming that the condition $(V_\mathrm{C}/E_\mathrm{F}^0)/(k_\mathrm{BZ}/k_\mathrm{F}^0)^2 = (2/\pi^2)\, e^2 m^* a/\hbar^2 \gg 1$ is satisfied [e.g., for $a \gg 2.6$ nm if $m^* = 0.1\, m_\mathrm{e}$, see Appendix F]. This behavior is observed in the band structure calculations presented in Fig. (6.3a), where the influence of the image potential is visible through a monotonic increase in the band gaps with increasing strength of the image interaction V_0 (i.e., when bringing the ribbon pattern closer to the semiconductor). The reshaping of the semiconductor energy bands also produces a wealth of new dynamical and static properties which we investigate below. It should be noted that, in order to open a band gap $V_\mathrm{gap} \sim k_\mathrm{BZ} V_0/k_\mathrm{F}^0$ in the infrared range (e.g., $0.1 - 0.2$ eV) using a ratio $V_0/E_\mathrm{F}^0 \sim 3$ and an image potential energy $V_0 \sim 0.3$ eV (requiring a patterning distance $d \sim 1.2$ nm) in combination with a period $a = 10$ nm, materials with $m^*/m_\mathrm{e} \sim 0.1 - 0.4$ are needed [see, for example, Fig. (6.3a)]. Such values are found in black phosphorus[267] and transition-metal dichalcogenides[268], from which monolayers can be isolated for a direct implementation of the concepts here explored.

6.2.3 Optical response of Q-phase materials

The modifications produced in the electronic band structure by the image interaction translate into substantial changes in the optical response. Given the symmetry of the system, we can work in the in-plane reciprocal space and separately deal with each 2D wave vector $\mathbf{q}_\parallel$ (with q_x within the 1BZ). In addition, our structures involve small distances and periods compared with the light wavelength, so that the optical response can be safely described in the electrostatic limit. Consequently, we consider an external electric potential $\phi^{\rm ext}(\mathbf{q}_\parallel,z,\omega)=\sum_G\phi^{\rm ext}_G(\mathbf{q}_\parallel,z,\omega){\rm e}^{{\rm i}(\mathbf{q}_\parallel+G\hat{\mathbf{x}})\cdot\mathbf{R}}$ acting on the Q-phase material at optical frequency ω and expanded in Fourier components labeled by 1D reciprocal lattice vectors G. Introducing a matrix notation, we can express the resulting induced potential in terms of the Coulomb interaction υ and the noninteracting 2D susceptibility $\tilde{\chi}^0$ as $\phi^{\rm ind}(\mathbf{q}_\parallel,z,\omega)=\upsilon_G(\mathbf{q}_\parallel,z)\cdot\tilde{\chi}^0(\mathbf{q}_\parallel,\omega)\cdot[\mathcal{I}-\upsilon(\mathbf{q}_\parallel,0)\cdot\tilde{\chi}^0(\mathbf{q}_\parallel,\omega)]^{-1}\cdot\phi^{\rm ext}(\mathbf{q}_\parallel,0,\omega)$ (see Section 1.4), where dots indicate matrix multiplication, $\phi^{\rm ext}$ and $\phi^{\rm ind}$ are vectors of components $\phi^{\rm ext}_G$ and $\phi^{\rm ind}_G$, respectively, and we use the matrices $\mathcal{I}_{GG'}=\delta_{GG'}$, $\upsilon_{GG'}=\delta_{GG'}\upsilon_G$, and $\tilde{\chi}^0_{GG'}$. More precisely, the diagonal Coulomb matrix elements take the form $\upsilon_G(\mathbf{q}_\parallel,z)=2\pi\,{\rm e}^{-|\mathbf{q}_\parallel+G\hat{\mathbf{x}}||z|}\big/|\mathbf{q}_\parallel+G\hat{\mathbf{x}}|$[1], while we adopt the RPA which allows us to input the one-electron eigenstates directly into Eqs. (1.67) and (1.71) to obtain (see Section 1.4)

$$\tilde{\chi}^0_{GG'}(\mathbf{q}_\parallel,\omega)=\frac{e^2}{2\pi^2\hbar}\sum_{nn'}\int_{-\pi/a}^{\pi/a}dk_x\,M_G^{nn'}(k_x,q_x)[M_{G'}^{nn'}(k_x,q_x)]^*$$
$$\times\int_{-\infty}^{\infty}dk_y\frac{f_{\mathbf{k}_\parallel-\mathbf{q}_\parallel,n'}-f_{\mathbf{k}_\parallel n}}{\omega-\varepsilon_{\mathbf{k}_\parallel n}+\varepsilon_{\mathbf{k}_\parallel-\mathbf{q}_\parallel n'}+{\rm i}0^+},\qquad(6.5)$$

where we have introduced the matrix elements

$$M_G^{nn'}(k_x,q_x)=(1/a)\int_0^a dx\,{\rm e}^{-{\rm i}Gx}\,u^*_{k_x-q_x,n'}(x)\,u_{k_xn}(x).$$

The energy differences in the denominator of Eq. (6.5) correspond to one-electron excitations, which show up as intraband ($n=n'$) and interband ($n\neq n'$) transitions in the plots of $\tilde{\chi}^0_{GG'}(\mathbf{q}_\parallel,\omega)$ presented in Fig. (6.3b-e) as a function of photon energy $\hbar\omega$ and parallel wave vector $q_\parallel$ for the $G=G'=0$ component and different strengths of the image interaction V_0. At low V_0, the dispersion diagram is dominated by the intraband excitation region that characterizes the conduction band of a doped semiconductor (i.e., the homogeneous 2DEG limit). As we increase V_0 [see Fig. (6.3b-e)], the gap openings discussed above [Fig. (6.3a)] enables interband excitations, and in particular, vertical transitions become available due to the proximity of the ribbon array.

The RPA accounts for the self-consistent interaction with the induced potential, thereby resulting in collective electron excitations. To explore these so-called plasmons, we calculate the Fresnel reflection coefficient for p-polarized waves $r^{\rm p}$, which relates the induced and external potentials via[269]

---

[1] For simplicity, we assume the material in the ribbon array to be perfectly conducting at zero frequency, but invisible at the infrared optical frequencies under consideration (e.g., by embedding the entire structure in an index-matching medium), so that υ can be well approximated by the bare Coulomb potential $\upsilon(\mathbf{r},\mathbf{r}')\approx 1/|\mathbf{r}-\mathbf{r}'|$ in the calculation of χ.

$\phi_G^{\mathrm{ind}}(\mathbf{q}_\parallel,0,\omega) = -\sum_{G'} r^{\mathrm{p}}_{GG'}(\mathbf{q}_\parallel,\omega)\,\phi_{G'}^{\mathrm{ext}}(\mathbf{q}_\parallel,0,\omega)$. Using the formalism outlined above, the Fourier components of r^{p} are given by

$$r^{\mathrm{p}}_{GG'}(\mathbf{q}_\parallel,\omega) = \left.\frac{1}{1-\left[\upsilon(\mathbf{q}_\parallel,0)\cdot\tilde{\chi}^0(\mathbf{q}_\parallel,\omega)\right]^{-1}}\right|_{GG'}.$$

In Fig. (6.3f-i), we plot the loss function $\mathrm{Im}\{r^{\mathrm{p}}_{GG'}\}$ obtained from this equation as a function of $q_\parallel$ and ω. We note that even though we concentrate on the specular-reflection coefficient corresponding to $G = G' = 0$, the condition $k_{\mathrm{BZ}} \ll k_{\mathrm{F}}^0$ requires the evaluation of G components up to $G \gg k_{\mathrm{F}}^0$ in the υ and $\tilde{\chi}^0$ matrices to correctly account for transitions happening close to the Fermi surface.

Collective plasmon excitations are identified as intense features in Fig. (6.3f-i), which should be measurable for instance through electron energy-loss spectroscopy. For relatively small V_0/E_{F}^0 [Fig. (6.3f)], the dispersion diagram is dominated by a single, continuous plasmon band, in excellent agreement with the plasmon dispersion of the textbook uniform 2DEG (superimposed). This agreement reflects the fact that the plasmon behavior is mainly controlled by the average electron density n_0, provided the external perturbation produced in the band structure by the periodic image potential is still weak [see the relatively small gap openings in Fig. (6.3a) for $V_0 = E_{\mathrm{F}}^0$]. Incidentally, at low V_0 the plasmon is qualitatively well described by the dispersion relation $\omega_{\mathrm{p}}(q_\parallel) \sim e\sqrt{nq_\parallel/m^*}$ obtained in the $q_\parallel/k_{\mathrm{F}}^0 \ll 1$ limit. In contrast, as the ribbon structure is brought closer to the semiconductor, so that the image potential energy increases and eventually dominates in the system, a zoo of excitations emerge in the dispersion diagram: besides the 2DEG plasmon, features associated with interband transitions and their hybridization with plasmons are revealed. In addition, all of these features are dressed by electron-electron interactions, leading to a blue shift of the plasmon relative to the 2DEG limit, as well as spectral shifts of the interband transitions relative to the undressed excitations depicted in Fig. (6.3b-e).

6.2.4 Metal-insulator transition

Beyond the optical response, we expect the image interaction to also modify the static properties of Q-phase materials. In this regard, an external static in-plane electric field $\mathbf{E}$ produces a 2D current density $\mathbf{j}^{\mathrm{e}} = \sigma^{\mathrm{DC}}\mathbf{E}$, where σ^{DC} is the local DC ($\omega = 0$) electrical conductivity tensor. We compute this quantity in the relaxation-time approximation[19], introducing a phenomenological inelastic scattering time τ, so the conductivity is uniquely determined by the band energies $\hbar\varepsilon_{\mathbf{k}_\parallel n}$ and the chemical potential, which we approximate by the Fermi energy E_{F} [Fig. (6.3a)]. We remark that this assumption safely holds for temperatures and doping levels such that $k_{\mathrm{B}}T \ll E_{\mathrm{F}}^0$, a condition that is satisfied over the range of parameters considered in this work. Because of the symmetry of the system, the 2×2 conductivity tensor should only contain diagonal xx and yy components (i.e., along directions parallel and perpendicular to the periodic modulation). In addition, the yy component remains unchanged with respect to the unperturbed semiconductor because the $x-$averaged electron density is conserved (i.e., $\sigma_{yy}^{\mathrm{DC}} = (e^2\tau/\pi^2 m^*)\sum_n \int_{-\pi/a}^{\pi/a} dk_x \int_0^\infty dk_y \left[\mathrm{e}^{(\hbar\varepsilon_{\mathbf{k}_\parallel n}-E_{\mathrm{F}})/k_{\mathrm{B}}T}+1\right]^{-1}$, which reduces to $\sigma_{yy}^{\mathrm{DC}} = e^2 E_{\mathrm{F}}^0\tau/\pi\hbar^2$ at zero temperature). The conductivity along x can then be directly

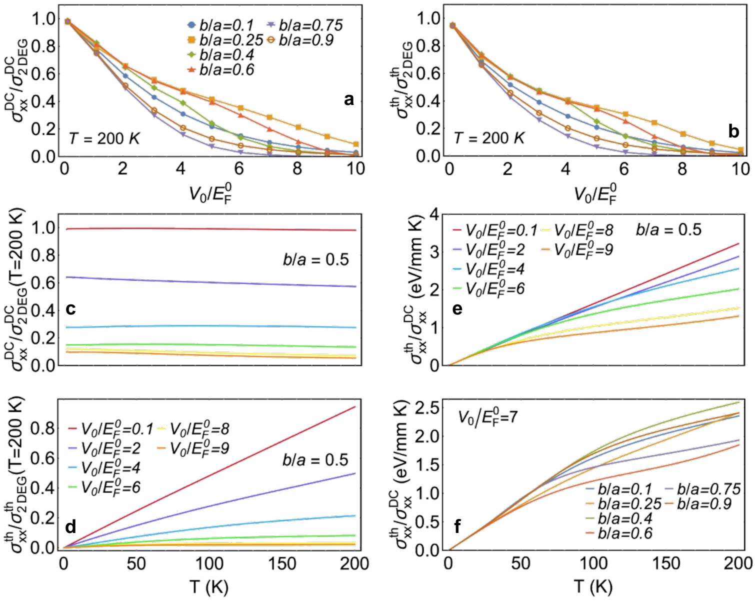

Figure 6.4: Q-phase modulation of the DC electrical and thermal conductivities. (a) Component of the 2D electrical (a) and thermal (b) conductivity tensors along the periodicity direction as a function of the normalized image potential strength $V_0/E_{\rm F}^0$ for several values of the b/a ratio (see legend), calculated at $T = 200\,$K and divided by the respective conductivities of a 2DEG at the same temperature. (c,d) Temperature dependence of the electrical (c) and thermal (d) conductivities for $b/a = 0.5$ and different values of $V_0/E_{\rm F}^0$, normalized to the respective 2DEG conductivity at $T = 200$ K. (e,f) Temperature-dependence of the ratio between thermal and electric conductivities, revealing deviations from from the Wiedemann-Franz law for $b/a = 0.5$ and various values of the ratio $V_0/E_{\rm F}^0$ (e), as well as for fixed $V_0/E_{\rm F}^0 = 5$ and several values of b/a (f). We use the same material parameters as in Fig. (6.4).

computed from the energy distribution in Eq. (6.4b) through the equation

$$\sigma_{xx}^{\rm DC} = \frac{e^2\tau}{\pi^2\hbar}\sum_n \int_{-\pi/a}^{\pi/a} dk_x \int_0^{\infty} dk_y\, (\partial^2_{k_x}\varepsilon^x_{k_x n}) \left[{\rm e}^{(\hbar\varepsilon_{\mathbf{k}_\parallel n}-E_{\rm F})/k_{\rm B}T}+1\right]^{-1}. \tag{6.6}$$

We use this expression in combination with the bands plotted in Fig. (6.3a) to obtain the results presented in Fig. (6.4). Remarkably, the thermal conductivity exhibits a steady decrease with increasing image interaction V_0, starting from the 2DEG value in the unperturbed semiconductor at $V_0 = 0$ and evolving towards a substantial suppression when the $V_0/E_{\rm F}$ ratio reaches a few times unity [see Fig. (6.4a)]. This behavior is a direct consequence of the reduction in the ability of charge carriers to move within the periodic potential landscape produced by the image interaction. We thus predict a metal-insulator transition as the latter is switched on by placing the conductive ribbons closer to the semiconductor (i.e., the transition happens with respect to the order parameter $V_0/E_{\rm F}^0$, not to be confused with a phase transition driven by a change in temperature). This phenomenon is observed for all ribbon sizes under consideration, with an optimum behavior found for $b/a \sim 0.75$, alongside a minor dependence on temperature up to $T = 200$ K [see Fig. (6.4c)].

6.2.5 Inhibition of the thermal conductivity

Similarly to the case of an external electric field, an in-plane temperature gradient induces a 2D thermal current density $\mathbf{j}^{\mathrm{th}} = -\sigma^{\mathrm{th}}\nabla_{\mathbf{R}}T$, where σ^{th} is the electronic thermal conductivity tensor. This latter undergoes strong modifications due to the image interaction, since it is equally mediated by carrier propagation. We adopt again the relaxation-time approximation[19] and compute σ^{th} from the electronic band structure (see below). Following similar arguments as above, we find the conductivity tensor to be diagonal, with its yy component almost unaffected by the image interaction, so it can be well approximated by the relation $\sigma^{\mathrm{th}}_{yy} \approx (\pi E^0_{\mathrm{F}} k_{\mathrm{B}}{}^2 T\tau/9\hbar^2)\left[3 - (\pi k_{\mathrm{B}}T/E^0_{\mathrm{F}})^2\right]$. The remaining xx component can be directly computed from

$$\sigma^{\mathrm{th}}_{xx} = \frac{1}{e^2 T}\left[\sigma^{(2)}_{xx} - \left(\sigma^{(1)}_{xx}\right)^2/\sigma^{\mathrm{DC}}_{xx}\right], \tag{6.7}$$

where $\sigma^{\mathrm{DC}}_{xx}$ is the DC electrical conductivity in Eq. (6.6) and

$$\begin{aligned}\sigma^{(\alpha)}_{xx} = \frac{e^2\tau}{\pi^2 k_{\mathrm{B}}T}\sum_n \int_{-\pi/a}^{\pi/a} dk_x \int_0^\infty dk_y\, (\hbar\varepsilon_{\mathbf{k}_\parallel n} - E_{\mathrm{F}})^\alpha \\ \times (\partial_{k_x}\varepsilon^x_{k_x n})^2 \frac{e^{(\hbar\varepsilon_{\mathbf{k}_\parallel n} - E_{\mathrm{F}})/k_{\mathrm{B}}T}}{\left[e^{(\hbar\varepsilon_{\mathbf{k}_\parallel n} - E_{\mathrm{F}})/k_{\mathrm{B}}T} + 1\right]^2}.\end{aligned} \tag{6.8}$$

The V_0-dependent thermal conductivity plotted in Fig. (6.4b,d) reveals a transition from a thermal conductor to a thermal insulator analogous to the electrical behavior both at low and at finite temperatures, which we also attribute to the reduction in carrier propagation produced by the periodic image potential. In addition, we observe a clear departure from the Wiedemann–Franz law[270] when comparing Fig. (6.4a) with Fig. (6.4b), as revealed by the different behavior at finite temperature displayed by $\sigma^{\mathrm{th}}_{xx}$ as a function of V_0 with respect to $\sigma^{\mathrm{DC}}_{xx}$. Such deviation from the linear regime, which is also highlighted by the ratio between thermal and electrical conductivities plotted in Fig. (6.4e,f) for several image potential strengths and different b/a ratios, stems from the fact that conduction electrons are not free, in contrast to the ideal-gas conditions for which the law is best suited. Incidentally, the thermal conductor-insulator transition is again faster for $b/a \sim 0.75$.

6.3 Concluding remarks

In conclusion, we have demonstrated, based on rigorous theory, that the optical, electrical, and thermal properties of a 2D material can be substantially modified by introducing a neutral, noncontact structure in its vicinity. This constitutes a genuinely radical departure from currently available methods to engineer material properties, as instead we capitalize on the image interaction, which translates into a quantum phase imprinted on the valence electrons of the 2D layer. We remark the nonresonant nature of such interaction, which should therefore be generally applicable to modulate the properties of different types of materials, provided their thickness is small enough as to be strongly influenced by the image interaction with the added structure.

As a possible realization of these engineered media, which we term Q-phase materials, we have studied the modification in the properties of a 2D semiconductor when an array of conductive ribbons is brought in close proximity. Specifically, energy gaps are induced in the electronic band structure, interband electronic transitions are enabled, a rich landscape of additional plasmon bands emerges, and the electrical/thermal conductivity displays a metal/conductor-insulator transition as the semiconductor-array distance is reduced and the image interaction is increased. In the limits of either small ribbons [e.g., $b/a = 0.1$ in Fig. (6.4a,b,f)] or a ribbon width approaching the period (e.g., $b/a = 0.9$), we obtain a spatially featureless image interaction, therefore resulting in a relatively small modulation of the material, and consequently, an optimized effect is observed at intermediate values of the width-to-period ratio b/a for a fixed separation from the 2D material.

In passing, we note that a transition of different nature is expected when the 2D semiconductor is in contact with the patterned structure (e.g., through structural reconstruction or via electron hopping), while here we are concerned instead with transitions occurring without touching, in which the order parameter is the strength of the image interaction. The predicted modifications in the optical, electrical, and thermal properties of the 2D material are driven by a rearrangement of its electronic bands in the presence of the image potential landscape, without requiring any physical contact. However, the strain caused by the structure could also play a role and introduce additional modifications in the material properties, although we expect this effect to be comparatively small when the 2D material and the patterned structure are separated by at least a few monolayers through which any possible microscopic reconstructions are attenuated.

As a practical realization of the present concept, materials such as black phosphorus[267] and transition-metal dichalcogenides[268] offer parameters similar to those considered above for the 2D layer. In addition, application of this scheme to graphene is anticipated to produce qualitatively different features due to the exotic nature of charge carriers in this material (e.g., electronic bands would be primarily renormalized in the direction parallel to the ribbons, in contrast to the results presented above). Furthermore, the decorating structure could be amenable to modulation through external means of control (e.g., by resorting to phase-change materials such as GST), still without having physical contact with the 2D layer. Although we focus here on large features of the decorating structure compared with the atomic lattice parameters of the material, so that conduction electrons in the latter are well described in the continuum limit, an interesting regime comes about when the characteristic patterning length is commensurate with the atomic lattice (e.g., by using a self-organized vicinal surface[271] stamp). From a more general perspective, arbitrarily structured external structures could be employed to, for example, shape the Q-phase material into quasicrystals, and even to draw electrical and thermal circuits controlled by the presence of a nontouching structure. Our results represent a first step towards the realization of gate-free material tunability, potentially granting us access into a whole range of properties that could find application in the design of nanodevices.

7

Nanophotonics for pair-production

Ludwig Boltzmann, who spent much of his life studying statistical mechanics, died in 1906, by his own hand. Paul Ehrenfest, carrying on the same work, died similarly in 1933. Now it is our turn to study statistical mechanics. Perhaps, it will be wise to approach the subject cautiously.
David Goodstein

In this chapter, we explore how optical field confinement, typical of electromagnetic waves bounded to material interfaces in the form of polaritons, can be used to tailor high-energy physics processes. In particular, we compute the cross section associated with the scattering between gamma-rays and surface polaritons propagating along a planar interface. What follows is based on a recently submitted unpublished work, Ref. 272.

7.1 Introduction

The creation of massive particles from electromagnetic energy emerged as a prominent focus of attention in 1934, when the materialization of an electron and its antiparticle –the positron– was predicted to occur with nonvanishing probability by Breit and Wheeler (BW) from the scattering of two photons[273], by Bethe and Heitler (BH) from the interaction of a photon and the Coulomb potential of a nucleus[274], and by Landau and Lifshitz (LL) from the collision of two other massive particles[275]. A main difference between these processes relates to the real or virtual nature of the involved photons. While only real electromagnetic quanta lying inside the light cone (i.e., satisfying the light dispersion relation in vacuum, $k = \omega/c$) participate in the BW mechanism for pair production, the LL process is mediated by two virtual photons, and both real and virtual photons participate in BH scattering. Eventually, pair production was achieved by colliding energetic electrons and real photons delivered by high-power lasers[276], and more recently using only real photons generated from atomic collisions[277].

Besides the fundamental interest of these processes, the generation of positrons finds application in surface science[278] through, for example, positron annihilation spectroscopy[279–281] and low-energy positron diffraction[282], as well as in the study of their interaction with atoms and molecules[283,284]. Positrons are also used to create antimatter (e.g., antihydrogen[285–288]) and positronium[289]). In these studies, slow positrons are commonly obtained from beta decay, decelerated through metallic moderators[290], and subsequently stored in different types of traps, from which they are extracted as low-energy, quasi-monochromatic pulses[291–294].

Direct positron generation from light would not require nuclear decay and could further leverage recent advances in optics to produce ultrashort photon pulses. However, the cross sections associated with the aforementioned processes are extremely small. As a possible avenue to increase the pair-production rate, we consider the replacement of free photons by confined optical modes in the hope that they alleviate the kinematic mismatch between the particles involved in BW scattering, for instance. In particular, surface polaritons, which are hybrids of light and polarization charges bound to material interfaces, can display short in-plane wavelengths compared with the free-space light wavelength. Actually, a broad suite of two-dimensional (2D) materials have recently been identified to sustain long-lived, strongly confined polaritons[295,296], including plasmonic[235,297,298], phononic[299,300], and excitonic[301] modes that cover a wide spectral range extending from mid-infrared frequencies[235,297,299,300] to the visible domain[298,301].

In this chapter, we calculate the pair-production cross section associated with the annihilation of γ-ray photons (γ-photons) and 2D surface polaritons, leading to a substantial enhancement compared to free-space BW scattering. Part of this enhancement relates to the in-plane spatial confinement of surface polaritons. In addition, the lack of translational invariance in the out-of-plane direction enables pair production for γ-photon energies just above the $2m_\mathrm{e}c^2$ threshold (e.g., $\hbar\omega_\gamma \sim 1.1$ MeV combined with a polariton energy $\hbar\omega_\mathrm{p}$ of a few eV), in contrast to free-space BW scattering, for which visible-range photons need to be paired with GeV photons such as those existing in astrophysical processes[302]. By demonstrating the advantages of using deeply confined light, our work inaugurates an avenue in the exploration of nanophotonic structures as a platform for high-energy physics.

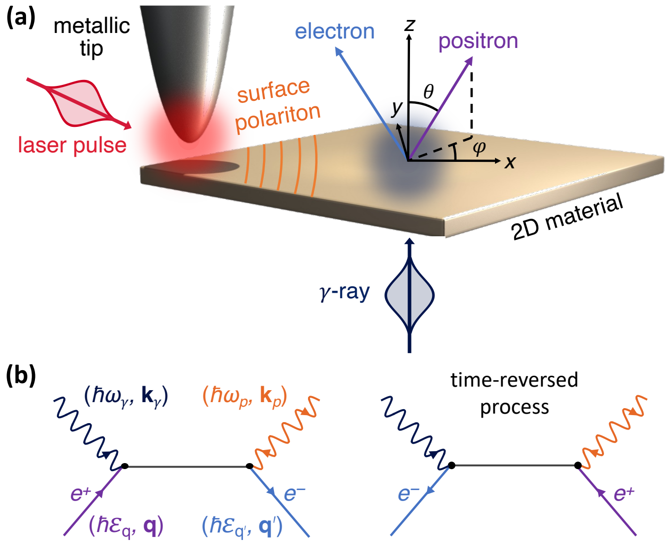

Figure 7.1: Pair production by interaction of surface polaritons and γ-photons. (a) Schematic representation of a possible realization of the studied interaction. An external laser pulse (red) is coupled to surface polaritons (orange) in a 2D material (e.g., through a metallic tip), while energetic γ-rays (dark gray) impinge normally to the surface. The interaction of these two fields gives rise to electron-positron pairs. The positron (purple) is emitted with angles (θ, φ) that also determine the electron direction (blue) by conservation of energy and in-plane momentum. (b) Direct and time-reversed Feynman diagrams contributing to the investigated pair production. We indicate the energies and wave vectors of the polariton, the γ-photon, and the fermions by color-coordinated labels. Both polariton absorption and emission processes (double arrow) contribute to pair production.

7.2 Pair production from the scattering of a surface-polariton and a γ-photon

We assume the configuration presented in Fig. (7.1a), where surface polaritons (frequency ω_{p}, wave vector $\mathbf{k}_p = k_{\mathrm{p}}\hat{\mathbf{x}}$) are launched on a 2D material ($z = 0$ plane) by in-coupling a laser through a metallic tip (or by a grating or a launching antenna), while γ-photons (frequency ω_γ, wave vector $\mathbf{k}_\gamma = \hat{\mathbf{z}}\,\omega_\gamma/c$) are normally impinging from the bottom. We study pair production using the relativistic minimal coupling Hamiltonian (see Chapter 1 and Ref. 303)

$$\hat{\mathcal{H}}_{\mathrm{int}}(t) = \frac{-1}{c}\int d^3\mathbf{r}\;\hat{\mathbf{j}}(\mathbf{r})\cdot\mathbf{A}(\mathbf{r},t), \tag{7.1}$$

where $\hat{\mathbf{j}}(\mathbf{r}) = -ec :\hat{\overline{\Psi}}(\mathbf{r})\vec{\gamma}\hat{\Psi}(\mathbf{r}):$ is the fermionic current, $\mathbf{A}(\mathbf{r},t)$ is the classical vector potential associated with the polariton and photon fields, and we adopt a gauge with vanishing scalar potential. Here, $:\cdot:$ denotes normal product concerning electron and positron annihilation ($\hat{c}_{\mathbf{q},s}$ and $\hat{d}_{\mathbf{q},s}$, respectively) and creation ($\hat{c}^\dagger_{\mathbf{q},s}$ and $\hat{d}^\dagger_{\mathbf{q},s}$) operators (for fermions of momentum $\hbar\mathbf{q}$, spin s, and energy $\hbar\varepsilon_q = c\sqrt{m_e^2c^2 + \hbar^2q^2}$), and $\hat{\Psi}(\mathbf{r}) =$

$\sum_{\mathbf{q},s}\left(u_{\mathbf{q},s}\hat{c}_{\mathbf{q},s}\mathrm{e}^{\mathrm{i}\mathbf{q}\cdot\mathbf{r}}+v_{\mathbf{q},s}\hat{d}^{\dagger}_{\mathbf{q},s}\mathrm{e}^{-\mathrm{i}\mathbf{q}\cdot\mathbf{r}}\right)$ is the fermionic field operator, with $u_{\mathbf{q},s}$ ($v_{\mathbf{q},s}$) representing 4-component electron (positron) spinors.

We work in the continuous-wave regime and eventually normalize the resulting production rate to the number of polaritons and photons in the system. The vector potential is thus the sum of two monochromatic components, $\mathbf{A}(\mathbf{r},t)=-(\mathrm{i}c/\omega_{\mathrm{p}})\,\vec{\mathcal{E}}_{\mathrm{p}}(\mathbf{r})\mathrm{e}^{-\mathrm{i}\omega_{\mathrm{p}}t}-(\mathrm{i}c/\omega_{\gamma})\,\vec{\mathcal{E}}_{\gamma}(\mathbf{r})\mathrm{e}^{-\mathrm{i}\omega_{\gamma}t}+\text{c.c.}$, expressed in terms of the polariton and γ-photon field amplitudes

$$\vec{\mathcal{E}}_{\mathrm{p}}(\mathbf{r})\propto\left[i\kappa_p\hat{\mathbf{x}}-k_p\mathrm{sign}\{z\}\hat{\mathbf{z}}\right]\mathrm{e}^{\mathrm{i}k_{\mathrm{p}}x-\kappa_p|z|},\tag{7.2a}$$

$$\vec{\mathcal{E}}_{\gamma}(\mathbf{r})\propto\hat{\mathbf{e}}_j\mathrm{e}^{\mathrm{i}k_{\gamma}z},\tag{7.2b}$$

where $\hat{\mathbf{e}}_j$ ($=\hat{\mathbf{x}}$ or $\hat{\mathbf{y}}$ for $j=1$ or 2, respectively) is the γ-ray polarization vector, $\kappa_p=\sqrt{k_p^2-\omega_p^2/c^2}$, and we neglect material losses and γ-ray screening.

We calculate the production rate for a state $\hat{d}^{\dagger}_{\mathbf{q},s}\hat{c}^{\dagger}_{\mathbf{q}',s'}\left|0\right\rangle$ comprising a positron (wave vector $\mathbf{q}$, spin s) and an electron (wave vector $\mathbf{q}'$, spin s') to the lowest (second) nonvanishing-order of time-dependent perturbation theory for the Hamiltonian in Eq. (7.1). This process involves the annihilation of a γ-photon accompanied by the emission (upper signs below) or absorption (lower signs) of a polariton, as indicated in the Feynman diagrams in Fig. (7.1b). Incidentally, we note that boson emission (polaritons in the present instance) is forbidden in free space. Parallel momentum conservation leads to $\mathbf{q}'_{\parallel\pm}=-\mathbf{q}_{\parallel}\mp\mathbf{k}_p$ for the in-plane electron wave vector components, while energy conservation determines the electron energy $\varepsilon_{q'_{\pm}}=\omega_{\gamma}\mp\omega_{\mathrm{p}}-\varepsilon_q$ and out-of-plane wave vector $q'_{z\pm}=\sqrt{\varepsilon^2_{q'_{\pm}}/c^2-m_{\mathrm{e}}^2c^2/\hbar^2-q'^2_{\parallel\pm}}$, subject to the threshold-energy conditions $\varepsilon^2_{q'_{\pm}}>m_{\mathrm{e}}^2c^4/\hbar^2-c^2q'^2_{\parallel\pm}$ and $\omega_{\gamma}>\pm\omega_{\mathrm{p}}+\varepsilon_q$. Following a standard procedure detailed in Appendix G, the positron-momentum-resolved pair-production cross section associated with polariton and γ-photon scattering is found to be

$$\frac{d\sigma^{\mathrm{pol}}}{d\mathbf{q}}=\frac{\alpha^2c^3\kappa_p}{\pi\,\omega_p\omega_{\gamma}k_p^2}\sum_{\pm}\frac{\varepsilon_{q'_{\pm}}}{q'_{z\pm}}\sum_{ss'j\mu}\left|\overline{u}_{\mathbf{q}'_{\mu\pm},s'}\mathcal{M}^{\pm}_j(\mathbf{q}'_{\mu\pm},\mathbf{q})\,v_{\mathbf{q}s}\right|^2,\tag{7.3}$$

where $\alpha\approx1/137$ is the fine-structure constant, $\mathbf{q}'_{\mu\pm}=\mathbf{q}'_{\parallel\pm}+\mu q'_{z\pm}\hat{\mathbf{z}}$ is the electron wave vector for upward ($\mu=1$) and downward ($\mu=-1$) emission contributions, we average over γ-ray polarizations $j=1,2$, and we define the 4×4 matrix

$$\begin{aligned}\mathcal{M}^{\pm}_j(\mathbf{q}',\mathbf{q})=&\gamma^j\,G_F(\mathbf{q}'-\mathbf{k}_{\gamma},\varepsilon_{q'}-\omega_{\gamma})\,\mathbf{f}_{\pm(k_{\gamma z}-q_z-q'_z)}\cdot\vec{\gamma}\\&+\vec{\gamma}\cdot\mathbf{f}_{\pm(k_{\gamma z}-q_z-q'_z)}\,G_F(\mathbf{k}_{\gamma}-\mathbf{q},\varepsilon_{q'}\pm\omega_p)\,\gamma^j\end{aligned}$$

in terms of the Dirac γ matrices, the Feynman propagator[303] $G_F(\mathbf{q},\omega)=[\omega\gamma^0-c\vec{\gamma}\cdot\mathbf{q}+(m_ec^2/\hbar)]/(\omega^2-\varepsilon_q^2+\mathrm{i}0^+)$, and the vector $\mathbf{f}_{k_z}=(\kappa_p^2\,\hat{\mathbf{x}}+k_{\mathrm{p}}k_z\,\hat{\mathbf{z}})/(\kappa_p^2+k_z^2)$ encapsulating the out-of-plane momentum distribution of the polariton field in Eq. (7.2a).

7.2.1 Consequences of polariton field compression and translational symmetry breaking

An immediate effect of out-of-plane symmetry breaking is that the allowed kinematical space for which we obtain nonzero pair-production cross sections extends down to the

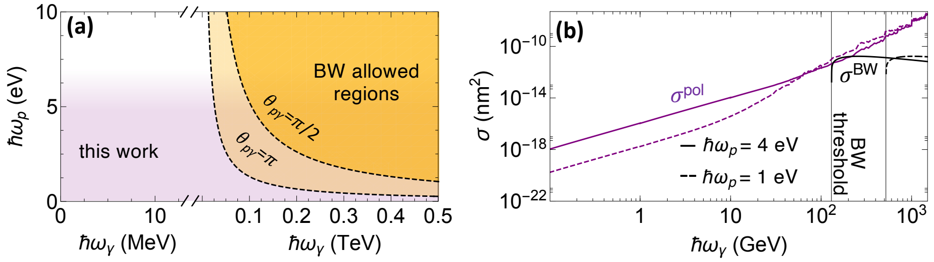

Figure 7.2: Enhanced pair-production enhancement. (a) Comparison between the regions allowed by energy-momentum conservation in either BW photon-photon scattering (yellow) and polariton-photon scattering under the configuration of Fig. (7.1a) (purple) as a function of polariton/photon energies. The BW threshold $\hbar^2\omega_{\rm p}\omega_\gamma = 2m_{\rm e}^2c^4/(1-\cos\theta_{p\gamma})$ [304] is indicated for a relative photon-photon angle $\theta_{p\gamma}$ of π (absolute threshold) and $\pi/2$. (b) Pair-production cross sections for polariton-photon scattering ($\sigma^{\rm pol}$, purple curves) and BW scattering ($\sigma^{\rm BW}$ for $\theta_{p\gamma}=\pi/2$, black curves [305]). Dashed and solid curves are obtained for $\hbar\omega_{\rm p}=1$ eV and 4 eV, respectively, with $k_{\rm p}=0.05$ nm^{-1} in both cases, while solid vertical lines indicate the γ-photon BW threshold energy [$\theta_{p\gamma}=\pi/2$ curve in (a)].

infrared polariton regime even when using γ-photons just above the absolute energy threshold $\gtrsim 2m_{\rm e}c^2 \approx 1.02$ MeV [Fig. (7.2a)]. In contrast, BW scattering with one of the photons in the optical regime requires the other photon to have energy exceeding ~ 0.1 TeV, which explains why free-space pair production has traditionally been observed only in its nonlinear version, where the energy-momentum mismatch is overcome by engaging a high number of photon exchanges [306,307].

In Fig. (7.2b), we show that, for low-energy polaritons/photons (up to a few eV), the momentum-integrated polariton-assisted pair-production cross section $\sigma^{\rm pol} = \int d^3\mathbf{q}\,(d\sigma^{\rm pol}/d\mathbf{q})$, with $d\sigma^{\rm pol}/d\mathbf{q}$ given by Eq. (7.3), takes substantial values at γ-photon energies far below the BW kinematical threshold (vertical solid lines). In addition, $\sigma^{\rm pol}$ is consistently several orders of magnitude higher than the BW cross section up to γ-photon energies in the TeV regime. Part of this enhancement can be attributed to the spatial compression of polaritons relative to free-space photons.

7.2.2 Pair production close to threshold

From the analysis above, we expect positron production by mixing polaritons and $\gtrsim 1$ MeV photons, such as those available from commonly used sources [308,309] (e.g., ^{60}Co [308,309], which emits at ~ 1.17 and ~ 1.33 MeV with a lifetime of ~ 5.13 years, yielding $\sim 10^{14}$ photons/s out of 1 g of material).

To put this in context, we note that the BW cross section [305] is too small for pair production out of such γ-photons alone (e.g., the maximum cross section is $\sigma^{\rm BW} \lesssim 1.7\times 10^{-11}$ nm^2 for two 1.33 MeV photons). We illustrate this by considering an arrangement consisting of two ^{60}Co sources spaced by a few meters so that $\sim 10^6$ photons are simultaneously traveling across that distance, and therefore, $\sim 10^{12}$ photon-photon collisions take place during the traveling time $\sim 10^{-8}$ s. Now, multiplying the number of collisions by $\sigma^{\rm BW}$ and dividing by both a transverse area of ~ 1 m^2 and the traveling time, we estimate a pair-production rate of $\sim 10^{-9}$/s.

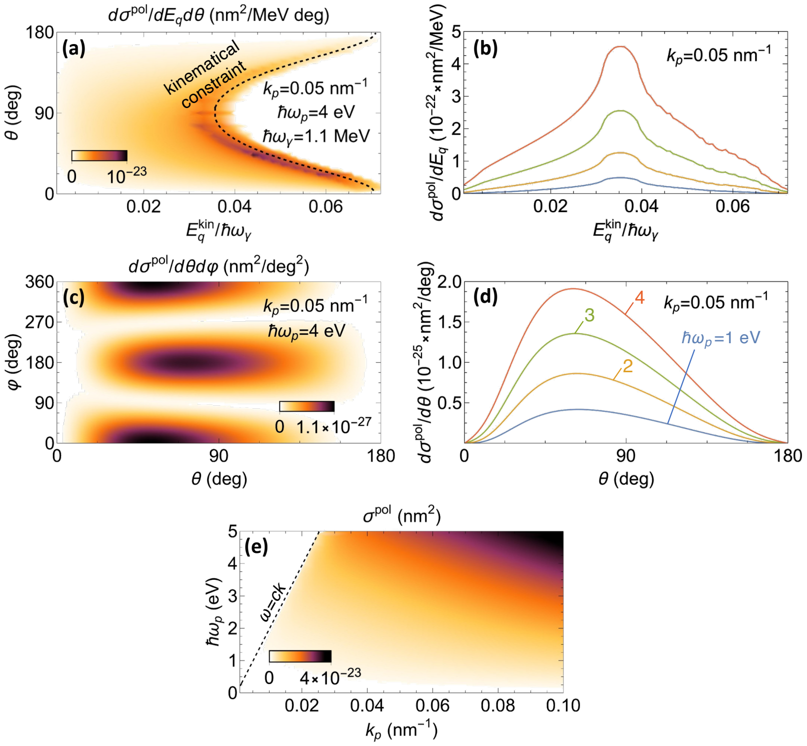

Figure 7.3: Pair-production cross section close to threshold. (a) Differential cross section for positron emission as a function of polar angle θ and kinetic energy $E_q^{\rm kin}=\hbar\varepsilon_q-m_{\rm e}c^2$ (normalized to the γ-photon energy $\hbar\omega_\gamma=1.1$ MeV and averaged over a window $\Delta E_q^{\rm kin}=8$ keV) for fixed polariton wave vector $k_{\rm p}=0.05$ nm^{-1} and energy $\hbar\omega_p=4$ eV, as computed from $d\sigma^{\rm pol}/dE_q d\theta=\sin\theta\,(q\varepsilon_q/\hbar c^2)\int_0^{2\pi}d\varphi\,(d\sigma^{\rm pol}/d\mathbf{q})$ with the integrand taken from Eq. (7.3). The dashed line represents the limit imposed by energy-momentum conservation for $\varphi=0$. (b) Same as (a) integrated over θ for different polariton energies $\hbar\omega_p$ [see color labels in (d)]. (c) Energy-integrated cross section $d\sigma^{\rm pol}/d\theta d\varphi=\sin\theta\int_0^\infty q^2dq\,(d\sigma^{\rm pol}/d\mathbf{q})$ as a function of polar and azimuthal emission angles (θ,φ) under the conditions of (a). (d) Same as (c) integrated over φ for different polariton energies. (e) Total cross section [$\mathbf{q}$-integral of Eq. (7.3)] as a function of polariton wave vector $k_{\rm p}$ and energy $\hbar\omega_{\rm p}$. We show the dispersion relation of free-space light $\omega=ck$ as a broken line for reference.

Polaritons can then be advantageous in this context because these optical modes are in large supply over small spatial regions by relying on ultrafast lasers (e.g., one has $\sim 10^{19}$ photons in 1 J pulses of 100 fs duration, such as those delivered by tabletop setups, which could be schemed to achieve nearly complete coupling to polaritons[310]). This allows us to compensate for the even smaller polariton-induced pair-production cross section at such relatively small γ-photon energies [e.g., $\sigma^{\rm pol}\sim 10^{-23}$ nm^2 for few-eV polaritons and 1.1 MeV γ-photons, see Fig. (7.3e) below]. For example, considering again γ-photons delivered by a ^{60}Co source close to a polariton-supporting surface, we can have a flux of 10^{14} γ-photons/s cm^2, which, when multiplied by $\sigma^{\rm pol}$, by a number of polaritons $N_p\sim 10^{19}$, by the polariton lifetime (e.g., nanoseconds for high-index planar dielectric waveguides with quality factors $\sim 10^6$), and by a pulse repetition rate of 10^8/s, leads to a production rate of $\sim 10^{-5}$ pairs per second.

Considering the use of these kinds of sources, we take $\hbar\omega_\gamma = 1.1$ MeV, close to the minimum required energy, and compute the emitted positron distribution predicted by Eq. (7.3) as a function of kinetic energy $E_q^{\rm kin} = \hbar\varepsilon_q - m_{\rm e}c^2$ and polar angle θ under the configuration depicted in Fig. 7.1(a). The result [Fig. 7.3(a)] indicates a preference for polar angles close to normal when the positron takes most of the energy (electron emitted nearly at rest), and conversely, grazing emission for low-energy positrons. The spectral distribution obtained by further integrating over θ displays a symmetric behavior with respect to the central peak found at $E_q^{\rm kin} = (\hbar\omega_\gamma - 2m_{\rm e}c^2)/2 \approx 39$ keV [Fig. 7.3(b)], as expected from the electron-positron kinematical symmetry. In addition, the energy-integrated positron-emission cross section exhibits two preferential azimuthal angles φ corresponding to forward and backward emission with respect to the plasmon propagation direction [Fig. 7.3(c)], while the polar dependence presents a maximum at $\theta \sim 59°$, in good correspondence with the symmetrically arranged electron-positron emission, dominated by the spectral maximum in Fig. 7.3(b). Finally, the full $\mathbf{q}$-integrated cross section [Fig. 7.3(e)] shows a nearly uniform increase with polariton frequency and plasmon wave vector as $\propto \omega_p$ and $\propto k_p$, respectively, except for the depletion observed when k_p moves close to the light cone (dashed line). Overall, we conclude that the studied process leads to a strong angular and energy dependence of the resulting positron emission, which should facilitate an experimental verification of these results.

7.2.3 Pair production by scattering polaritons and GeV γ-photons

Incidentally, $\sigma^{\rm pol}$ increases as $\sim \omega_\gamma^3$ with the γ-photon frequency, and thus, much higher production rates are expected at 1 GeV. We analyze the emitted positron distribution in Fig. (7.4) for γ-photons at such energy, which are experimentally produced by bremsstrahlung and Compton backscattering[311], while several proposals for more efficient sources have recently been put forward based on electron-beam collisions with intense laser spots[312,313], strong laser irradiation of electron plasma[314,315], simultaneous laser and electron plasma bombardment[316], and electrons impinging on solid targets[317].

Similarly to Fig. (7.3), Fig. (7.4a) illustrates how the differential cross section is strongly peaked around normal emission (polar angle $\theta \sim 0$). The positrons are preferentially sharing about half of the photon energy [Fig. (7.4b)], with a spectral distribution unaffected by the polariton energy and a strong increase in emission efficiency with ω_p [already observed in Fig. (7.2b) at ~ 1 GeV].

We remark that polaritonic modes can be strongly populated by irradiation with ultrafast laser pulses at fluences creating a surface polariton density as high as $\rho_p \sim 1/\text{nm}^2$ without causing material damage, such that the scattering of 1 GeV photons [$\sigma^{\rm pol} \sim 10^{-16}$ nm^2, see Fig. (7.4b)] at a currently attainable illumination rate $r_\gamma \sim 10^6$/s[318] would lead to a pair-production rate $\rho_p r_\gamma \sigma^{\rm pol} \sim 10^{-10}$/s, while higher rates could potentially be achieved with alternative designs for efficient GeV photon sources[312,316].

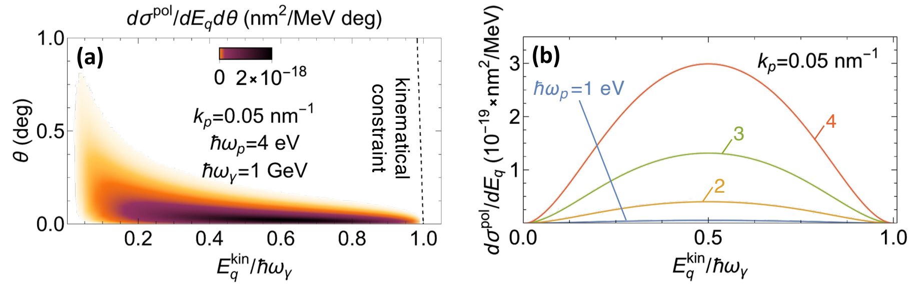

Figure 7.4: Pair production with polaritons and GeV γ-photons. (a) Pair-production differential cross section as a function of positron polar angle θ and kinetic energy $E_q^{\rm kin} = \hbar\varepsilon_q - m_{\rm e}c^2$ (normalized to the γ-photon energy $\hbar\omega_\gamma = 1$ GeV and averaged over an energy window $\Delta E_q^{\rm kin} = 1$ keV) for fixed polariton momentum $k_{\rm p} = 0.05$ nm^{-1} and energy $\hbar\omega_{\rm p} = 4$ eV. The dashed line represents the limit imposed by energy-momentum conservation for an azimuthal angle $\varphi = 0$. (b) Spectral distribution of positron emission (integrated over θ) for different polariton energies.

7.3 Concluding remarks

In summary, in this chapter we advocate for the use of optical excitations confined to nanostructured materials in combination with γ-rays as a way of producing electron-positron pairs with higher efficiency than free-space BW scattering and requiring substantially lower photon energies. Spatial symmetry breaking is responsible for the latter, whereas the spatial compression of the optical fields associated with surface polaritons facilitates the coupling to high-momentum products (the fermions), thus resulting in larger emission cross sections. We have analyzed in particular the interaction between γ-rays and polaritons confined to a 2D material, for which different types of modes exist[295,296], covering a broad range of energies and levels of spatial confinement. We remark that the combination of polaritons with the relatively low-energy γ-photons that we consider in this work (e.g., radioactivity from ^{60}Co) can lead to positron emission thanks to the breaking of translational symmetry associated with surface confinement, as otherwise, BW scattering is kinematically forbidden for collisions of few-eV and few-MeV free-space photons. The positron-creation probability can be further enhanced by concatenating several polaritonic structures (e.g., in a multilayer fashion). In a more general scenario, one could also consider γ-rays combined with the near fields produced upon laser irradiation of nanostructured materials, such as particle arrays, for which a higher degree of confinement commensurate with the particle size can be achieved in all three spatial dimensions[10]. An appealing advantage of the current positron creation scheme relates to spatiotemporal localization, as determined by the spatial distribution of the polaritons and the duration of the laser pulses used to create them. Future work in this direction could lead to a new generation of pulsed positron sources based on γ-ray interaction with confined optical excitations that are strongly populated by short laser pulses. Besides its practical use, the predicted effect of antimatter production from a collective optical excitation bears fundamental interest as an example of the application of nanophotonics to high-energy physics.

8

Conclusions and outlook

You should call it "entropy". No one knows what entropy really is, so in a debate you will always have the advantage.
John von Neumann to Claude Shannon

In conclusion, this Thesis tries to answer, by means of analytical and numerical tools, several questions regarding the fast dynamics associated with charged free particles traversing regions permeated by evanescent electromagnetic fields. We showed that this interaction can be exploited to meet different needs: from extracting information contained in a sample by measuring e-beam properties, encoded in their spatio-temporal correlations; from redesigning the transport properties of solid state systems by changing the dynamics of their charge carriers, to completely redraw the kinematical constraints of high-energy physics processes.

In particular, since each chapter addresses a specific topic but still leaves several open questions, in what follows we both summarize the conclusions drawn in each of them and provide some perspectives for future research:

- **Quantum photon-induced near-field electron microscopy (Chapter 2)**: this work, together with another published article by O. Kfir[87], sets the basis for the study of quantum correlations between fast electrons and optical excitations stored in long-lived cavity modes. In this regard, we explored the intimate relation between the initial cavity population and the peaks recorded in the electron spectra by showing how the latter are distributed for different scenarios [see Eqs. (2.11) and (2.12)] as well as their connection with the ℓ-th order correlation function [see Eq. (2.7)]. In addition, we showed how these results can be applied to track the time evolution of the mode population, when coupled to several types of excited three-level systems, by following the post-interaction electron energy distribution.

After this work was published, other theoretical studies pursued the same line of research, trying to merge the field of quantum optics with free electron beams. Among them, the possibility of producing exotic quantum cavity states by either relying on the sequential interaction of multiple electrons and their subsequent energy post-selection[319] or by going to low-energy ($\sim$ eV) e-beams, where kinematical recoil becomes significant[88], represents an interesting route to explore new quantum regimes. In parallel, advances in experimental designs have already showed to be capable of strongly coupling an electron and a cavity[106], which recently, in combination with electron-photon coincidence measurements, led to the corroboration of the strong correlations described by Eq. (2.1)[320].

- **Free-electron shaping using quantum light (Chapter 3)**: in this chapter, we showed how the wave function of a free electron can be molded through a PINEM interaction in which coherent laser illumination is replaced by quantum light. We focus on the effect on the modulation of the beam density after a macroscopic propagation in free space takes place by comparing equal-intensity coherent, amplitude- and phase-squeezed states. Here, the control over the phase uncertainty of the light state transforms into a control over the coherence of the electron temporal dynamics transitioning from a vanishing modulation in the limit of an incoherent state of light to a faster beam compression when phase-squeezing is employed.

  In a more general context, the idea of gaining additional control over scattering processes involving free electrons and light may still deserve some attention. In this respect, a recent theoretical study investigated the spectrum of emission connected to Compton scattering and predicted a band-width broadening when driven by thermal and squeezed vacuum states of light[321].

- **Electron diffraction by vacuum fluctuations (Chapter 4)**: this work was devoted to the exploration of the quantum phase arising from the solution of the electrodynamical problem of a nonrecoil e-beam coupling to a macroscopic electromagnetic environment. Here, we first connected it to the Aharonov-Bohm effect (see Section 4.2) induced by the self-image interaction acting back on the electron, and then, we explored its connection to elastic diffraction in different configurations. In addition, we found that electron decoherence, linked to the inelastic scattering events taking place during the trip from the electron gun to the analyzer, represents the resonant counterpart of such phase [see Eq. (4.8) in relation with Eq. (4.9)], thus suggesting the existence of a parameter space in which one of the two (inelastic and elastic scattering) prevails over the other.

  From the the two quantities explored, decoherence somehow represents the one having the closest connection to practical applications such as sensing and holography. In this regard, the effect of small-frequency excitations, leading to infrared divergences in the EEL probability [see Eq. (4.9) and Ref. 322], supported by macroscopic samples, still represents a theoretical challenge but has strong practical implications due to the fact that the detection of distant objects directly implies the exchange of photons with commensurate wavelenghts.

- **Modulation of cathodoluminescence emission by interference with external light (Chapter 5)**: in this chapter, we carried out an analysis of the far-field emission originated from the phase-locked interaction of a dimmed laser and a previously modulated electron. In particular, we demonstrated how interference between the two synchronized far fields (from CL emission and from light scattering) can strongly modulate the total CL signal, showing a complete suppression at optical frequencies by employing attosecond-compressed electrons. This effect may lead to a new path towards pump-probe measurements able to resolve excitations in time with meV-nm-fs precision.

  Even though this interference could directly be observed at a detector placed far from the sample, by producing CL emission coming from its interaction with the e-beam, as suggested in Ref. 144, both configurations share the same main practical challenge of designing a CL setup equipped with PINEM capabilities to shape the electron before its interaction with the specimen. Therefore, future efforts could be directed towards the realization of a compact and practical methodology, for instance leveraging all three space dimensions in which the electron is moving, capable of rendering a free electron beam fully coherent.

- **An image interaction approach to quantum-phase engineering of two-dimensional materials (Chapter 6)**: in this work, we analyzed the modifications of the transport properties induced in a 2D semiconductor by the presence of a neutral neighboring structure composed by a periodic patterning of conductive ribbons. We computed the modified band-structure, where we found that the opened band-gaps yield to a new zoo of single-particle and collective excitations.

  Besides the use of thin semiconductors, graphene may represent another viable option. Unfortunately, due to the spinorial nature of its charge carriers, gaps in graphene cannot be opened by acting with an external scalar potential[323]. Nonetheless, effects similar to the one presented in our work could still originate from the formation of satellite Dirac cones. In this respect, modulation of the static conductivity has been already demonstrated by directly shaping an applied gating potential[324], thus suggesting that equivalent results could be obtained with our configuration based on quantum-phase interactions.

- **Nanophotonics for pair-production (Chapter 7)**: in this submitted work, we advocate for the use of optical field confinement provided by electromagnetic modes bounded to material surfaces to redesign the rules associated with high-energy processes. Specifically, we propose a configuration in which a surface polariton traveling on a thin conductive material scatters with gamma rays to generate electron-positron pairs. While the kinematical constrains related to similar processes taking place in free space forbid their exploration, here we show how the breaking of translational symmetry along the direction perpendicular to the material surface relaxes them and, as one of the consequences, opens the door to the production of positrons with commercially available low-energy gamma ray sources.

  In light of these results, the question "*can nanophotonics have a significant impact in high-energy physics?*" naturally arises. In principle, the idea of compensating for the dramatically low probabilities associated with these kinds of processes through intense stimulation by external pumping of polaritonic modes could be generally applied as long as electromagnetic forces mediate the interaction. For instance, muons (with mass $m_\mu/m_\mathrm{e} \sim 211$) represent an other example of charged particle whose rate of creation could be similarly boosted by the interaction between strong near-fields and GeV photons. In this scenario, the currently feasible ability of molding the spatial field distribution of these collective excitations introduces an additional unexplored research path, which may lead to a new level of control over matter creation out of electromagnetic energy.

Particles characterized by a nonzero net charge have the ability to both create and being influenced by an electromagnetic field, which, in the presence of material boundaries, can be confined to the nanometer scale. The efficient light-matter coupling deriving from this property gives rise to a variety of effects, among which, only a few have been studied in this Thesis. However, we hope that the findings outlined here will serve as the starting point for future research in the field of nanophotonics combined with charged particles.

Appendices

A

SI and Gaussian units

Because the International System of Units (SI) is widely used in many fields, especially in engineering, which has a deep connection with physics, it is convenient to provide a guide to the link between the units used in this Thesis and SI. In particular, we use Gaussian Units (GU) throughout the entire manuscript.

We remark that conversions between quantities in these two unit systems are not direct unit conversions, because the quantities themselves are defined differently in each system. As a result, the equations expressing laws of physics governing the electromagnetic interactions, such as MEQS, will change depending on the system of units that is adopted. Therefore, with the objective of helping the reader in this task, below we provide a table that can be used to transform any equation from one unit system into the other.

Quantity	**Symbol**	SI	GU	**Conversion**
Electric charge	q	$\mathrm{A \cdot s}$	$L^{3/2}M^{1/2}/T$	$q^{\mathrm{GU}} = q^{\mathrm{SI}}/\sqrt{4\pi\varepsilon_0}$
Current density	$\mathbf{j}$	$\mathrm{A/m^2}$	$M^{1/2}/T^2L^{1/2}$	$\mathbf{j}^{\mathrm{GU}} = \mathbf{j}^{\mathrm{SI}}/\sqrt{4\pi\varepsilon_0}$
Scalar potential	ϕ	V	$M^{1/2}L^{1/2}/T$	$\phi^{\mathrm{GU}} = \sqrt{4\pi\varepsilon_0}\,\phi^{\mathrm{SI}}$
Vector potential	$\mathbf{A}$	$\mathrm{T/m}$	$M^{1/2}/L^{3/2}T$	$\mathbf{A}^{\mathrm{GU}} = \sqrt{4\pi/\mu_0}\,\mathbf{A}^{\mathrm{SI}}$
Electric field	$\mathbf{E}$	$\mathrm{V/m}$	$M^{1/2}/L^{1/2}T$	$\mathbf{E}^{\mathrm{GU}} = \sqrt{4\pi\epsilon_0}\,\mathbf{E}^{\mathrm{SI}}$
Displacement field	$\mathbf{D}$	$\mathrm{A \cdot s/m^2}$	$M^{1/2}/L^{1/2}T$	$\mathbf{D}^{\mathrm{GU}} = \sqrt{4\pi/\varepsilon_0}\,\mathbf{D}^{\mathrm{SI}}$
Magnetic field	$\mathbf{B}$	T	$M^{1/2}/L^{1/2}T$	$\mathbf{B}^{\mathrm{GU}} = \sqrt{4\pi/\mu_0}\,\mathbf{B}^{\mathrm{SI}}$
Magnetizing field	$\mathbf{H}$	$\mathrm{A/m}$	$M^{1/2}/L^{1/2}T$	$\mathbf{H}^{\mathrm{GU}} = \sqrt{4\pi\mu_0}\,\mathbf{H}^{\mathrm{SI}}$

Table A.1: Conversion between SI and Gaussian units. In the first column (starting from the left) the electromagnetic quantity under analysis is specified and the corresponding symbol, as it appears in this Thesis, is shown in the second column. In the third column, the units in SI are shown and in the fourth column we provide the associated dimensions of the same quantity in GU. In the latter, we use the nomenclature M = mass = g, T = time = s, and L = length = cm. The right-most column provides the conversion relations between the two systems of units through the vacuum permittivity $\epsilon_0 \approx 8.854 \times 10^{-12}$ F/m and permeability $\mu_0 \approx 1.256 \times 10^{-6}$ $\mathrm{N/A^2}$.

B

Derivation of the quantum PINEM Hamiltonian from the Dirac equation

In this appendix, we follow Ref. 30 to show how to reduce the spinorial Dirac equation to a scalar Schrödinger equation governed by the Hamiltonians in Eqs. 1.33 (Section 1.2), in which a classical electromagnetic field is introduced through the vector $\mathbf{A}(\mathbf{r},t)$ by using the general minimal coupling scheme and maintaining A^2 terms, but neglecting kinetic energy corrections beyond the nonrecoil approximation.

We begin by writing the Dirac equation reported in Eq. (1.29)

$$\left\{mc^2\beta + c\vec{\alpha}\cdot\left[\mathbf{p}+\frac{e}{c}\mathbf{A}(\mathbf{r},t)\right]\right\}\Psi(\mathbf{r},t) = \mathrm{i}\hbar\partial_t\Psi(\mathbf{r},t), \tag{B.1}$$

where the matrices β and $\vec{\alpha}$ are the ones introduced in Section 1.2. Then, by using a complete basis set of eigenstates $\Psi^{\pm}_{\mathbf{k}s}$ with fixed spin and momentum, s and $\mathbf{k}$ respectively, given by Eqs. (1.30) (provided that one dismisses the complex exponentials and pulls out the factor $1/\sqrt{V}$) satisfying the eigenvalue relations

$$(m_{\mathrm{e}}c^2\beta + \hbar c\vec{\alpha}\cdot\mathbf{k})\Psi^{\pm}_{\mathbf{k}s} = \pm\hbar\varepsilon_k\Psi^{\pm}_{\mathbf{k}s},$$

we expand the 4-component spinor solution as

$$\Psi(\mathbf{r},t) = \sum_{\pm}\sum_{\mathbf{k}s}\alpha^{\pm}_{\mathbf{k}s}\Psi^{\pm}_{\mathbf{k}s}\mathrm{e}^{\mathrm{i}\mathbf{k}\cdot\mathbf{r}\mp\mathrm{i}\varepsilon_k t}. \tag{B.2}$$

Now, under the conditions stated in Section 1.2, which are commonly met in EMs, with electron beams composed by a combination of momentum states lying close to a central value $\mathbf{k}_0$, namely satisfying the condition $|\mathbf{k}-\mathbf{k}_0| \ll k_0$, and interacting with an electromagnetic field of energy and momentum producing final electron states satisfying the same condition, we insert Eq. (B.2) into Eq. (B.1) and take the following approximations: (1) for each component $\Psi^\pm_{\mathbf{k}s}$, we linearize the energy (nonrecoil approximation) as $\varepsilon_k \approx \varepsilon_0\mathbf{v}\cdot(\mathbf{k}-\mathbf{k}_0) \to \varepsilon_0-(\mathrm{i}\nabla+\mathbf{k}_0)$, where $\varepsilon_0=\varepsilon_{k_0}$, and $\mathbf{v}=c^2\mathbf{k}_0/\varepsilon_0$ is the central electron velocity; (2) the momentum variation of $\Psi^\pm_{\mathbf{k}s}$ under a photon exchanges is neglected, so these spinors are replaced by $\Psi^\pm_{\mathbf{k}_0s}$. The latter assumption allows us to write the full spinor solution as

$$\Psi(\mathbf{r},t)=\sum_\pm\sum_s \psi^\pm_s(\mathbf{r},t)\Psi^\pm_{\mathbf{k}_0s}, \tag{B.3}$$

where we have defined the scalar wave functions

$$\psi^\pm_s(\mathbf{r},t)=\sum_{\mathbf{k}}\alpha^\pm_{\mathbf{k}s}\mathrm{e}^{\mathrm{i}\mathbf{k}\cdot\mathbf{r}\mp\mathrm{i}\varepsilon_k t}/\sqrt{V}. \tag{B.4}$$

We now multiply both sides of Eq. (B.1) by the hermitian conjugate of $\Psi^\pm_{\mathbf{k}_0s}$ from the left in order to obtain the following coupled equations

$$\begin{aligned}&\big[\hbar\varepsilon_0-\hbar\mathbf{v}\cdot(\mathrm{i}\nabla+\mathbf{k}_0)+(e\mathbf{v}/c)\cdot\mathbf{A}(\mathbf{r},t)-\mathrm{i}\hbar\partial_t\big]\psi^+_s(\mathbf{r},t) && \text{(B.5a)}\\ &\qquad\qquad+e\sum_{s'}\mathbf{A}(\mathbf{r},t)\cdot\mathbf{b}_{ss'}\psi^-_{s'}(\mathbf{r},t)=0,\\ -&\big[\hbar\varepsilon_0-\hbar\mathbf{v}\cdot(\mathrm{i}\nabla+\mathbf{k}_0)+(e\mathbf{v}/c)\cdot\mathbf{A}(\mathbf{r},t)-\mathrm{i}\hbar\partial_t\big]\psi^-_s(\mathbf{r},t) && \text{(B.5b)}\\ &\qquad\qquad+e\sum_{s'}\mathbf{A}(\mathbf{r},t)\cdot\mathbf{b}_{ss'}\psi^+_{s'}(\mathbf{r},t)=0.\end{aligned}$$

In the evaluation of Eqs. (B.5), we made use of the following spinorial relations

$$\begin{aligned}\Psi^{\pm\dagger}_{\mathbf{k}_0s}\Psi^\pm_{\mathbf{k}_0s'}&=\delta_{ss'}, && \text{(B.6a)}\\ \Psi^{\pm\dagger}_{\mathbf{k}_0s}\Psi^\mp_{\mathbf{k}_0s'}&=0, && \text{(B.6b)}\\ \Psi^{\pm\dagger}_{\mathbf{k}_0s}\vec{\alpha}\Psi^\pm_{\mathbf{k}_0s'}&=\pm(\mathbf{v}/c)\delta_{ss'}, && \text{(B.6c)}\\ \mathbf{b}_{ss'}\equiv\Psi^{\pm\dagger}_{\mathbf{k}_0s}\vec{\alpha}\Psi^\mp_{\mathbf{k}_0s'}&=\hat{\mathbf{s}}^\dagger[\vec{\sigma}-(1-1/\gamma)\hat{\mathbf{v}}(\hat{\mathbf{v}}\cdot\vec{\sigma})]\hat{\mathbf{s}}'. && \text{(B.6d)}\end{aligned}$$

In order to proceed with the proof, we introduce the slowing varying functions $\phi^\pm_s(\mathbf{r},t)$ as $\psi^\pm_s(\mathbf{r},t)=\mathrm{e}^{\mathrm{i}\mathbf{k}_0\cdot\mathbf{r}\mp\mathrm{i}\varepsilon_0t}\phi^\pm_s(\mathbf{r},t)$, which upon insertion into Eqs. (B.5) yield

$$\begin{aligned}&[-\mathrm{i}\hbar\mathbf{v}\cdot\nabla+e(\mathbf{v}/c)\cdot\mathbf{A}(\mathbf{r},t)]\phi^+_s(\mathbf{r},t)\\ &\qquad+e\mathbf{A}(\mathbf{r},t)\cdot\sum_{s'}\mathbf{b}_{ss'}\phi^-_{s'}(\mathbf{r},t)\mathrm{e}^{2\mathrm{i}\varepsilon_0t}=\mathrm{i}\hbar\partial_t\phi^+_s(\mathbf{r},t), && \text{(B.7a)}\\ &[\mathrm{i}\hbar\mathbf{v}\cdot\nabla-e(\mathbf{v}/c)\cdot\mathbf{A}(\mathbf{r},t)]\phi^-_s(\mathbf{r},t)\\ &\qquad+e\mathbf{A}(\mathbf{r},t)\cdot\sum_{s'}\mathbf{b}_{ss'}\phi^+_{s'}(\mathbf{r},t)\mathrm{e}^{-2\mathrm{i}\varepsilon_0t}=\mathrm{i}\hbar\partial_t\phi^-_s(\mathbf{r},t). && \text{(B.7b)}\end{aligned}$$

These equations describe the coupling between positive and negative energy components, ϕ^+_s and ϕ^-_s, respectively. We expect the one associated with positrons (ϕ^-_s) to be small at the energy scale on which we focus in this Thesis, so we decouple them by first neglecting the ϕ^-_s term in the left-hand side of Eq. (B.7b) compared with the $\phi^+_{s'}$ terms, as well as by noticing that the $\mathrm{e}^{2\mathrm{i}\varepsilon_0 t}$ factor dominates the time variation close to the latter. This allows us to integrate Eq. (B.7b) to yield the relation

$$\phi_s^-(\mathbf{r},t) \approx \frac{e}{2\hbar\varepsilon_0}\mathbf{A}(\mathbf{r},t)\cdot\sum_{s'}\mathbf{b}_{ss'}\phi_{s'}^+(\mathbf{r},t)\mathrm{e}^{-2\mathrm{i}\varepsilon_0 t}. \tag{B.8}$$

Then, we plug it into Eq. (B.7a) to retrieve the differential equation

$$\begin{aligned}&[-\mathrm{i}\hbar\mathbf{v}\cdot\nabla + (e\mathbf{v}/c)\cdot\mathbf{A}(\mathbf{r},t)]\phi_s^+(\mathbf{r},t) \\ &\quad+ \frac{e^2}{2\hbar\varepsilon_0}\sum_{s',s''}\left(\mathbf{A}(\mathbf{r},t)\cdot\mathbf{b}_{ss'}\right)\left(\mathbf{A}(\mathbf{r},t)\cdot\mathbf{b}_{s's''}\right)\phi_{s''}^+(\mathbf{r},t) = \mathrm{i}\hbar\partial_t\phi_s^+(\mathbf{r},t).\end{aligned} \tag{B.9}$$

By assuming the electron to travel along the z axis (i.e., $\mathbf{v} = v\hat{\mathbf{z}}$), and evaluating the spin summations through a long, but straightforward algebra, we find the identity $\sum_{s''}(\mathbf{A}\cdot\mathbf{b}_{ss''})(\mathbf{A}\cdot b_{s''s'}) = \delta_{ss'}(A_x^2 + A_y^2 + A_z^2/\gamma^2)$, which transforms Eq. (B.9) into the more familiar form

$$\mathrm{i}\hbar\partial_t\phi_s^+(\mathbf{r},t) = \mathcal{H}\phi_s^+(\mathbf{r},t), \tag{B.10}$$

with the Hamiltonian

$$\begin{aligned}\mathcal{H} = &-\mathrm{i}\hbar\mathbf{v}\cdot\nabla + (e\mathbf{v}/c)\cdot\mathbf{A}(\mathbf{r},t) \\ &+ \frac{e^2}{2m_\mathrm{e}c^2\gamma}\left[A_x^2(\mathbf{r},t) + A_y^2(\mathbf{r},t) + \frac{1}{\gamma^2}A_z^2(\mathbf{r},t)\right],\end{aligned} \tag{B.11}$$

where we used the relativistic relation $\hbar\varepsilon_0 = \gamma m_\mathrm{e}c^2$. Finally, Eq. (B.11) reduces to the sum of Eqs. (1.33) when Eq. (B.10) is written for the ψ_s^+ component.

We remark that in Section 1.2 we dismiss the negative energy solutions as smaller compared to ϕ_s^+ according to the ratio $|\phi_s^-/\phi_s^+| \sim eA/m_\mathrm{e}\gamma c^2$, which is obtained by inspecting Eq. (B.8) and, since the Hamiltonian in Eq. (B.11) is spin independent, we neglect any possibility of spin-flip.

C

On the field commutator and the electromagnetic Green tensor

C.1 Relevant field commutators

In this appendix, we provide a derivation of commutators between quantum fields in the interaction picture extensively used in Section 1.3 and Chapter 5. In addition, we use them to prove the correspondence between the quantum retarded response in Eq. (1.43) and its classical counterpart defined in Eq. (1.11).

Commutator between two vector potentials. One key relation in the computation of quantum electrodynamical quantities is represented by the commutator $[\hat{\mathbf{A}}^{\mathrm{I}}(\mathbf{r},t), \hat{\mathbf{A}}^{\mathrm{I}}(\mathbf{r}',t')]$ as it is required for the evaluation of the retarded response function G^{R} [Eq. (1.43)]. Its computation is done by recalling that the potential frequency components are related to the time-dependent components through (see Section 1.3)

$$\hat{\mathbf{A}}^{\mathrm{I}}(\mathbf{r},t) = \int_0^\infty \frac{d\omega}{2\pi} \mathrm{e}^{-\mathrm{i}\omega t} \hat{\mathbf{A}}^{\mathrm{I}}(\mathbf{r},\omega) + \text{ h.c.}, \tag{C.1}$$

which, together with the use of the explicit form of $\hat{\mathbf{A}}^{\mathrm{I}}(\mathbf{r},\omega)$ in terms of the noise current [see Eq. (1.46) and Eq. (1.47)] and by exploiting the commutators between bosonic operators and Eq. (1.48), leads to

$$\left[\hat{\mathbf{A}}^{\mathrm{I}}(\mathbf{r},t), \hat{\mathbf{A}}^{\mathrm{I}}(\mathbf{r}',t')\right] = 8\mathrm{i}c^2\hbar \int_0^\infty d\omega \sin\left[\omega(t-t')\right] \mathrm{Im}\{G(\mathbf{r},\mathbf{r}',\omega)\}. \tag{C.2}$$

As in vacuum, this commutator is a purely imaginary c-number, i.e. represents a multiple of the identity matrix in the Fock space of the dressed excitations. Incidentally, by using the fact that $G(\mathbf{r},\mathbf{r}',\omega)$ satisfies the Kramers-Kronig relations, as well as the causality property $G(-\omega)=G^*(\omega)$, we can plug Eq. (C.2) into Eq. (1.43) to find

$$G_{i,i'}(\mathbf{r},\mathbf{r}',\omega)=\int_{-\infty}^{\infty}dt\,\mathrm{e}^{\mathrm{i}\omega t}G^{\mathrm{R}}(\mathbf{r},\mathbf{r}',t), \tag{C.3}$$

which corroborates that within the MQED framework the quantum retarded Green tensor coincides with the classical Green tensor as Eq. (1.42) requires.

Commutators between the electric/magnetic field operators and the vector potential. Of particular interest are the different-time commutators between the quantum electromagnetic vector potential and the fields. These quantities can easily be obtained by using Eqs. (1.46) and (C.1), together with the relations $\hat{\mathbf{E}}(\mathbf{r},t)=(-1/c)\,\partial_t\hat{\mathbf{A}}(\mathbf{r},t)$ and $\hat{\mathbf{B}}(\mathbf{r},t)=\nabla\times\hat{\mathbf{A}}(\mathbf{r},t)$, which lead to

$$\left[\hat{B}^{\mathrm{I}}(\mathbf{r},t),\hat{A}^{\mathrm{I}}(\mathbf{r}',t')\right]=8\mathrm{i}c^2\hbar\int_0^{\infty}d\omega\;\sin[\omega(t-t')]\nabla\times\;\mathrm{Im}\left\{G(\mathbf{r},\mathbf{r}',\omega)\right\}, \tag{C.4a}$$

$$\left[\hat{E}^{\mathrm{I}}(\mathbf{r},t),\hat{A}^{\mathrm{I}}(\mathbf{r}',t')\right]=-8\mathrm{i}c\hbar\int_0^{\infty}\omega\,d\omega\;\cos[\omega(t-t')]\mathrm{Im}\left\{G(\mathbf{r},\mathbf{r}',\omega)\right\}. \tag{C.4b}$$

where again we made use of Eq. (1.48). In the calculation of the CL emission probability [Eq. (5.1)], we also need the retarded Green tensors constructed from the commutators in Eqs. (C.4) as

$$G^{\mathrm{R}}_{\mathrm{BA}}(\mathbf{r},\mathbf{r}',t-t')=-\frac{\mathrm{i}}{4\pi c^2\hbar}\left[\hat{B}^{\mathrm{I}}(\mathbf{r},t),\hat{A}^{\mathrm{I}}(\mathbf{r}',t')\right]\theta(t-t'), \tag{C.5a}$$

$$G^{\mathrm{R}}_{\mathrm{EA}}(\mathbf{r},\mathbf{r}',t-t')=-\frac{1}{4\pi c\hbar}\left[\hat{E}^{\mathrm{I}}(\mathbf{r},t),\hat{A}^{\mathrm{I}}(\mathbf{r}',t')\right]\theta(t-t') \tag{C.5b}$$

in the time domain, or equivalently,

$$G^{\mathrm{R}}_{\mathrm{BA}}(\mathbf{r},\mathbf{r}',\omega)=\int_{-\infty}^{\infty}dt\,\mathrm{e}^{\mathrm{i}\omega t}\,G^{\mathrm{R}}_{\mathrm{BA}}(\mathbf{r},\mathbf{r}',t)=\nabla\times G(\mathbf{r},\mathbf{r}',\omega), \tag{C.6a}$$

$$G^{\mathrm{R}}_{\mathrm{EA}}(\mathbf{r},\mathbf{r}',\omega)=\int_{-\infty}^{\infty}dt\,\mathrm{e}^{\mathrm{i}\omega t}\,G^{\mathrm{R}}_{\mathrm{EA}}(\mathbf{r},\mathbf{r}',t)=\omega\,G(\mathbf{r},\mathbf{r}',\omega) \tag{C.6b}$$

in the frequency domain. In the derivation of Eqs. (C.6), we used the fact that the electromagnetic Green tensor $G(\mathbf{r},\mathbf{r}',\omega)$ satisfies the Kramers-Kronig relations and the causality property $G(\mathbf{r},\mathbf{r}',-\omega)=G^*(\mathbf{r},\mathbf{r}',\omega)$.

Zero-time commutator between the displacement operator and the vector potential. In order to verify the connection between the Heisenberg and Maxwell's equations in the MQED formalism, the rest of the commutators already computed must be complemented with the zero-time product $[\hat{\mathbf{D}}(\mathbf{r}),\hat{\mathbf{A}}(\mathbf{r}')]$. In order to evaluate the latter expression, we make use of Eq. (1.45) and of the relations previously exploited to obtain

$$\left[\hat{\mathbf{D}}(\mathbf{r}),\hat{\mathbf{A}}(\mathbf{r}')\right]=-8c\hbar\mathrm{i}\int_0^{\infty}d\omega\,\mathrm{Im}\left\{\epsilon(\mathbf{r},\omega)G(\mathbf{r},\mathbf{r}',\omega)\right\}. \tag{C.7}$$

Due to the fact that the Green function $G(\omega)$ and the dielectric function $\epsilon(\omega)$ are analytic function in the upper-half of the complex plane [see below and Eqs. (1.67), (1.68)], the integral in Eq. (C.7) can be translated into an integral over an infinitely distant arch as

$$\left[\hat{\mathbf{D}}(\mathbf{r}), \hat{\mathbf{A}}(\mathbf{r}')\right] = 4\mathrm{i}c\hbar \lim_{|\omega|\to\infty} \int_0^\pi d\theta\, z^2 \epsilon(\mathbf{r}, z) G(\mathbf{r}, \mathbf{r}', z), \tag{C.8}$$

where $z = |\omega|\mathrm{e}^{\mathrm{i}\theta}$, we used again the aforementioned causality property and we wrote $\mathrm{Im}\{G(\omega)\} = [G(\omega) - G(-\omega)]/2\mathrm{i}$. Now, by plugging the relations

$$\lim_{|\omega|\to\infty} \begin{cases} z^2 G(\mathbf{r}, \mathbf{r}', z) = \delta(\mathbf{r} - \mathbf{r}')\mathcal{I}, \\ \epsilon(\mathbf{r}, z) = 1, \end{cases}$$

into Eq. (C.8), it becomes

$$\left[\hat{\mathbf{D}}(\mathbf{r}), \hat{\mathbf{A}}(\mathbf{r}')\right] = 4\mathrm{i}c\hbar\pi\delta(\mathbf{r} - \mathbf{r}')\mathcal{I}. \tag{C.9}$$

Finally, we remark that the same procedure to obtain Eq. (C.9) can be implemented in the calculation of the zero-time commutators in Eqs. (C.4) in order to render simpler expressions.

C.2 Derivation of Eq. (1.44)

In order to establish the validity of Eq. (1.44), we first wish to derive a few properties of the retarded tensor G^{R}. In order to do so, we start with its definition in a gauge with zero scalar potential at zero temperature [see Eq. (1.43)],

$$G^{\mathrm{R}}(\mathbf{r}, \mathbf{r}', t - t') = -\frac{\mathrm{i}}{4\pi\hbar c^2} \langle g| \left[\hat{\mathbf{A}}^{\mathrm{I}}(\mathbf{r}, t), \hat{\mathbf{A}}^{\mathrm{I}}(\mathbf{r}', t')\right] |g\rangle \theta(t - t'),$$

where θ is the step function, whereas $|g\rangle$ represents the system ground state. Now, we introduce a complete set of eigenstates $|n\rangle$ of the light+matter Hamiltonian $\hat{\mathcal{H}}_0^{\mathrm{f}}$ (i.e., $\hat{\mathcal{H}}_0^{\mathrm{f}}|n\rangle = \hbar\varepsilon_n|n\rangle$), use the relation $\hat{\mathbf{A}}^{\mathrm{I}}(\mathbf{r}, t) = \mathrm{e}^{\mathrm{i}\hat{\mathcal{H}}_0^{\mathrm{f}} t/\hbar} \hat{\mathbf{A}}(\mathbf{r}) \mathrm{e}^{-\mathrm{i}\hat{\mathcal{H}}_0^{\mathrm{f}} t/\hbar}$ between operators in the Schrödinger and interaction pictures, and apply the integral $\int_0^\infty dt\, \mathrm{e}^{\mathrm{i}st} = \mathrm{i}/(s + \mathrm{i}0^+)$ to write[325]

$$G^{\mathrm{R}}(\mathbf{r}, \mathbf{r}', \omega) = \frac{1}{4\pi\hbar c^2} \int_0^\infty d\omega' \left[\frac{J(\mathbf{r}, \mathbf{r}', \omega')}{\omega - \omega' + \mathrm{i}0^+} - \frac{J^*(\mathbf{r}, \mathbf{r}', \omega')}{\omega + \omega' + \mathrm{i}0^+}\right], \tag{C.10}$$

where

$$J(\mathbf{r}, \mathbf{r}', \omega) = \sum_n \langle g|\hat{\mathbf{A}}(\mathbf{r})|n\rangle\langle n|\hat{\mathbf{A}}(\mathbf{r}')|g\rangle\delta(\omega - \varepsilon_{n0})$$

is the spectral tensor and $\varepsilon_{n0} = \varepsilon_n - \varepsilon_0$, and $G^{\mathrm{R}}(\mathbf{r}, \mathbf{r}', \omega) = \int_{-\infty}^\infty dt\, \mathrm{e}^{\mathrm{i}\omega t}\, G^{\mathrm{R}}(\mathbf{r}, \mathbf{r}', t)$. As we have seen from Eq. (1.42), the retarded Green tensor in Eq. (C.10) directly corresponds to the classical electromagnetic Green tensor defined by Eq. (1.11), provided the optical response of the system is assumed to be described by a local, frequency-dependent permittivity $\epsilon(\mathbf{r}, \omega)$. Now, we introduce the quantum mechanical version of the time-reversal operator $\hat{\Theta}$. Under the assumption of time-reversal symmetry, we have $[\hat{\mathcal{H}}_0^{\mathrm{f}}, \hat{\Theta}] =$

0, and consequently, $\hat{\mathcal{H}}_0^{\rm f}|\hat{\Theta}n\rangle = \hbar\omega_n|\hat{\Theta}n\rangle$. Furthermore, assuming a non-degenerate ground state $|g\rangle$, it must obviously satisfy $|\hat{\Theta}g\rangle = |g\rangle$, and therefore, because the time-reversed eigenstates form a complete basis set with the same energies, we can rewrite the spectral tensor as

$$J(\mathbf{r},\mathbf{r}',\omega) = \sum_n \langle\hat{\Theta}g|\hat{\mathbf{A}}(\mathbf{r})|\hat{\Theta}n\rangle\langle\hat{\Theta}n|\hat{\mathbf{A}}(\mathbf{r}')|\hat{\Theta}g\rangle\delta(\omega-\varepsilon_{n0}).$$

Then, using the relation[326]

$$\langle n|\hat{O}|n'\rangle^* = \pm\langle\hat{\Theta}n|\hat{O}|\hat{\Theta}n'\rangle,$$

which is valid for any Hermitian operator $\hat{O}$ (e.g., with $-$ for $\hat{O}=\hat{\mathbf{A}}$), we find that

$$J(\mathbf{r},\mathbf{r}',\omega) = J^*(\mathbf{r},\mathbf{r}',\omega)$$

is real. Finally, taking the imaginary part of Eq. (C.10) and using the above property of J, together with $1/(s+\mathrm{i}0^+) = P[1/s] - \mathrm{i}\pi\delta(s)$, we obtain

$$J(\mathbf{r},\mathbf{r}',\omega) = -4\hbar c^2\,\mathrm{Im}\left\{G(\mathbf{r},\mathbf{r}',\omega)\right\}, \tag{C.11}$$

for $\omega > 0$. Then, we by just taking the Fourier transform of the fields in the interaction picture and by restricting ourselves to positive frequencies, we can write

$$\frac{1}{2}\langle g|\left\{\hat{\mathbf{A}}^{\rm I}(\mathbf{r},\omega),\hat{\mathbf{A}}^{\rm I}(\mathbf{r}',\omega')\right\}|g\rangle = 2\pi^2 J(\mathbf{r},\mathbf{r}',\omega),$$

which by making use of Eq. (C.11) directly leads to Eq. (1.44).

D

Solution of the quantum PINEM Hamiltonian

D.1 Solution for a single nonrecoil electron and a multi-mode system

In this section, we prove how the effective Schrödinger equation presented in Chapters 2 and 3 for a single-mode cavity, and in Chapter 4 for a medium supporting an infinite set of modes, admits the analytical solution in Eqs. (2.1), (3.2), and (4.10), respectively.

We start by describing the quantum radiation field by incorporating the radiation Hamiltonian $\hat{\mathcal{H}}_0^{\rm f}$ [see Eq. (1.51)] into Eq. (1.33a), and using the quantum vector field $\hat{\mathbf{A}}$ instead of $\mathbf{A}$ in Eq. (1.33b). In this effective theory, we now expand the wave function of the joint electron-field system as $|\psi(\mathbf{r},t)\rangle=\sum_{\{n\}}\psi_{\{n\}}(\mathbf{r},t)|\{n\}\rangle$ to describe a distinct scalar electron wave function $\psi_{\{n\}}(\mathbf{r},t)$ for each of the possible number states $|\{n\}\rangle$ of the boson ensemble, so that we finally write the Schrödinger equation by disregarding the ponderomotive terms:

$$(\hat{\mathcal{H}}_0^{\rm par}+\hat{\mathcal{H}}_1^{\rm par})|\psi(\mathbf{r},t)\rangle={\rm i}\hbar\partial_t|\psi(\mathbf{r},t)\rangle \tag{D.1}$$

with

$$\hat{\mathcal{H}}_0^{\rm par}=\sum_i\hbar\omega_i\,\hat{a}_i^\dagger\hat{a}_i+\hbar\varepsilon_0-\hbar\mathbf{v}\cdot({\rm i}\nabla+\mathbf{k}_0), \tag{D.2}$$

$$\hat{\mathcal{H}}_1^{\rm par}=(e\mathbf{v}/c)\cdot\hat{\mathbf{A}}(\mathbf{r}). \tag{D.3}$$

Taking the electron beam to be oriented along the z direction, we can write the ansatz solution

$$|\psi(\mathbf{r},t)\rangle=\psi_0(\mathbf{r},t)\sum_{\{n\}\{\ell\}}{\rm e}^{{\rm i}\sum_i\omega_i[\ell_i(z/v-t)-n_it]}f_{\{\ell\}}^{\{n\}}(\mathbf{r})|\{n\}\rangle, \tag{D.4}$$

where $\psi_0(\mathbf{r},t) = \mathrm{e}^{\mathrm{i}\mathbf{k}_0\cdot\mathbf{r}-\mathrm{i}\varepsilon_0 t}\phi_0(\mathbf{r}-\mathbf{v}t)$, while $\{\ell\}$ denotes the set of net numbers of photons exchanged with each of the modes $\ell_1,\dots,\ell_i,\dots$ (positive ℓ_i for photon absorption and negative for emission). By plugging Eq. (D.4) into Eq. (D.1), we find that the expansion coefficients in this expression must satisfy the differential equation

$$\partial_z f_{\{\ell\}}^{\{n\}} = \sum_i \left[\sqrt{n_i}\, u_i^*\, f_{\ell_1,\dots,\ell_i+1,\dots}^{n_1,\dots,n_i-1,\dots} - \sqrt{n_i+1}\, u_i\, f_{\ell_1,\dots,\ell_i-1,\dots}^{n_1,\dots,n_i+1,\dots}\right], \tag{D.5}$$

where $u_i(z) = (e/\hbar\omega_i)\mathcal{E}_{i,z}(z)\mathrm{e}^{-\mathrm{i}\omega_i z/v}$. We note that Eq. (D.5) guarantees that $n_i+\ell_i$ is conserved along the interaction for each i, indicating that the number of excitations in the electron-boson system is preserved. This interesting property implies that Eq. (D.5) corresponds to the time evolution of a set of classically driven quantum harmonic oscillators, and therefore, it can be solved analytically[89]. Indeed, we can write the Hamiltonian of such harmonic oscillators as

$$\hat{\mathcal{H}} = \sum_i \left[\hbar\omega_i \hat{a}_i^\dagger \hat{a}_i + g_j(t)\hat{a}_i + g_i^*(t)\hat{a}_i^\dagger\right],$$

which, by introducing a general state $|\psi(t)\rangle = \sum_{\{n\}} c_{\{n\}}(t)\mathrm{e}^{-\mathrm{i}\sum_i n_i\omega_i t}|\{n\}\rangle$ into the associated Schrödinger equation, leads to

$$\mathrm{i}\hbar\partial_t c_{\{n\}} = \sum_i \left[\sqrt{n_i}\, g_i^*\, c_{n_1,\dots,n_i-1,\dots}\mathrm{e}^{\mathrm{i}\omega_i t} + \mathrm{e}^{-\mathrm{i}\omega_i t}\sqrt{n_i+1}\, g_i\, c_{n_1,\dots,n_i+1,\dots}\right]. \tag{D.6}$$

We immediately notice that Eq. (D.6) is equivalent to Eq. (D.5) if we make the substitutions

$$g_i\mathrm{e}^{-\mathrm{i}\omega_i t} \to -\mathrm{i}\hbar v u_i, \quad t \to z/v. \tag{D.7}$$

This allows us to use the well-known solution of Eq. (D.6) in terms of the evolution operator[52]

$$\hat{\mathcal{S}}(t,t_0) = \mathrm{e}^{\mathrm{i}\chi}\prod_i \mathrm{e}^{\beta_i^*\hat{a}_i^\dagger - \beta_i\hat{a}_i}, \tag{D.8}$$

where $\beta_i(t,t_0) = \frac{\mathrm{i}}{\hbar}\int_{t_0}^t dt' g_i(t')\mathrm{e}^{-\mathrm{i}\omega_i t'}$ and $\chi = -\frac{1}{\hbar}\sum_i \int_{t_0}^t dt' \mathrm{Re}\{\beta_i(t',t_0)g_i^*(t')\mathrm{e}^{\mathrm{i}\omega_i t'}\}$. Incidentally, χ has been shown to be a Berry phase[327] in the context of a driven quantum harmonic oscillator, so it underlies the fact that the system under study is open, and not all the degrees of freedom are taken into account. We show below that the role of χ in the interaction with the electron is to produce a phase shift in its wave function. Incidentally, this phase is exploited in Chapter 6 as a way to modify material properties through the presence of neighboring neutral structures. From Eq. (D.8), we can calculate the transition amplitudes between photon number states as

$$\langle\{n\}|\hat{\mathcal{S}}(t,t_0)|\{n_0\}\rangle = \mathrm{e}^{\mathrm{i}\chi}\prod_i A_i,$$

where we define the single-mode transition amplitude as

$$\begin{aligned} A_i &= \langle n_i|\mathrm{e}^{\beta_i^*\hat{a}_i^\dagger - \beta_i\hat{a}_i^\dagger}|n_{0,i}\rangle \\ &= \sqrt{n_{0,i}!n_i!}\,\mathrm{e}^{-|\beta_i|^2/2}(-\beta_i)^{n_{0,i}-n_i}\sum_{n_i'=\max\{0,n_i-n_{0,i}\}}^{n_i}\frac{(-|\beta_i|^2)^{n_i'}}{n_i'!(n_{0,i}-n_i+n_i')!(n_i-n_i')!}. \end{aligned} \tag{D.9}$$

Now, we can perform the substitution (D.7) to solve our QED model by finding the coefficients of Eq. (D.4). In particular, taking the photon field state to be represented by some coefficients $\alpha_{\{n_0\}}$ right before interaction with the electron, we have

$$f_{\{\ell\}}^{\{n\}}(\mathbf{r}) = \mathrm{e}^{\mathrm{i}\chi(\mathbf{r})} c_{\{n+\ell\}} \prod_i \sqrt{(n_i+\ell_i)!n_i!}\, \mathrm{e}^{-|\beta_i(\mathbf{r})|^2/2} (-\beta_i(\mathbf{r}))^{\ell_i} \\ \times \sum_{n_i'=\max\{0,-\ell_i\}}^{n_i} \frac{(-|\beta_i(\mathbf{r})|^2)^{n_i'}}{n_i'!(\ell_i+n_i')!(n_i-n_i')!}, \tag{D.10}$$

where we have used the conservation of quantum numbers $n_{0,i} = \ell_i + n_i$ together with the fact that the initial electron state has $\ell_{0,i} = 0$ for all modes. Finally, by restricting to a single mode with label $i = 0$, we recover the solutions given in Chapters 2 and 3.

D.2 Solution using second-quantized operators and MQED

General evolution operator

A solution of the dynamics in the nonrecoil approximation, as provided in the previous section, can be equally obtained in the context of second quantization, therefore also allowing for the presence of several electrons in a beam. Within this framework, by using the recipe described in Section 1.2 to go from first to second quantization, we can write the free electron part of Eq. (D.2) as $\hat{\mathcal{H}}_0^{\mathrm{el}} = \sum_{\mathbf{k}} [\hbar\varepsilon_0 + \hbar\mathbf{v}\cdot(\mathbf{k}-\mathbf{k}_0)]\, \hat{c}_{\mathbf{k}}^\dagger \hat{c}_{\mathbf{k}}$ and Eq. (D.3) in the interaction picture as

$$\hat{\mathcal{H}}_{\mathrm{int}}(t) = \frac{-1}{c} \int d^3\mathbf{r}\, \hat{\mathbf{j}}^{\mathrm{el}}(\mathbf{r},t)\cdot\hat{\mathbf{A}}^{\mathrm{I}}(\mathbf{r},t), \tag{D.11}$$

where the electron current reads

$$\hat{\mathbf{j}}^{\mathrm{el}}(\mathbf{r},t) = -\frac{e\mathbf{v}}{V}\sum_{\mathbf{q},\mathbf{k}} \mathrm{e}^{\mathrm{i}\mathbf{k}\cdot(\mathbf{r}-\mathbf{v}t)}\, \hat{c}_{\mathbf{q}}^\dagger \hat{c}_{\mathbf{q}+\mathbf{k}}. \tag{D.12}$$

V is the volume of the quantization box, so wave vector sums can be transformed into integrals using the prescription $\sum_{\mathbf{k}} \to (V/8\pi^3)\int d^3\mathbf{k}$. A fundamental property of the current in Eq. (D.12) can be found by repeatedly using the anticommutation relations to pull all electron creation operators to the left, leading to

$$\left[\hat{\mathbf{j}}^{\mathrm{el}}(\mathbf{r},t), \hat{\mathbf{j}}^{\mathrm{el}}(\mathbf{r}',t')\right] = 0. \tag{D.13}$$

Equation (D.13) tells us that, by commuting at different times, the electron current can be treated as a scalar function by at the same time maintaining its operatorial character. An important consequence of this property is given by the commutator between two Hamiltonian operators, which reads

$$\left[\hat{\mathcal{H}}_{\mathrm{int}}(t), \hat{\mathcal{H}}_{\mathrm{int}}(t')\right] = \frac{1}{c^2}\int d^3\mathbf{r} d^3\mathbf{r}'\, \hat{\mathbf{j}}^{\mathrm{el}}(\mathbf{r},t)\cdot\left[\hat{\mathbf{A}}^{\mathrm{I}}(\mathbf{r},t), \hat{\mathbf{A}}^{\mathrm{I}}(\mathbf{r}',t')\right]\cdot\hat{\mathbf{j}}^{\mathrm{el}}(\mathbf{r}',t').$$

Additionally, Eq. (C.2) directly implies that $\left[\hat{\mathbf{A}}^{\rm I}(\mathbf{r},t),\hat{\mathbf{A}}^{\rm I}(\mathbf{r}',t')\right]$ is a c-number, which in turn leads to the nested commutation relation

$$\left[\hat{\mathcal{H}}_{\rm int}(t''),\left[\hat{\mathcal{H}}_{\rm int}(t),\hat{\mathcal{H}}_{\rm int}(t')\right]\right]=0. \tag{D.14}$$

This expression is important to derive the expression in Eq. (4.2) for the scattering operator starting from its definition $\hat{\mathcal{S}}(t,t_0)=\mathrm{T}\exp\left[(-\mathrm{i}/\hbar)\int_{t_0}^{t}dt'\,\hat{\mathcal{H}}_{\rm int}(t')\right]$, where T denotes time ordering. This can be done by resorting to the so-called Magnus expansion[328], which asserts that $\hat{\mathcal{S}}$ can be written in terms of a perturbative expansion of an operator in the exponent as

$$\hat{\mathcal{S}}(t,t_0)=\exp\left\{\sum_{i=1}^{\infty}\hat{\Omega}^{(i)}(t,t_0)\right\},$$

with

$$\begin{aligned}
\hat{\Omega}^{(1)}(t,t_0)&=\frac{-\mathrm{i}}{\hbar}\int_{t_0}^{t}dt'\,\hat{\mathcal{H}}_{\rm int}(t'),\\
\hat{\Omega}^{(2)}(t,t_0)&=\frac{-1}{2\hbar^2}\int_{t_0}^{t}dt'dt''\,\theta(t'-t'')\left[\hat{\mathcal{H}}_{\rm int}(t'),\hat{\mathcal{H}}_{\rm int}(t'')\right],\\
&\;\;\vdots\\
\hat{\Omega}^{(n)}(t,t_0)&=\dots,
\end{aligned}$$

and where the n-th order operator is formed by nesting $n-1$ commutators. By making use of the property in Eq. (D.14), the chain of commutators can be closed to $\hat{\Omega}^{(2)}(t,t_0)$, which allows us to write the scattering operator in the simple form (by setting $t_0=-\infty$)

$$\hat{\mathcal{S}}(t,-\infty)=\mathrm{e}^{\mathrm{i}\hat{\chi}(t,-\infty)}\hat{\mathcal{U}}(t,-\infty), \tag{D.15}$$

where we have introduced the phase operator

$$\begin{aligned}\hat{\chi}(t,-\infty)=\frac{\mathrm{i}}{2\hbar^2c^2}\int_{-\infty}^{t}dt'dt''\int d^3\mathbf{r}\,d^3\mathbf{r}'\,\theta(t'-t'')\\
\times\hat{\mathbf{j}}^{\rm el}(\mathbf{r},t')\cdot\left[\hat{\mathbf{A}}^{\rm I}(\mathbf{r},t'),\hat{\mathbf{A}}^{\rm I}(\mathbf{r}',t'')\right]\cdot\hat{\mathbf{j}}^{\rm el}(\mathbf{r}',t'')\end{aligned} \tag{D.16}$$

and the inelastic operator

$$\hat{\mathcal{U}}(t,-\infty)=\exp\left\{\frac{\mathrm{i}}{\hbar c}\int_{-\infty}^{t}dt'\int d^3\mathbf{r}\,\hat{\mathbf{j}}^{\rm el}(\mathbf{r},t')\cdot\hat{\mathbf{A}}^{\rm I}(\mathbf{r},t')\right\}. \tag{D.17}$$

Interestingly, since the commutator between the electromagnetic potentials is a c-number, the operator $\hat{\chi}(t,-\infty)$ acts only on the degrees of freedom associated with the currents and represents the effect of the image potential acting on the free charges (see Chapter 4).

One is often interested in calculating asymptotic quantities such as electron spectra at $t=\infty$. We then need to know the scattering operator $\hat{\mathcal{S}}(\infty,-\infty)$, which can be obtained by using Eqs. (C.1) and (D.12), leading to

$$\hat{\mathcal{U}} = \exp\left\{\left[\frac{-\mathrm{i}e}{2\pi\hbar c L^2}\sum_{\mathbf{q},\mathbf{k}}\int_0^\infty d\omega\int d^3\mathbf{r}\,\mathrm{e}^{\mathrm{i}\mathbf{k}\cdot\mathbf{R}}\mathrm{e}^{-\mathrm{i}\omega z/v}\hat{A}_z(\mathbf{r},\omega)\,\hat{c}^\dagger_{\mathbf{q}}\hat{c}_{\mathbf{q}+\mathbf{k}-(\omega/v)\hat{\mathbf{z}}}\right] - \text{h.c.}\right\}.$$

When the electron is focused around a point $\mathbf{R} = \mathbf{R}_0$ and its wave function can be separated in longitudinal and transverse components, we can approximate $\hat{c}_{\mathbf{q}} \approx \hat{c}_{\mathbf{q}_\perp}\hat{c}_{q_z}$ and replace the operator in the exponent of $\hat{\mathcal{U}}$ by its average over a transverse electron state $|\psi_\perp\rangle = \sum_{\mathbf{q}_\perp}\alpha_{\mathbf{q}_\perp}|\mathbf{q}_\perp\rangle$ satisfying the relation $\sum_{\mathbf{k}_\perp}\alpha_{\mathbf{k}_\perp}\alpha^*_{\mathbf{k}_\perp+\mathbf{q}_\perp} = \mathrm{e}^{\mathrm{i}\mathbf{q}_\perp\cdot\mathbf{R}_0}$, from which we find

$$\hat{\mathcal{U}} = \exp\left[\int_0^\infty d\omega\, g_\omega(\hat{b}^\dagger_\omega\hat{a}_\omega - \hat{b}_\omega\hat{a}^\dagger_\omega)\right]. \tag{D.18}$$

Here, we have introduced the operators $\hat{a}_\omega = (-\mathrm{i}e/2\pi\hbar c\, g_\omega)\int_{-\infty}^\infty dz\mathrm{e}^{-\mathrm{i}\omega z/v}\hat{A}_z(\mathbf{R}_0,z,\omega)$ and $\hat{b}_\omega = \sum_{q_z}\hat{c}^\dagger_{q_z}\hat{c}_{q_z+\omega/v}$, as well as the coupling coefficient $g_\omega = \sqrt{\Gamma_{\mathrm{EEL}}(\mathbf{R}_0,\omega)}$, which reduces to the square root of the classical EEL probability (see Section 1.1)

$$\Gamma_{\mathrm{EEL}}(\mathbf{R}_0,\omega) = \frac{4e^2}{\hbar}\int_{-\infty}^\infty dz\,dz'\cos\left[\omega(z-z')/v\right]\mathrm{Im}\left\{-G_{zz}(\mathbf{R}_0,z,\mathbf{R}_0,z',\omega)\right\}.$$

We define these operators in such a way that they satisfy the commutation relations $[\hat{a}_\omega,\hat{a}^\dagger_{\omega'}] = \delta(\omega-\omega')$ and $[\hat{b}_\omega,\hat{b}^\dagger_{\omega'}] = 0$, where the former can be proven by using Eq. (1.48). Importantly, Eq. (D.18) allows us to quickly compute observables after electron-sample interaction. As an example of this, we find that the average of the positive-energy electric field operator $\hat{\mathbf{E}}^{(+)}(\mathbf{r},\omega) = \mathrm{i}k\hat{\mathbf{A}}(\mathbf{r},\omega)$ over the state $|\psi(\infty)\rangle = \hat{\mathcal{S}}(\infty,-\infty)|\psi(-\infty)\rangle$ with $|\psi(-\infty)\rangle = \sum_{q_z}\alpha_{q_z}\hat{c}^\dagger_{q_z}|0\rangle$ (proportional to the photonic vacuum) reduces to $\langle\hat{\mathbf{E}}^{(+)}(\mathbf{r},\omega)\rangle = 8\pi e\omega\,\mathbf{G}(\mathbf{r},\omega)M^*_{\omega/v}$, where $\mathbf{G}(\mathbf{r},\omega) = \int_{-\infty}^\infty dz'\,\mathrm{e}^{\mathrm{i}\omega z'/v}\mathrm{Im}\{G(\mathbf{r},\mathbf{R}_0,z',\omega)\}\cdot\hat{\mathbf{z}}$. To derive this result, we need to use the relation $[\hat{A},\mathrm{e}^{\hat{B}}] = C\mathrm{e}^{\hat{B}}$ (valid if $[\hat{A},\hat{B}] = C$ is a c-number), as well as the commutation relation $[\hat{\mathbf{f}}(\mathbf{r},\omega),\int_0^\infty d\omega' g_{\omega'}(\hat{b}_{\omega'}\hat{a}^\dagger_{\omega'} - \hat{b}^\dagger_{\omega'}\hat{a}_{\omega'})] = (-2\mathrm{i}e\omega/\hbar)\,\hat{b}_\omega\sqrt{\hbar\mathrm{Im}\{\epsilon(\mathbf{r},\omega)\}}\int_{-\infty}^\infty dz'\,\mathrm{e}^{\mathrm{i}\omega z'/v}G(\mathbf{r},\mathbf{R}_0,z',\omega)\cdot\hat{\mathbf{z}}$ together with the fact that the fermionic operators $\hat{b}_\omega$ and $\hat{b}^\dagger_\omega$ commute.

E

Quantum CL emission: proofs of some expressions presented in Chapter 5

E.1 Far-field radiation emission: derivation of Eq. (5.1)

In this section, we calculate the far-field emission produced by quantum currents taking into consideration the quantum nature of the electromagnetic excitations. To this aim and similarly for the classical case, we define the average electromagnetic energy flow through a solid angular region $\Delta\Omega$ as

$$\Delta E = \lim_{kr\to\infty} r^2 \int_{-\infty}^{\infty} dt \int_{\Delta\Omega} d^2\Omega_{\hat{\mathbf{r}}} \, \big\langle\psi(-\infty)\big|\hat{\mathbf{S}}^{\mathrm{H}}(\mathbf{r},t)\cdot\hat{\mathbf{r}}\big|\psi(-\infty)\big\rangle, \tag{E.1}$$

where $k=\omega/c$, $\hat{\mathbf{S}}^{\mathrm{H}}(\mathbf{r},t)=(c/8\pi)\,\Big[\hat{\mathbf{E}}^{\mathrm{H}}(\mathbf{r},t)\times\hat{\mathbf{B}}^{\mathrm{H}}(\mathbf{r},t)-\hat{\mathbf{B}}^{\mathrm{H}}(\mathbf{r},t)\times\hat{\mathbf{E}}^{\mathrm{H}}(\mathbf{r},t)\Big]$ is the quantum mechanical counterpart of the classical Poynting vector defined in Eq. (1.5b), and $|\psi(-\infty)\rangle$ is the initial quantum state at time $t=-\infty$. The superscript H indicates that operators have to be calculated in the Heisenberg picture, and thus evolved with the total Hamiltonian

$$\hat{\mathcal{H}}_{\mathrm{tot}} = \hat{\mathcal{H}}_0^{\mathrm{f}} + \hat{\mathcal{H}}_0^{\mathrm{el}} + \hat{\mathcal{H}}_{\mathrm{int}},$$

where the Hamiltonians $\hat{\mathcal{H}}_0^{\mathrm{el}}$ and $\hat{\mathcal{H}}_{\mathrm{int}}$ are the ones used in Section D.2. As already done in Section 1.3, the full time evolution can be expressed in terms of the scattering operator $\hat{\mathcal{S}}(t,-\infty)$ by incorporating an adiabatic switching of the interaction, which leads to the relation $\mathrm{e}^{-\mathrm{i}\hat{\mathcal{H}}_{\rm tot}t/\hbar}=\mathrm{e}^{-\mathrm{i}(\hat{\mathcal{H}}_0^{\rm f}+\hat{\mathcal{H}}_0^{\rm el})t/\hbar}\hat{\mathcal{S}}(t,-\infty)$[40], and from here, Eq. (E.1) becomes

$$\begin{aligned}\Delta E = \lim_{kr\to\infty}\ r^2\int_{-\infty}^{\infty}dt\int_{\Delta\Omega}d^2\Omega_{\hat{\mathbf{r}}} \\ \times\langle\psi(-\infty)|\hat{\mathcal{S}}^\dagger(t,-\infty)\,\hat{\mathbf{S}}(\mathbf{r},t)\cdot\hat{\mathbf{r}}\,\hat{\mathcal{S}}(t,-\infty)|\psi(-\infty)\rangle.\end{aligned} \tag{E.2}$$

We now describe the interaction between the electromagnetic field and a total quantum current $\hat{\mathbf{j}}(\mathbf{r},t)$ through the minimal coupling Hamiltonian in the WG as

$$\hat{\mathcal{H}}_{\rm int}(t) = -\frac{1}{c}\int d^3\mathbf{r}\ \hat{\mathbf{A}}(\mathbf{r},t)\cdot\hat{\mathbf{j}}(\mathbf{r},t), \tag{E.3}$$

where the time dependence in $\hat{\mathcal{H}}_{\rm int}(t)$ indicates that it is expressed in the interaction picture (i.e., the free part of the Hamiltonian, $\hat{\mathcal{H}}_0^{\rm f}+\hat{\mathcal{H}}_0^{\rm el}$, is taken care of through the scattering matrix). If we now assume that the current $\hat{\mathbf{j}}$ commutes at different times, we can use the results obtain in Section D.2 to write the scattering operator as $\hat{\mathcal{S}}(t,-\infty)=\exp\left[\mathrm{i}\,\hat{\chi}(t,-\infty)\right]\ \exp\left[(-\mathrm{i}/\hbar)\int_{-\infty}^{t}dt'\,\hat{\mathcal{H}}_{\rm int}(t')\right]$. From here, we plug it into Eq. (E.2) and then use twice the identity $[\hat{A},\mathrm{e}^{\hat{B}}]=C\mathrm{e}^{\hat{B}}$ (valid if $[\hat{A},\hat{B}]=C$ is a c-number) to bring the rightmost scattering operator to cancel its Hermitian conjugate on the left. This leads us to

$$\begin{aligned}\Delta E = \lim_{kr\to\infty}\frac{c\,r^2}{8\pi}\int_{-\infty}^{\infty}dt\int_{\Delta\Omega}d^2\Omega_{\hat{\mathbf{r}}}\ \Bigg\langle\left\{\hat{\mathbf{E}}(\mathbf{r},t)-\frac{\mathrm{i}}{\hbar}\int_{-\infty}^{t}dt'\left[\hat{\mathbf{E}}(\mathbf{r},t),\hat{\mathcal{H}}_{\rm int}(t')\right]\right\} \\ \times\left\{\hat{\mathbf{B}}(\mathbf{r},t)-\frac{\mathrm{i}}{\hbar}\int_{-\infty}^{t}dt'\left[\hat{\mathbf{B}}(\mathbf{r},t),\hat{\mathcal{H}}_{\rm int}(t')\right]\right\}\Bigg\rangle\cdot\hat{\mathbf{r}}+\text{c.c.},\end{aligned} \tag{E.4}$$

where we have defined the quantum average as $\langle\cdot\rangle=\langle\psi(-\infty)|\cdot|\psi(-\infty)\rangle$. The term $\hat{\mathbf{E}}(\mathbf{r},t)\times\hat{\mathbf{B}}(\mathbf{r},t)$ in Eq. (E.4), which is independent of the sources, represents the contribution from the zero-point energy, so it bears no relevance to this analysis. In addition, since the commutators between the vector potential and the field operators are c-numbers, the terms linear in the currents (i.e., through $\hat{\mathcal{H}}_{\rm int}$) in Eq. (E.4) vanish when they are averaged over an initial state $|\psi(-\infty)\rangle$ in which the radiation part is prepared in the photonic vacuum. Now, we use the retarded Green functions [Eqs. (C.5)] and their Fourier transforms [Eqs. (C.6)] to obtain

$$\Delta E = \int_0^\infty\hbar\omega\,d\omega\int_{\Delta\Omega}d^2\Omega_{\hat{\mathbf{r}}}\ \frac{d\Gamma_{\rm ff}}{d\Omega_{\hat{\mathbf{r}}}d\omega},$$

where

$$\frac{d\Gamma_{\rm ff}}{d\Omega_{\hat{\mathbf{r}}}d\omega} = \lim_{kr\to\infty}\ \frac{r^2}{4\pi^2\hbar k}\mathrm{Re}\left\{\left\langle\hat{\mathcal{E}}(\mathbf{r},\omega)\times\hat{\mathcal{B}}^\dagger(\mathbf{r},\omega)\right\rangle\right\}\cdot\hat{\mathbf{r}} \tag{E.5}$$

is the angle- and frequency-resolved, time-integrated, far-field (ff) photon emission probability of Eq. (5.1). Here, we have defined the new field operators

$$\begin{aligned}\hat{\mathcal{E}}(\mathbf{r},\omega) &= -\,4\mathrm{i}\pi\,\omega\int d^3\mathbf{r}'\,G(\mathbf{r},\mathbf{r}',\omega)\cdot\hat{\mathbf{j}}(\mathbf{r}',\omega),\\ \hat{\mathcal{B}}(\mathbf{r},\omega) &= -\,4\pi\,c\,\nabla\times\int d^3\mathbf{r}'\,G(\mathbf{r},\mathbf{r}',\omega)\cdot\hat{\mathbf{j}}(\mathbf{r}',\omega),\end{aligned}$$

and we have introduced $\hat{\mathbf{j}}(\mathbf{r},\omega)=\int_{-\infty}^{\infty}dt\,\mathrm{e}^{\mathrm{i}\omega t}\,\hat{\mathbf{j}}(\mathbf{r},t)$. We note that Eq. (E.5) resembles its classical counterpart given by Eq. (1.28), but now the currents are commuting quantum mechanical operators.

E.2 Photon intensity produced by a free electron and a laser pulse: derivation of Eq. (5.2)

We consider that the quantum current operator $\hat{\mathbf{j}}$ is the sum of a classical term $\mathbf{j}^{\mathrm{ext}}$ (i.e., the source of the external laser light) and the quantum part associated with the free electrons $\hat{\mathbf{j}}^{\mathrm{el}}$. According to the analysis in Section D.2, for a highly energetic electron the second-quantized currents commute at different times and thus Eq. (E.5) can be directly employed to compute the far-field emission connected to this configuration. Then without loss of generality, we take $\mathbf{v}$ along the z and calculate the Fourier transform of Eq. (E.5)

$$\hat{\mathbf{j}}^{\mathrm{el}}(\mathbf{r},\omega)=-\hat{\mathbf{z}}\,\frac{e}{L^2}\mathrm{e}^{\mathrm{i}\omega z/v}\sum_{\mathbf{q},\mathbf{k}_\perp}\mathrm{e}^{\mathrm{i}\mathbf{k}_\perp\cdot\mathbf{R}}\,\hat{c}^\dagger_{\mathbf{q}}\hat{c}_{\mathbf{q}+\mathbf{k}_\perp+(\omega/v)\hat{\mathbf{z}}},\tag{E.6}$$

where $\mathbf{k}_\perp\perp\hat{\mathbf{z}}$ is the transverse component of the exchanged wave vector $\mathbf{k}$. This allows us to evaluate the average in Eq. (E.5) for an initial state consisting of an electron prepared in a wave function $\psi_0(\mathbf{r})=\sum_{\mathbf{q}}\alpha_{\mathbf{q}}\langle\mathbf{r}|\hat{c}^\dagger_{\mathbf{q}}|0\rangle$ and zero photons (i.e., $|\psi(-\infty)\rangle=\sum_{\mathbf{q}}\alpha_{\mathbf{q}}\hat{c}^\dagger_{\mathbf{q}}|0\rangle$) by first computing the intermediate results

$$\langle\hat{\mathbf{j}}^{\mathrm{el}}(\mathbf{r}',\omega)\hat{\mathbf{j}}^{\mathrm{el}\dagger}(\mathbf{r}'',\omega)\rangle=e^2\,\hat{\mathbf{z}}\otimes\hat{\mathbf{z}}\,\delta(\mathbf{R}'-\mathbf{R}'')\mathrm{e}^{\mathrm{i}\omega(z'-z'')/v}M_0(\mathbf{R}'),\tag{E.7a}$$

$$\langle\hat{\mathbf{j}}^{\mathrm{el}}(\mathbf{r}',\omega)\rangle=-e\,\hat{\mathbf{z}}\,\mathrm{e}^{\mathrm{i}\omega z'/v}M^*_{\omega/v}(\mathbf{R}'),\tag{E.7b}$$

where we use the notation $\mathbf{r}=(\mathbf{R},z)$. Also, $M_{\omega/v}(\mathbf{R})=\int_{-\infty}^{\infty}dz\;\mathrm{e}^{\mathrm{i}\omega z/v}\,|\psi_0(\mathbf{r})|^2$ is a coherence factor that captures the dependence on the electron wave function through the probability density $|\psi_0(\mathbf{r})|^2$. We note that there is no dependence on the phase of $\psi_0(\mathbf{r})$. By using Eqs. (E.7) to work out the evaluation of Eq. (E.5), we obtain

$$\begin{aligned}\frac{d\Gamma_{\mathrm{ff}}}{d\Omega_{\hat{\mathbf{r}}}d\omega}=\lim_{kr\to\infty}\frac{r^2}{4\pi^2\hbar k}\mathrm{Re}\Bigg\{&\mathbf{E}^{\mathrm{light}}(\mathbf{r},\omega)\times\mathbf{B}^{\mathrm{light}*}(\mathbf{r},\omega)\\&+\int d^2\mathbf{R}'\,M_{\omega/v}(\mathbf{R}')\,\mathbf{E}^{\mathrm{CL}*}(\mathbf{r},\mathbf{R}',\omega)\times\mathbf{B}^{\mathrm{light}}(\mathbf{r},\omega)\\&+\frac{\mathrm{i}}{k}\int d^2\mathbf{R}'\,M_0(\mathbf{R}')\,\mathbf{E}^{\mathrm{CL}}(\mathbf{r},\mathbf{R}',\omega)\times\left[\nabla\times\mathbf{E}^{\mathrm{CL}}(\mathbf{r},\mathbf{R}',\omega)\right]^*\\&+\frac{\mathrm{i}}{k}\int d^2\mathbf{R}'\,M_{\omega/v}(\mathbf{R}')\,\mathbf{E}^{\mathrm{light}}(\mathbf{r},\omega)\times\left[\nabla\times\mathbf{E}^{\mathrm{CL}}(\mathbf{r},\mathbf{R}',\omega)\right]^*\Bigg\}\cdot\hat{\mathbf{r}},\end{aligned}\tag{E.8}$$

where we have defined the CL-related vector

$$\mathbf{E}^{\mathrm{CL}}(\mathbf{r},\mathbf{R}',\omega)=4\pi\mathrm{i}e\omega\int_{-\infty}^{\infty}dz'\;\mathrm{e}^{\mathrm{i}\omega z'/v}\,G(\mathbf{r},\mathbf{R}',z',\omega)\cdot\hat{\mathbf{z}}\tag{E.9}$$

and the total (external+scattered) light fields

$$\mathbf{E}^{\rm light}(\mathbf{r},\omega) = -4\pi{\rm i}\,\omega \int d^3\mathbf{r}'\; G(\mathbf{r},\mathbf{r}',\omega)\cdot\mathbf{j}^{\rm ext}(\mathbf{r}',\omega)$$

and $\mathbf{B}^{\rm light}(\mathbf{r},\omega) = (-{\rm i}/k)\,\nabla\times\mathbf{E}^{\rm light}(\mathbf{r},\omega)$. At this point, it is convenient to separate the light field into external and scattered components as $\mathbf{E}^{\rm light}(\mathbf{r},\omega) = \mathbf{E}^{\rm ext}(\mathbf{r},\omega) + \mathbf{E}^{\rm scat}(\mathbf{r},\omega)$, where the first term arises from the free-space part of the Green tensor, whereas the second-term decays as $1/r$ far from the sample. We consider first emission directions in which the external light does not interfere with the scattered and CL fields. Then, in the far-field limit ($kr \gg 1$), we can approximate $\nabla \approx {\rm i}k\hat{\mathbf{r}}$ in the above expressions, and the electric and magnetic fields only retain components perpendicular to $\mathbf{r}$. This allows us to rewrite Eq. (E.8) in the form given by Eq. (5.2) in terms of far-field electric field amplitudes $\mathbf{f}^{\rm CL}_{\hat{\mathbf{r}}}(\mathbf{R}',\omega)$ and $\mathbf{f}^{\rm scat}_{\hat{\mathbf{r}}}(\omega)$ associated with CL emission and laser scattering contributions [see definitions in Eqs. (5.4)]. Under typical electron microscope conditions, for a well-focused electron beam, we can factorize the electron wave function as $\psi_0(\mathbf{r}) = \psi_\perp(\mathbf{R})\psi_\parallel(z)$ and approximate $|\psi_\perp(\mathbf{R})|^2 \approx \delta(\mathbf{R}-\mathbf{R}_0)$, where $\mathbf{R}_0$ defines the beam position. Inserting this wave function into Eq. (5.2), we find

$$\begin{aligned}\frac{d\Gamma_{\rm rad}(\mathbf{R}_0)}{d\Omega_{\hat{\mathbf{r}}}d\omega} = \frac{1}{4\pi^2\hbar k}\Big[&|\mathbf{f}^{\rm CL}_{\hat{\mathbf{r}}}(\mathbf{R}_0,\omega)|^2 + |\mathbf{f}^{\rm scat}_{\hat{\mathbf{r}}}(\omega)|^2 \\ &+ 2\,{\rm Re}\left\{M_{\omega/v}\,\mathbf{f}^{\rm CL*}_{\hat{\mathbf{r}}}(\mathbf{R}_0,\omega)\cdot\mathbf{f}^{\rm scat}_{\hat{\mathbf{r}}}(\omega)\right\}\Big],\end{aligned} \tag{E.10}$$

where now $M_{\omega/v} = \int_{-\infty}^{\infty} dz\; {\rm e}^{{\rm i}\omega z/v}\,|\psi_\parallel(z)|^2$.

E.3 Generalization to multiple electrons: derivation of Eq. (5.5)

The above formalism can be readily extended to deal with more than one electron by taking the initial state as $|\psi(-\infty)\rangle = \prod_j\left(\sum_{\mathbf{k}_j}\alpha^j_{\mathbf{k}_j}c^\dagger_{\mathbf{k}_j}\right)|0\rangle$, where j runs over different electrons and the photonic field is prepared in the vacuum state. Then, using the definition of the electron current operator $\hat{\mathbf{j}}^{\rm el}(\mathbf{r},\omega)$ in Eq. (E.6), the averages in Eqs. (E.7) can be readily computed for the multi-electron state to yield

$$\begin{aligned}\langle\hat{\mathbf{j}}^{\rm el}(\mathbf{r}',\omega)\hat{\mathbf{j}}^{\rm el\dagger}(\mathbf{r}'',\omega)\rangle &= e^2\,\hat{\mathbf{z}}\otimes\hat{\mathbf{z}}\,{\rm e}^{{\rm i}\omega(z'-z'')/v} \\ &\times\left[\delta(\mathbf{R}'-\mathbf{R}'')\sum_j M^j_0(\mathbf{R}') + \sum_{j\neq j'} M^{j*}_{\omega/v}(\mathbf{R}')M^{j'}_{\omega/v}(\mathbf{R}'')\right],\end{aligned} \tag{E.11a}$$

$$\langle\hat{\mathbf{j}}^{\rm el}(\mathbf{r}',\omega)\rangle = -e\,\hat{\mathbf{z}}\,{\rm e}^{{\rm i}\omega z'/v}\sum_j M^{j*}_{\omega/v}(\mathbf{R}'), \tag{E.11b}$$

where $M^j_{\omega/v}$ is given by Eq. (5.8) with $\psi_0(\mathbf{r})$ substituted by $\psi_j(\mathbf{r}) = \sum_{\mathbf{k}}\alpha^j_{\mathbf{k}}\langle\mathbf{r}|\hat{c}^\dagger_{\mathbf{k}}|0\rangle$ (the wave function of electron j). Finally, plugging Eqs. (E.11) into Eq. (E.5) and following similar steps as done above for a single electron, we obtain Eq. (5.5).

E.4 Cathodoluminescence from a dipolar object: derivation of Eq. (5.6)

We present results in Chapter 5 for sample objects whose response is dominated by an electric dipolar mode represented through an isotropic polarizability $\alpha(\omega)$ placed at $\mathbf{r}=0$. We now carry out the limit in Eq. (5.4a) by realizing that the free-space component of the Green tensor [Eq. (1.14)] to the z' integral vanishes exponentially away from the electron beam (i.e., just like the electromagnetic field accompanying a freely moving classical charge), so we only need to account for the contribution from the scattering part [see Eq. (1.24)]

$$G^{\rm scat}(\mathbf{r},\mathbf{r}',\omega)\xrightarrow[kr\to\infty]{}-\frac{\alpha(\omega)}{4\pi c^2}\frac{{\rm e}^{{\rm i}kr}}{r}(1-\hat{\mathbf{r}}\otimes\hat{\mathbf{r}})\cdot(k^2+\nabla_{\mathbf{r}'}\otimes\nabla_{\mathbf{r}'})\frac{{\rm e}^{{\rm i}kr'}}{r'}.$$

Plugging this expression into Eq. (5.4a), we can carry out the z' integral by using the identities $\int_{-\infty}^{\infty}dz\,{\rm e}^{{\rm i}\omega(z/v+r/c)}/r=2K_0\left(\omega R/v\gamma\right)$ and $\int_{-\infty}^{\infty}dz\,(1+{\rm i}/kr)\,{\rm e}^{{\rm i}\omega(z/v+r/c)}/r^2=(2{\rm i}c/Rv\gamma)\,K_1\left(\omega R/v\gamma\right)$, where $r=\sqrt{R^2+z^2}$ and $\gamma=1/\sqrt{1-v^2/c^2}$ [see Eqs. (3.914-4) and (3.914-5) in Ref. 95]. This leads to

$$\mathbf{f}^{\rm CL}_{\hat{\mathbf{r}}}(\mathbf{R}',\omega)=k^2\,\alpha(\omega)\,\left(1-\hat{\mathbf{r}}\otimes\hat{\mathbf{r}}\right)\cdot\mathbf{E}^{\rm el}(\mathbf{R}',\omega),\tag{E.12}$$

where $\mathbf{E}^{\rm el}(\mathbf{R}',\omega)$, defined in Eq. (5.7), coincides with the electric field produced at the particle position $\mathbf{r}=0$ by a classical point electron whose trajectory crosses $(\mathbf{R}',0)$ at time $t=0$. Similarly, from Eq. (5.4b), the scattered external field amplitude is readily found to be

$$\mathbf{f}^{\rm scat}_{\hat{\mathbf{r}}}(\omega)=k^2\,\alpha(\omega)\,\left(1-\hat{\mathbf{r}}\otimes\hat{\mathbf{r}}\right)\cdot\mathbf{E}^{\rm ext}(0,\omega),\tag{E.13}$$

where $\mathbf{E}^{\rm ext}(0,\omega)$ is the external laser field acting on the particle. Finally, by inserting Eqs. (E.12) and (E.13) into Eq. (E.10), we obtain

$$\begin{aligned}\frac{d\Gamma_{\rm rad}}{d\Omega_{\hat{\mathbf{r}}}d\omega}&=\frac{k^3}{4\pi^2\hbar}|\alpha(\omega)|^2\\&\times\Big\{\left(|\mathbf{E}^{\rm el}(\mathbf{R}_0,\omega)|^2-|\hat{\mathbf{r}}\cdot\mathbf{E}^{\rm el}(\mathbf{R}_0,\omega)|^2\right)\\&+\left(|\mathbf{E}^{\rm ext}(0,\omega)|^2-|\hat{\mathbf{r}}\cdot\mathbf{E}^{\rm ext}(0,\omega)|^2\right)\\&+2\,{\rm Re}\left\{M_{\omega/v}\left[\mathbf{E}^{\rm el*}(\mathbf{R}_0,\omega)\cdot\mathbf{E}^{\rm ext}(0,\omega)-\left(\hat{\mathbf{r}}\cdot\mathbf{E}^{\rm el*}(\mathbf{R}_0,\omega)\right)\left(\hat{\mathbf{r}}\cdot\mathbf{E}^{\rm ext}(0,\omega)\right)\right]\right\}\Big\}.\end{aligned}\tag{E.14}$$

The total far-field photon probability per unit frequency is then obtained by integrating Eq. (E.14) over solid angles, leading to

$$\begin{aligned}\frac{d\Gamma_{\rm rad}(\mathbf{R}_0)}{d\omega}=\frac{2k^3}{3\pi\hbar}|\alpha(\omega)|^2\Big[&|\mathbf{E}^{\rm el}(\mathbf{R}_0,\omega)|^2+|\mathbf{E}^{\rm ext}(0,\omega)|^2\\&+2{\rm Re}\left\{M_{\omega/v}\mathbf{E}^{\rm el*}(\mathbf{R}_0,\omega)\cdot\mathbf{E}^{\rm ext}(0,\omega)\right\}\Big].\end{aligned}\tag{E.15}$$

This expression can readily be recast in the form of Eq. (5.6).

E.5 Energy pathways from the MQED formalism

Derivation of Eq. (5.14c)

There is an additional component in $d\Gamma_{\rm ff}/d\Omega_{\hat{\mathbf{r}}}d\omega$ [Eq. (E.8)] arising from the interference between the external light field $\mathbf{E}^{\rm ext}(\mathbf{r},\omega)$ and the scattered+CL far-field amplitudes. For plane wave light incidence with wave vector $\mathbf{k}_{\rm inc}$, the former can be written $\mathbf{E}^{\rm ext}(0,\omega){\rm e}^{{\rm i}\mathbf{k}_{\rm inc}\cdot\mathbf{r}}$, which contributes to $d\Gamma_{\rm ff}/d\Omega_{\hat{\mathbf{r}}}d\omega$ through the three last terms of Eq. (E.8). In particular, using the notation $2{\rm Re}\left\{\mathbf{E}^{\rm ext}(0,\omega){\rm e}^{{\rm i}\mathbf{k}_{\rm inc}\cdot\mathbf{r}-{\rm i}\omega t}\right\}$ for the time-dependent external light electric field, the frequency-space light electric far-field ($kr \gg 1$) takes the form $\mathbf{E}^{\rm light}(\mathbf{r},\omega) \approx \mathbf{E}^{\rm ext}(0,\omega)\,{\rm e}^{{\rm i}\mathbf{k}_{\rm inc}\cdot\mathbf{r}} + \mathbf{f}^{\rm scat}_{\hat{\mathbf{r}}}(\omega)\,{\rm e}^{{\rm i}kr}/r$, where $k = |\mathbf{k}_{\rm inc}| = \omega/c$ which we insert into Eq. (E.8), to separate $d\Gamma_{\rm ff}/\Omega_{\hat{\mathbf{r}}}d\omega = (d\Gamma_{\rm rad}/\Omega_{\hat{\mathbf{r}}}d\omega) + (d\Gamma_{\rm forward}/\Omega_{\hat{\mathbf{r}}}d\omega)$ into the contributions coming from the $1/r$ part (i.e., $d\Gamma_{\rm rad}/\Omega_{\hat{\mathbf{r}}}d\omega$, which is extensively discussed in Chapter 5) and the remaining interference between $\mathbf{E}^{\rm ext}(0,\omega){\rm e}^{{\rm i}\mathbf{k}_{\rm inc}\cdot\mathbf{r}}$ and $\mathbf{f}^{\rm CL/scat}_{\hat{\mathbf{r}}}$ terms [see also Eqs. (5.4)]. The latter generates $d\Gamma_{\rm forward}/\Omega_{\hat{\mathbf{r}}}d\omega$, which can be integrated over angles $\Omega_{\hat{\mathbf{r}}}$ following a similar asymptotic analysis as used in the derivation of the optical theorem[329], based on the integral $\int d^2\Omega_{\hat{\mathbf{r}}}\,{\rm e}^{{\rm i}(k+{\rm i}0^+)r-{\rm i}\mathbf{k}_{\rm inc}\cdot\mathbf{r}} = 2\pi{\rm i}/kr$ (valid in the $kr \to \infty$ limit), where k is supplemented by an infinitesimal imaginary part ${\rm i}0^+$, in accordance with the retarded formalism here adopted. This leads to

$$\frac{d\Gamma_{\rm forward}}{d\omega} = -\frac{1}{\pi\hbar k^2}{\rm Im}\left\{\mathbf{E}^{\rm ext*}(0,\omega)\cdot\left[\mathbf{f}^{\rm scat}_{\hat{\mathbf{k}}_{\rm inc}}(\omega) + M^*_{\omega/v}\mathbf{f}^{\rm CL}_{\hat{\mathbf{k}}_{\rm inc}}(\omega)\right]\right\},$$

which, using Eqs. (E.12) and (E.13), reduces to Eq. (5.14c) for a dipolar particle.

Derivation of Eq. (5.14a)

In order to compute the probability linked to the electron energy variation [i.e., Eq. (5.14a)] for a dipolar particle, we start from the electron mean energy after interaction at $t \to \infty$:

$$\Delta E_{\rm el} = \langle \hat{\mathcal{S}}^\dagger(\infty,-\infty)\hat{\mathcal{H}}^{\rm el}_0\hat{\mathcal{S}}(\infty,-\infty)\rangle - \langle\hat{\mathcal{H}}^{\rm el}_0\rangle,$$

where the average $\langle\cdot\rangle$ is defined as in Eq. (E.4). Noticing that the interaction Hamiltonian [Eq. (E.3)] is linear in the total current $\hat{\mathbf{j}}$, we use the evolution operator [Eq. (D.15)] and retain terms just up to quadratic order in $\hat{\mathbf{j}}$ to find

$$\begin{aligned}\Delta E_{\rm el} \approx & -{\rm i}\left\langle\left[\hat{\chi}(\infty,-\infty),\hat{\mathcal{H}}^{\rm el}_0\right]\right\rangle \\ & + \frac{1}{\hbar^2}\int_{-\infty}^{\infty} dt\,dt'\left\langle\left[\hat{\mathcal{H}}_{\rm int}(t)\hat{\mathcal{H}}^{\rm el}_0\hat{\mathcal{H}}_{\rm int}(t') - \frac{1}{2}\left\{\hat{\mathcal{H}}_{\rm int}(t)\hat{\mathcal{H}}_{\rm int}(t'),\hat{\mathcal{H}}^{\rm el}_0\right\}\right]\right\rangle.\end{aligned} \tag{E.16}$$

Following the same approach as in Section E.2, we consider the total current to be the sum of the classical laser source $\mathbf{j}^{\rm ext}$ and the electron current operator $\hat{\mathbf{j}}^{\rm el}$ [Eq. D.12]. An important technical point refers to the operator $\hat{\chi}(\infty,-\infty)$ [Eq. (D.16)], in which only the terms that are linear in $\hat{\mathbf{j}}^{\rm el}$ are not commuting with $\hat{\mathcal{H}}_{\rm el}$. In the absence of external illumination, such linear terms disappear and the remaining part of $\hat{\chi}$ gives rise to an image-potential interaction with the sample, which produces elastic diffraction of the electron, but does not change its energy. However, in the present scenario of combined electron and light interactions with the sample, $\hat{\chi}$ gives rise to changes in the electron energy, so it needs to be retained in the calculation. We now use Eqs. (C.1), (C.5) and (C.6), together with the Onsager reciprocity relation $G(\mathbf{r},\mathbf{r}',\omega)=G^{\mathrm{T}}(\mathbf{r}',\mathbf{r},\omega)$, to rewrite Eq. (E.16) as

$$\begin{aligned}\Delta E_{\mathrm{el}} \approx\, & \frac{4\mathrm{i}}{\hbar}\sum_{i,i'}\int_0^\infty d\omega\int d^3\mathbf{r}\,d^3\mathbf{r}' \\ & \times\Big\{\mathrm{i}\,\mathrm{Im}\{G_{i,i'}(\mathbf{r},\mathbf{r}',\omega)\}\Big\langle\hat{j}_i^\dagger(\mathbf{r},\omega)\hat{\mathcal{H}}_{\mathrm{el}}\hat{j}_{i'}(\mathbf{r}',\omega)-\frac{1}{2}\Big\{\hat{j}_i(\mathbf{r},\omega)\hat{j}_{i'}(\mathbf{r}',\omega),\hat{\mathcal{H}}_{\mathrm{el}}\Big\}\Big\rangle \\ & +\frac{1}{2}\mathrm{Re}\{G_{i,i'}(\mathbf{r},\mathbf{r}',\omega)\}\Big\langle\Big[\hat{j}_i^{\mathrm{el}\dagger}(\mathbf{r},\omega),\hat{\mathcal{H}}_{\mathrm{el}}\Big]\,j_{i'}^{\mathrm{ext}}(\mathbf{r}',\omega)+j_i^{\mathrm{ext}*}(\mathbf{r},\omega)\Big[\hat{j}_{i'}^{\mathrm{el}}(\mathbf{r}',\omega),\hat{\mathcal{H}}_{\mathrm{el}}\Big]\Big\rangle\Big\}.\end{aligned}$$

Finally, we evaluate the averages $\langle\cdot\rangle$ using Eqs. (E.7) and the definition of $\hat{\mathcal{H}}_0^{\mathrm{el}}$. After some algebra, this leads to $\Delta E_{\mathrm{el}}=\int_0^\infty d\omega\,\hbar\omega\,d\Gamma_{\mathrm{el}}/d\omega$ with

$$\begin{aligned}\frac{d\Gamma_{\mathrm{el}}}{d\omega}\approx & -\int d^2\mathbf{R}\,M_0(\mathbf{R})\,\Gamma_{\mathrm{EELS}}(\mathbf{R},\omega) \\ & -\frac{4e}{\hbar}\int d^3\mathbf{r}\int d^3\mathbf{r}'\mathrm{Im}\left\{\mathrm{e}^{-\mathrm{i}\omega z/v}M_{\omega/v}(\mathbf{R})\,\hat{\mathbf{z}}\cdot G(\mathbf{r},\mathbf{r}',\omega)\cdot\mathbf{j}^{\mathrm{ext}}(\mathbf{r}',\omega)\right\},\end{aligned} \tag{E.17}$$

where $M_{\omega/v}(\mathbf{R})$ is the same as in Eqs. (E.7) and $\Gamma_{\mathrm{EEL}}(\mathbf{R},\omega)$ is the classical EEL probability for an electron beam focused at $\mathbf{R}$ [see Eq. (1.26)]. Equation (E.17) represents a generalization of Eq. (5.14a) to arbitrary samples and incident electron wave functions. Indeed, this result reduces to Eq. (5.14a) if the electron wave function can be factorized as $\psi_0(\mathbf{r})=\psi_\perp(\mathbf{R})\psi_\parallel(z)$ with $|\psi_\perp(\mathbf{R})|^2\approx\delta(\mathbf{R}-\mathbf{R}_0)$ (i.e., the tightly focused beam limit) and the sample can be described by a dipolar polarizability $\alpha(\omega)$. Under such conditions, taking the particle at the origin, we can write the scattered part of the Green tensor as $G^{\mathrm{scat}}(\mathbf{r},\mathbf{r}',\omega)=-4\pi\omega^2\alpha(\omega)G^{\mathrm{free}}(\mathbf{r},\omega)\cdot G^{\mathrm{free}}(\mathbf{r}',\omega)$, in terms of the free-space component $G^{\mathrm{free}}(\mathbf{r},\omega)=(-1/4\pi\omega^2)(k^2+\nabla\otimes\nabla)\left(\mathrm{e}^{\mathrm{i}kr}/r\right)$, and then, combining all of these elements, using the integral $\int_{-\infty}^{\infty}dz\,\mathrm{e}^{\mathrm{i}\omega(z/v+r/c)}/r=2K_0\left(\omega R/v\gamma\right)$ [see Eq. (3.914-4) in Ref. 95], and identifying $\mathbf{E}^{\mathrm{ext}}(0,\omega)=-4\pi\mathrm{i}\omega\int d^3\mathbf{r}\,G^{\mathrm{free}}(\mathbf{r},\omega)\cdot\mathbf{j}^{\mathrm{ext}}(\mathbf{r},\omega)$, we obtain Eq. (5.14a).

Derivation of Eq. (5.14b)

In order to obtain Eq. (5.14b), we present an alternative treatment of a dipolar scatterer that hosts a single optical mode. This approach does not require photon quantization and it can be applied to any two-level system that can be characterized by a transition dipole. As a starting point, we write the Hamiltonian

$$\hat{\mathcal{H}}=\hbar\omega_0\,\hat{a}^\dagger\hat{a}+\hbar\sum_q\varepsilon_q\hat{c}_q^\dagger\hat{c}_q+g(t)\left(\hat{a}^\dagger+\hat{a}\right)+\sum_{qq'}g_{qq'}\hat{c}_q^\dagger\hat{c}_{q'}\left(\hat{a}^\dagger+\hat{a}\right), \tag{E.18}$$

where ω_0 is the mode frequency, $\hat{a}^\dagger$ and $\hat{a}$ represent the corresponding creation and annihilation operators, $\hat{c}_q^\dagger$ and $\hat{c}_q$ create and annihilate an electron of wave vector q and kinetic energy $\hbar\varepsilon_q$ along the e-beam direction, the real coefficient $g(t)$ describes the mode coupling to classical external light, and $g_{qq'}$ are electron-scatterer coupling coefficients.

In what follows, we ignore transverse coordinates under the nonrecoil approximation, together with the assumption that the e-beam is focused around a lateral position $\mathbf{R}_0 = (x_0, y_0)$ relative to the scatterer, with a small focal spot compared to both c/ω_0 and R_0. A basis set of longitudinal wave vector states $\langle z|q\rangle = \mathrm{e}^{\mathrm{i}qz}/\sqrt{L}$ is then used to describe the electron, where L is the quantization length along the e-beam direction. In addition, the scatterer is considered to be prepared in its ground state before interaction with the external light and the electron. We further assume typical conditions in electron microscopy, characterized by a weak electron-scatterer interaction, so that we can work to the lowest possible order of perturbation theory. The external light is taken to be dimmed, such that its interaction strength becomes commensurate with that of the electron. Under these conditions, the density matrix of the combined electron-scatterer system can be written as

$$\hat{\rho} = \sum_{nn',qq'} \alpha_{nn',qq'}(t)\, \mathrm{e}^{\mathrm{i}(n'-n)\omega_0 t + \mathrm{i}\varepsilon_{q'q} t}\, |nq\rangle\langle n'q'|, \tag{E.19}$$

where $|nq\rangle \equiv (\hat{a}^\dagger)^n \hat{c}_q^\dagger |0\rangle/\sqrt{n!}$ and we adopt the notation $\varepsilon_{q'q} = \varepsilon_{q'} - \varepsilon_q$. A finite lifetime τ_0 of the optical mode is now introduced through the equation of motion

$$\frac{d\hat{\rho}}{dt} = \frac{\mathrm{i}}{\hbar}\left[\hat{\rho}, \hat{\mathcal{H}}\right] + \frac{1}{2\tau_0}\left(2\hat{a}\hat{\rho}\hat{a}^\dagger - \hat{a}^\dagger\hat{a}\hat{\rho} - \hat{\rho}\hat{a}^\dagger\hat{a}\right). \tag{E.20}$$

Before interaction, the coefficients of the density matrix are $\alpha_{nn',qq'}(-\infty) = \delta_{n0}\delta_{n'0}\alpha_q^0\alpha_{q'}^{0*}$, where α_q^0 defines the incident longitudinal electron wave function

$$\psi_{\parallel}(z) = \sum_q \alpha_q^0 \langle z|q\rangle = \sqrt{L}\int_{-\infty}^{\infty} \frac{dq}{2\pi}\, \alpha_q^0\, \mathrm{e}^{\mathrm{i}qz}. \tag{E.21}$$

Here, we have used the prescription $\sum_q \rightarrow (L/2\pi)\int_{-\infty}^{\infty} dq$ to transform the sum over the electron wave vector q into an integral.

We consider external light characterized by an electric field $\mathbf{E}^{\mathrm{ext}}(\mathbf{r}, t)$ at the position of the scatterer, so we have

$$g(t) = -\mathbf{p}_0 \cdot \mathbf{E}^{\mathrm{ext}}(0, t), \tag{E.22}$$

where $\mathbf{p}_0$ is the transition dipole, which is taken to be real. Additionally, the electron-scatterer coupling coefficients are given by[330]

$$g_{qq'} = g_{q'q}^* = -\frac{v}{L}\, \mathbf{p}_0 \cdot \mathbf{g}_{q'-q}, \tag{E.23}$$

where

$$\mathbf{g}_q = \frac{2e}{v\gamma}\left[|q|\, K_1\left(|q|R_0/\gamma\right)\, \hat{\mathbf{R}}_0 + \frac{\mathrm{i}q}{\gamma}\, K_0\left(|q|R_0/\gamma\right)\, \hat{\mathbf{z}}\right],$$

v is the average electron velocity, and $\gamma = 1/\sqrt{1 - v^2/c^2}$.

The excitation probabilities here investigated are determined by the diagonal elements $\alpha_{nn,qq}(t)$, which we calculate to the lowest order of perturbation theory by plugging Eqs. (E.18) and (E.19) into Eq. (E.20). Identifying the coefficient of each $|nq\rangle\langle n'q'|$ term in both sides of the resulting equation, iteratively evaluating the correction to $\alpha_{nn',qq'}$ at perturbation order $l+1$ by inserting the order-l correction into the $[\hat{\rho},\hat{\mathcal{H}}]$ term of Eq. (E.20), and starting with $\alpha_{nn',qq'}(-\infty)$ for $l=0$ (see above), we find

$$\begin{aligned}\frac{d\alpha_{01,qq'}(t)}{dt} =&\frac{\mathrm{i}}{\hbar}g(t)\,\alpha_q^0\,\alpha_{q'}^{0*}\;\mathrm{e}^{-\mathrm{i}\omega_0 t} \\ &+\frac{\mathrm{i}}{\hbar}\sum_{q''}g_{q''q'}\,\alpha_q^0\,\alpha_{q''}^{0*}\;\mathrm{e}^{-\mathrm{i}(\omega_0+\varepsilon_{q'q''})t}-\frac{1}{2\tau_0}\alpha_{01,qq'}(t),\end{aligned} \tag{E.24a}$$

$$\begin{aligned}\frac{d\alpha_{11,qq}(t)}{dt} =&\frac{2}{\hbar}g(t)\,\mathrm{Im}\left\{\alpha_{01,qq}(t)\;\mathrm{e}^{\mathrm{i}\omega_0 t}\right\} \\ &+\frac{2}{\hbar}\sum_{q'}\mathrm{Im}\left\{g_{qq'}\,\alpha_{01,q'q}(t)\;\mathrm{e}^{\mathrm{i}(\omega_0+\varepsilon_{qq'})t}\right\}-\frac{1}{\tau_0}\,\alpha_{11,qq}(t),\end{aligned} \tag{E.24b}$$

$$\begin{aligned}\frac{d\alpha_{00,qq}(t)}{dt} =&-\frac{2}{\hbar}g(t)\,\mathrm{Im}\left\{\alpha_{01,qq}(t)\;\mathrm{e}^{\mathrm{i}\omega_0 t}\right\} \\ &-\frac{2}{\hbar}\sum_{q'}\mathrm{Im}\left\{g_{q'q}\,\alpha_{01,qq'}(t)\;\mathrm{e}^{\mathrm{i}(\omega_0+\varepsilon_{q'q})t}\right\}+\frac{1}{\tau_0}\,\alpha_{11,qq}(t),\end{aligned} \tag{E.24c}$$

where we have used the Hermiticity of $\hat{\rho}$ and $\hat{\mathcal{H}}$. The integral of Eq. (E.24a) can be readily written as

$$\begin{aligned}\alpha_{01,qq'}(t) = \frac{\mathrm{i}}{\hbar}\,\alpha_q^0\,\alpha_{q'}^{0*}\int_{-\infty}^{t}dt'\,g(t')\,\mathrm{e}^{-\mathrm{i}\omega_0 t'-(t-t')/2\tau_0} \\ -\frac{1}{\hbar}\sum_{q''}g_{q''q'}\,\alpha_q^0\,\alpha_{q''}^{0*}\,\frac{\mathrm{e}^{-\mathrm{i}(\omega_0+\varepsilon_{q'q''})t}}{\omega_0+\varepsilon_{q'q''}+\mathrm{i}/2\tau_0}.\end{aligned}$$

At this point, we express the coupling coefficients in terms of the scatterer mode dipole $\mathbf{p}_0$ through Eqs. (E.22) and (E.23), use the nonrecoil approximation (see Section 1.2) to write $\varepsilon_{q'q''}\approx(q'-q'')v$, and convert the q'' sum into an integral by means of the prescription noted above. Following this procedure, we find

$$\alpha_{01,qq'}(t) = \int_{-\infty}^{\infty}\frac{d\omega}{2\pi}\,\mathrm{e}^{-\mathrm{i}\omega t}\,\tilde{\alpha}_{01,qq'}(\omega),$$

where

$$\begin{aligned}\tilde{\alpha}_{01,qq'}(\omega) = \frac{1}{\hbar}\,\frac{1}{\omega+\mathrm{i}/2\tau_0}\,\mathbf{p}_0\cdot\Big[\mathbf{E}^{\rm ext}(0,\omega-\omega_0)\,\alpha_q^0\,\alpha_{q'}^{0*} \\ +\mathbf{g}_{(\omega-\omega_0)/v}\,\alpha_q^0\,\alpha_{q'-(\omega-\omega_0)/v}^{0*}\Big]\end{aligned} \tag{E.25}$$

and $\mathbf{E}^{\rm ext}(\mathbf{r},\omega) = \int_{-\infty}^{\infty}dt\,\mathrm{e}^{\mathrm{i}\omega t}\,\mathbf{E}^{\rm ext}(\mathbf{r},t)$. In order to compute the probability of inelastic losses (see below) , we need to compute the time-integrated quantity $T_q =$

$\int_{-\infty}^{\infty} dt\, \alpha_{11,qq}(t)$. From Eq. (E.24b), we find $T_q = \int_{-\infty}^{\infty} dt\, \mathrm{e}^{-t/\tau_0} \int_{-\infty}^{t} dt'\, \mathrm{e}^{t'/\tau_0}\, F(t') = \tau_0 \int_{-\infty}^{\infty} dt\, F(t)$, where $F(t)$ is given by the first two terms in the right-hand side of that equation. This leads to

$$T_q = \frac{2\tau_0}{\hbar} \int_{-\infty}^{\infty} dt\, \mathrm{Im}\bigg\{ g(t)\, \alpha_{01,qq}(t)\, \mathrm{e}^{\mathrm{i}\omega_0 t} + \sum_{q'} g_{qq'}\, \alpha_{01,q'q}(t)\, \mathrm{e}^{\mathrm{i}(\omega_0+\varepsilon_{qq'})t} \bigg\}. \tag{E.26}$$

We note that the accumulated probability of decay from the excited state of the particle is given by $\Gamma_{\mathrm{decay}} = (1/\tau_0) \sum_q T_q$. Now, by identifying the particle polarizability as[96]

$$\alpha(\omega) = \frac{|p_0|^2}{\hbar} \left(\frac{1}{\omega_0 - \omega - \mathrm{i}/2\tau_0} + \frac{1}{\omega_0 + \omega + \mathrm{i}/2\tau_0} \right), \tag{E.27}$$

and by assuming $\omega_0\tau_0 \gg 1$, which allows us to approximate Eq. (E.27) by the first (resonant) term for $\omega > 0$, and by taking $\omega \approx \omega_0$ in the multiplicative factors, we obtain

$$\begin{aligned} \frac{d\Gamma_{\mathrm{decay}}}{d\omega} \approx \frac{1}{\pi\hbar} \mathrm{Im}\{\alpha(\omega)\} \bigg[&|\mathbf{E}^{\mathrm{ext}}(0,\omega)|^2 + |\mathbf{E}^{\mathrm{el}}(\mathbf{R}_0,\omega)|^2 \\ &+ 2\,\mathrm{Re}\big\{\mathbf{E}^{\mathrm{ext}}(0,\omega)\cdot \mathbf{E}^{\mathrm{el}*}(\mathbf{R}_0,\omega) M_{\omega/v}\big\} \bigg], \end{aligned}$$

which exactly corresponds to the term shown in Eq. (5.14b). We remark that in order to retrieve this last expression, we made use of the normalization property $\sum_q |\alpha_q^0|^2 = 1$, the spatial form of the wave function in Eq. (E.21) and of the definition of $M_{\omega/v}$ appearing in Eq. (E.10).

F

Contribution of Coulomb repulsion to a 2DEG Q-phase material

F.1 The Hartree potential in reciprocal space: derivation of V^{H}_G in Eq. (6.3)

In this section, we show how the Hartree potential of Eq. (1.66) can be easily evaluated in reciprocal space for a structure where charge neutrality is assumed. In order to do so, we start from its 2D version, which we compute for the case of a Q-phase material by using the eigenstates in Eq. (6.4a) to evaluate the carrier density $n(\mathbf{R})$. We employ the prescription $\sum_{\mathbf{k}_\parallel} \to (L/2\pi)^2 \int d^2\mathbf{k}_\parallel$, use the integral and limit $\int_0^b dy/\sqrt{(x-x')^2+y^2} = \log[b+\sqrt{(x-x')^2+b^2}] - \log|x-x'| \xrightarrow[b\to\infty]{} \log(2b) - \log|x-x'|$, and apply the condition of charge neutrality $\int d^2\mathbf{R}\,[n(\mathbf{R})-n_0] = 0$ to eliminate x-independent terms, to finally obtain the expression

$$V^{\mathrm{H}}(x) = -2e^2 \int_{-\infty}^{\infty} dx' \left[n(x') - n_0\right] \log|x-x'|, \tag{F.1}$$

where $n(x) = (1/\pi^2)\sum_n \int_{-\pi/a}^{\pi/a} dk_x \int_0^\infty dk_y\, |u_{k_x n}(x)|^2\, \theta(E_{\mathrm{F}} - \hbar\varepsilon^x_{k_x n} - \hbar^2 k_y^2/2m^*)$ is the 1D electron density profile. Now, we move to Fourier space defined via the relations $f_G = (1/a)\int_0^a dx\, f(x)\mathrm{e}^{-\mathrm{i}Gx}$ and $f(x) = \sum_G f_G \mathrm{e}^{\mathrm{i}Gx}$, to compute the coefficients of the Hartree potential which read

$$V^{\mathrm{H}}_G = 2\pi e^2 \begin{cases} n_G/|G|, & \text{for } G \neq 0, \\ 0, & \text{for } G = 0, \end{cases}, \tag{F.2}$$

where we made use of the integral $\int_{-\infty}^{\infty} dx\, \mathrm{e}^{\mathrm{i}Gx} \log|x| = -\pi/|G|$ [see Eq. (4.441-2) in Ref. 95]. Equation (F.2) is used in Chapter 6 in order to numerically integrate the self-consistent Schrödinger equation.

F.2 Quantification of the image energy

In this section, we intend to quantify the influence of the image interaction on the electronic behavior in the semiconductor considering the different parameters that define the system. We start from the density $n = k_\mathrm{F}^2/2\pi$ and the kinetic energy $E^\mathrm{kin} = L^2\pi\hbar^2 n^2/2m^*$ of a 2DEG. Following a density functional theory approach in the local-density approximation, we write the total energy as a functional of the electronic density $n(\mathbf{R})$:

$$E[n] = \frac{\pi\hbar^2}{2m^*}\int d^2\mathbf{R}\, n^2(\mathbf{R}) + \int d^2\mathbf{R}\, V^\mathrm{im}(\mathbf{R})n(\mathbf{R}) + \frac{e^2}{2}\int d^2\mathbf{R}d^2\mathbf{R}'\,\frac{\Delta n(\mathbf{R})\Delta n(\mathbf{R}')}{|\mathbf{R}-\mathbf{R}'|}, \tag{F.3}$$

where $\Delta n(\mathbf{R}) = n(\mathbf{R}) - n_0$. The ground-state density in the many-electron system is then obtained by minimizing Eq. (F.3), subject the constraint $\int d^2\mathbf{R}\,\Delta n(\mathbf{R}) = 0$. By introducing a Lagrange multiplier λ and imposing the vanishing of the functional derivative with respect to n (i.e., $\delta_n E[n] = \lambda$), we find

$$\frac{\pi\hbar^2}{m^*}[\Delta n(\mathbf{R}) + n_0] + V^\mathrm{im}(x) + \frac{e^2}{2}\int d^2\mathbf{R}'\,\frac{\Delta n(\mathbf{R}')}{|\mathbf{R}-\mathbf{R}'|} = \lambda,$$

which, transforming all quantities to reciprocal space as in done Section F.1, can be written as

$$\frac{\pi\hbar^2}{m^*}[\Delta n(x) + n_0] + V^\mathrm{im}(x) + e^2\pi\sum_{G\neq 0}\frac{\Delta n_G}{|G|}\mathrm{e}^{\mathrm{i}Gx} = \lambda. \tag{F.4}$$

Now, as a crude approximation, we assume that $\Delta n(x)$ has the same periodicity and shape as $V^\mathrm{im}(x)$, oscillating between the values n_1 and $-n_1$ for $b = a/2$ so that the average electron density is conserved. By specifying Eq. (F.4) at two different points $0 < x_1 < b$ and $b < x_2 < a$, and then subtracting the two resulting equations, we find the ratio

$$\frac{n_1}{n_0} = \frac{1}{2}\,\frac{V_0/E_\mathrm{F}{}^0}{1 + \mathcal{A}[(V_\mathrm{C}/E_\mathrm{F}{}^0)/(k_\mathrm{BZ}/k_\mathrm{F}{}^0)^2]}, \tag{F.5}$$

where $\mathcal{A} = \sum_{G\neq 0}(\pi^2/4a|G|^2)K_G(\mathrm{e}^{\mathrm{i}Gx_1} - \mathrm{e}^{\mathrm{i}Gx_2})$, $K_G = \Delta n_G/n_1 = (2\mathrm{i}/aG)(\mathrm{e}^{-\mathrm{i}Gb} - 1)$, and we use the coefficients $V_\mathrm{C} = e^2/a$ and $k_\mathrm{BZ} = \pi/a$ defined in Chapter 6. We have verified that $\mathcal{A}$ evolves in the $(0,1)$ interval as the values of $x_1 < x_2$ are varied. For instance, if $x_1 = a/4$ and $x_2 = 3a/4$, we obtain $\mathcal{A} = \sum_{n=0}^{\infty}(-1)^n/(2n+1)^2 \sim 0.91$. We are interested in finding the ratio of the kinetic energy to the image potential energy, which in this approximation becomes

$$\left|\frac{E^{\mathrm{kin}}}{E^{\mathrm{im}}}\right| = \frac{\pi\hbar^2}{2m^*}\frac{\int dx\, n^2(x)}{\left|\int dx\, V^{\mathrm{im}}(x)n(x)\right|} = \frac{E_{\mathrm{F}}{}^0}{2V_0}\frac{1+n_1^2/n_0^2}{|1+n_1/n_0|},$$

and finally, for small perturbations ($|n_1| \ll n_0$), it reduces to

$$\left|\frac{E^{\mathrm{kin}}}{E^{\mathrm{im}}}\right| \approx \left|\frac{E_{\mathrm{F}}{}^0}{2V_0} - \frac{1/4}{1+\mathcal{A}[(V_{\mathrm{C}}/E_{\mathrm{F}}{}^0)/(k_{\mathrm{BZ}}/k_{\mathrm{F}}{}^0)^2]}\right|. \tag{F.6}$$

The second fraction in the right-hand side of this equation can be neglected under the conditions investigated in Chapter 6 (i.e., for $V_{\mathrm{C}}/E_{\mathrm{F}}{}^0/(k_{\mathrm{BZ}}/k_{\mathrm{F}}{}^0)^2 \gg 1$), so the influence of the image potential on the material is simply quantified through the parameter $V_0/E_{\mathrm{F}}{}^0$.

G

Pair-production rate in the interaction picture: derivation of Eq. (7.3)

In this appendix, we provide a detailed derivation of the pair-production cross section [Eq. 7.3] based on the quantum field theory formalism of QED [303], of more common use in the high-energy physics community. An alternative derivation based on standard second order perturbation theory can be found in the Supplemental Material of Ref. 272.

G.1 QED Hamiltonian and matrix elements for a general polychromatic field

We study pair production produced by a classical electromagnetic field that is described through the vector potential $\mathbf{A}(\mathbf{r},t)$ in the WG (see Section 1.1). We adopt the minimal-coupling relativistic QED Hamiltonian in the Schrödinger picture (see Section 1.2 and Ref. 303)

$$\hat{\mathcal{H}}_{\mathrm{int}}(t) = -\frac{1}{c}\int d^3\mathbf{r}\;\hat{\mathbf{j}}(\mathbf{r},t)\cdot\mathbf{A}(\mathbf{r},t),$$

where now the current operator takes the form $\hat{\mathbf{j}}(\mathbf{r},t) = -ec : \overline{\Psi}(\mathbf{r},t)\vec{\gamma}\hat{\Psi}(\mathbf{r},t) :$, we define $\overline{\Psi} = \hat{\Psi}^\dagger\gamma^0$, and the notation $:\cdot:$ is used to indicate normal product acting on the fermionic field operators $\hat{\Psi}(\mathbf{r})$ and $\hat{\Psi}^\dagger(\mathbf{r})$ in analogy with the ordering of the bosonic operators seen in Section 1.3. Here, $\vec{\gamma}$ and γ^0 [303] are the spatial and temporal Dirac matrices[1]. The field operator is then expanded as

$$\hat{\Psi}(\mathbf{r},t) = \frac{1}{\sqrt{V}}\sum_{\mathbf{q},s}\left(u_{\mathbf{q},s}\hat{c}_{\mathbf{q},s}\mathrm{e}^{\mathrm{i}\mathbf{q}\cdot\mathbf{r}-\mathrm{i}\varepsilon_q t} + v_{\mathbf{q},s}\hat{d}^\dagger_{\mathbf{q},s}\mathrm{e}^{-\mathrm{i}\mathbf{q}\cdot\mathbf{r}+\mathrm{i}\varepsilon_q t}\right),$$

---

[1] These matrices connect to the ones used in Section 1.2 through the relations $\gamma^0 = \beta$ and $\vec{\gamma} = \gamma^0\vec{\alpha}$.

where V is the normalization volume and we introduce the anticommuting annihilation operators $\hat{c}_{\mathbf{q},s}$ and $\hat{d}_{\mathbf{q},s}$ and the corresponding creation operators $\hat{c}^\dagger_{\mathbf{q},s}$ and $\hat{d}^\dagger_{\mathbf{q},s}$ for electron and positron plane waves of wave vector $\mathbf{q}$ and spin s. The associated 4-component electron and positron spinors $u_{\mathbf{q},s}$ and $v_{\mathbf{q},s}$ are chosen to satisfy the equations[2]

$$(\hbar c\,\vec{\gamma}\cdot\mathbf{q} + m_e c^2 \mathcal{I}_4)\, u_{\mathbf{q},s} = \hbar\varepsilon_q \gamma^0 u_{\mathbf{q},s}, \tag{G.1a}$$

$$(\hbar c\,\vec{\gamma}\cdot\mathbf{q} - m_e c^2 \mathcal{I}_4)\, v_{\mathbf{q},s} = \hbar\varepsilon_q \gamma^0 v_{\mathbf{q},s}, \tag{G.1b}$$

subject to the orthonormalization conditions $u^\dagger_{\mathbf{q},s} u_{\mathbf{q},s'} = \delta_{s,s'}$, $v^\dagger_{\mathbf{q},s} v_{\mathbf{q},s'} = \delta_{s,s'}$ and $u^\dagger_{\mathbf{q},s} v_{-\mathbf{q},s'} = 0$. Here, m_e is the electron/positron mass, $\hbar\varepsilon_q = c\sqrt{m_\mathrm{e}^2 c^2 + \hbar^2 q^2}$ is the relativistic particle energy, and $\mathcal{I}_4$ is the 4×4 identity matrix.

We are interested in obtaining the leading contribution to the probability amplitude connecting the initial fermionic vacuum state $|0\rangle$ to a final pair state $|p\mathbf{q}s, e\mathbf{q}'s'\rangle$, which we write as $C_{p\mathbf{q}s,e\mathbf{q}'s'} = \langle p\mathbf{q}s, e\mathbf{q}'s'|\, \hat{\mathcal{S}}(\infty)\, |0\rangle$ in terms of the scattering operator $\hat{\mathcal{S}}(t) = \mathrm{T}\, \mathrm{e}^{-(\mathrm{i}/\hbar)\int_{-\infty}^{t} dt'\, \hat{\mathcal{H}}_{\mathrm{int}}(t')}$. By retaining only quadratic terms in the electromagnetic field and working out time ordering through Wick's theorem[303], we obtain

$$\begin{aligned} C_{p\mathbf{q}s,e\mathbf{q}'s'} \approx & \frac{-\mathrm{i}e^2}{\hbar^2} \int_{-\infty}^{\infty} dt \int_{-\infty}^{t} dt' \int d^3\mathbf{r} \int d^3\mathbf{r}' \\ & \times \langle p\mathbf{q}s, e\mathbf{q}'s'|\, :\overline{\Psi}(\mathbf{r},t)\vec{\gamma}\cdot\mathbf{A}(\mathbf{r},t) G_F(\mathbf{r}-\mathbf{r}', t-t')\vec{\gamma}\cdot\mathbf{A}(\mathbf{r}',t')\hat{\Psi}(\mathbf{r}',t') :\, |0\rangle\,, \end{aligned} \tag{G.2}$$

where $G_F(\mathbf{r},t) = (2\pi)^{-4}\int_{-\infty}^{\infty} d\omega \int d^3\mathbf{q}\, \mathrm{e}^{\mathrm{i}\mathbf{q}\cdot\mathbf{r}-\mathrm{i}\omega t} G_F(\mathbf{q},\omega)$ is the real-spacetime representation of the Feynman propagator given by

$$G_F(\mathbf{q},\omega) = \frac{\omega\gamma^0 - c\vec{\gamma}\cdot\mathbf{q} + (m_e c^2/\hbar)\,\mathcal{I}_4}{\omega^2 - \varepsilon_q^2 + \mathrm{i}0^+}, \tag{G.3}$$

where 0^+ is a positive infinitesimal. Plugging a vector potential taken to consist of monochromatic components of frequencies ω_i, such that can be written as

$$\mathbf{A}(\mathbf{r},t) = -\mathrm{i}\, c \sum_i \frac{1}{\omega_i}\, \vec{\mathcal{E}}_i(\mathbf{r}) \mathrm{e}^{-\mathrm{i}\omega_i t} + \mathrm{c.c.}, \tag{G.4}$$

where $\vec{\mathcal{E}}_i(\mathbf{r})$ are the time-independent amplitudes of the field components, and carrying out the required Dirac matrix algebra, this expression reduces to

$$\begin{aligned} C^{\pm}_{p\mathbf{q}s,e\mathbf{q}'s'} \approx \frac{2\pi\mathrm{i}e^2c^2}{V^2\hbar^2} {\sum_{ii'}}' \sum_{\mathbf{q}''} \frac{1}{\omega_i\omega_{i'}}\, \delta(\varepsilon_q + \varepsilon_{q'} - \omega_i \pm \omega_{i'}) & \\ \times\, \overline{u}_{\mathbf{q}'s'}\, \vec{\gamma}\cdot \Big[\vec{\mathcal{E}}_{i,\mathbf{q}'-\mathbf{q}''}\, G_F(\mathbf{q}'', \varepsilon_{q'} - \omega_i)\, \vec{\mathcal{E}}^{\pm}_{i',\mathbf{q}+\mathbf{q}''} & \\ + \vec{\mathcal{E}}^{\pm}_{i',\mathbf{q}'-\mathbf{q}''}\, G_F(\mathbf{q}'', \varepsilon_{q'} \pm \omega_{i'})\, \vec{\mathcal{E}}_{i,\mathbf{q}+\mathbf{q}''} \Big] \cdot \vec{\gamma}\, v_{\mathbf{q}s}, & \end{aligned}$$

where we have defined $\vec{\mathcal{E}}^{+}_{i',\mathbf{k}} \equiv \vec{\mathcal{E}}^{*}_{i',-\mathbf{k}}$ and $\vec{\mathcal{E}}^{-}_{i',\mathbf{k}} \equiv \vec{\mathcal{E}}_{i',\mathbf{k}}$ with $\vec{\mathcal{E}}_{i,\mathbf{k}} = \int d^3\mathbf{r}\, \mathrm{e}^{-\mathrm{i}\mathbf{k}\cdot\mathbf{r}} \vec{\mathcal{E}}_i(\mathbf{r})$ and the ± sign refers to channels involving either two frequencies of opposite sign $(+)$ or

---

[2] These spinors are directly related to the solutions of the Dirac equation presented in Appendix B through the relations $u_{\mathbf{q},s} = \Psi^{+}_{\mathbf{q}s}$ (for $s = \pm 1$), $v_{\mathbf{q},-1} = \Psi^{-}_{-\mathbf{q}1}$, and $v_{\mathbf{q},1} = -\Psi^{-}_{-\mathbf{q}-1}$.

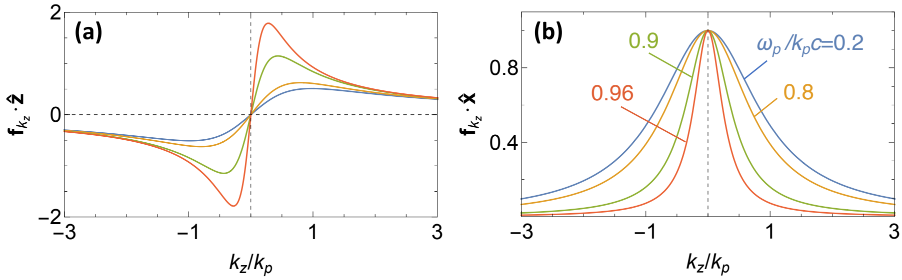

Figure G.1: Momentum distribution associated with the polariton field. We plot the components of $\mathbf{f}_{k_z}$ [Eq. (G.7)] along (a) out-of-plane and (b) in-plane directions as a function of k_z (normalized to the polariton wave vector k_p) for various polariton frequencies ω_p (normalized to $k_p c$).

two positive frequencies $(-)$. The prime in the summation symbol restricts it to $\omega_{i'} < \omega_i$ terms because the rest of the terms vanish due to energy conservation. Finally, the transition rate is obtained as $\Gamma^{(2)}_{\mathbf{pq}s,\mathbf{eq}'s'} = |C^{\pm}_{\mathbf{pq}s,\mathbf{eq}'s'}|^2/T$, where T is the interaction time. This expression produces a squared δ-function that we need to reinterpret by retaining one of such functions coming from one of the two $C^{\pm}_{\mathbf{pq}s,\mathbf{eq}'s'}$ factors and then undoing the time integral in the other factor through the prescription $\delta \rightarrow (2\pi)^{-1}\int dt$; the remaining δ-function still imposes energy conservation, whereas the undone time integral yields a factor T that cancels with the denominator. Following this procedure, we readily find the second-order pair-production rate

$$\begin{aligned}\Gamma^{(2)}_{\mathbf{pq}s,\mathbf{eq}'s'} =& \frac{2\pi e^4 c^4}{V^4\hbar^4}\sum_{ii'}{}' \frac{1}{\omega_i^2\omega_{i'}^2}\sum_{\pm}\delta(\varepsilon_q+\varepsilon_{q'}-\omega_i\pm\omega_{i'}) \\ &\times\Bigg|\overline{u}_{\mathbf{q}'s'}\,\vec{\gamma}\cdot\sum_{\mathbf{q}''}\Big[\vec{\mathcal{E}}_{i,\mathbf{q}'-\mathbf{q}''}\,G_F(\mathbf{q}'',\varepsilon_{q'}-\omega_i)\,\vec{\mathcal{E}}^{\pm}_{i',\mathbf{q}+\mathbf{q}''} \\ &\qquad\qquad + \vec{\mathcal{E}}^{\pm}_{i',\mathbf{q}'-\mathbf{q}''}\,G_F(\mathbf{q}'',\varepsilon_{q'}\pm\omega_{i'})\,\vec{\mathcal{E}}_{i,\mathbf{q}+\mathbf{q}''}\Big]\cdot\vec{\gamma}\,v_{\mathbf{q}s}\Bigg|^2,\end{aligned} \tag{G.5}$$

G.2 Pair production by scattering of a surface polariton and a γ-photon

While the rate in Eq. (G.5) can be generally applied to an arbitrary number of field components, we are here interested in calculating the pair-production rate associated with the scattering of surface polaritons of frequency ω_p $(i=p)$ and highly energetic $(>1\,\mathrm{MeV})$ γ-ray photons of frequency ω_γ $(i=\gamma)$.

We consider polaritons bound to a planar material interface of area A placed in the $z=0$ plane (e.g., a two-dimensional material capable of supporting strongly confined polaritons[295,296], such as graphene[235], few-atomic-layer hexagonal boron nitride[300], or ultrathin metal films[298]). Polaritons are taken to be lossless and traveling with a real in-plane wave vector $\mathbf{k}_p = k_\mathrm{p}\hat{\mathbf{x}}$ (with $k_p > \omega_p/c$) oriented along the x direction, so that their associated electric field can be written as $\vec{\mathcal{E}}_p(\mathbf{r}) = (E_p c/\omega_{\rm p})\big(\mathrm{i}\kappa_p\,\hat{\mathbf{x}} - k_{\rm p}\,\mathrm{sign}\{z\}\,\hat{\mathbf{z}}\big)\mathrm{e}^{\mathrm{i}k_{\rm p}x-\kappa_p|z|}$, where E_p is a global amplitude and $\kappa_p = \sqrt{k_p^2 - \omega_p^2/c^2}$ describes the evanescent field decay away from the interface. Likewise, we write $\vec{\mathcal{E}}_\gamma(\mathbf{r}) = E_\gamma\,\hat{\mathbf{e}}_\sigma\,\mathrm{e}^{\mathrm{i}\mathbf{k}_\gamma\cdot\mathbf{r}}$ for a γ-ray field of amplitude E_γ, arbitrarily oriented wave vector $\mathbf{k}_\gamma$ (with $\mathbf{k}_\gamma\cdot\hat{\mathbf{z}} > 0$), and unit polarization vector $\hat{\mathbf{e}}_\sigma$. The two possible polarization vectors (for $\sigma =$ s or p) together with $\hat{\mathbf{k}}_\gamma$ form a right-handed triad, such that $\hat{\mathbf{e}}_{\rm s}\otimes\hat{\mathbf{e}}_{\rm s} + \hat{\mathbf{e}}_{\rm p}\otimes\hat{\mathbf{e}}_{\rm p} + \hat{\mathbf{k}}_\gamma\otimes\hat{\mathbf{k}}_\gamma = \mathcal{I}_3$ is the 3×3 identity matrix. Here, we neglect material polarization at the high γ-photon frequency. Under these conditions, the Fourier components of the two fields read

$$\vec{\mathcal{E}}_{p\mathbf{k}} = \frac{2\mathrm{i}A\,c}{\omega_{\rm p}}\,E_p\,\mathbf{f}_{k_z}\,\delta_{\mathbf{k}_\parallel,\mathbf{k}_p}, \tag{G.6a}$$

$$\vec{\mathcal{E}}_{\gamma\mathbf{k}} = V\,E_\gamma\,\hat{\mathbf{e}}_\sigma\,\delta_{\mathbf{k},\mathbf{k}_\gamma}, \tag{G.6b}$$

where the subscript $\parallel$ denotes the in-plane x-y components. Here, we have performed the $\mathbf{r}$ integral over the quantization volume V and defined the real vector

$$\mathbf{f}_{k_z} = \frac{\kappa_p^2\,\hat{\mathbf{x}} + k_{\rm p}k_z\,\hat{\mathbf{z}}}{\kappa_p^2 + k_z^2}. \tag{G.7}$$

The lack of translational symmetry along the out-of-plane direction enables a finite range of momentum mismatch in that direction relative to the $q_z + q_z' = k_{\gamma z}$ condition, as described by the k_z dependence of $\mathbf{f}_{k_z}$, which we illustrate in Fig. (G.1) [see also Eq. (G.8) below]. Inserting Eqs. (G.6) in Eq. (G.5), and noticing that the only term in the (i,i') sum satisfying $\omega_{i'} < \omega_i$ corresponds to the choice $i=\gamma$ and $i'=p$, we find the rate

$$\begin{aligned}\Gamma^{(2)}_{p\mathbf{q}s,e\mathbf{q}'s'} =& \frac{8\pi A^2\alpha^2c^8\,\big|E_pE_\gamma\big|^2}{V^2\hbar^2\omega_p^4\omega_\gamma^2}\\ &\times\sum_\pm\Big|\overline{u}_{\mathbf{q}'s'}\,\mathcal{M}_\sigma^\pm(\mathbf{q},\mathbf{q}')\,v_{\mathbf{q}s}\Big|^2\,\delta_{\mathbf{k}_{\gamma\parallel}-\mathbf{q}_\parallel-\mathbf{q}'_\parallel,\pm\mathbf{k}_p}\;\delta(\varepsilon_q+\varepsilon_{q'}-\omega_\gamma\pm\omega_p),\end{aligned}$$

where $\alpha\approx 1/137$ is the fine-structure constant, we recall that primed (unprimed) quantities refer to the electron (positron), and the 4×4 matrix

$$\begin{aligned}\mathcal{M}_\sigma^\pm(\mathbf{q},\mathbf{q}') = \vec{\gamma}\cdot\Big[&\hat{\mathbf{e}}_\sigma\,G_F(\mathbf{q}'-\mathbf{k}_\gamma,\varepsilon_{q'}-\omega_\gamma)\,\mathbf{f}_{\pm(k_{\gamma z}-q_z-q_z')}\\ &+\mathbf{f}_{\pm(k_{\gamma z}-q_z-q_z')}\,G_F(\mathbf{k}_\gamma-\mathbf{q},\varepsilon_{q'}\pm\omega_p)\,\hat{\mathbf{e}}_\sigma\Big]\cdot\vec{\gamma}\end{aligned} \tag{G.8}$$

incorporates the anticipated finite out-of-plane momentum distribution through $\mathbf{f}_{\pm(k_{\gamma z}-q_z-q_z')}$.

It is convenient to recast this result in the form of a polariton-driven pair-production cross section $\sigma^{\rm pol}_{p\mathbf{q}s,e\mathbf{q}'s'} = \Gamma^{(2)}_{p\mathbf{q}s,e\mathbf{q}'s'}/N_pF_\gamma$, calculated by normalizing the rate to both the number of polaritons in the material (N_p) and the γ-photon flux traversing the polariton-supporting interface (F_γ). More precisely, we obtain N_p as the space integral of the field energy density divided by the polariton energy:

$N_p = (1/4\pi\hbar\omega_{\rm p}) \int d^3\mathbf{r} \left[|\vec{\mathcal{E}}_p(\mathbf{r})|^2 + (c/\omega_{\rm p})^2|\nabla\times\vec{\mathcal{E}}_p(\mathbf{r})|^2\right] = A\,|E_p|^2k_p^2c^2/2\pi\hbar\omega_p^3\kappa_p$. Likewise, the γ-photon flux is derived from the associated intensity divided by the photon energy as $F_\gamma = |\hat{\mathbf{k}}_\gamma\cdot\hat{\mathbf{z}}|\,c|E_\gamma|^2/2\pi\hbar\omega_\gamma$. Putting these elements together, we find

$$\begin{aligned}\sigma^{\rm pol}_{p\mathbf{q}s,e\mathbf{q}'s'} &= \frac{16\pi^3\alpha^2c^5\kappa_p}{VL\omega_p\omega_\gamma k_p^2}\,\frac{1}{|\hat{\mathbf{k}}_\gamma\cdot\hat{\mathbf{z}}|}\\ &\quad\times\sum_{\sigma=\rm s,p}\sum_{\pm}\left|\overline{u}_{\mathbf{q}'s'}\,\mathcal{M}^\pm_\sigma(\mathbf{q},\mathbf{q}')\,v_{\mathbf{q}s}\right|^2\,\delta_{\mathbf{k}_{\gamma\parallel}-\mathbf{q}_\parallel-\mathbf{q}'_\parallel,\pm\mathbf{k}_p}\;\delta(\varepsilon_q+\varepsilon_{q'}-\omega_\gamma\pm\omega_p),\end{aligned}$$

where L is the out-of-plane quantization length (i.e., $V = AL$) and we average over photon polarization σ. For a given emitted positron wave vector $\mathbf{q}$, the electron wave vector $\mathbf{q}'$ is determined by the Kronecker (in-plane components) and Dirac (out-of-plane component) δ-functions. Therefore, we use these functions to carry out the sum over electron wave vectors and, in addition, also sum over spin degrees of freedom. In particular, the in-plane electron wave vector is given by $\mathbf{q}'_{\parallel\pm} = \mathbf{k}_{\gamma\parallel} - \mathbf{q}_\parallel \mp \mathbf{k}_p$. Also, by applying standard properties of the Dirac δ-function and noticing that $\partial_{q'_z}\varepsilon_{q'} = q'_zc^2/\varepsilon_{q'}$, we can recast it into

$$\begin{aligned}\delta(\varepsilon_q+\varepsilon_{q'}-\omega_\gamma\pm\omega_p) =& \frac{\varepsilon_{q'_\pm}}{c^2q'_{z\pm}}\left[\delta(q'_z-q'_{z\pm})+\delta(q'_z+q'_{z\pm})\right]\\ &\times\,\theta\big(\varepsilon^2_{q'_\pm}-m_{\rm e}^2c^4/\hbar^2-c^2q'^2_{\parallel\pm}\big)\,\theta\big(\omega_\gamma\mp\omega_{\rm p}-\varepsilon_q\big)\end{aligned}$$

with

$$q'_{z\pm} = \sqrt{\varepsilon^2_{q'_\pm}/c^2 - m_{\rm e}^2c^2/\hbar^2 - q'^2_{\parallel\pm}} \tag{G.9}$$

denoting the out-of-plane electron wave-vector component and $\varepsilon_{q'_\pm} = \omega_\gamma \mp \omega_{\rm p} - \varepsilon_q$ the electron energy. This allows us to write the wave-vector-resolved differential positron emission cross section as

$$\begin{aligned}\frac{d\sigma^{\rm pol}}{d\mathbf{q}} &= \frac{V}{(2\pi)^3}\sum_{ss'}\sum_{\mathbf{q}'}\sigma^{\rm pol}_{p\mathbf{q}s,e\mathbf{q}'s'}\\ &= \frac{\alpha^2c^3\kappa_p}{\pi\,\omega_p\omega_\gamma k_p^2}\,\frac{1}{|\hat{\mathbf{k}}_\gamma\cdot\hat{\mathbf{z}}|}\sum_\pm\frac{\varepsilon_{q'_\pm}}{q'_{z\pm}}\,\theta\big(\varepsilon^2_{q'_\pm}-m_{\rm e}^2c^4/\hbar^2-c^2q'^2_{\parallel\pm}\big) \qquad\qquad (\text{G.10})\\ &\quad\times\theta\big(\omega_\gamma\mp\omega_{\rm p}-\varepsilon_q\big)\sum_{ss'\mu=\pm1}\;\sum_{\sigma=\rm s,p}\left|\overline{u}_{\mathbf{q}'_{\parallel\pm}+\mu q'_{z\pm}\hat{\mathbf{z}},s'}\,\mathcal{M}^\pm_\sigma(\mathbf{q},\mathbf{q}'_{\parallel\pm}+\mu q'_{z\pm}\hat{\mathbf{z}})\,v_{\mathbf{q}s}\right|^2,\end{aligned}$$

with $q'_{z\pm}$ given in Eq. (G.9), such that the two terms inside the square brackets stand for the contributions associated with upward ($q'_z = +q'_{z\pm}$) and downward ($q'_z = -q'_{z\pm}$) electron emission, respectively. The cross section in Eq. (G.10) [which corresponds to Eq. (7.3) in Chapter 7] is normalized such that the total positron-emission cross section is given by $\sigma^{\rm pol} = \int d^3\mathbf{q}\,(d\sigma^{\rm pol}/d\mathbf{q})$. In deriving this result, we have used the prescription $\sum_{\mathbf{q}} \to (2\pi)^{-3}V\int d^3\mathbf{q}$ to transform the positron wave-vector sum into an integral, and likewise $\sum_{q'_z} \to (L/2\pi)\int dq'_z$ for the out-of-plane electron wave vector.

Finally, the energy- and polar-angle-resolved positron-emission cross section is obtained by integrating Eq. (G.10) over the azimuthal emission angle φ as

$$\frac{d\sigma^{\rm pol}}{dE_q d\theta} = \sin\theta \, \frac{q\varepsilon_q}{\hbar c^2} \int_0^{2\pi} d\varphi \, \frac{d\sigma^{\rm pol}}{d\mathbf{q}}, \tag{G.11}$$

where $E_q = \hbar\varepsilon_q$ is the positron energy and θ is the emission angle relative to the surface normal [see Fig. (7.1a) in Chapter 7]. In Figs. (7.3) and (7.4), we present this quantity after further integrating over a finite positron energy range ΔE_q just to make the plot clearer by smoothing the integrable divergence introduced by the $1/q'_{z\pm}$ factor in Eq. (G.10) at the onset of positron emission, as also done in Fig. (7.3a,b).

List of Figures

List of Acronyms

1BZ	First Brillouin Zone 36, 37, 115, 116, 118
1D	One-Dimensional 113–115, 118, 163
2D	Two-Dimensional 9, 112–114, 117–122, 124, 125, 133, 163
2DEG	Two-Dimensional Electron Gas xii, 35, 36, 112, 116–120, 163, 164
BH	Bethe-Heitler 124
BW	Breit-Wheeler 124, 127
CG	Coulomb Gauge 13, 15, 28
CL	Cathodoluminescence x, xi, 17, 19, 94–97, 99, 101–106, 108, 109, 133, 144, 153, 154, 156, 158, 160, 162, 167
DOC	Degree of Coherence 99
e-beam	Electron Beam 16, 20, 22, 23, 25, 30, 79, 131–133, 160
EEL	Electron Energy-Loss 17, 19, 20, 151, 159
EELS	Electron Energy-Loss Spectroscopy 40, 42, 49, 51, 69, 78, 85, 87, 94, 108
EM	Electron Microscope 16, 19, 23, 87, 139
FWHM	Full Width at Half Maximum 25, 64–66, 100
GU	Gaussian Units 10, 137, 138
LDOS	Local Density of States 49
LG	Lorentz Gauge 13
LL	Landau-Lifshitz 124
MEQS	Maxwell's Equations 10–14, 27, 29, 138
MPU	Minimum-Phase Uncertainty 64, 66, 70
MQED	Macroscopic Quantum Electrodynamics ix, xi, 28, 29, 75, 96, 144, 149, 151, 158, 159, 161
PINEM	Photon-Induced Near-field Electron Microscopy ix–xi, 3, 5, 8, 23–26, 39, 40, 43, 46, 53, 56, 57, 59–71, 94, 100, 102–106, 108, 132, 133, 139, 140, 142, 167
Q-phase	Quantum phase xi, xii, 112–114, 117–119, 121, 122, 163, 164, 167, 168
QE	Quantum Emitter 41, 49, 51–53
QED	Quantum Electrodynamics x, 21, 26, 58, 77, 79, 149
QO	Quantum Optics 30, 31
RPA	Random-Phase Approximation ix, 9, 33, 34, 86, 118
RWA	Rotating-Wave Approximation 46
SEM	Scanning Electron Microscope 22
SI	International System of Units 10, 137, 138
TEM	Transmission Electron Microscope 22
UC	Unit Cell 36, 37
UTEM	Ultrafast Transmission Electron Microscopy 94
WG	Weyl Gauge 13, 28
ZLP	Zero-Loss Peak 40

List of publications and conference contributions

The research carried out throughout this doctoral period has led to the following publications and conference contributions:

Articles on which this Thesis is based

1. **Probing quantum optical excitations with fast electrons.**
   V. Di Giulio, M. Kociak, and F. Javier García de Abajo.
   Optica, **6**, 1524–1534, (2019).
   https://doi.org/10.1364/OPTICA.6.001524

2. **Electron diffraction by vacuum fluctuations.**
   V. Di Giulio and F. Javier García de Abajo.
   New Journal of Physics, **22**, 103057, (2020).
   https://doi.org/10.1088/1367-2630/abbddf

3. **Free-electron shaping using quantum light.**
   V. Di Giulio and F. Javier García de Abajo.
   Optica, **7**, 1820–1830, (2020).
   https://doi.org/10.1364/OPTICA.404598

4. **Modulation of cathodoluminescence emission by interference with external light.**
   V. Di Giulio, O. Kfir, C. Ropers, and F. Javier García de Abajo.
   ACS Nano, **15**, 7290–7304, (2021).
   https://doi.org/10.1021/acsnano.1c00549

5. **Optical excitations with electron beams: challenges and opportunities.**
   F. Javier García de Abajo and V. Di Giulio.
   ACS Photonics, **8**, 945–974, (2021). **[Cover Image]**
   https://doi.org/10.1021/acsphotonics.0c01950

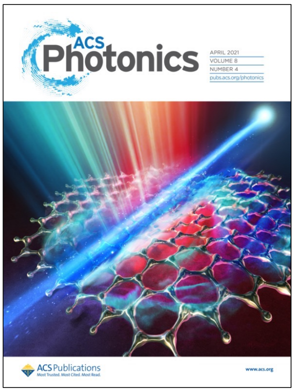

Figure G.2: Cover image, ACS Photonics, **8**, 945–974, (2021).

6. **An image interaction approach to quantum-phase engineering of two-dimensional materials.**
   V. Di Giulio, P. A. D. Gonçalves, and F. Javier García de Abajo.
   Nature Communications, **13**, 5175, (2022).
   https://doi.org/10.1038/s41467-022-32508-5

7. **Nanophotonics for Pair Production.**
   V. Di Giulio and F. Javier García de Abajo.
   arXiv, 10.48550, (2023).
   https://doi.org/10.48550/arXiv.2301.07377

Articles related to this Thesis

1. **Nanoscale nonlinear spectroscopy with electron beams.**
   A. Konečná, V. Di Giulio, V. Mkhitaryan, C. Ropers, and F. Javier García de Abajo.
   ACS Photonics, **7**, 1290–1296, (2019).
   https://doi.org/10.1021/acsphotonics.0c00326

2. **Optical coherence transfer mediated by free electrons.**
   O. Kfir, V. Di Giulio, F. Javier García de Abajo, and C. Ropers
   Science Advances, **7**, eabf6380, (2021).
   https://doi.org/10.1126/sciadv.abf6380

3. **Atomic Floquet physics revealed by free electrons.**
   E. Arqué López, V. Di Giulio, and F. Javier García de Abajo.
   Physical Review Research, **4**, 013241, (2022).
   https://doi.org/10.1103/PhysRevResearch.4.013241

4. **Sub-nanometer mapping of strain-induced band structure variations in planar nanowire core-shell heterostructures.**
   S. Martí-Sánchez, M. Botifoll, E. Oksenberg, C. Koch, C. Borja, M. C. Spadaro, V. Di Giulio, Q. Ramasse, F. Javier García de Abajo, E. Joselevich, and J. Arbiol.
   Nature Communications, **13**, 4089, (2022).
   https://doi.org/10.1038/s41467-022-31778-3

5. **Complete excitation of discrete quantum systems by single free electrons.**
   F. Javier García de Abajo, Eduardo J. C. Dias, and V. Di Giulio.
   Physical Review Letters, **129**, 093401, (2022).
   https://doi.org/10.1103/PhysRevLett.129.093401

6. **Optical manipulation of matter waves.**
   K. Akbari, V. Di Giulio, and F. Javier García de Abajo.
   Science Advances, **8**, eabq2659, (2022).
   https://doi.org/10.1126/sciadv.abq2659

7. **Optical-cavity mode squeezing by free electrons.**
   V. Di Giulio and F. Javier García de Abajo.
   Nanophotonics, (2022).
   https://doi.org/10.1515/nanoph-2022-0481

Oral and invited contributions to international conferences

1. *Probing out-of-equilibrium optical excitations with fast electrons.*
   V. Di Giulio, V. Mkhitaryan, and F. Javier García de Abajo.
   NANOP, Rome, Italy. September 2018.

2. *Toward strong coupling between free electrons and confined optical modes.*
   V. Di Giulio, V. Mkhitaryan, and F. Javier García de Abajo.
   Nanometa19, Seefeld in Tirol, Austria. January 2019.

3. *Probing out-of-equilibrium optical excitations with fast electrons..*
   V. Di Giulio, M. Kociak, and F. Javier García de Abajo.
   SPP9, Copenhagen, Denmark. May 2019.

4. *Toward strong coupling between free electrons and confined optical modes.*
   V. Di Giulio, V. Mkhitaryan, and F. Javier García de Abajo.
   PIERS19, Rome, Italy. June 2019.

5. *Toward strong coupling between free electrons and confined optical modes.*
   V. Di Giulio, V. Mkhitaryan, and F. Javier García de Abajo.
   CLEO Europe 2019, Munich, Germany. June 2019.

6. *Probing out-of-equilibrium optical excitations with fast electrons..*
   V. Di Giulio, M. Kociak, and F. Javier García de Abajo.
   EBSN, Orsay (Paris), France. September 2019.

7. *Quantum effects in the Interaction of optical excitations and fast electrons.*
   V. Di Giulio, M. Kociak, and F. Javier García de Abajo.
   OSA - Frontiers in Optics, Online format (supposed to be held in Washington, USA). September 2020.

8. *Quantum effects in the interaction of optical excitations and fast electrons.*
   V. Di Giulio, M. Kociak, and F. Javier García de Abajo.
   Metamaterials, Online format (supposed to be held in New York, USA). October 2020.

9. *Quantum effects in the interaction of optical excitations and fast electrons.*
   V. Di Giulio, M. Kociak, and F. Javier García de Abajo.
   MRS, Online format (supposed to be held in Boston, USA). December 2020.

10. *Modulation of cathodoluminescence emission by interference with external Light.*
    V. Di Giulio, O. Kfir, C. Ropers, and F. Javier García de Abajo.
    EBEAMS Colloquium, Online format. March 2021.

11. *Optical coherence transfer by free electrons and its effects on CL emission.*
    V. Di Giulio, O. Kfir, C. Ropers, and F. Javier García de Abajo.
    EBSN, Online format [supposed to be held in Orsay (Paris), France]. June 2021. Invited contribution.

12. *Modulation of cathodoluminescence emission by interference with external light.*
    V. Di Giulio, O. Kfir, C. Ropers, and F. Javier García de Abajo.
    CLEO Europe, Online format (supposed to be held in Munich, Germany). June 2021.

13. *Modulation of cathodoluminescence emission by interference with external light.*
    V. Di Giulio, O. Kfir, C. Ropers, and F. Javier García de Abajo.
    SPIE Photonics Asia, Online format contribution (supposed to be held Nantong, Jiangsu, China). October 2021.

14. *Modulation of cathodoluminescence emission by interference with external light.*
    V. Di Giulio, O. Kfir, C. Ropers, and F. Javier García de Abajo.
    SPIE Photonics West, San Francisco, USA. January 2022.

15. *Shaping electron beams with quantum light.*
    V. Di Giulio and F. Javier García de Abajo.
    SPIE Photonics West, San Francisco, USA. January 2022.

16. *Modulation of cathodoluminescence emission by interference with external light.*
    V. Di Giulio, O. Kfir, C. Ropers, and F. Javier García de Abajo.
    Nanometa22, Seefeld in Tirol, Austria. March 2022.

17. *Nonclassical behaviour of an electron current: the creation of quantum light by free electron beams*
    V. Di Giulio and F. Javier García de Abajo.
    Quantum Electron Optics, Nahsholim, Israel. June 2022.

18. *Optical manipulation of matter waves.*
    K. Akbari, V. Di Giulio, and F. Javier García de Abajo.
    SPIE Optics and Photonics, San Diego, United States. August 2022.

19. *An image interaction approach to quantum-phase engineering of two-dimensional materials.*
    V. Di Giulio, P. A. D. Gonçalves, and F. Javier García de Abajo.
    SPIE Optics and Photonics, San Diego, United States. August 2022.

Additionally, the research performed during the doctoral period has resulted in 8 poster contributions to conferences, presented by the author.

Bibliography

[1] E. Ruska. The development of the electron microscope and of electron microscopy. *Rev. Mod. Phys.*, 59:627–638, 1987.

[2] J. C. Maxwell. *Electricity and Magnetism.* Oxford, Clarendon, 1873.

[3] J. D. Jackson. *Classical Electrodynamics.* Wiley, New York, 1975.

[4] F. J. García de Abajo and A. Howie. Retarded field calculation of electron energy loss in inhomogeneous dielectrics. *Phys. Rev. B*, 65:115418, 2002.

[5] W. Heitler. *The Quantum Theory of Radiation.* Dover Publications, Inc., New York, 1984.

[6] C. Cohen-Tannoudji, J. Dupont-Roc, and G. Grynberg. *Photons and Atoms - Introduction to Quantum Electrodynamics.* Wiley-Interscience, New York, 1997.

[7] S. Y. Buhmann. *Dispersion Forces I. Macroscopic Quantum Electrodynamics and Ground-state Casimir, Casimir-polder and van der Waals Forces.* Springer-Verlag Berlin Heidelberg, Verlag Berlin Heidelberg, 2012.

[8] F. J. García de Abajo. Optical excitations in electron microscopy. *Rev. Mod. Phys.*, 82:209–275, 2010.

[9] R. J. Glauber and M. Lewenstein. Quantum optics of dielectric media. *Phys. Rev. A*, 43:467–491, 1991.

[10] R. Yu, L. M. Liz-Marzán, and F. J. García de Abajo. Universal analytical modeling of plasmonic nanoparticles. *Chem. Soc. Rev.*, 46:6710–6724, 2017.

[11] E. S. C. Ching, P. T. Leung, A. Maassen van den Brink, W. M. Suen, S. S. Tong, and K. Young. Quasinormal-mode expansion for waves in open systems. *Rev. Mod. Phys.*, 70:1545–1554, 1998.

[12] Rong-Chun Ge and Stephen Hughes. Quantum dynamics of two quantum dots coupled through localized plasmons: an intuitive and accurate quantum optics approach using quasinormal modes. *Phys. Rev. B*, 92:205420, 2015.

[13] M. Abramowitz and I. A. Stegun. *Handbook of Mathematical Functions.* Dover, New York, 1972.

[14] J. V. Julley. *Cherenkov Radiation and Its Application.* Pergamon, New York, 1958.

[15] F. J. García de Abajo. Relativistic energy loss and induced photon emission in the interaction of a dielectric sphere with an external electron beam. *Phys. Rev. B*, 59:3095–3107, 1999.

[16] C. J. Powell. Characteristic energy losses of 8-keV electrons in liquid Al, Bi, In, Ga, Hg, and Au. *Phys. Rev.*, 175:972–982, 1968.

[17] M. G. Walls and A. Howie. Dielectric theory of localised valence energy loss spectroscopy. *Ultramicroscopy*, 28:40–42, 1989.

[18] P. Moreau, N. Brun, C. A. Walsh, C. Colliex, and A. Howie. Relativistic effects in electron-energy-loss-spectroscopy observations of the si/sio$_2$ interface plasmon peak. *Phys. Rev. B*, 56:6774–6781, 1997.

[19] N. W. Ashcroft and N. D. Mermin. *Solid State Physics.* Harcourt College Publishers, Philadelphia, 1976.

[20] J. A. Stratton. *Electromagnetic Theory.* McGraw-Hill, New York, 1941.

[21] A. Messiah. *Quantum Mechanics.* North-Holland, New York, 1966.

[22] J. Nelayah, O. Stéphan, M. Kociak, F. J. García de Abajo, L. Henrard, I. Pastoriza-Santos, L. M. Liz-Marzán, and C. Colliex. Mapping surface plasmons on single metallic nanoparticles using sub-nm resolved EELS spectrum-imaging. *Microsc. Microanal.*, 13:144–145, 2007.

[23] M. Kuttge, E. J. R. Vesseur, A. F. Koenderink, H. J. Lezec, H. A. Atwater, F. J. García de Abajo, and A. Polman. Local density of states, spectrum, and far-field interference of surface plasmon polaritons probed by cathodoluminescence. *Phys. Rev. B*, 79:113405, 2009.

[24] P. A. M. Dirac. The quantum theory of the electron. *Proc. R. Soc. A*, 117:610–624, 1928.

[25] J. J. Sakurai. *Advanced Quantum Mechanics.* Pearson Education, Incorporated, Boston, 2006.

[26] B. Barwick, D. J. Flannigan, and A. H. Zewail. Photon-induced near-field electron microscopy. *Nature*, 462:902–906, 2009.

[27] S. T. Park, M. Lin, and A. H. Zewail. Photon-induced near-field electron microscopy (PINEM): theoretical and experimental. *New J. Phys.*, 12:123028, 2010.

[28] F. J. García de Abajo, A. Asenjo-Garcia, and M. Kociak. Multiphoton absorption and emission by interaction of swift electrons with evanescent light fields. *Nano Lett.*, 10:1859–1863, 2010.

[29] Armin Feist, Katharina E. Echternkamp, Jakob Schauss, Sergey V. Yalunin, Sascha Schäfer, and Claus Ropers. Quantum coherent optical phase modulation in an ultrafast transmission electron microscope. *Nature*, 521:200–203, 2015.

[30] F. J. García de Abajo and A. Konečná. Optical modulation of electron beams in free space. *Phys. Rev. Lett.*, 126:123901, 2021.

[31] A. Konečná, V. Di Giulio, V. Mkhitaryan, C. Ropers, and F. J. García de Abajo. Nanoscale nonlinear spectroscopy with electron beams. *ACS Photonics*, 7:1290–1296, 2020.

[32] M. Kozák, T. Eckstein, N. Schönenberger, and P. Hommelhoff. Inelastic ponderomotive scattering of electrons at a high-intensity optical travelling wave in vacuum. *Nat. Phys.*, 14:121–125, 2018.

[33] F. J. García de Abajo and V. Di Giulio. Optical excitations with electron beams: Challenges and opportunities. *ACS Photonics*, 8:945–974, 2021.

[34] A. Feist, S. V. Yalunin, S. Schäfer, and C. Ropers. High-purity free-electron momentum states prepared by three-dimensional optical phase modulation. *Phys. Rev. Research*, 2:043227, 2020.

[35] R. Dahan, S. Nehemia, M. Shentcis, O. Reinhardt, Y. Adiv, X. Shi, O. Be'er, M. H. Lynch, Y. Kurman, K. Wang, and I. Kaminer. Resonant phase-matching between a light wave and a free-electron wavefunction. *Nat. Phys.*, 16:1123–1131, 2020.

[36] G. M. Vanacore, I. Madan, G. Berruto, K. Wang, E. Pomarico, R. J. Lamb, D. McGrouther, I. Kaminer, B. Barwick, F. J. García de Abajo, and F. Carbone. Attosecond coherent control of free-electron wave functions using semi-infinite light fields. *Nat. Commun.*, 9:2694, 2018.

[37] P. L. Kapitza and P. A. M. Dirac. The reflection of electrons from standing light waves. *Proc. Cambridge Philos. Soc.*, 29:297–300, 1933.

[38] Daniel L. Freimund, Kayvan Aflatooni, and Herman Batelaan. Observation of the Kapitza-Dirac effect. *Nature*, 413:142–143, 2001.

[39] K. E. Echternkamp, A. Feist, S. Schäfer, and C. Ropers. Ramsey-type phase control of free-electron beams. *Nat. Phys.*, 12:1000–1004, 2016.

[40] A. A. Abrikosov, L. P. Gorkov, and I. Y. Dzyaloshinskii. *Quantum Field Theoretical Methods in Statistical Physics.* Pergamon Press, New York, 1965.

[41] B. E. Sernelius. Retarded interactions in graphene systems. *Phys. Rev. B*, 85:195427, 2012.

[42] M. Boustimi, J. Baudon, P. Candori, and J. Robert. van der waals interaction between an atom and a metallic nanowire. *Phys. Rev. B*, 65:155402, 2002.

[43] S. Y. Buhmann and D.-G. Welsch. Born expansion of the casimir–polder interaction of a ground-state atom with dielectric bodies. *Appl. Phys. B*, 82:189–201, 2006.

[44] J. A. Crosse, S. Å Ellingsen, K. Clements, S. Y. Buhmann, and S. Scheel. Thermal casimir-polder shifts in rydberg atoms near metallic surfaces. *Phys. Rev. A*, 82:010901, 2010.

[45] Nicholas Rivera, Liang Jie Wong, Marin Soljačić John D. Joannopoulos, and Ido Kaminer. Light emission based on nanophotonic vacuum forces. *Nat. Photon.*, 15:1284–1289, 2019.

[46] R. Loudon. *The Quantum Theory of Light.* Oxford University Press, Oxford, 2000.

[47] P. W Milonni. *The Quantum Vacuum: An Introduction to Quantum Electrodynamics.* Academic Press, San Diego, 1994.

[48] Sebastian Franke, Stephen Hughes, Mohsen Kamandar Dezfouli, Philip Tr¿st Kristensen, Kurt Busch, Andreas Knorr, and Marten Richter. Quantization of quasinormal modes for open cavities and plasmonic cavity quantum electrodynamics. *Phys. Rev. Lett.*, 122:213901, 2019.

[49] H. P. Breuer and F. Petruccione. *The Theory of Open Quantum Systems.* Oxford University Press, Oxford, 2002.

[50] P. Meystre and M. Sargent. *Elements of Quantum Optics.* Springer-Verlag, Berlin, 2007.

[51] E. Scrödinger. Der stetige Übergang von der mikro-zur makromechanik. *Die Naturwissenschaften*, 14:664–666, 1926.

[52] R. J. Glauber. Coherent and incoherent states of the radiation field. *Phys. Rev.*, 131:2766–2788, 1963.

[53] R. J. Glauber. The quantum theory of optical coherence. *Phys. Rev.*, 130:2529–2539, 1963.

[54] C. Brunel, B. Lounis, P. Tamarat, and M. Orrit. Triggered source of single photons based on controlled single molecule fluorescence. *Phys. Rev. Lett.*, 83:2722–2725, 1999.

[55] R. Loudon and P. L. Knight. Squeezed light. *J. Mod. Opt.*, 34:709–759, 1987.

[56] F. J. García de Abajo. Nonlocal effects in the plasmons of strongly interacting nanoparticles, dimers, and waveguides. *J. Phys. Chem. C*, 112:17983–17987, 2008.

[57] Richard Denk, Michael Hohage, Peter Zeppenfeld, Jinming Cai, Carlo A. Pignedoli, Hajo Söde, Roman Fasel, Xinliang Feng, Klaus Müllen, Shudong Wang, Deborah Prezzi, Andrea Ferretti, Alice Ruini, Elisa Molinari, and Pascal Ruffieux. Exciton-dominated optical response of ultra-narrow graphene nanoribbons. *Nat. Commun.*, 5:4253, 2014.

[58] Giovanni Scuri, You Zhou, Alexander A. High, Dominik S. Wild, Chi Shu, Kristiaan De Greve, Luis A. Jauregui, Takashi Taniguchi, Kenji Watanabe, Philip Kim, Mikhail D. Lukin, and Hongkun Park. Large excitonic reflectivity of monolayer $MoSe_2$ encapsulated in hexagonal boron nitride. *Phys. Rev. Lett.*, 120:037402, 2018.

[59] W. S. M. Werner. Dielectric function of cu, ag, and Au obtained from reflection electron energy loss spectra, optical measurements, and density functional theory. *Appl. Phys. Lett.*, 89:213106, 2006.

[60] M. A. L. Marques, C. A. Ullrich, F. Nogueira, A. Rubio, K. Burke, and E. K. U. Gross. *Time-dependent Density Functional Theory*, volume 706 of *Lecture Notes in Physics*. Springer, 2006.

[61] L. Hedin and S. Lundqvist. Effects of electron-electron and electron-phonon interactions on the one-electron states of solids. In David Turnbull Frederick Seitz and Henry Ehrenreich, editors, *Solid State Physics*, volume 23 of *Solid State Physics*, pages 1–181. Academic Press, 1970.

[62] G. Giuliani and F. Vignale. *Quantum Theory of the Electron Liquid*. Cambridge University Press, Cambridge, 2005.

[63] S. L. Adler. Quantum theory of the dielectric constant in real solids. *Phys. Rev.*, 126:413–420, 1961.

[64] V. Di Giulio, M. Kociak, and F. J. García de Abajo. Probing quantum optical excitations with fast electrons. *Optica*, 6:1524–1534, 2019.

[65] A. Howie. Valence excitations in electron microscopy: resolved and unresolved issues. *Micron*, 34:121–125, 2003.

[66] K. A. Mkhoyan, T. Babinec, S. E. Maccagnano, E. J. Kirkland, and J. Silcox. Separation of bulk and surface-losses in low-loss EELS measurements in STEM. *Ultramicroscopy*, 107:345–355, 2007.

[67] O. L. Krivanek, T. C. Lovejoy, N. Dellby, T. Aoki, R. W. Carpenter, P. Rez, E. Soignard, J. Zhu, P. E. Batson, M. J. Lagos, R. F. Egerton, and P. A. Crozier. Vibrational spectroscopy in the electron microscope. *Nature*, 514:209–214, 2014.

[68] D. A. Muller, L. Fitting Kourkoutis, M. Murfitt, J. H. Song, H. Y. Hwang, J. Silcox, N. Dellby, and O. L. Krivanek. Atomic-scale chemical imaging of composition and bonding by aberration-corrected microscopy. *Science*, 319:1073–1076, 2008.

[69] G. Zhu, G. Radtke, and G. A. Botton. Bonding and structure of a reconstructed (001) surface of $SrTiO_3$ from TEM. *Nature*, 490:384–387, 2012.

[70] David Rossouw and Gianluigi A. Botton. Plasmonic response of bent silver nanowires for nanophotonic subwavelength waveguiding. *Phys. Rev. Lett.*, 110:066801, 2013.

[71] M. Kociak and O. Stéphan. Mapping plasmons at the nanometer scale in an electron microscope. *Chem. Soc. Rev.*, 43:3865–3883, 2014.

[72] Andreas Trügler Anton Hörl and Ulrich Hohenester. Full three-dimensonal reconstruction of the dyadic Green tensor from electron energy loss spectroscopy of plasmonic nanoparticles. *ACS Photonics*, 2:1429–1435, 2015.

[73] G. Guzzinati, A. Beche, H. Lourenço-Martins, J. Martin, M. Kociak, and J. Verbeeck. Probing the symmetry of the potential of localized surface plasmon resonances with phase-shaped electron beams. *Nat. Commun.*, 8:14999, 2017.

[74] A. Ryabov and P. Baum. Electron microscopy of electromagnetic waveforms. *Science*, 353:374–377, 2016.

[75] M. Kozák, J. McNeur, K. J. Leedle, H. Deng, N. Schönenberger, A. Ruehl, I. Hartl, J. S. Harris, R. L. Byer, and P. Hommelhoff. Optical gating and streaking of free electrons with sub-optical cycle precision. *Nat. Commun.*, 8:14342, 2017.

[76] F. O. Kirchner, A. Gliserin, F. Krausz, and P. Baum. Laser streaking of free electrons at 25 keV. *Nat. Photon.*, 8:52–57, 2014.

[77] L. Piazza, T. T. A. Lummen, E. Quiñonez, Y. Murooka, B.W. Reed, B. Barwick, and F. Carbone. Simultaneous observation of the quantization and the interference pattern of a plasmonic near-field. *Nat. Commun.*, 6:6407, 2015.

[78] T. T. A. Lummen, R. J. Lamb, G. Berruto, T. LaGrange, L. Dal Negro, F. J. García de Abajo, D. McGrouther, B. Barwick, and F. Carbone. Imaging and controlling plasmonic interference fields at buried interfaces. *Nat. Commun.*, 7:13156, 2016.

[79] A. Feist, N. Bach, T. Danz N. Rubiano da Silva, M. Mäller, K. E. Priebe, T. Domräse, J. G. Gatzmann, S. Rost, J. Schauss, S. Strauch, R. Bormann, M. Sivis, S. Schäfer, and C. Ropers. Ultrafast transmission electron microscopy using a laser-driven field emitter: femtosecond resolution with a high coherence electron beam. *Ultramicroscopy*, 176:63–73, 2017.

[80] K. E. Priebe, C. Rathje, S. V. Yalunin, T. Hohage, A. Feist, S. Schäfer, and C Ropers. Attosecond electron pulse trains and quantum state reconstruction in ultrafast transmission electron microscopy. *Nat. Photon.*, 11:793–797, 2017.

[81] E. Pomarico, I. Madan, G. Berruto, G. M. Vanacore, K. Wang, I. Kaminer, F. J. García de Abajo, and F. Carbone. meV resolution in laser-assisted energy-filtered transmission electron microscopy. *ACS Photonics*, 5:759–764, 2018.

[82] W. Cai, O. Reinhardt, I. Kaminer, and F. J. García de Abajo. Efficient orbital angular momentum transfer between plasmons and free electrons. *Phys. Rev. B*, 98:045424, 2018.

[83] Y. Morimoto and P. Baum. Attosecond control of electron beams at dielectric and absorbing membranes. *Phys. Rev. A*, 97:033815, 2018.

[84] L. H. G. Tizei and M. Kociak. Spatially resolved quantum nano-optics of single photons using an electron microscope. *Phys. Rev. Lett.*, 110:153604, 2013.

[85] S. Meuret, L. H. G. Tizei, T. Cazimajou, R. Bourrellier, H. C. Chang, F. Treussart, and M. Kociak. Photon bunching in cathodoluminescence. *Phys. Rev. Lett.*, 114:197401, 2015.

[86] Romain Bourrellier, Sophie Meuret, Anna Tararan, Odile Stéphan, Mathieu Kociak, Luiz H. G. Tizei, and Alberto Zobelli. Bright uv single photon emission at point defects in h-bn. *Nano Lett.*, 16:4317–4321, 2016.

[87] O. Kfir. Entanglements of electrons and cavity photons in the strong-coupling regime. *Phys. Rev. Lett.*, 123:103602, 2019.

[88] F. J. García de Abajo, E. J. C. Dias, and V. Di Giulio. Complete excitation of discrete quantum systems by single free electrons. *Phys. Rev. Lett.*, 129:093401, 2022.

[89] P. Carruthers and M. M. Nieto. Coherent states and the forced quantum oscillator. *Am. J. Phys.*, 33:537–544, 1965.

[90] A. A. Lucas, E. Kartheuser, and R. G. Badro. Electron-phonon interaction in dielectric films. Application to electron energy loss and gain spectra. *Phys. Rev. B*, 2:2488–2499, 1970.

[91] F. J. García de Abajo. Multiple excitation of confined graphene plasmons by single free electrons. *ACS Nano*, 7:11409–11419, 2013.

[92] M. O. Scully and M. S. Zubairy. *Quantum Optics.* Cambridge University Press, Cambridge, 1997.

[93] F. J. García de Abajo, B. Barwick, and F. Carbone. Electron diffraction by plasmon waves. *Phys. Rev. B*, 94:041404(R), 2016.

[94] W. Feller. *An Introduction to Probability Theory and Its Applications.* John Wiley, New York, 1968.

[95] I. S. Gradshteyn and I. M. Ryzhik. *Table of Integrals, Series, and Products.* Academic Press, London, 2007.

[96] D. Pines and P. Noziéres. *The Theory of Quantum Liquids.* W. A. Benjamin, Inc., New York, 1966.

[97] P. B. Johnson and R. W. Christy. Optical constants of the noble metals. *Phys. Rev. B*, 6:4370–4379, 1972.

[98] E. J. C. Dias and F. J. García de Abajo. Fundamental limits to the coupling between light and 2D polaritons. *ACS Nano*, 13:5184–5197, 2019.

[99] F. J. García de Abajo and M. Kociak. Probing the photonic local density of states with electron energy loss spectroscopy. *Phys. Rev. Lett.*, 100:106804, 2008.

[100] P. Das, J. D. Blazit, M. Tencé, L. F. Zagonel, Y. Auad, Y. H. Lee, X. Y. Ling, A. Losquin, O. Stéphan C. Colliex, F. J. García de Abajo, and M. Kociak. Stimulated electron energy loss and gain in an electron microscope without a pulsed electron gun. *Ultramicroscopy*, 203:44–51, 2019.

[101] J. H. Eberly, B.W. Shore, Z. Białynicka-Birula, and I. Białynicki-Birula. Coherent dynamics of n-level atoms and molecules. I. Numerical experiments. *Phys. Rev. A*, 16:2038–2047, 1977.

[102] J. K. Hyun, M. Couillard, P. Rajendran, C. M. Liddell, and D. A. Muller. Measuring far-ultraviolet whispering gallery modes with high energy electrons. *Appl. Phys. Lett.*, 93:243106, 2008.

[103] Andreas Reiserer and Gerhard Rempe. Cavity-based quantum networks with single atoms and optical photons. *Rev. Mod. Phys.*, 87:1379–1418, 2015.

[104] Renato Barbosa-Silva, Andrea F. Silva, Antonio M. Brito-Silva, and Cid B. de Araújo. Bichromatic random laser from a powder of rhodamine-doped sub-micrometer silica particles. *J. Appl. Phys.*, 115:043515, 2014.

[105] Yoshiaki Nishijima, Kosei Ueno, Saulius Juodkazis, Vygantas Mizeikis, Hideki Fujiwara, Keiji Sasaki, and Hiroaki Misawa. Lasing with well-defined cavity modes in dye-infiltrated silica inverse opals. *Opt. Express*, 17:2976–2983, 2009.

[106] O. Kfir, H. Lourenço-Martins, G. Storeck, M. Sivis, T. R. Harvey, T. J. Kippenberg, A. Feist, and C. Ropers. Controlling free electrons with optical whispering-gallery modes. *Nature*, 582:46–49, 2020.

[107] K. Wang, R. Dahan, M. Shentcis, Y. Kauffmann, A. Ben Hayun, O. Reinhardt, S. Tsesses, and I. Kaminer. Coherent interaction between free electrons and a photonic cavity. *Nature*, 582:50–54, 2020.

[108] V. Di Giulio and F. J. García de Abajo. Free-electron shaping using quantum light. *Optica*, 7:1820–1830, 2020.

[109] P. M. Paul, E. S. Toma, P. Breger, G. Mullot, F. Augé, Ph. Balcou, H. G. Muller, and P. Agostini. Observation of a train of attosecond pulses from high harmonic generation. *Science*, 292:1689–1692, 2001.

[110] P. B. Corkum and Ferenc Krausz. Attosecond science. *Nat. Phys.*, 3:381–387, 2007.

[111] Ferenc Krausz and Misha Ivanov. Attosecond physics. *Rev. Mod. Phys.*, 81:163–234, 2009.

[112] B. W. McNeil and N. R. Thompson. X-ray free-electron lasers. *Nat. Photon.*, 4:814–821, 2010.

[113] C. Kealhofer, W. Schneider, D. Ehberger, A. Ryabov, F. Krausz, and P. Baum. All-optical control and metrology of electron pulses. *Science*, 352:429–433, 2016.

[114] G. M. Vanacore, A. W. P. Fitzpatrick, and A. H. Zewail. Four-dimensional electron microscopy: ultrafast imaging, diffraction and spectroscopy in materials science and biology. *Nano Today*, 11:228–249, 2016.

[115] G. M. Vanacore, G. Berruto, I. Madan, E. Pomarico, P. Biagioni, R. J. Lamb, D. McGrouther, O. Reinhardt, I. Kaminer, B. Barwick, H. Larocque, V. Grillo, E. Karimi, F. J. García de Abajo, and F. Carbone. Ultrafast generation and control of an electron vortex beam via chiral plasmonic near fields. *Nat. Mater.*, 18:573–579, 2019.

[116] S. T. Park and A. H. Zewail. Relativistic effects in photon-induced near field electron microscopy. *J. Phys. Chem. A*, 116:11128–11133, 2012.

[117] P. Baum. Quantum dynamics of attosecond electron pulse compression. *J. Appl. Phys.*, 122:223105, 2017.

[118] O. Reinhardt, C. Mechel, M. Lynch, and I. Kaminer. Free-electron qubits. *Ann. Phys.*, 533:2000254, 2021.

[119] Y. Morimoto and P. Baum. Diffraction and microscopy with attosecond electron pulse trains. *Nat. Phys.*, 14:252–256, 2018.

[120] J. Verbeeck, H. Tian, and P. Schattschneider. Production and application of electron vortex beams. *Nature*, 467:301–304, 2010.

[121] J. Verbeeck, G. Guzzinati, L. Clark, R. Juchtmans, R. Van Boxem, H. Tian, A. Béché, A. Lubk, and G. Van Tandeloo. Shaping electron beams for the generation of innovative measurements in the (s)tem. *C. R. Physique*, 15:190–199, 2014.

[122] J. Verbeeck, A. Béché, Knut Müller-Caspary, G. Guzzinati, M. A. Luong, and M. D. Hertog. Demonstration of a 2×2 programmable phase plate for electrons. *Ultramicroscopy*, 190:58–65, 2018.

[123] R. Shiloh, P. Lu, R. Remez, A. H. Tavabi, G. Pozzi, R. E. Dunin-Borkowski, and A. Arie. Nanostructuring of electron beams. *Phys. Scr.*, 94:034004, 2019.

[124] Daniel L. Freimund and Herman Batelaan. Bragg scattering of free electrons using the Kapitza-Dirac effect. *Phys. Rev. Lett.*, 89:283602, 2002.

[125] Jonathan Handali, Pratistha Shakya, and Brett Barwick. Creating electron vortex beams with light. *Opt. Express*, 23:5236–5243, 2015.

[126] A. Konečná and F. J. García de Abajo. Electron beam aberration correction using optical near fields. *Phys. Rev. Lett.*, 125:030801, 2020.

[127] P. E. Batson, N. Dellby, and O. L. Krivanek. Sub-ångstrom resolution using aberration corrected electron optics. *Nature*, 418:617–620, 2002.

[128] A. Howie. Electrons and photons: exploiting the connection. *Inst. Phys. Conf. Ser.*, 161:311–314, 1999.

[129] F. J. García de Abajo and M. Kociak. Electron energy-gain spectroscopy. *New J. Phys.*, 10:073035, 2008.

[130] N. Talebi. Interaction of electron beams with optical nanostructures and metamaterials: from coherent photon sources towards shaping the wave function. *J. Opt.*, 19:103001, 2017.

[131] N. Talebi. Electron-light interactions beyond the adiabatic approximation: recoil engineering and spectral interferometry. *Adv. Phys. X*, 3:1499438, 2018.

[132] N. Talebi. Strong interaction of slow electrons with near-field light visited from first principles. *Phys. Rev. Lett.*, 125:080401, 2020.

[133] M. A. Nielsen and I. L. Chuang. *Quantum Computation and Quantum Information (Cambridge Series on Information and the Natural Sciences).* Cambridge University Press, Cambridge, 1 edition, 2004.

[134] H. F. Talbot. Facts relating to optical science, No. IV. *Philos. Mag.*, 9:401–407, 1836.

[135] Lord Rayleigh. On copying diffraction-grating and on some phenomena connected with therewith. *Philos. Mag.*, 11:196–205, 1881.

[136] A. W. Lohmann and D. E. Silva. An interferometer based on the Talbot effect. *Opt. Commun.*, 2:413–415, 1971.

[137] A. W. Lohmann. An array illuminator based on the Talbot effect. *Optik*, 79:41–45, 1988.

[138] E. Noponen and J. Turunen. Electromagnetic theory of Talbot imaging. *Opt. Commun.*, 98:132–140, 1993.

[139] M. V. Berry and S. Klein. Integer, fractional and fractal Talbot effects. *J. Mod. Opt.*, 43:2139–2164, 1996.

[140] Y. Morimoto and P. Baum. Single-cycle optical control of beam electrons. *Phys. Rev. Lett.*, 125:193202, 2020.

[141] A. A. Kulaga and F. Ya. Khalili. Quantum states with minimum phase uncertainty. *JETP*, 77:587–592, 1993.

[142] R. H. Ritchie and A. Howie. Inelastic-scattering probabilities in scanning-transmission electron-microscopy. *Philos. Mag. A*, 58:753–767, 1988.

[143] Y. Pan and A. Gover. Spontaneous and stimulated emissions of a preformed quantum free-electron wave function. *Phys. Rev. A*, 99:052107, 2019.

[144] O. Kfir, V. Di Giulio, F. J. García de Abajo, and C. Ropers. Optical coherence transfer mediated by free electrons. *Sci. Adv.*, 7:eabf6380, 2021.

[145] M. Šunjić and A. A. Lucas. Multiple plasmon effects in the energy-loss spectra of electrons in thin films. *Phys. Rev. B*, 3:719–729, 1971.

[146] J. Itatani, F. Quéré, G. L. Yudin, M. Yu. Ivanov, F. Krausz, and P. B. Corkum. Attosecond streak camera. *Phys. Rev. Lett.*, 88:173903, 2002.

[147] Mark I. Stockman, Matthias F. Kling, Ulf Kleineberg, and Ferenc Krausz. Attosecond nanoplasmonic-field microscope. *Nat. Photon.*, 6:539–544, 2007.

[148] V. Di Giulio and F. J. García de Abajo. Electron diffraction by vacuum fluctuations. *New J. Phys.*, 22:103057, 2020.

[149] L. H. Ford. Electromagnetic vacuum fluctuations and electron coherence. *Phys. Rev. D*, 47:5571–5580, 1993.

[150] Y. Aharonov and D. Bohm. Significance of electromagnetic potentials in the quantum theory. *Phys. Rev.*, 115:485–491, 1959.

[151] J.-T. Hsiang and D.-S. Lee. Influence on electron coherence from quantum electromagnetic fields in the presence of conducting plates. *Phys. Rev. D*, 73:065022, 2006.

[152] H. Yoshioka. Effect of inelastic waves on electron diffraction. *J. Phys. Soc. Jpn.*, 12:618–628, 1957.

[153] P. Rez. Virtual inelastic scattering in high-energy electron diffraction. *Acta. Cryst.*, 34:48–51, 1978.

[154] Y. Levinson. Decoherence of electron beams by electromagnetic field fluctuations. *J. Phys. A: Math. Gen.*, 37:3003’963017, 2005.

[155] A. Howie. Mechanisms of decoherence in electron microscopy. *Ultramicroscopy*, 00:00, 2010.

[156] S. Scheel and S. Y. Buhmann. Path decoherence of charged and neutral particles near surfaces. *Phys. Rev. A*, 85:030101, 2012.

[157] Peter Sonnentag and Franz Hasselbach. Measurement of decoherence of electron waves and visualization of the quantum-classical transition. *Phys. Rev. Lett.*, 98:200402, 2007.

[158] P. J. Beierle, L. Zhang, and H. Batelaan. Experimental test of decoherence theory using electron matter waves. *New J. Phys.*, 20:113030, 2018.

[159] N. Kerker, R. Röpke, L. M. Steinert, A. Pooch, and A. Stibor. Quantum decoherence by Coulomb interaction. *New J. Phys.*, 22:063039, 2020.

[160] A. Howie and R. M. Stern. The optical potential in electron diffraction. *Z. Naturforsch. A*, 27:382–389, 1972.

[161] P. H. Dederichs. Dynamical diffraction theory by optical potential methods. *Solid State Physics*, 27:135–236, 1972.

[162] U. Kreibig and M. Vollmer. *Optical Properties of Metal Clusters.* Springer-Verlag, Berlin, 1995.

[163] J. D. Cox and F. J. García de Abajo. Nonlinear interactions between free electrons and nanographenes. *Nano Lett.*, 20:4792–4800, 2020.

[164] A. Rodríguez Echarri, E. J. H. Skjølstrup, T. G. Pedersen, and F. J. García de Abajo. Theory of electron energy-loss spectroscopy in atomically thin metallic films. *Phys. Rev. Research*, 2:023096, 2020.

[165] A. Liebsch. Surface-plasmon dispersion and size dependence of mie resonance: silver versus simple metals. *Phys. Rev. B*, 48:11317–11328, 1993.

[166] A. Liebsch. Surface plasmon dispersion of ag. *Phys. Rev. Lett.*, 71:145–148, 1993.

[167] F. Bloch. Bremsvermögen von atomen mit mehreren elektronen. *Z. Phys.*, 81:363–376, 1933.

[168] N. A. Mortensen, S. Raza, M. Wubs, T. Søndergaard, and S. I. Bozhevolnyi. A generalized non-local optical response theory for plasmonic nanostructures. *Nat. Commun.*, 5:3809, 2014.

[169] Christin David and F. J. García de Abajo. Surface plasmon dependence on the electron density profile at metal surfaces. *ACS Nano*, 8:9558–9566, 2014.

[170] R. H. Ritchie. Plasma losses by fast electrons in thin films. *Phys. Rev.*, 106:874–881, 1957.

[171] R. H. Ritchie and A. L. Marusak. The surface plasmon dispersion relation for an electron gas. *Surf. Sci.*, 4:234–240, 1966.

[172] Peter J. Feibelman. Surface electromagnetic fields. *Prog. Surf. Sci.*, 12:287–407, 1982.

[173] Yi Yang, Di Zhu, Wei Yan, Akshay Agarwal, Mengjie Zheng, John D. Joannopoulos, Philippe Lalanne, Thomas Christensen, Karl K. Berggren, and Marin Soljačić. A general theoretical and experimental framework for nanoscale electromagnetism. *Nature*, 576:248–252, 2019.

[174] S. Y. Buhmann, D. T. Butcher, and S. Scheel. Macroscopic quantum electrodynamics in nonlocal and nonreciprocal media. *New J. Phys.*, 14:083034, 2012.

[175] E. D. Palik. *Handbook of Optical Constants of Solids.* Academic Press, San Diego, 1985.

[176] A. Howie. Continued skirmishing on the wave-particle duality frontier. *Ultramicroscopy*, 203:52–59, 2019.

[177] G. Barton. Quantum mechanics of charged particles near a plasma surface. *J. Phys. A: Math. Gen.*, 31:601–612, 1977.

[178] P. A. D. Gonçalves, T. Christensen, N. Rivera, Antti-Pekka Jauho, N. A. Mortensen, and M. Soljačić. Plasmon–emitter interactions at the nanoscale. *Nat. Commun.*, 11:366, 2020.

[179] P. A. D. Gonçalves. *Plasmonics and Light–Matter Interactions in Two-Dimensional Materials and in Metal Nanostructures: Classical and Quantum Considerations.* Springer Nature, Switzerland, 2020.

[180] F. H. L. Koppens, D. E. Chang, and F. J. García de Abajo. Graphene plasmonics: A platform for strong light-matter interactions. *Nano Lett.*, 11:3370–3377, 2011.

[181] V. P. Gusynin, S. G. Sharapov, and J. P. Carbotte. On the universal ac optical background in graphene. *New J. Phys.*, 11:095013, 2009.

[182] R. Yu, A. Manjavacas, and F. J. García de Abajo. Ultrafast radiative heat transfer. *Nat. Commun.*, 8:2, 2017.

[183] P. L. Potapov, H. Lichte, J. Verbeeck, and D. van Dyck. Experiments on inelastic electron holography. *Ultramicroscopy*, 106:1012–1018, 2006.

[184] L. Mandel and E. Wolf. *Optical Coherence and Quantum Optics.* Cambridge University Press, Cambridge, 1995.

[185] S. Uhlemann, H. Müller, J. Zach, and M. Haider. Thermal magnetic field noise: electron optics and decoherence. *Ultramicroscopy*, 151:199–210, 2014.

[186] A. Howie. Addressing Coulomb's singularity, nanoparticle recoil and johnson's noise. *J. Phys. Conf. Ser.*, 522:012001, 2014.

[187] V. Di Giulio, O. Kfir, C. Ropers, and F. J. García de Abajo. Modulation of cathodoluminescence emission by interference with external light. *ACS Nano*, 15:7290–7304, 2021.

[188] Wei Zhang, Liron Stern, David Carlson, Douglas Bopp, Zachary Newman, Songbai Kang, John Kitching, and Scott B. Papp. Ultranarrow linewidth photonic-atomic laser. *Laser Photonics Rev.*, 14:1900293, 2020.

[189] Chonglei Zhang, Changjun Min, Luping Du, and X.-C. Yuan. Perfect optical vortex enhanced surface plasmon excitation for plasmonic structured illumination microscopy imaging. *Appl. Phys. Lett.*, 108:201601, 2016.

[190] Eric Betzig, George H. Patterson, Rachid Sougrat, O. Wolf Lindwasser, Scott Olenych, Juan S. Bonifacino, Michael W. Davidson, Jennifer Lippincott-Schwartz, and Harald F. Hess. Imaging intracellular fluorescent proteins at nanometer resolution. *Science*, 313:1642–1645, 2006.

[191] N. I. Zheludev. What diffraction limit? *Nat. Mater.*, 7:420–422, 2008.

[192] Guang Hui Yuan and Nikolay I. Zheludev. Detecting nanometric displacements with optical ruler metrology. *Science*, 364:771–775, 2019.

[193] R. Hillenbrand, T. Taubner, and F. Keilmann. Phonon-enhanced light-matter interaction at the nanometer scale. *Nature*, 418:159–162, 2002.

[194] M. Burresi, T. Kampfrath, D. van Osten, J. C. Prangsma, B. S. Song, S. Noda, and L. Kuipers. Magnetic light-matter interactions in photonics crystal nanocavity. *Phys. Rev. Lett.*, 105:123901, 2010.

[195] M. Wagner, Z. Fei, A. S. McLeod, A. S. Rodin, W. Bao, E. G. Iwinski, Z. Zhao, M. Goldflam, M. Liu, G. Dominguez, M. Thiemens, M. M. Fogler, A. H. Castro Neto, C. N. Lau, S. Amarie, F. Keilmann, and D. N. Basov. Ultrafast and nanoscale plasmonic phenomena in exfoliated graphene revealed by infrared pump–probe nanoscopy. *Nano Lett.*, 14:894–900, 2014.

[196] O. L. Krivanek, N. Dellby, J. A. Hachtel, J.-C. Idrobo, M. T. Hotz, B. Plotkin-Swing, N. J. Bacon, A. L. Bleloch, G. J. Corbin, M. V. Hoffman, C. E. Meyer, and T. C. Lovejoy. Progress in ultrahigh energy resolution EELS. *Ultramicroscopy*, 203:60–67, 2019.

[197] A. Polman, M. Kociak, and F. J. García de Abajo. Electron-beam spectroscopy for nanophotonics. *Nat. Mater.*, 18:1158–1171, 2019.

[198] M. S. Grinolds, V. A. Lobastov, J. Weissenrieder, and A. H. Zewail. Four-dimensional ultrafast electron microscopy of phase transitions. *Proc. Natl. Academ. Sci.*, 103:18427–18431, 2006.

[199] B. Barwick, H. S. Park, O. H. Kwon, J. S. Baskin, and A. H. Zewail. 4D imaging of transient structures and morphologies in ultrafast electron microscopy. *Science*, 322:1227–1231, 2008.

[200] D. J. Flannigan and A. H. Zewail. 4D electron microscopy: principles and applications. *Acc. Chem. Res.*, 45:1828–1839, 2012.

[201] L. Piazza, D. J. Masiel, T. LaGrange, B. W. Reed, B. Barwick, and Fabrizio Carbone. Design and implementation of a fs-resolved transmission electron microscope based on thermionic gun technology. *Chem. Phys.*, 423:79–84, 2013.

[202] K. Bücker, M. Picher, O. Crégut, T. LaGrange, B. W. Reed, S. T. Park, D. J. Masiel, and F. Banhart. Electron beam dynamics in an ultrafast transmission electron microscope with wehnelt electrode. *Ultramicroscopy*, 171:8–18, 2016.

[203] F. Houdellier, G. M. Caruso, S. Weber, M. Kociak, and A. Arbouet. Development of a high brightness ultrafast transmission electron microscope based on a laser-driven cold field emission source. *Ultramicroscopy*, 186:128–138, 2018.

[204] S. A. Aseyev, E. A. Ryabov, B. N. Mironov, and A. A. Ischenko. The development of ultrafast electron microscopy. *Crystals*, 10:452, 2020.

[205] Chunhui Zhu, Dingguo Zheng, Hong Wang, Ming Zhang, Zhongwen Li, Shuaishuai Sun, Peng Xu, Huanfang Tian, Zian Li, Huaixin Yang, and Jianqi Li. Development of analytical ultrafast transmission electron microscopy based on laser-driven schottky field emission. *Ultramicroscopy*, 209:112887, 2020.

[206] Y. Pan, B. Zhang, and A. Gover. Anomalous photon-induced near-field electron microscopy. *Phys. Rev. Lett.*, 122:183204, 2019.

[207] O. Reinhardt and I. Kaminer. Theory of shaping electron wavepackets with light. *ACS Photonics*, 7:2859–2870, 2020.

[208] I. Madan, G. M. Vanacore, S. Gargiulo, T. LaGrange, and F. Carbone. The quantum future of microscopy: wave function engineering of electrons, ions, and nuclei. *Appl. Phys. Lett.*, 116:230502, 2020.

[209] G. M. Vanacore, I. Madan, and F. Carbone. Spatio-temporal shaping of a free-electron wave function via coherent light-electron interaction. *Riv. Nuovo Cimento*, 43:567–597, 2020.

[210] C. M. S. Sears, E. Colby, R. Ischebeck, C. McGuinness, J. Nelson, and R. Noble. Production and characterization of attosecond electron bunch trains. *Phys. Rev. Accel. Beams*, 11:061301, 2008.

[211] P. Baum and A. H. Zewail. Attosecond electron pulses for 4D diffraction and microscopy. *Proc. Natl. Academ. Sci.*, 104:18409–18414, 2007.

[212] M. Kozák, N. Schönenberger, and P. Hommelhoff. Ponderomotive generation and detection of attosecond free-electron pulse trains. *Phys. Rev. Lett.*, 120:103203, 2018.

[213] N. Schönenberger, A. Mittelbach, P. Yousefi, J. McNeur, U. Niedermayer, and P. Hommelhoff. Generation and characterization of attosecond microbunched electron pulse trains via dielectric laser acceleration. *Phys. Rev. Lett.*, 123:264803, 2019.

[214] A. Ryabov, J. W. Thurner, D. Nabben, M. V. Tsarev, and P. Baum. Attosecond metrology in a continuous-beam transmission electron microscope. *Sci. Adv.*, 6:eabb1393, 2020.

[215] A. Gover and A. Yariv. Free-electron–bound-electron resonant interaction. *Phys. Rev. Lett.*, 124:064801, 2020.

[216] A. Ben Hayun, O. Reinhardt, J. Nemirovsky, A. Karnieli, N. Rivera, and I. Kaminer. Shaping quantum photonic states using free electrons. *Sci. Adv.*, 7:eabe4270, 2021.

[217] Z. Zhao, X.-Q. Sun, and S. Fan. Quantum entanglement and modulation enhancement of free-electron–bound-electron interaction, 2021.

[218] X. M. Bendaña, A. Polman, and F. J. García de Abajo. Single-photon generation by electron beams. *Nano Lett.*, 11:5099–5103, 2011.

[219] M. Grzelczak, J. Pérez-Juste, P. Mulvaney, , and L. M. Liz-Marzán. Shape control in gold nanoparticle synthesis. *Chem. Soc. Rev.*, 37:1783–1791, 2008.

[220] S. E. Lohse and C. J. Murphy. The quest for shape control: A history of gold nanorod synthesis. *Chem. Mater.*, 25:1250–1261, 2013.

[221] Taeko Matsukata, F. J. García de Abajo, and Takumi Sannomiya. Chiral light emission from a sphere revealed by nanoscale relative-phase mapping. *ACS Nano*, 15:2219–2228, 2021.

[222] M. Aeschlimann, M. Bauer, D. Bayer, T. Brixner, F. J. García de Abajo, W. Pfeiffer, M. Rohmer, C. Spindler, and F. Steeb. Adaptive subwavelength control of nano-optical fields. *Nature*, 446:301–304, 2007.

[223] Christopher Bäuerle, D Christian Glattli, Tristan Meunier, Fabien Portier, Patrice Roche, Preden Roulleau, Shintaro Takada, and Xavier Waintal. Coherent control of single electrons: a review of current progress. *Rep. Prog. Phys.*, 81:056503, 2018.

[224] V. Di Giulio, P. A. D. Gonçalves, and F. J. García de Abajo. An image interaction approach to quantum-phase engineering of two-dimensional materials. *Nat. Commun.*, 13:5175, 2022.

[225] Paul Harrison and Alex Valavanis. *Quantum Wells, Wires and Dots: Theoretical and Computational Physics of Semiconductor Nanostructures.* John Wiley & Sons, West Sussex, 2016.

[226] Leroy L. Chang and B. C. Giessen. *Synthetic Modulated Structures.* Academic Press, Orlando, 1985.

[227] L. Esaki and R. Tsu. Superlattice and negative differential conductivity in semiconductors. *IBM J. Res. Dev.*, 14:61–65, 1970.

[228] G. H. Döhler. Solid-state superlattices. *Sci. Am.*, 249:144–151, 1983.

[229] L. Esaki. A bird's-eye view on the evolution of semiconductor superlattices and quantum wells. *IEEE J. Quantum Electron.*, 22:1611–1624, 1986.

[230] D. L. Smith and C. Mailhiot. Theory of semiconductor superlattice electronic structure. *Rev. Mod. Phys.*, 62:173–234, 1990.

[231] Eougenious L. Ivchenko and Grigory Pikus. *Superlattices and Other Heterostructures*. Springer Series in Solid-State Sciences. Springer, 2nd edition, 1997.

[232] K. S. Novoselov, D. Jiang, F. Schedin, T. J. Booth, V. V. Khotkevich, S. V. Morozov, and A. K. Geim. Two-dimensional atomic crystals. *Proc. Natl. Academ. Sci.*, 102:10451–10453, 2005.

[233] A. K. Geim and I. V. Grigorieva. van der Waals heterostructures. *Nature*, page 419, 2013.

[234] K. S. Novoselov, A. Mishchenko, A. Carvalho, and A. H. Castro Neto. 2d materials and van der Waals heterostructures. *Science*, 353:aac9439, 2016.

[235] F. J. García de Abajo. Graphene plasmonics: challenges and opportunities. *ACS Photonics*, 1:135–152, 2014.

[236] Matthew Yankowitz, Jiamin Xue, Daniel Cormode, J. D. Sanchez-Yamagishi, K. Watanabe, T. Taniguchi, Pablo Jarillo-Herrero, Philippe Jacquod, and Brian J. LeRoy. Emergence of superlattice Dirac points in graphene on hexagonal boron nitride. *Nat. Phys.*, 8:382–386, 2012.

[237] Saien Xie, Lijie Tu, Yimo Han, Lujie Huang, Kibum Kang, Ka Un Lao, Preeti Poddar, Chibeom Park, David A. Muller, Robert A. DiStasio, and Jiwoong Park. Coherent, atomically thin transition-metal dichalcogenide superlattices with engineered strain. *Science*, 359:1131–1136, 2018.

[238] Wu Zhou, Yu-Yang Zhang, Jianyi Chen, Dongdong Li, Jiadong Zhou, Zheng Liu, Matthew F. Chisholm, Sokrates T. Pantelides, and Kian Ping Loh. Dislocation-driven growth of two-dimensional lateral quantum-well superlattices. *Sci. Adv.*, 4:eaap9096, 2018.

[239] C. Forsythe, X. Zhou, K. Watanabe, T. Taniguchi, A. Pasupathy, P. Moon, M. Koshino, Ph. Kim, and C. R. Dean. Band structure engineering of 2D materials using patterned dielectric superlattices. *Nat. Nanotech.*, 13:566–571, 2018.

[240] Bjarke S. Jessen, Lene Gammelgaard, Morten R. Thomsen, David M. A. Mackenzie, Joachim D. Thomsen, José M. Caridad, Emil Duegaard, Kenji Watanabe, Takashi Taniguchi, Timothy J. Booth, Thomas G. Pedersen, Antti-Pekka Jauho, and Peter Bøggild. Lithographic band structure engineering of graphene. *Nat. Nanotech.*, 14:340–346, 2019.

[241] Yutao Li, Scott Dietrich, Carlos Forsythe, Takashi Taniguchi, Kenji Watanabe, Pilkyung Moon, and Cory R. Dean. Anisotropic band flattening in graphene with one-dimensional superlattices. *Nat. Nanotech.*, 16:525–530, 2021.

[242] José M. Caridad, Stephen Connaughton, Christian Ott, Heiko B. Weber, and Vojislav Krstić. An electrical analogy to Mie scattering. *Nat. Commun.*, 7:12894, 2016.

[243] R. Yu, Q. Guo, F. Xia, and F. J. García de Abajo. Photothermal engineering of graphene plasmons. *Phys. Rev. Lett.*, 121:057404, 2018.

[244] Sheng Wang, Diego Scarabelli, Lingjie Du, Yuliya Y. Kuznetsova, Loren N. Pfeiffer, Ken W. West, Geoff C. Gardner, Michael J. Manfra, Vittorio Pellegrini, Shalom J. Wind, and Aron Pinczuk. Observation of Dirac bands in artificial graphene in small-period nanopatterned GaAs quantum wells. *Nat. Nanotech.*, 13:29–33, 2017.

[245] Lingjie Du, Ziyu Liu, Shalom J. Wind, Vittorio Pellegrini, Ken W. West, Saeed Fallahi, Loren N. Pfeiffer, Michael J. Manfra, and Aron Pinczuk. Observation of flat bands in gated semiconductor artificial graphene. *Phys. Rev. Lett.*, 126:106402, 2021.

[246] Yang Xu, Connor Horn, Jiacheng Zhu, Yanhao Tang, Liguo Ma, Lizhong Li, Song Liu, Kenji Watanabe, Takashi Taniguchi, James C. Hone, Jie Shan, and Kin Fai Mak. Creation of moiré bands in a monolayer semiconductor by spatially periodic dielectric screening. *Nat. Mater.*, 20:645–649, 2021.

[247] C. R. Dean, L. Wang, P. Maher, C. Forsythe, F. Ghahari, Y. Gao, J. Katoch, M. Ishigami, P. Moon, M. Koshino, T. Taniguchi, K. Watanabe, K. L. Shepard, J. Hone, and P. Kim. Hofstadter's butterfly and the fractal quantum hall effect in moiré superlattices. *Nature*, 497:598–602, 2013.

[248] Willi Pabst and Eva Gregorova. Elastic properties of silica polymorphs-a review. *Ceramics-Silikaty*, 57:167–184, 2013.

[249] R. Krishna Kumar, X. Chen, G. H. Auton, A. Mishchenko, D. A. Bandurin, S. V. Morozov, Y. Cao, E. Khestanova, M. Ben Shalom, A. V. Kretinin, K. S. Novoselov, L. Eaves, I. V. Grigorieva, L. A. Ponomarenko, V. I. Fal'ko, and A. K. Geim. High-temperature quantum oscillations caused by recurring Bloch states in graphene superlattices. *Science*, 357:181–184, 2017.

[250] Matthew Yankowitz, Qiong Ma, Pablo Jarillo-Herrero, and Brian J. LeRoy. van der Waals heterostructures combining graphene and hexagonal boron nitride. *Nat. Rev. Phys.*, 1:112–125, 2019.

[251] Kha Tran, Galan Moody, Fengcheng Wu, Xiaobo Lu, Junho Choi, Kyounghwan Kim, Amritesh Rai, Daniel A. Sanchez, Jiamin Quan, Akshay Singh, Jacob Embley, André Zepeda, Marshall Campbell, Travis Autry, Takashi Taniguchi, Kenji Watanabe, Nanshu Lu, Sanjay K. Banerjee, Kevin L. Silverman, Suenne Kim, Emanuel Tutuc, Li Yang, Allan H. MacDonald, and Xiaoqin Li. Evidence for moiré excitons in van der Waals heterostructures. *Nature*, 567:71–75, 2019.

[252] Chenhao Jin, Emma C. Regan, Aiming Yan, M. Iqbal Bakti Utama, Danqing Wang, Sihan Zhao, Ying Qin, Sijie Yang, Zhiren Zheng, Shenyang Shi, Kenji Watanabe, Takashi Taniguchi, Sefaattin Tongay, Alex Zettl, and Feng Wang. Observation of moiré excitons in WSe_2/WS_2 heterostructure superlattices. *Nature*, 567:76–80, 2019.

[253] Michael Förg, Anvar S. Baimuratov, Stanislav Yu. Kruchinin, Ilia A. Vovk, Johannes Scherzer, Jonathan Förste, Victor Funk, Kenji Watanabe, Takashi Taniguchi, and Alexander Högele. Moiré excitons in MoSe2-WSe2 heterobilayers and heterotrilayers. *Nat. Commun.*, 12:1656, 2021.

[254] Justin C. W. Song, Polnop Samutpraphoot, and Leonid S. Levitov. Topological Bloch bands in graphene superlattices. *Proc. Natl. Academ. Sci.*, 112:10879–10883, 2015.

[255] Guorui Chen, Aaron L. Sharpe, Eli J. Fox, Ya-Hui Zhang, Shaoxin Wang, Lili Jiang, Bosai Lyu, Hongyuan Li, Kenji Watanabe, Takashi Taniguchi, Zhiwen Shi, T. Senthil, David Goldhaber-Gordon, Yuanbo Zhang, and Feng Wang. Tunable correlated Chern insulator and ferromagnetism in a moiré superlattice. *Nature*, 579:56–61, 2020.

[256] Luojun Du, Tawfique Hasan, Andres Castellanos-Gomez, Gui-Bin Liu, Yugui Yao, Chun Ning Lau, and Zhipei Sun. Engineering symmetry breaking in 2D layered materials. *Nat. Rev. Phys.*, 3:193–206, 2021.

[257] D. Pan, R. Yu, H. Xu, and F. J. García de Abajo. Topologically protected Dirac plasmons in a graphene superlattice. *Nat. Commun.*, 8:1243, 2017.

[258] Scott H. Brewer and Stefan Franzen. Indium tin oxide plasma frequency dependence on sheet resistance and surface adlayers determined by reflectance ftir spectroscopy. *J. Phys. Chem. B*, 106:12986–12992, 2002.

[259] P.J. Jennings and R.O. Jones. Beyond the method of images—the interaction of charged particles with real surfaces. *Adv. Phys.*, 37:341–358, 1988.

[260] Peter J. Feibelman, C. B. Duke, and A. Bagchi. Microscopic description of electron-solid interactions at a surface. *Phys. Rev. B*, 5:2436–2462, 1972.

[261] Adolfo G. Eguiluz. Screening near a metal surface: Plasmon effects. *Phys. Rev. B*, 23:1542–1558, 1981.

[262] C. H. Hodges. Harris and jones image-potential formalism for a quantum particle : application to surface states. *J. Phys. C*, 8:1849–1861, 1975.

[263] J. R. Manson, R. H. Ritchie, P. M. Echenique, A. Gras-Marti, and T. L. Ferrell. Self-energies and the interactions of particles with many-body systems. *Phys. Scr.*, 39:725–730, 1989.

[264] F. J. García de Abajo and P. M. Echenique. Surface wake in the random-phase approximation. *Phys. Rev. B*, 48:13399–13407, 1993.

[265] Mark B. Lundeberg, Yuanda Gao, Reza Asgari, Cheng Tan, Ben Van Duppen, Marta Autore, Pablo Alonso-González, Achim Woessner, Kenji Watanabe, Takashi Taniguchi, Rainer Hillenbrand, James Hone, Marco Polini, and Frank H. L. Koppens. Tuning quantum nonlocal effects in graphene plasmonics. *Science*, 357:187–191, 2017.

[266] R. De L. Kronig and W. G. Penney. Quantum mechanics of electrons in crystal lattices. *Proc. R. Soc. London, Ser. A*, 130:499–513, 1931.

[267] J. Qiao, X. Kong, Z.-X. Hu, F. Yang, and W. Ji. High-mobility transport anisotropy and linear dichroism in few-layer black phosphorus. *Nat. Commun.*, 5:4475, 2014.

[268] A. Kormányos, G. Burkard, M. Gmitra, J. Fabian, V. Zólyomi, N. D Drummond, and V. Fal'ko. $\mathbf{k} \cdot \mathbf{p}$ theory for two-dimensional transition metal dichalcogenide semiconductors. *2D Mater.*, 2:022001, 2015.

[269] R. Yu and F. J. García de Abajo. Chemical identification through two-dimensional electron energy-loss spectroscopy. *Sci. Adv.*, 6:eabb4713, 2020.

[270] R. Franz and G. Wiedemann. Ueber die Wärme-Leitungsfähigkeit der Metalle. *Annalen der Physik*, 8:497–531, 1853.

[271] K. Ali, L. Fernández, M. A. Kherelden, A. A. Makarova, I. Píš, F. Bondini, J. Lawrence, D. G. de Oteyza, D. Y. Usachov, D. V. Vyalikh, F. J. García de Abajo, Z. M. Abd El-Fattah, J. E. Ortega, and F. Schiller. Atomically-precise texturing of hexagonal boron nitride nanostripes. *Adv. Sci.*, 8:2101455, 2021.

[272] V. Di Giulio and J. García de Abajo. Nanophotonics for pair production. *arXiv*, page 2301.07377, 2023.

[273] G. Breit and John A. Wheeler. Collision of two light quanta. *Phys. Rev.*, 46:1087–1091, 1934.

[274] H. Bethe and W. Heitler. On the stopping of fast particles and on the creation of positive electrons. *Proc. R. Soc. London, Ser. A*, 146:83–112, 1934.

[275] L. D. Landau and E. M. Lifschitz. On the production of electrons and positrons by a collision of two particles. *Phys. Z.*, 6:244, 1934.

[276] D. L. Burke and others. Positron production in multiphoton light-by-light scattering. *Phys. Rev. Lett.*, 9:1626–1629, 1997.

[277] J. Adam and others. Measurement of e^+e^- momentum and angular distributions from linearly polarized photon collisions. *Phys. Rev. Lett.*, 127:052302, 2021.

[278] P. J. Schultz and K. G. Lynn. Interaction of positron beams with surfaces, thin films, and interfaces. *Rev. Mod. Phys.*, 60:701–779, 1988.

[279] R. W. Siegel. Positron annihilation spectroscopy. *Annu. Rev. Mater. Sci.*, 10:393–425, 1980.

[280] S. W. H. Eijt, A. T. Van Veen, H. Schut, P. Mijnarends, A. B. Denison, B. Barbiellini, and A. Bansil. Study of colloidal quantum-dot surfaces using an innovative thin-film positron 2d-acar method. *Nat. Mater.*, 5:23–26, 2006.

[281] F. Tuomisto and I. Makkonen. Defect identification in semiconductors with positron annihilation: Experiment and theory. *Rev. Mod. Phys.*, 85:1583–1631, 2013.

[282] P. G. Coleman. Surface physics with slow positron beams. *Appl. Surf. Sci.*, 194:264–270, 2002.

[283] C. M. Surko, G. F. Gribakin, and S. J. Buckman. Low-energy positron interactions with atoms and molecules. *J. Phys. B: At. Mol. Opt. Phys.*, 38:R57–R126, 2005.

[284] G. F. Gribakin, J. A. Young, and C. M. Surko. Positron-molecule interactions: Resonant attachment, annihilation, and bound states. *Rev. Mod. Phys.*, 82:2557–2607, 2010.

[285] M. Amoretti and others. Production and detection of cold antihydrogen atoms. *Nature*, 419:456–459, 2002.

[286] G. Gabrielse, N. S. Bowden, P. Oxley, A. Speck, C. H. Storry, J. N. Tan, M. Wessels, D. Grzonka, W. Oelert, G. Schepers, T. Sefzick, J. Walz, H. Pittner, T. W. Hänsch, and E. A. Hessels. Background-free observation of cold antihydrogen with field-ionization analysis of its states. *Phys. Rev. Lett.*, 89:213401, 2002.

[287] G. B. Andresen and others. Trapped antihydrogen. *Nature*, 468:673–676, 2010.

[288] G. Gabrielse, R. Kalra, W. S. Kolthammer, R. McConnell, P. Richerme, D. Grzonka, W. Oelert, T. Sefzick, M. Zielinski, D. W. Fitzakerley, M. C. George, E. A. Hessels, C. H. Storry, M. Weel, A. Müllers, and J. Walz. Trapped antihydrogen in its ground state. *Phys. Rev. Lett.*, 108:113002, 2012.

[289] D. B. Cassidy and A. P. Mills, Jr. The production of molecular positronium. *Nature*, 449:195–197, 2007.

[290] A. P. Mills, Jr. Sources and physics of positrons. *Hyperfine Interact.*, 44:105–123, 1988.

[291] S. J. Gilbert, C. Kurz, R. G. Greaves, and C. M. Surko. Creation of a monoenergetic pulsed positron beam. *Appl. Phys. Lett.*, 70:1944–1946, 1997.

[292] S. J. Gilbert, J. P. Sullivan, J. P. Marler, L. D. Barnes, P. Schmidt, S. J. Buckman, and C. M. Surko. Low-energy positron-matter interactions using trap-based beams. *AIP Conf. Proc.*, 606:24–34, 2002.

[293] D. B. Cassidy, S. H. M. Deng, R. G. Greaves, and A. P. Mills, Jr. Accumulator for the production of intense positron pulses. *Rev. Sci. Instrum.*, 77:073106, 2006.

[294] M. R. Natisin, J. R. Danielson, and C. M. Surko. Formation mechanisms and optimization of trap-based positron beams. *Phys. Plasmas*, 23:023505, 2016.

[295] D. N. Basov, M. M. Fogler, and F. J. García de Abajo. Polaritons in van der Waals materials. *Science*, 354:aag1992, 2016.

[296] Tony Low, Andrey Chaves, Joshua D. Caldwell, Anshuman Kumar, Nicholas X. Fang, Phaedon Avouris, Tony F. Heinz, Francisco Guinea, Luis Martin-Moreno, and Frank Koppens. Polaritons in layered two-dimensional materials. *Nat. Mater.*, 16:182, 2017.

[297] David Alcaraz Iranzo, Sébastien Nanot, Eduardo J. C. Dias, Itai Epstein, Cheng Peng, Dmitri K. Efetov, Mark B. Lundeberg, Romain Parret, Johann Osmond, Jin-Yong Hong, Jing Kong, Dirk R. Englund, Nuno M. R. Peres, and Frank H. L. Koppens. Probing the ultimate plasmon confinement limits with a van der Waals heterostructure. *Science*, 360:291–295, 2018.

[298] Z. M. Abd El-Fattah, V. Mkhitaryan, J. Brede, L. Fernández, C. Li, Q. Guo, A. Ghosh, A. Rodríguez Echarri, D. Naveh, F. Xia, J. E. Ortega, and F. J. García de Abajo. Plasmonics in atomically thin crystalline silver films. *ACS Nano*, 13:7771–7779, 2019.

[299] Peining Li, Irene Dolado, F. J. Alfaro-Mozaz, Félix Casanova, Luis E. Hueso, Song Liu, James H. Edgar, Alexey Y. Nikitin, Saül Vélez, and Rainer Hillenbrand. Infrared hyperbolic metasurface based on nanostructured van der Waals materials. *Science*, 359:892–896, 2018.

[300] J. D. Caldwell, I. Aharonovich, G. Cassabois, J. H. Edgar, B. Gil, and D. N. Basov. Photonics with hexagonal boron nitride. *Nat. Rev. Mater.*, 4:552–567, 2019.

[301] Yilei Li, Alexey Chernikov, Xian Zhang, Albert Rigosi, Heather M. Hill, Arend M. van der Zande, Daniel A. Chenet, En-Min Shih, James Hone, and Tony F. Heinz. Measurement of the optical dielectric function of monolayer transition-metal dichalcogenides: MoS_2, $MoSe_2$, WS_2, and WSe_2. *Phys. Rev. B*, 90:205422, 2014.

[302] S. Röser. *Cosmic Matter.* Wiley-VCH, New York, 2008.

[303] F. Mandl and G. Shaw. *Quantum Field Theory.* Wiley, Hoboken, 2010.

[304] J. M. Jauch and F. Rohrlich. *The Theory of Photons and Electrons.* Springer, Berlin, 1976.

[305] The BW cross section is[304] $\sigma^{\rm BW} = (e^4\pi/2m_{\rm e}^2c^4)(1-x^2)\big\{(3-x^4)\log[(1+x)/(1-x)] - 2x(2-x^2)\big\}$ with $x = \sqrt{1-2m_{\rm e}^2c^4/[\hbar^2\omega_p\omega_g(1-\cos\theta_{p\gamma})]}$.

[306] H. R. Reiss. Absorption of light by light. *J. Math. Phys.*, 3:59–67, 1961.

[307] V. I. Ritus. Quantum effects of the interaction of elementary particles with an intense electromagnetic field. *J. Russ. Laser. Res.*, 6:497–617, 1985.

[308] A. Ansón-Casaos, J. A. Puértolas, F. J. Pascual, J. Hernández-Ferrer, P. Castell, A. M. Benito, W. K. Maser, and M. T. Martínez. The effect of gamma-irradiation on few-layered graphene materials. *Appl. Surf. Sci.*, 301:264–272, 2014.

[309] L. F. Dumée, C. Feng, L. He, F.-M. Allioux, Z. Yi, W. Gao, C. Banos, J. B. Davies, and L. Kong. Tuning the grade of graphene: Gamma ray irradiation of free-standing graphene oxide films in gaseous phase. *Appl. Surf. Sci.*, 322:126–135, 2014.

[310] E. J. C. Dias and F. J. García de Abajo. Complete coupling of focused light to surface polaritons. *Optica*, 8:520–531, 2021.

[311] V. G. Nedorezov, A. A. Turinge, and Yu M. Shatunov. Photonuclear experiments with Compton-backscattered gamma beams. *Phys.-Uspekhi*, 47:341–358, 2004.

[312] A. Gonoskov, A. Bashinov, S. Bastrakov, E. Efimenko, A. Ilderton, A. Kim, M. Marklund, I. Meyerov, A. Muraviev, and A. Sergeev. Ultrabright GeV photon source via controlled electromagnetic cascades in laser-dipole waves. *Phys. Rev. X*, 7:041003, 2017.

[313] J. Magnusson, A. Gonoskov, M. Marklund, T. Zh. Esirkepov, J. K. Koga, K. Kondo, M. Kando, S. V. Bulanov, G. Korn, and S. S. Bulanov. Laser-particle collider for multi-GeV photon production. *Phys. Rev. Lett.*, 122:254801, 2019.

[314] Chen Liu, Baifei Shen, Xiaomei Zhang, Liangliang Ji, Zhigang Bu, Wenpeng Wang, Longqing Yi, Lingang Zhang, Jiancai Xu, Tongjun Xu, , and Zhikun Pei. Ultra-bright, well-collimated, GeV gamma-ray production in the QED regime. *Phys. Plasmas*, 25:023107, 2018.

[315] Xing-Long Zhu, Tong-Pu Yu, Min Chen, Su-Ming Weng, , and Zheng-Ming Sheng. Generation of GeV positron and γ-photon beams with controllable angular momentum by intense lasers. *New J. Phys.*, 20:083013, 2018.

[316] Xing-Long Zhu, Min Chen, Su-Ming Weng, Tong-Pu Yu, Wei-Min Wang, Feng He, Zheng-Ming Sheng, Paul McKenna, Dino A. Jaroszynski, and Jie Zhang. Extremely brilliant GeV γ-rays from a two-stage laser-plasma accelerator. *Sci. Adv.*, 6:eaaz7240, 2020.

[317] Archana Sampath and others. Extremely dense gamma-ray pulses in electron beam-multifoil collisions. *Phys. Rev. Lett.*, 126:064801, 2021.

[318] N. Muramatsu and others. SPring-8 LEPS2 beamline: A facility to produce a multi-gev photon beam via laser Compton scattering. *Nucl. Instrum. Methods Phys. Res. A*, 1033:166677, 2022.

[319] R. Dahan, G. Baranes, A. Gorlach, R. Ruimy, N. Rivera, and I .Kaminer. Creation of optical cat and GKP states using shaped free electrons. *arXiv*, page 2206.08828, 2022.

[320] A. Feist, G. Huang, G. Arend, Y. Yang, J.-W. Henke, A. S. Raja, F. J. Kappert, R. N. Wang, H. Lourenço-Martins, Z. Qiu, J. Liu, O. Kfir, T. J. Kippenberg, and C. Ropers. Cavity-mediated electron-photon pairs, 2022.

[321] M. Khalaf and I. Kaminer. Compton scattering driven by quantum light. *arXiv*, page 2209.05079, 2022.

[322] F. J. García de Abajo. Optical emission from the interaction of fast electrons with metallic films containing a circular aperture: A study of radiative decoherence of fast electrons. *Phys. Rev. Lett.*, 102:237401, 2009.

[323] C.-H. Park, L. Yang, Y.-W. Son, M. L. Cohen, and S. G. Louie. Anisotropic behaviours of massless Dirac fermions in graphene under periodic potentials. *Nat. Phys.*, 4:213–217, 2008.

[324] M. Drienovsky, F.-X. Schrettenbrunner A. Sandner, D. Weiss, J. Eroms, M.-H. Liu, F. Tkatschenko, and K. Richter. Towards superlattices: Lateral bipolar multibarriers in graphene. *Phys. Rev. B*, 89:115421, 2014.

[325] V. L. Bonch-Bruevich and S. V. Tyablikov. *The Green Function Method in Statistical Mechanics.* North Holland, Amsterdam, 1962.

[326] J. J. Sakurai. *Modern Quantum Mechanics.* Addison-Wesley, Boston, 1994.

[327] S. Chaturvedi, M. S. Sriram, and V. Srinivasan. Berry's phase for coherent states. *J. Phys. A: Math. Gen.*, 20:L1071–L1075, 1987.

[328] M. Wilhelm. On the exponential solution of differential equations for a linear operator. *Communications on Pure and Applied Mathematics*, 7:649–673, 1954.

[329] J. D. Jackson. *Classical Electrodynamics.* Wiley, New York, 1999.

[330] A. Asenjo-Garcia and F. J. García de Abajo. Plasmon electron energy-gain spectroscopy. *New J. Phys.*, 15:103021, 2013.